ACADEMIE DE MONTPELLIER

Université Montpellier II

– SCIENCES ET TECHINQUES DU LANGUEDOC –

THESE

Pour obtenir le grade de

DOCTEUR DE L'UNIVERSITE MONTPELLIER II

Formation Doctorale : *Electronique*

Discipline : *Composants et Systèmes*

Ecole Doctorale : *I2S*

présentée et soutenue publiquement le 17 Novembre 2006

par

Federico RAVOTTI

Development and Characterisation of Radiation Monitoring Sensors for the High Energy Physics Experiments of the CERN LHC Accelerator

devant le Jury composé de :

M L. Dusseau	Professeur, Université Montpellier II	*Directeur de thèse*
M G. Sarrabayrouse	Directeur de Recherche, CNRS-LAAS, Toulouse	*Rapporteur*
M P. Fouillat	Professeur, IXL, Talence	*Rapporteur*
M F. Forest	Professeur, Université Montpellier II	*Président*
M J.R. Vaillé	Maitre de conférence, Université Montpellier II	*Examinateur*
M C. Joram	Docteur, CERN, Genève	*Examinateur*
M E. Tsesmelis	Docteur, CERN, Genève	*Invité*
M M. Moll	Docteur, CERN, Genève	*Invité*
M M. Glaser	Ingénieur, CERN, Genève	*Invité*

Prepared at :
European Organization for Nuclear Research (CERN)
Geneva 23, CH-1211, Switzerland

ACADEMIE DE MONTPELLIER

Université Montpellier II

– SCIENCES ET TECHINQUES DU LANGUEDOC –

THESE

Pour obtenir le grade de

DOCTEUR DE L'UNIVERSITE MONTPELLIER II

Formation Doctorale : *Electronique*

Discipline : *Composants et Systèmes*

Ecole Doctorale : *I2S*

présentée et soutenue publiquement le 17 Novembre 2006

par

Federico RAVOTTI

Développement et caractérisation de capteurs pour la métrologie du rayonnement dans les expériences du futur accélérateur LHC du CERN

devant le Jury composé de :

M L. Dusseau	Professeur, Université Montpellier II	*Directeur de thèse*
M G. Sarrabayrouse	Directeur de Recherche, CNRS-LAAS, Toulouse	*Rapporteur*
M P. Fouillat	Professeur, IXL, Talence	*Rapporteur*
M F. Forest	Professeur, Université Montpellier II	*Président*
M J.R. Vaillé	Maitre de conférence, Université Montpellier II	*Examinateur*
M C. Joram	Docteur, CERN, Genève	*Examinateur*
M E. Tsesmelis	Docteur, CERN, Genève	*Invité*
M M. Moll	Docteur, CERN, Genève	*Invité*
M M. Glaser	Ingénieur, CERN, Genève	*Invité*

Préparée au :
Laboratoire Européen pour la Physique des Particules (CERN)
Genève 23, CH-1211, Suisse

Resumé

La vérification des théories qui expliquent comment la vie s'est formée sur notre planète, a poussé la physique des hautes énergies vers de nouveaux défis technologiques. La fonction du CERN (Laboratoire européen pour la physique des particules), est de construire des accélérateurs de particules et des Expériences pour la physique des hautes énergies qui ont pour but la découverte de nouvelles particules sub-nucléaires et la vérification des models qui expliquent leurs interactions.

Les accélérateurs SPS et LEP au CERN ont permis la découverte et la vérification d'un grand nombre de particules qui étaient prévues par le Model Standard (SM). Il y a quand même encore des questions ouvertes et toutes les particules prévues par la théorie du SM, en particulier le boson de Higgs, n'ont pas encore été découvertes avec les énergies atteintes par l'accélérateur LEP.

La prochaine étape au CERN est donc la construction et la mise en service du grand collisionneur d'hadrons, le LHC. Le LHC pourra atteindre les énergies nécessaires pour la vérification de l'existence du boson de Higgs et d'autres particules avec des masses plus élevées. La détection de ces particules sera faite grâce aux expériences pour la physique des hautes énergies associes aux LHC qui seront installées aux quatre points d'interaction ou les deux faisceaux de protons de 7 TeV rentreront en collision.

Le LHC et ses expériences sont des machines très complexes, non seulement en raison de la technologie employée pour la constructions des détecteurs, mais aussi pour les systèmes de control et de protection qui doivent assurer la fiabilité et la survie des équipements pendant les 10 ans de fonctionnement du LHC et en cas d'accident. Les systèmes pour la métrologie du rayonnement sont partie intégrante des systèmes de protection de l'accélérateur et de ses Expériences.

Les systèmes pour la métrologie du rayonnement sont des systèmes distribués supposés mesurer les niveaux de rayonnement dans des endroits très proche du point d'interaction des protons ainsi que dans les régions des expériences qui logent les détecteurs plus externes. Le champ de rayonnement diffère en composition et en intensité en fonction du positionnement dans le volume de l'expérience. Dans la partie centrale, le champ de rayonnement sera très intense (doses totales de 1×10^5 Gy et fluences équivalentes silicium – Φ_{eq} – de plus que 1×10^{14} cm^{-2}) et dominé par les particules chargées produite directement par les collision des protons à 7 TeV. Dans les régions les plus externes, le champ est dominé par le rayonnement secondaire développé par

les interactions des particules chargées avec les matériaux des expériences elles-mêmes. Un champ de rayonnement composé principalement de neutrons et rayons gamma est alors attendu en ces endroits. Il est donc évident que les capteurs a employer au LHC doivent être capables travailler dans un environnement très agressif avec des niveaux de rayonnements très intenses, mais ils doivent aussi être capables de fournir une grande sensibilité pour mesurer des champs à faible intensité où des doses de quelque Gy et des fluences équivalentes silicium dans l'ordre de $1{\times}10^{8}$ cm^{-2} sont attendues par an. Détails par rapport aux systèmes qui composent LHC, ses expériences et le champ de rayonnement seront donnés dans le deuxième chapitre de ce travail.

Les buts des systèmes pour la métrologie du rayonnement sont principalement la vérification des prédictions des codes de calcul Monte Carlo et la quantification des dégâts induits par les rayonnements dans les détecteurs et dans les composants électroniques. Les deux quantités caractéristiques, d'intérêt pour ces types des mesures, sont donc le nombre de particules par unité de surface (fluence équivalente normalisée au dégât induits dans le silicium par les neutrons d'un MeV, Φ_{eq}) et l'énergie déposée dans les mariaux irradies (dose totale ou TID). Les différent types de capteurs aptes a la métrologie de ces deux quantités sont deux dispositifs a semi-conducteur (le dosimètres RadFETs et les diodes silicium *p-i-n*) ainsi que les matériaux qui basent leur propriétés dosimétriques sur le principe de la Luminescence Stimulées Optiquement (OSL). Tous ces capteurs ont la caractéristique commune de pouvoir être employés pour effectuer des mesures en temps réel et ils sont constitués de matériaux avec des valeurs de A et Z_{eff} idéales pour la mesure des effet des rayonnement dans les détecteurs et dans les composants électroniques. Les détails relatifs au fonctionnement des différentes technologies de dosimètres employés dans ce travail de thèse seront donnés dans le chapitre 3.

Les différents capteurs en temps réel, fournis par différents producteurs, ont été caractérisés et exposés en plusieurs facilités d'irradiation pour simuler les conditions attendues au LHC en terme de composition du champ de rayonnement et d'intensité. Pour ce travail de caractérisation, le rôle des facilitées d'irradiations à l'accélérateur PS (Proto-Syncrotron) du CERN a donc été très important car, les systèmes d'irradiation IRRAD1 et IRRAD2, reproduisent bien l'environnement radiatif attendu au LHC. Dans les chapitres 4 et 5 de ce travail une description exhaustive de ces deux systèmes d'irradiation a était faite ainsi qu'une caractérisation détaillée en dosimétrie utilisant différentes technologies de dosimètres passifs.

A l'issue de la procédure de qualification, deux RadFETs (chapitre 6) et deux diodes *p-i-n* (chapitre 7) ont été sélectionnés. Pour les dispositifs sélectionnés, un test spécifique dans un environnement mixte de la facilité IRRAD6 sera aussi présenté au chapitre 9. Ce test a eu comme but d'évaluer la réponse des quatre capteurs dans un champ de rayonnement avec des débits de dose et intensités de particules plus proches de l'environnement attendu au LHC. L'intégration de ces dispositifs au LHC, a enfin été étudiée au chapitre 10. La totalité des capteurs présentés dans cette thèse seront installés en quatre des cinq expériences du LHC (ATLAS, ALICE, LHCb et TOTEM). Certain seront aussi installés dans le tunnel du LHC ainsi que sur les infrastructures des cavernes qui contiennentăles expériences mêmes. En parallèle, différents matériaux OSL synthétisés pour la dosimétrie en champ mixte ont été caractérisés en vue d'une future utilisation au LHC dans le chapitre 8.

La présentation effectuée dans ce résume vise à introduire, dans un premier temps, les différents types de dosimètres considérés et les caractéristiques des facilités d'irradiation utilisées dans ce travail de thèse. Dans une deuxième partie, les principaux résultats obtenus seront exposes pour chaque technologie de capteurs. Ces résultats seront enfin utilisés pour sélectionner les capteurs adaptés aux expériences du LHC et pour discuter des problèmes concernant leur intégration. Le texte à suivre fait référence a certaines figures, certaines équations ou indication bibliographiques correspondant au corps de la thèse écrit en anglais.

0.1 Les moyens pour la dosimétrie au LHC

Le but de la dosimétrie est de quantifier le champ de rayonnement en faisant de mesures de fluence de particule et/ou de dépôt d'énergie [Leo93]. Dans le cas particulier du LHC, l'utilité de ce type de mesure a était déjà clarifiée au début de ce résumé [Rav04b, Hol02]. Plusieurs types de *dosimètres passifs* existent, parmi lesquels, les différents types utilisés d'intérêt pour ce travail sont l'Alanine (PAD), les RPL, les TLDs, les films Gafchromic, les feuilles d'aluminium utilisées pour les mesures d'activation, et le diodes silicium utilisées pour quantifier la dégradation du courant de fuite lors de leur irradiation. Tandis que les premiers dispositifs sont utilisés pour la mesure de la dose, les deux derniers sont utilises pour la détermination de la fluence de particules.

L'emploi des *dosimètres passifs* au LHC sera limité à cause du haut niveau de rayonnement rémanent attendu en certains endroits et aussi pour l'impossibilité d'atteindre certaines stations de mesure a cause des espaces très étroits disponibles entre les différents détecteurs. De plus, très fréquemment les dosimètres passifs sont étalonnes pour la mesure de la dose de rayonnement dans le tissue humain. Cette valeur reste difficile à interpréter pour l'évaluation des dégâts dans les dispositifs électroniques.

Les *dosimètres actifs* (ou en temps réel) représentent donc la solution à tous ces problèmes. Les principales caractéristiques de ces types de capteurs, étudiées en cette thèse sont énumérées ici :

0.1.1 Les transistors MOS utilisés comme dosimètre (RadFETs)

Le principe du RadFET repose sur les propriétés de piégeage de charges dans l'oxyde de grille d'un transistor MOS soumis à un rayonnement ionisant. Cet effet se manifeste par une variation sensible de la tension de seuil, il est donc possible d'utiliser un tel composant pour faire un capteur de radiations. Si on considère que le nombre de paires électron-trou générées dans l'oxyde du transistor MOS est proportionnel à la dose déposée et que le nombre de charges piégées est proportionnel au nombre de paires créées, on peut admettre que la charge piégée dans l'oxyde est proportionnelle à la dose ionisante. Il sera donc possible à partir de la mesure de la variation de la tension de seuil de déterminer après un étalonnage convenable, la valeur de la dose reçue [Hol74, Hol86]. La mesure de la tension de seuil peut se faire en temps réel sans avoir recours à une remise à zéro. Il est important de noter que ce type de dosimètre permet une mesure globale de la dose reçue jusqu'à saturation, il ne peut être réinitialisé. Il est donc à usage unique. D'une façon générale, si on néglige la contribution des états d'interface, on peut démontrer que la variation de la tension de seuil suite à une irradiation est due à la charge équivalente Q_{ot} (voir Eq. 3.1 de Pag. 26) que, située en bordure de l'oxyde, produirait le décalage en tension [Hol86, Dre89, Hug85]. De plus, toujours depuis l'Eq. 3.1 est possible de voir qu'en appliquant une tension sur la grille pendant l'irradiation (afin de mieux séparer toutes les charges créées), la charge positive se retrouve repoussée à l'interface Si/SiO_2, maximisant la variation du seuil du transistor et donc la sensibilité de RadFETs. Enfin, depuis des considération électrostatiques faites pour deriver l'équation 3.4, on peut encore augmenter la sensibilité du capteur en augmentant l'épaisseur d'oxyde du transistor.

Comme pour tout capteur, il est indispensable que la grandeur de sortie (ici la tension de seuil du transistor definies par l'Eq. 3.3) soit la moins dépendante possible d'autres grandeurs afin d'assurer une stabilité de l'information dans le temps. Ceci est particulièrement vrai ici car l'information doit être conservée par le capteur plusieurs mois voire plusieurs années comme dans le cas du LHC.

Les charges pigées dans l'oxyde résultant d'un dépôt de dose dans le transistor peuvent se recombiner et provoquer ainsi une variation de la tension de seuil indépendamment de la dose reçue. Ceci a pour effet de donner une grandeur de sortie erronée [Hol83]. Deux phénomènes physiques participent à cette recombinaison, l'effet tunnel d'une part et la guérison thermique d'autre part. L'effet tunnel qui est prépondérant à l'interface Si/SiO_2 fait intervenir le passage d'un électron depuis le silicium vers l'oxyde entraînant la recombinaison de ce dernier avec un trou piégé à l'interface (voir paragraphe 3.2.1.4) [Fle93, Fle95].

Un autre facteur qui va perturber la mesure est la variation de la tension de seuil du transistor en fonction de la température ambiante. Comme montre dans le Par. 3.2.1.5, une solution consiste à connaître avant irradiation l'influence de la température afin d'en tenir compte lors de la mesure [Har04, Sar94].

0.1.2 Les diodes silicium *p-i-n* utilisées en polarisation directe

Lors d'une série des collisions nucléaires, une particule libère un ou plusieurs atomes de recul très énergétiques qui vont ioniser ou exciter le cortège électronique du silicium mais aussi induire des autres collisions élastiques et inélastiques avec les atomes du silicium même [Mol99a]. Les résultats expérimentaux montrent que des zones de défauts sont ainsi crées dans le réticule cristallin du silicium et celles-ci se comportent comme des centres accepteurs pour les porteur de charges libres dans le matériel semiconducteur. D'un point de vue macroscopique, après une irradiation importante en champ de particules neutres et/ou chargées, la vie des porteurs de charges minoritaires (τ) diminue selon l'Eq. 3.9 [Swa66]. De plus, dans le cas d'un matériau semi-conducteur hautement résistif on remarque aussi un effet sur la résistivité du silicium qui augmente selon l'Eq. 3.12 [Ros90].

En produisant des diodes silicium du type *p-i-n* avec une partie intrinsèque (i) d'épaisseur W et de haute résistivité, il est donc possible d'exploiter l'augmentation globale de résistance due aux deux phénomènes décrits par les Eq. 3.9 et Eq. 3.12 dans le Par. 3.2.2.2. Ces phénomènes apparaissent lors de l'injection d'un courant constant dans la diode en polarisation directe. On observe alors une linéarité de la tension directe (V_F) aux bornes de la diode avec la fluence de particules (Φ_{eq}). Les courants direct à appliquer aux bornes des diodes pour leur lecture sont relativement élevées (de l'ordre du mA, appelé aussi haut niveau d'injection). Avec l'augmentation de la résistance ces courants de lecture élevés peuvent induire des phénomènes ohmiques de réchauffement dans les dispositifs. Pour faire face à ces problèmes, différentes techniques de mesure, basées sur l'utilisation de pulses rapides de courant ont été développées [Ant77, Car00].

Comme dans le cas précèdent de dosimètres RadFETs, l'effet de la température et l'annealing des défauts dans le cristal de silicium doivent être étudiés et pris en compte pour assurer la fiabilité des mesures faites avec ces dispositifs [Nag92].

0.1.3 Dosimètres basé sur le phénomène de Luminescence Stimulée Optiquement (OSL)

Dans ce travail de thèse, les matériaux mis au point par l'équipe *Electronique et Rayonnement* au laboratoire du CEM[2] de Montpellier ont été utilisés [Dus95]. Le choix du laboratoire était d'utiliser comme substrat des sulfures alcalino-terreux comme le SrS pour des raisons de simplicité de fabrication. Afin de créer des niveaux d'energie dans la bande interdite, ces sulfures sont dopés par l'adjonction d'une faible concentration (de l'ordre de quelques dizaines de ppm) d'impuretés de la famille des Lanthanides appelée aussi terres rares comme le Cérium (Ce) et le Samarium (Sm) [Mis92]. Dans le cas d'un matériau doublement dopé, l'expérience montre que le spectre de luminescence est dû à l'un des dopant (appelé activateur). Le spectre de stimulation est donné par l'autre dopant (appelé co-activateur). Il est donc possible de choisir judicieusement le couple de dopants afin de séparer au maximum les spectres d'émission et de stimulation de manière à perturber le moins possible la mesure. Fig. 3.10 montre les spectres de stimulation et d'émission du sulfure de strontium (SrS) dopé Samarium pour le co-activateur et pour le Cérium comme activateurs. Pour les matériaux de cet étude, le spectre de stimulation s'étendant de 700 à 1300 nm (proche infra-rouge) avec un maximum autour de 1 μm. L'avantage de ces longueurs d'onde de faible énergie est de ne pas pouvoir créer de paires électron-trou par effet photoélectrique lors de la stimulation. Le spectre d'émission s'étend au contraire de 450 à 650 nm (visible) avec un maximum aux alentours de 500 nm (vert) [Dus04b]. Pour ces longueurs d'ondes, il existe beaucoup de capteurs qui permettent de mesurer la luminescence des matériaux.

La mesure de la dose est obtenue à partir de la détection de l'intensité optique émise par le matériau lors de sa stimulation par un flux infrarouge constant. La Fig. 3.11 de Pag. 41 présente la forme du signal obtenu [Vai03b]. En mesurant le maximum du pic est possible d'obtenir une grandeur proportionnelle à la dose. Concernant la sensibilité des matériaux, le minimum détectable par la chaîne de mesure (matériau et système de détection) est de l'ordre de 10 μGy. On observe également une très bonne linéarité jusqu'à au moins 100 Gy soit environ une dynamique de sept décades.

De même que dans le cas des RadFETs, il existe dans les matériaux OSL des pièges peu profonds susceptibles d'être vidés après (ou même pendant l'irradiation) en dehors de toute stimulation optique. Ceci est dû à l'apport d'énergie sous forme de chaleur par les interactions phonon-électron. Si on irradie un échantillon à l'instant $t = 0$ et qu'on relève le signal OSL à l'instant t, on peut observer une courbe de décroissance appelée courbe de fading [Vai03a]. En effet, plus la température sera importante et plus le temps de stockage sera court. Ceci doite être pris en compte lors de mesure pour ne pas compromettre leur fiabilité, mais en même temps, il permet en outre de faire un reset thermique des matériaux.

0.2 Les moyens expérimentaux et les facilites d'irradiation au CERN-PS

Pour caractériser les différentes typologies de *dosimètres actifs*, différent facilitées d'irradiations ont été utilisées dans le cadre de cette thèse. Les chapitres 4 et 5 contiennent une description exhaustive des systèmes suivants :

1. **Réacteur TRIGA Mark II** au centre de recherche Jozef Stefan Institute (JSI) de Ljubljana en Slovénie : spectre de neutrons (voir Fig.4.4(b)) [Kri98] ;
2. **Faisceau neutron T2** à l'Université Catholique de Louvain-La-Neuve (UCL) en Belgique : neutrons a 20.4 MeV [Meu75] ;
3. **Faisceau proton PIF** au centre de recherche Paul Scherrer Institut (PSI) à Villigen en Suisse : protons de 60 MeV à 254 MeV [Haj02] ;
4. **Sources gamma** ^{137}Cs et ^{60}Co au CERN (GIF), au CEA - Saclay (PAGURE) et à l'Université Montpellier II : gammas a 662 keV et 1.17-1.33 MeV à différents débits de dose (see Sec. 4.1.5).
5. **Générateur rayons X SEIFERT** au CERN : spectre de la cible tungstène avec le choix de différents débits de dose ;
6. **Faisceau proton 24 GeV/c de la facilité IRRAD1** : en cette zone expérimentale, les protons accélères par l'accélérateur PS du CERN sont délivrés en "paquets" de $5{\times}10^{10}$ $particules/cm^2$ chacun [Gla99]. La fluence de protons est mesurée généralement avec la technique d'activation de feuilles d'aluminium, tandis que les profils du faisceau sont obtenus avec différents films sensibles aux rayonnements comme les OSL et les films Gafchromic. Avec ces techniques, la fluence est déterminée avec une précision de ± 7 % et des profils de faisceau avec la résolution de quelque 100 μm peuvent être obtenus. Parmi les différentes campagnes

de mesures conduites avec le but de caractériser le faisceau proton IRRAD1, en ce travail de thèse le paragraphe 5.1.4 décrit le premier test exécuté pour la construction d'un moniteur de profil en ligne, basé sur le phénomène d'émission d'électrons secondaires d'une feuille d'aluminium (SEE) [Pug02]. Associé a cette facilité, dans ce travail de thèse, l'environnement radiatif autour de la cible pour le faisceau proton IRRAD1 a été aussi beaucoup utilisé [Ler98]. La composition et la dosimétrie de cet endroit (baptisée IRRAD6 en ce travail) sont assurés par des simulations MonteCarlo comme expliqué au paragraphe 4.1.1.2.

7. **Environnement mixte neutrons/gamma de la facilité IRRAD2** : dans cet environnement radiatif, la fluence de neutrons est déterminées par la mesure de la dégradation du courant de fuite de diodes silicium [Mol99a, Gla00]. La dose est mesurée avec les différentes technologies de dosimètres passifs PAD, RPL, films, etc., comme montré sur la Fig. 5.8 de Pag. 65 [Con93]. Le résultat des mesures expérimentales montre que dans IRRAD2 la TID de 1 Gy dans le Si est accompagnée d'une Φ_{eq} de $4{\times}10^{11}$ cm^{-2}. La comparaison des mesures présentées dans le paragraphe 5.2 avec une série de simulation Monte Carlo exécutées pour IRRAD2 montrent un accord dans la détermination du Φ_{eq} de 21 %.

0.3 Principaux résultats dans la caractérisation des différents capteurs

0.3.1 Dosimètres RadFETs

Un lot de 7 RadFETs provenant de différents producteurs et avec des oxydes de grille d'épaisseurs (t_{ox}) différentes a été soumis à une procédure de sélection. Comme indiqué dans le schéma de Fig. 6.1, cette procédure comprend l'évaluation des différents capteurs aux types de rayonnements typiques du LHC et des études de stabilité temporelle suivant la méthode de l'annealing isochrone [Dus97, Sai00, Sai97]. A la fin de cette procédure deux type de RadFETs ont été sélectionnés et considérés comme adaptés aux besoins du LHC. Les RadFETs **LAAS 1600** avec une épaisseur d'oxyde de 1.6 μm pour mesurer dans les champs de rayonnement de faible LET et de faible intensité où une haute sensibilité est demandée. Les **REM TOT-501C du type K** avec une épaisseur d'oxyde de 0.25 μm pour mesurer les champs de rayonnement de LET élevé et de haute intensité où minimiser les effets de la recombinaison initiale dans l'oxyde [Aug82, Old00, Pea01] est plus important que la sensitibilité dans la détermination de la dose comme expliqué en détail au paragraphe 6.1.1.

Les RadFETs **LAAS 1600**, lors des différentes irradiations, ont démontré une sensibilité de 500 mV/Gy et une gamme dynamique a partir de quelque mGy jusqu'a quelques dizaine de Gy. Ces dispositifs sont donc le bon choix pour la métrologie des détecteurs installés dans les zones externes des expériences du LHC où des champs de rayonnement composés principalement de neutrons et de rayons gammas sont attendus. Dans le test d'irradiation à faible-débit à la facilité IRRAD6 (voir le Chapitre 9) des débits de dose de 2-3 mGy/h ont été mesurés pour ces capteurs. Les études d'annealing détaillées ont démontré que dans l'environnement LHC, ces dispositifs peuvent souffrir de l'effets des dégâts de déplacement, quoi que ce phénomène de perturbation de la mesure reste inférieur à 6 % après plus d'un an de prise de données. Dans la gamme de mesure d'intérêt pour l'LHC, ces capteurs se sont montrés insensibles aux neutrons rapides. En conclusion, ces caractéristiques permettent de garantir une précision de ± 10 % sur la mesure de la dose totale dans le temps.

Le RadFETs **REM TOT-501C type K**, lors des différents irradiations, ont démontré une sensibilité de 20 mV/Gy et une gamme dynamique a partir de 100 mGy jusqu'à quelques dizaine de kGy. Ces dispositifs sont donc le meilleur choix pour la métrologie des détecteurs installés dans les zones internes des expériences du LHC où des champs de rayonnement composés principalement de particules au minimum d'ionisation sont attendus. Dans le test d'irradiation à la facilité IRRAD6 (voir le Chapitre 9) ces dispositifs ont prouvé qu'ils fonctionnaient bien dans des champs mixtes a faible débit. Les études d'annealing détaillées et les mesures directes des courbes de drain des transistors, ont démontrés que dans l'environnement LHC jusqu'a une TID de 30 kGy et une Φ_{eq} supérieure à 1×10^{13} cm^{-2}, ces dispositif sont immunes aux effets des dégâts de déplacement. Apres avoir été exposes a plusieurs kGy de dose, les capteurs REM montrent de signes d'annealing inférieurs à 8 % après plus d'un an et avec des variation de température de plus de 15 °C pendant la prise de données. Pour ces dispositifs, opérés au courent de lecture conseillé par le producteur de 160 μA, une formule expérimentale a été proposée pour corriger les effets de la température à Pag. 94. Dans la gamme de mesure d'intérêt pour l'LHC, ces capteurs ont montré une sensibilité réduite d'un facteur 2 pour les neutrons rapides [Rav05b]. En conclusion, ces caractéristiques permettent de garantir une précision de ± 10 % sur la mesure de la dose totale dans le temps.

0.3.2 Diodes silicium *p-i-n*

Dans ce travail de thèse les diodes commerciales BPW34F [Bpw] ont été étudiées pour la métrologie des hauts niveaux attendus de Φ_{eq} dans les détecteurs les plus proches des points d'interaction aux expériences du LHC. L'étude effectuée dans ce travail de thèse a permis de déterminer les conditions optimales pour la lecture de ces dispositifs (pulses de courant de 1 mA avec une durée de moins d'1 seconde). Une étude complète des courbes I/V après différentes étapes d'irradiation aux neutrons et protons a aussi était menée. Au courant de 1 mA, ces dispositifs ont démontré une sensibilité de 9.1×10^{9} cm^{2}/mV et une gamme dynamique à partir de 2×10^{12} cm^{-2} et jusqu'à 4×10^{14} cm^{-2}. Pour $\Phi_{eq} < 2\times10^{12}$ cm^{-2} les dispositifs ne montrent pas de sensibilité aux déplacements produits par les particules dans le volume sensible du dispositif. Dans le test d'irradiation à la facilité IRRAD6 (voir Chapitre 9) ces dispositifs ont montré que les phénomènes d'annealing doivent être corrigés pour garantir une précision de ± 20 % sur la mesure à long terme. Pour cette raison, un paramétrage de correction du signal des diodes a été proposé comme rapporté dans l'équation 7.4 de page 126. Enfin, dans ce travail de thèse, a été propose de récupérer le manque de sensitivité de ces dispositifs, aux faible valeurs de Φ_{eq} avec une procedure de pre-irradiation.

Les diodes du producteur CMRP [Ros03] ont été étudiées pour la métrologie des faibles niveaux de Φ_{eq} attendus dans les détecteurs les plus éloignés des points d'interaction des expériences du LHC. L'étude effectuée en ce travail de thèse a permis de déterminer que, au courant de 1 mA, ces dispositifs ont démontré une sensibilité de 1.7×10^8 cm^2/mV et une gamme dynamique jusqu'à 2×10^{12} cm^{-2} avec un accord entre les différentes courbes d'étalonnage de ± 13 %. Pour $\Phi_{eq} > 2\times10^{12}$ cm^{-2} les dispositifs montrent de courbes de réponse supralineaires qui ne peuvent pas être utilisées pour la dosimétrie. Dans le test d'irradiation à la facilité IRRAD6 (voir Chapitre 9) ces dispositifs ont montré leur capacité à mesurer jusqu'au faible débit de 1×10^9 $cm^{-2}\cdot h^{-1}$ et que les phénomènes d'annealing restaient inférieurs aux erreurs de mesure. Une précision de mesure de ± 16 % a été déterminée en faisant la comparaison entre les mesures obtenues dans IRRAD6 et un set de simulations Monte Carlo exécutées pour le même environnement. Les détails relatifs à la dépendance en température du signal des dispositifs sont donnes dans la Sec. 7.2.2.

Enfin, une première caractérisation de diodes *p-i-n* en provenance de république Chèque a été effectuée. Ces dispositifs nommés LBSD existent en deux versions la diode Si-1 et la diode Si-2 [Pro89]. La caractérisation des deux types a été faite avec des protons de 254 MeV et dans le champ neutron du réacteur de l'institut JSI de Ljubljana en Slovénie. Le détails des mesures effectuées, en utilisant les diodes a un courant de 25 mA, sont donnés dans la section 7.3 et dans la Fig. 7.18. Les premières mesures montrent que ces dispositifs peuvent représenter une alternative valide aux diodes CMRP pour la dosimétrie des expériences du LHC.

0.3.3 Matériaux OSL

L'évaluation des OSLs dans le faisceau 23 GeV de la facilité expérimentale IRRAD1 est présentée dans ce travail. La réponse de l'OSL pur ce faisceau proton a confirmé la linéarité de la luminescence émise par le matériau jusqu'à une dose totale de 100 Gy. Des mesures de fading du même matériau sont présentées dans la Sec. 8.4.3. Ce dernier phénomène a été identifié comme facteur limitant potentiel dans l'assemblage des capteurs en temps réels basés sur cette technologie de matériaux. Pour la première fois dans ce travail de thèse, la caractérisation de matériaux OSL spéciaux, synthétisés pour augmenter leur réponse aux neutrons thermiques et rapides a aussi été présentée en Sec. 8.6. Les échantillons considèrés pour ce travail étaient préparés a partir du matériau OSL de base dopé bore (sensibilité aux neutrons thermiques) et mélangés avec du polyethilene (sensibilité aux neutrons rapides). Le test d'irradiations dans deux champs de neutrons différents (IRRAD2 au CERN et le réacteur nucléaire de l'institut JSI) ont démontré la possibilité de discriminer les différentes composantes neutroniques avec une précision de 20 %. D'autre part, ces matériaux restent encore en phase de développement et la reproductibilité des mesures avec les différents sets de matériaux sensibles doit encore être améliorée.

La caractérisation des systèmes temps réel qui s'articulent autour des matériaux OSL, dans l'environnement typique LHC, a aussi été présentée en cette thèse. Les systèmes intégrées qui basent leur fonctionnement sur la structure émetteur infrarouge/matériel OSL/récepteur de lumière visible [Vai03b], ont montré leur faiblesse vis-à-vis des dégâts induits par le rayonnement dans les composant électroniques exposées au rayonnement en même temps que l'OSL. Pour faire face à ce problème, cette thèse propose l'approche d'un système OSL fibré (matériel OSL au bout d'un couple de fibres optiques qui véhiculent les signaux lumineux vers l'électronique de lecture déportée hors du champ de rayonnement). Un premier prototype a été construit avec des fibres optiques déjà utilisées au CERN [Mer05] dans des champs de rayonnements très durs et les premiers résultats très prometteurs (sensibilité de l'ordre du mGy) ont été présentés dans ce travail.

0.4 Intégration dans les expériences du LHC et conclusions

Dans la partie finale de cette thèse (chapitre 10), le quatre capteurs a semiconducteurs sélectionnes et retenus comme adaptes pour la dosimétrie au LHC (RadFETs LAAS et REM, diodes *p-i-n* BPW34F et CMRP) ont été intégrés dans une carte électronique de lecture unique. L'intégration de ces dispositifs est basée sur le fait que tous ces dosimètres peuvent être lus de la même façon avec l'injection d'un courant de lecture et que les quatre doivent être utilisés en même temps pour avoir une mesure quantitative des champs de rayonnement mixtes complexes du LHC.

L'intégration de dosimètres RadFETs est la plus difficile car la mesure de dose effectuée par ces dispositifs peut être affectée par les matériaux qui l'entourent, comme le boiter. Pour cette dernière raison, un boîtier spécifique a été conçu et son choix a été validé avec l'utilisation du code de calcul Monte Carlo GEANT4 (voir la Section 6.5). En particulier dans cette thèse sont présentés les premiers travaux de validation expérimentale de ce code avec des protons de 254 MeV et avec les neutrons du réacteur de l'institut JSI de Ljubljana en Slovénie. Pour les protons de 254 MeV il a de plus été possible de démontrer le bon accord entre les résultats simulés et les mesures expérimentales.

Plusieurs séries de capteurs présentés en cette thèse sont actuellement (Octobre 2006) en phase d'installation dans les différentes expérience du LHC au CERN.

Contents

Chapter 1

Introduction

The verification of theories aiming to explain how the world in which we all live is formed, pushes Particle Physics towards new technological challenges. At CERN (European Organization for Nuclear Research) particle accelerators and High Energy Physics experiments are built in order to discover new sub-nuclear particles and to verify the models that explain the interactions of these particles. The SPS (Super Proton Synchrotron) and the LEP (Large Electron Positron) colliders at CERN, and other accelerators around the world allowed the discovery of a whole set of particles that were predicted by the Standard Model (SM), making a big step towards its verification. However, some questions still remain open and not all the particles that were predicted have appeared. In particular, the Higgs boson, has still not been detected, as well as other massive particles that did not appear up to the highest energies reached in LEP collisions.

The next step of CERN is therefore the construction and commissioning of the Large Hadron Collider (LHC). The LHC accelerator will reach the energies necessary to verify the existence of the Higgs boson and other particles. The task to detect new particles is given to the experiments that surround the four interaction points where the two 7 TeV beams of the LHC accelerator will collide.

The LHC and its experiments are not only complex because of the technology needed in order to detect particles, but also because of the protection and safety systems that must ensure the reliability of the measurements over time and survival of the equipment in case of accidents that, in such a complex machine, may happen.

One of those systems is the Radiation Monitoring. Radiation Monitoring systems will be installed in the LHC machine as well as in the various sub-detectors that constitute its experiments. The sensors presented in this thesis are the ones that will be used in four of the five experiments (ATLAS, ALICE, LHCb and TOTEM). Some of them will be also installed in the LHC tunnel and experimental areas cavern walls.

The Radiation Monitoring equipment for the LHC experiments are distributed systems that are intended to work relatively close to the interaction points as well as far away from them in the outer detector regions. The radiation environment encountered in the selected measurement locations will thus be varying in composition and intensity depending on the position within the volume of the experiment. The radiation field in the central part of the experiments will be very intense (TID of 1×10^5 Gy and Φ_{eq} of more than 1×10^{14} cm^{-2} per year) and dominated by charged hadrons directly produced by the collisions of the 7 TeV protons. In the outer detector regions, the field is instead dominated by the secondary radiation generated from the interaction of the charged hadrons with the materials of the sub-detectors themselves. A radiation field manly composed by neutrons and γ-rays is expected there. For this reason the sensors that have to be employed must be able to withstand a hostile, high-intensity radiation environment but also provide high sensitivity to monitor low intensity fields where the TID of some Gy and Φ_{eq} in the order of 1×10^8 cm^{-2} are expected per year.

The aim of the Radiation Monitoring is manly to cross check the predictions of Monte Carlo simulations and to assess the radiation induced damage in materials, detectors and electronic components during both normal operation as well as after accidents. For the first purpose, the accuracy of the Monte Carlo models developed to predict the radiation field in LHC and its experiments, is intended within a factor two. Therefore the radiation monitoring measurements are needed for their validation. For the second purpose, dosimetric measurements can provide a valuable indication on which element should be replaced to guarantee the reliability of the overall system over time.

From all above reasons it is therefore clear that dosimetric measurements have to be performed over the LHC lifetime to quantify the radiation fields in terms of particle fluence (Φ_{eq} in cm^{-2}) and the energy imparted to the irradiated material (Deposed Dose in Gy). The radiation monitoring sensors (or dosimeters) play therefore a key role in the monitoring of the above described challenging environment expected at the LHC experiments.

The type of sensors investigated in this thesis work are solid-state semiconductor devices (Radiation-sensing Metal Oxide Semiconductor sensors or RadFETs and *p-i-n* silicon diodes) as well as Optically Stimulated Luminescent (OSL) Materials. The studied sensors have the common characteristic that they can be employed to perform on-line remote measurements and they are made of materials suitable to measure the effect of the radiation in semiconductor components and detector equipment. In this thesis, several sensor samples have been characterized, irradiated in various radiation facilities and tested in a dedicated radiation field (variable-intensity mixed hadron field) that simulate the exposure conditions that the sensors will face at the LHC experiments. For this last purpose, the irradiation facilities at the CERN Proton Synchrotron (PS) accelerator play a privileged role in the framework of this thesis work. Therefore their detailed dosimetric characterization will be also presented here.

The results of the characterization tests, the data analysis and the conclusions extracted are presented in this work and brought to a selection of a set of devices that, at the present state-of-the-art, have been proven to fulfill the LHC experiment requirements in terms of radiation response and measurement reliability. For these "selected" sensors the issue of the integration at the LHC experiments have been also faced with the study and the conception of a dedicated packaging and a dedicated sensor carrier PCB suitable for the installation into the LHC.

The study presented here has been carried out working with the DT2 group of the CERN Physics (PH) Department in collaboration with the LEA group of the CERN Technical Support (TS) Department in the framework of the CERN Doctoral student program.

Chapter 2 serves as introduction to the CERN-LHC and its experiments: ATLAS, CMS, LHCb, ALICE and TOTEM. In this chapter details about the radiation environment expected at the LHC accelerator, and in the sub-detector systems that will be monitored, are presented. Moreover the possible effects the radiation field induce on the electronics and the particle detectors will be discussed.

Chapter 3 gives an overview about the different dosimetric technologies employed around particle accelerators. This overview includes the *Passive Devices* that in this thesis work are widely used to compare and validate the measurement performed with the *Active Sensors*. These late ones are described in detail in this chapter as they are the main subject of this thesis work.

Chapter 4 and Chapter 5 are dedicated to the description of the different irradiation facilities used to test the sensors and the dosimetry at the CERN-PS irradiation facility. The experimental procedures and methods described in this chapter and the performed calibration campaigns allow to assess the particle fluxes and the energy deposition in the high-energy proton beam of the IRRAD1 facility, in the mixed γ-neutron environment of the IRRAD2 facility and in the hadron environment of the IRRAD6 facility.

Chapter 6 and 7 details the characterization of the **RadFET** and ***p-i-n* diode** dosimeters. The device responses in charged particles, fast neutron fields and in mixed radiation environments are discussed here in detail. Moreover RadFET stability studies with means of Isochronal and Isothermal annealing techniques have been carried out with the goal to select the devices that best suit the operation in the LHC experiments radiation fields. Once the devices had been selected, a detailed characterization and the determination of the devices key parameters have been carried out. For RadFETs only (Chapter 6) packaging studies with the help of a GEANT4 Monte Carlo simulation code were also carried out.

Chapter 8 is entirely dedicated to the **OSL dosimeters**. The characterization of this material for CERN-LHC applications span here from the measurement of the materials response in the MIP beams and neutrons of different energies, to the development of different kinds of on-line sensors based on this sensitive material. The advantages and the limitation of the use of this devices at the LHC will be discussed in detail. Moreover, the first characterization of OSL materials with enhanced sensitivity to different energy neutrons will be also presented.

Finally, before drawing the conclusions, in Chapter 9 the validation of the selected sensors in a radiation environment with similar conditions as the LHC will be presented. The integration issue involving the installation of the selected sensors at the LHC machine and Experiments is instead discussed in Chapter 10.

Chapter 2

LHC radiation environment and its effects on the equipment

The radiation environment encountered at the experiments of the Large Hadron Collider (LHC) at CERN will differ strongly from the ones in which the existing dosimetric technologies are typically used (space applications, medicine, radiation protection, etc.).

The mixed field expected at the four big experiments located around the LHC ring will be composed of neutrons, photons and both charged and neutral hadrons[1]. This complex field, which has been simulated by Monte Carlo codes [Daw00, Huh95], is due to particles generated by the proton-proton collisions and reaction products of these particles with the sub-detector materials of the experiments themselves. The proportion of the different particle species in the field will depend on the distance and on the angle with respect to the interaction point (i.e. the radiation environment will be unique in each sub-detector constituting the experiments). For example, in the EndCap modules of the electromagnetic calorimeter of the CMS Experiment [CMS94], the Total Ionizing Dose (TID) over a 10-year period is estimated to reach 100 kGy and the fast hadron fluence is expected to exceed 10^{14} particle/cm^2. These radiation levels are much lower if we consider instead the muon chambers location at the ATLAS Experiment [ATL97]. Cumulated radiation doses of some tens of mGy and hadron fluences of 10^8 particle/cm^2 are expected there.

The main concern related to radiation damage in accelerator facilities is to avoid that the kinetic energy of the particles is released unintentionally into the equipment. However, it will be also inevitable that a certain amount of particles will be lost from the beam, even under optimum conditions [Gil05].

Due to these energy losses, detectors as well as microelectronic equipment and all materials at LHC will suffer from radiation damage being exposed to different kinds of radiation. The energy deposition due to ionization processes will be responsible for the accumulation of charge in insulator materials (e.g. Silicon dioxide present in microelectronics circuits and detectors) and it will be thus responsible for instance for the aging of gas detectors, scintillators and optical fibers. The energy deposed by particles producing defects in semiconductor crystals will be instead the main concern in the loss of performances of silicon detector devices. Finally, the high amount of energy released

[1]Hadrons are particles which interact via the strong force such as p, π, μ, n, etc.

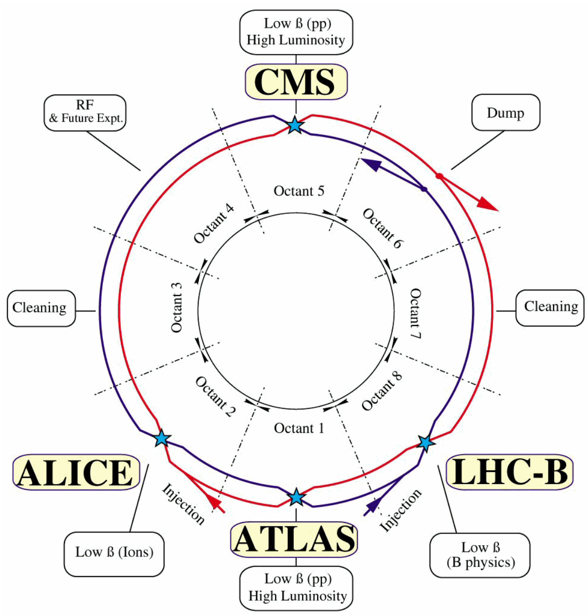

Figure 2.1: Layout of the LHC accelerator.

by the fast hadron component present in the LHC field, will be responsible for Single Event Effect phenomena that may compromise the operation of memories and other digital circuits.

The aim of this chapter is to introduce the LHC and its High Energy Physics (HEP) experiments and to describe in detail the radiation environment expected around them. Moreover, in this chapter, a brief review on the radiation effects induced by the different components of the radiation filed on electronics and detector systems will be given.

2.1 The CERN Large Hadron Collider

The Large Hadron Collider (LHC) is a proton-proton (pp) collider expected to deliver the first beams during 2007 in the existing infrastructures previously used at CERN by the Large Electron Positron (LEP) accelerator [CER04]. This new machine will accelerate protons reaching an unprecedent center-of-mass energy of 14 TeV and a luminosity[2] of 10^{34} $cm^{-2}s^{-1}$ during pp runs. The LHC will also accelerate heavy ions. For Pb-Pb collisions the maximum center-of-mass energy per participating nucleon will be of 5.5 TeV and the achievable luminosity for these runs will be of 10^{27} $cm^{-2}s^{-1}$. In order to accelerate particles to such high energies within the confines of the existing LEP tunnel of 26.6 km circumference, the machine uses a magnetic system composed of 1232 dipole magnets with a strength of 8.33 T that employ superconducting coils operating with 11.2 kA current. To achieve superconductivity at these strong magnetic fields the magnets must be operated at 1.8 K with superfluid helium. Contrary to the case of the LEP, in

[2]Unit of measure of the number of events per second generated by the interaction of two particle beams.

which electrons and positrons were circulating in the same beam pipe, the LHC requires two beam pipes in which protons travel in opposite directions.

The two LHC beams intersect in four points of the ring called Interaction Points (IPs), where the five high-energy physics experiments are located. The main goals of these experiments are the discovery of the Higgs particle and the study of rare events with high center-of-mass collision energies. The ATLAS [ATL97] and the CMS experiment [CMS94], located in IP1 and IP5 respectively, are general purpose detectors optimized for the operation during the high luminosity *pp* runs. In addition to them, the LHC has two low luminosity experiments: LHCb [LHC98], located in IP8, for the physics of the B-meson and the TOTEM Experiment [TOT99] (located in IP5 as CMS) for the detection of protons from elastic scattering at small angles with respect to the direction of the incoming primary beams. Finally the LHC has the ALICE experiment [ALI95] located in IP2 and optimized for the study of Pb-Pb collisions.

As shown in Fig. 2.1, the LHC machine is composed of eight octants. In each of this octants there are eight sections named *ARCs* where the beams are bent and eight Insertion Regions *IRs* that are the parts of the ring between the *ARCs* that host both the intersections and the interaction points. More in detail, the insertion regions consist of one Dispersion Suppressors (*DS*) a full long straight section *LSS* and a second *DS*. The *LSS* include insertion magnets which have the task to join both beams into the same beam-pipe for the collisions. Moreover, in order to get a low betatron oscillation in the *LSS* region, the beams are focused by means of inner triplet magnets. The four insertions that don't host IPs are used for the beam-dump system, the beam-cleaning system (collimation), the RF-cavities system (to accelerate the particles) and the injection beam-lines that transfer the particles at 450 GeV coming from the SPS machine into the LHC.

While the LHC and its experiments will run, the particles generated at the IPs, together with the ones arising from other type of interactions, will loose their energy inside the equipment surrounding them. The major radiation sources at the LHC are thus the particle production from proton interactions, local beam losses and beam-gas interactions.

2.1.1 Radiation levels around the LHC machine

When the LHC beams will circulate, the stopping of high energy protons will trigger reactions in the nuclei of the atoms of the residual gas in the beam pipe and in all materials surrounding it. These initial reactions will produce secondary lower-energy particles such as neutrons, protons and pions. This process is at the origin of prompt radiation and it will continue until the particles do not have sufficient energy to create further nuclear reactions. Moreover, the nuclei of the struck atoms will fragment and create a range of lower mass instable nuclei that decay via electron capture or via β-emission. This effect occurs in a time scale varying from minutes to several days even when the beam is off, is at the origin of the remnant radiation in the LHC tunnel [Wij05b].

Fig. 2.2 gives an overview of distribution of radiation along the LHC ring. Radiation close to the mid-*ARC* region is expected to come from the beam-gas interactions (yellow colored parts of Fig. 2.2). Occasionally, radiation may also come from He or air leaks,

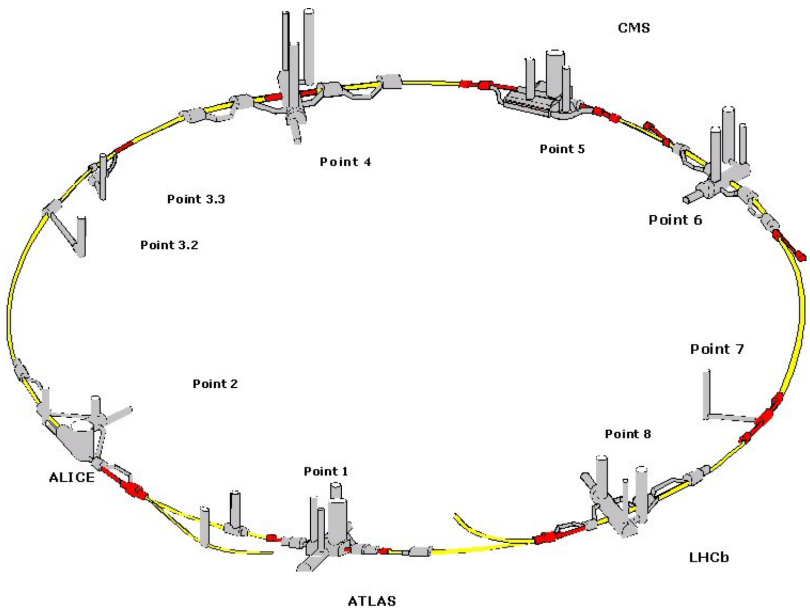

Figure 2.2: Radiation levels along the LHC ring. In the picture the yellow-colored parts correspond to the *ARC* regions in which the radiation field is dominated by beam-gas interactions. Red-colored are instead the section of the ring in which the point-losses are main responsible of the radiation levels.

obstruction of the beam channel, or because of bad beam orbits due to faulty corrector magnets.

When the LHC machine will be operational at full luminosity, the beam losses are expected to be lower than 10^7 protons/s. Beam-gas interactions are estimated to be around 10^2 particles/(m×s). Thus, the main source of radiation are the secondary particles generated from the proton collisions of the LHC beams (around 10^9 particles/s). Therefore, approaching the *IRs* from the mid-*ARC*, point losses start to make an increasingly important contribution (red colored parts of Fig. 2.2). The point losses are caused not only by the *pp* collisions in IP1 and IP5, but also by injection errors (IP2, IP8), by collimators (IP3, IP7), RF, beam instrumentation operation (IP4) and from the beam-dump system (IP6). As a "rule of the thumb", the dose rates close to the cryostats of the main magnets are of the order of 10 Gy per year in the *ARCs*, 100 Gy per year in the *DS* regions and more than 1 kGy in the *LSS* [Bai00, Fyn02].

2.2 Detectors for high energy physics experiments at the LHC

Collider experiments are made up of different components called *sub-detectors*. These components are usually posed as almost-concentric layers around the IPs. Each *sub-detector* is specialized in detecting a set of properties for a definite particle type.

Starting from the IP, in the innermost parts of the experiments are the tracking devices. They operate in strong magnetic field in order to measure points on the bent

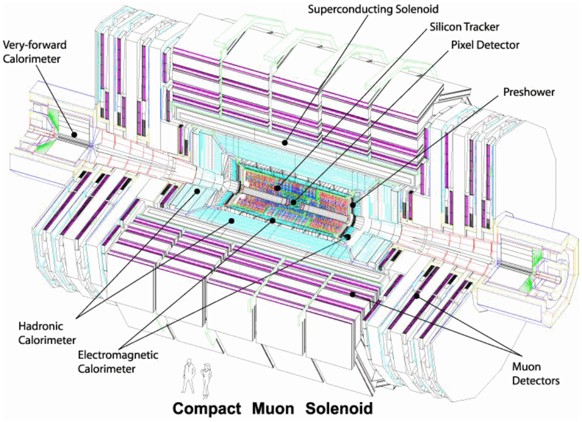

(a) Complete view of the CMS Experiment

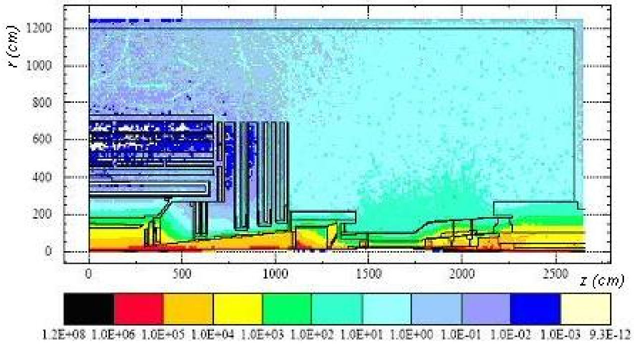

(b) Radiation Dose (rad)

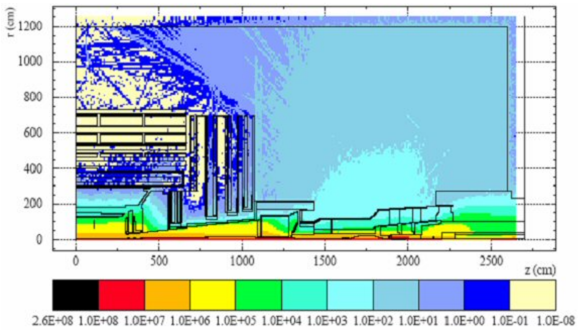

(c) Charged hadron Flux ($cm^2 s^{-1}$)

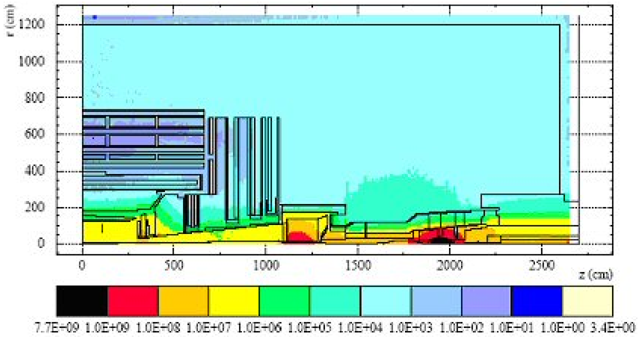

(d) Neutron Flux ($cm^2 s^{-1}$)

Figure 2.3: Radiation Field inside the CMS Experiment (a). The dose map (b) has been determined for 10 years operation of the machine while charged hadrons (c) and neutron (d) fluxes have been calculated for normal operational conditions (see text) [Huh02].

particle trajectories. From the measurement of the bending radius it is then possible to calculate the particles charge (q) and momentum (p).

All charged particles detected in the tracking devices deposit their energy in the calorimeter devices that are located in the following detector layer. According to the type of interaction of particles with matter, the calorimeters are divided in two categories: electromagnetic or hadronic. Photons are detected by the electromagnetic calorimeter while neutrons are seen by the energy they deposit in the hadron calorimeters. If a charged particle traverses large amounts of absorber (e.g. *sub-detectors*) with minor energy losses and small angular displacement such a particle is considered as a muon. Muons are thus finally identified in the muon chambers, after having penetrated through all the detector systems. This "typical" layout of an HEP experiment is visible, for example, in the CMS cross section shown in Fig. 2.3(a).

2.2.1 ATLAS and CMS radiation environment

The radiation environment close to the Interaction Points (IPs) of ATLAS and CMS, is going to be extremely hostile. The LHC will produce around 8x10^8 *pp* inelastic events per second, at a luminosity of 10^{34} $cm^{-2}s^{-1}$ and for a total cross section of 80 mb. The

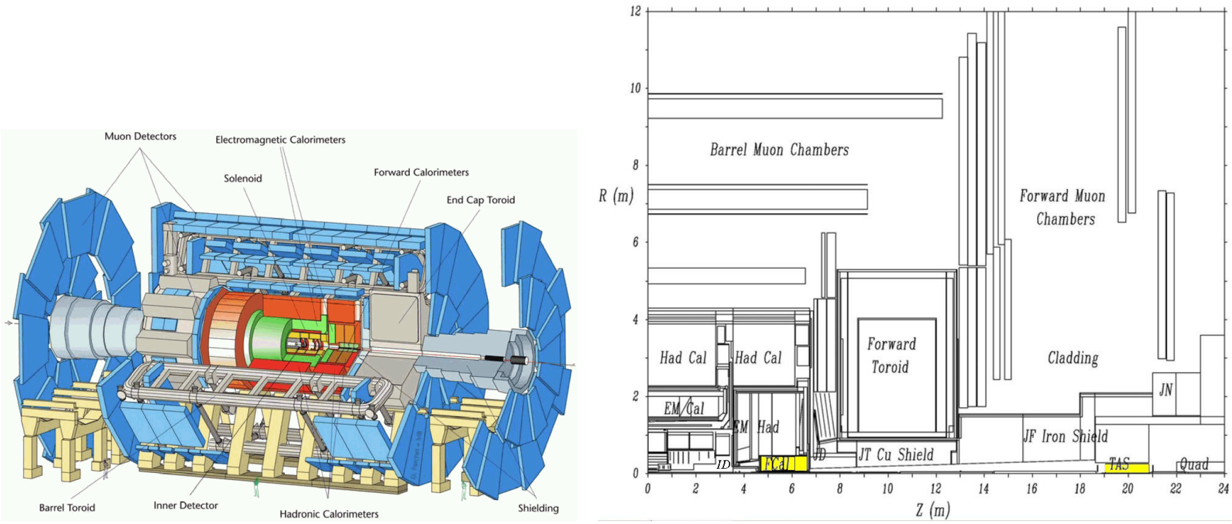

(a) Complete view of the ATLAS Experiment

(b) Cross-section of the ATLAS Experiment

Figure 2.4: The ATLAS Experiment at LHC.

high amount of secondary particles and collision products generated, will deposit their energy in the material surrounding the interaction point (ionization) or will damage it by inducing displacement in the material bulks. To quantify these energy losses FLUKA Monte Carlo simulations [Huh95] are used to calculate the absorbed dose and the time-integrated particle flux per unit surface. In some cases, the simulated particle fluences have been normalized in terms of the damage produced in semiconductor materials by neutrons of an energy of 1-MeV (Φ_{eq} as will be explained after in Sec. 2.3.3).

To obtain year-averages for radiation studies the recommended assumption [Pot95] is that during the first year LHC would reach 1/10 of the design luminosity and in the two following years 1/3 and 2/3, respectively. From the fourth year onwards LHC would operate at full luminosity. For the above calculation the assumed annual operation time of LHC was fixed to 1.5x10^7 s ($\sim$ 220 days). Integrated luminosity, which is the best measure for the time required to obtain a physics discovery, is usually expressed in terms of inverse femtobarn (fb^{-1}). The standard LHC physics program is then based on 500 fb^{-1}, which corresponds to 5x10^7 s at peak luminosity. The quoted numbers are equivalent to roughly 10 years of LHC operation.

In the case of the Compact muon Solenoid (CMS) experiments, Fig. 2.3(b) gives the dose map after 500 fb^{-1} while in Fig. 2.3(c) and Fig. 2.3(d) the expected fast charged hadron and neutron fluxes are plotted respectively. The central region of the experiment is exposed directly to the particle flux coming from the interaction region and to neutron albedo emerging from the calorimeters. Moving in the outer layers of the experiments, this second contribution becomes dominant. Tab. 2.1 details, for the different CMS *sub-detectors*, the doses expected over a year of normal operation, the calculate dose-rate and the dose expected during a 12 hour physics run. In the same table, the annual neutron and charged hadron fluences are reported. It has to be noted here that the fluence and dose can vary by several orders of magnitude when moving along the radial component (r) with respect to the IP. Moving along the z direction in the central part

Position	Dose/y [Gy]	Dose rate [Gy/sec.]	Dose/run [Gy]	Neut. Φ/y [n/cm^2]	Ch. Had. Φ/y [p/cm^2]
Pixel	1x10^5	2x10^{-2}	8.6x10^2	2x10^{13}	2x10^{14}
Tracker	1x10^4	2x10^{-3}	8.6x10^1	1x10^{13}	5x10^{13}
ECAL EB/EE	1x10^3	2x10^{-4}	8.6	10^{12}/10^{13}	negligible
HCAL HB/HE	1x10^1	2x10^{-6}	8.6x10^{-2}	10^{13}/10^{14}	$<$10^{12}/10^{13}
MB	1x10^{-2}	2x10^{-9}	8.6x10^{-5}	10^{10}/10^{11}	10^8/10^9
Cavern Side	1x10^{-3}	2x10^{-10}	8.6x10^{-6}	$<$10^{10}	negligible
Cavern End	1	2x10^{-7}	8.6x10^{-3}	$<$10^{10}	negligible

Table 2.1: Maximum dose and particle fluence estimations in the different sub-detectors of CMS. ECAL and HCAL stand for Electromagnetic CALorimeter and Hadron CALorimeter respectively. EB and EE identify the Barrel and the EndCap part of the ECAL sub-detector. The same apply for the HCAL (HB/HE). MB stands for MUON Barrel sub-detector.

of the experiment (e.g. along the beam axis) those values are almost constant [Her04].

In the ATLAS Experiment (A Toroidal LHC ApparatuS) shown in Fig. 2.4(a), most of the energy from primary protons is dumped in two regions: the TAS collimator and the forward calorimeter, that are then strong sources of secondary radiation. These two sources, yellow colored in the vertical section of Fig. 2.4(b), are compact and they have been shielded with layers of dense materials and cladding to reduce their radiation emissions. On the other hand, the beam vacuum system (e.g. beam-pipe tube) spans the length of the experiment and is in the forward region a major source of radiation backgrounds. Primary particles from the IP strike the beam-pipe at very shallow angles, so the projected material depth is large, and by this mechanism the beam pipe becomes an extended line radiation source illuminating the interior of the forward cavity. Studies have shown that the beam-line material contributes more than half of the radiation backgrounds in the muon system. Unfortunately extra shielding in this region is not possible due to access constraints [Bar05].

Tab. 2.2 reports the annual doses and Φ_{eq} for the most important ATLAS *sub-detectors*.

2.2.2 ALICE and LHCb radiation environment

For the ALICE (A Large Ion Collider Experiment) at LHC, the Monte Carlo simulations were run to predict its radiation environment by using the following source terms [Pas02]:

- Particle production at the interaction points during a typical running scenario with protons, Calcium and Lead ions according with the experiment Technical Design Report [ALI95];
- Beam loss due to beam misinjection (IP2 is located near the injection point from the SPS);
- Beam-gas interactions.

Position	Dose [kGy]	Neutron Φ [1 MeV_{eq} n/cm^{-2}]	Ch. Hadron Φ [1 MeV_{eq} n/cm^{-2}]
Pixel (ID)	17-160	1-5x10^{13}	2-20x10^{13}
SCT (ID)	4-8	1x10^{13}	4-8x10^{12}
TRT (ID)	1-5	4-15x10^{12}	0.5-4x10^{12}
LAr	0.6-5x10^{-3}	10^{10}-10^{11}	4-40x10^{9}
TILE	1x10^{-5}	5-30x10^{9}	10^{8}-10^{9}
FCAL	2.3	>10^{15}	-
MUON	3-20x10^{-5}	10^{9}-10^{11}	10^{8}-10^{10}

Table 2.2: Annual dose and particle fluence estimations in the different ATLAS sub-detectors at full luminosity. The Pixel, SCT and TRT tracking sub-detectors of ATLAS constitute the Inner Detector (ID) part of the experiment. LAr stands for Liquid Argon calorimeter. TILE and FCAL are two hadronic calorimeters installed in different ATLAS locations. MUON is instead the acronym to identify the muon chambers sub-detector.

The results of these calculations in terms of annual dose and total particle fluence are reported in Tab. 2.3 [Tav05]. It has to be noted here that the radiation levels expected in this experiment are much lower with respect to the ones calculated for ATLAS and CMS. This is due to the fact that the operational luminosity during particle runs will be much lower going from 10^{27} $cm^{-2}s^{-1}$ to 10^{30} $cm^{-2}s^{-1}$.

Position in ALICE	Dose / year [Gy]	Φ_{TOT} / year [cm^{-2}]	Position in LHCb	Dose / year [Gy]	Φ_{eq}/ year [cm^{-2}]
SPD1	200	3x10^{11}	VELO	5x10^{4}	2.4x10^{14}
SPD2	26	2x10^{10}	Si TRACK	4.8x10^{3}	5x10^{12}
TPC	10	1x10^{11}	RICH	2x10^{3}	2x10^{11}
TDR+TOF	0.1	3x10^{9}	CAL	200-300	9x10^{10}
MUON	0.5	6x10^{10}	MUON	60-300	1-5x10^{10}
Cavern	0.001	7x10^{6}	Cavern	0.06	-

Table 2.3: Dose and Fluence estimations in the different sub-detectors of ALICE and LHCb.

Similar considerations apply also to the case of the LHCb experiment. In this case, the annual values presented in Tab. 2.3 [Cor03] have been simulated assuming an average luminosity of 2x10^{32} $cm^{-2} \cdot s^{-1}$ and a cross-section for inelastic and diffractive proton events of 80 mb, hence 1.6x10^{7} interaction/s and 10^{7} seconds of data taking per year.

Even if the expected radiation field for these experiments is globally much less intense, some of the sub-detectors will sit at a few mm from the LHC beam, where the radiation environment is still very intense. This is for example the case of the VELO detector at the LHCb experiment. Therefore, due to radiation damage, it is expected that a replacement or upgrade of some of these detector equipments will be required after a few years from the first collision runs [Gou05].

The results presented in this section have been obtained with simulation codes based on a certain number of assumptions and uncertainties coming from various sources. Comparisons test between different radiation transport codes and bench-marking studies allow to assume an overall accuracy of the results within a factor 2-3 over a wide range of energies. These radiation levels (increased by opportune safety factors) are the base for testing and for the specifications of electronic parts and systems [Gil05].

2.3 Radiation damage at the LHC

Detectors, semiconductor components and all devices at the LHC will be thus irradiated with many different kind of particles at energies ranging from a few eV to several hundreds of GeV as explained in the previous sections. This is referred to as a complex radiation field. In order to parametrize this environment it is convenient to distinguish between the different contributions to this field [Wij03b, Wij04]. In the following sections the different components of the radiation filed will be classified in function of their effect on electronic devices. Moreover the dosimetric quantities employed to parametrize the mixed radiation field will be also introduced.

2.3.1 Total Ionizing Dose Effects

The electromagnetic component is constituted of high-energy photons, and particle such as electrons and positrons which have radiation lengths of only a few centimeters. These radiations depose a large amount of their energy ionizing the atoms of the materials they are interacting with (generation of an electron and a positively-charged ion). This energy deposition is conventionally termed ”dose”, ”Total Ionizing Dose (TID)” or ”IEL” and measured in *Gray (Gy)*. 1 Gy corresponds to the energy of 1 Joule released in 1 Kg of matter.

The radiation effect of these particles on electronic equipment is referred to as **surface damage** and is proportional to the TID released in the devices. For example, the production and subsequent trapping of charges in oxide films can cause serious problems in MOS[3] and bipolar devices [Hol02].

2.3.2 Single Event Effects

Single Event Effect Phenomena (SEE) cover both soft errors (Single Event Upset – SEU –) and latch-up. SEU is the change of state of a bistable element caused by the impact of an energetic particle that deposes a huge amount of ionizing energy in the sensitive volume of the component. This effect is not destructive and can be corrected by ”re-writing” the affected element. In some cases, as for the bulk CMOS structures, the quantity of charge deposed by ionization during an SEU, can lower the impedance in a certain region of the component allowing the conduction of parasitic transistors structures present in it (latch-up). If the current flow in the low-impedance region is not limited, the latch-up can evolve in a destructive burn-out as it has been observed for Power MOS transistors. SEE can affect thus both bipolar and MOS technologies [Hol02].

[3] Metal-Oxide-Semiconductors

In the case of the LHC, hadronic showers that consists mainly of pions ($\pi^{\pm}$,π^{0}), protons and neutrons may initiate nuclear reactions if the energy of the primary particle if sufficiently high. Spallation processes can afterwards break the nuclei in large fragments with a high Z that are slowed down on a short length in dense materials. Such events can thus lead to the deposition of a large amount of energy in a small volume as required to generate SEUs. In such a conditions it has been shown [Huh00] that the SEE rate in the LHC environment will be dominated by hadrons with an energy above 20 MeV.

The SEE rate is thus proportional to the number of particles, above the energy cutoff of 20 MeV, per unit surface hitting on the devices ($\Phi_{>20MeV}$).

2.3.3 Displacement Damage Effects

The neutron component, but more in general any (neutral or charged) particle that carries a momentum, needs to be treated separately because they have large elastic scattering cross sections on nuclei at all energies. Neutrons colliding with the atoms of crystalline materials like silicon, can loose a fraction of their energy displacing a primary atom out of its lattice site resulting in a silicon interstitial and left over vacancy (*Frenkel Pair*). This pair, migrating through the material can thus provide the building block for extended defects [Mol99a]. The neutron energy threshold for this effect in silicon is about 100 keV. Bulk damage can degrade the performances of a large range of semiconductor devices going from the particle detectors to the charged-coupled devices, solar cells, etc [Hol02].

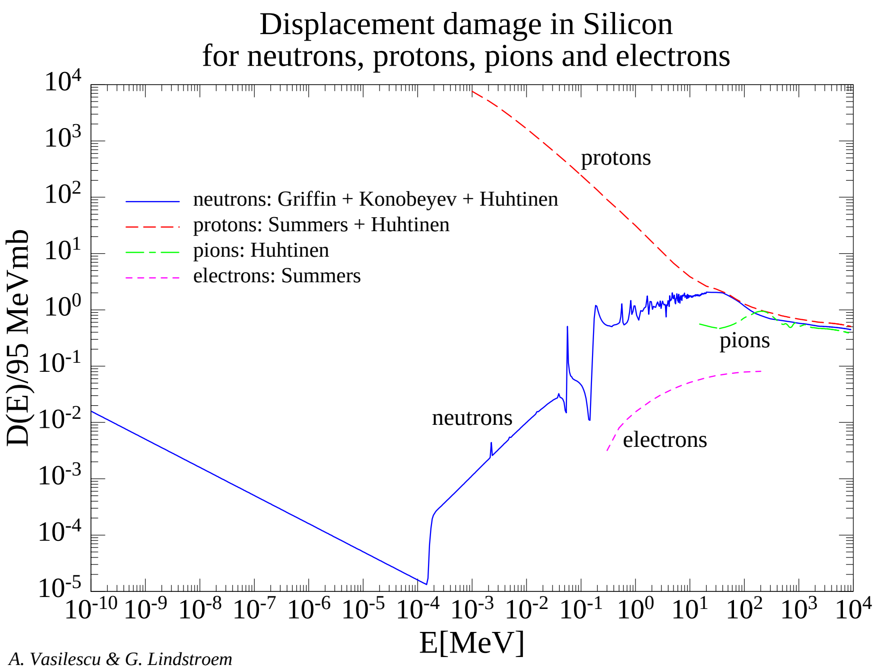

Figure 2.5: Displacement damage functions $D(E)$ normalized to 95 MeVmb for neutrons (10^{-10} to 20 MeV [Gri96], 20 to 400 MeV [Kon92], 805 MeV to 9 GeV [Huh93b]), protons [Huh93b, Sum93, Huh93a], pions [Huh93b] and electrons [Sum93]. Due to the normalization to 95 MeVmb the ordinate represents the damage equivalent to 1 MeV neutrons (see text).

The above described effect on semiconductors caused by neutrons and other fast particles is referred as **displacement damage** and it is scaling proportional to the total number of particles hitting the devices per unit surface. This quantity is called particle fluence, it is indicated with the symbol Φ and measured in *particles/cm*^{2}. Since momentum transfer to atoms is involved in the displacement damage effect (elastic scattering), the type and the energy of the primary particle are critical parameters for an accurate description of such a mechanism. Moreover, for neutrons above 1.8 MeV on silicon, nuclear reactions take place [Lin80] and they also have to be taken into account for this type of damage. Hence to scale the radiation damage produced by different kind of particles of various energy, with respect to the radiation induced changes observed in the materials, the so-called *Non Ionizing Energy Loss (NIEL) hypothesis* has been introduced.

The basic assumption of the NIEL hypothesis is that any displacement damage induced change in the material scales linearly with the amount of energy imparted in displacing collisions, without taking into account the spatial distribution of the introduced displacement defects and the various annealing sequences taking place after the initial damage event [Mol99a]. In this way the NIEL can be calculated and is expressed by the *displacement damage cross section D(E)*[4].

Fig. 2.5 shows the displacement damage cross sections for neutrons, protons, pions and electrons in an energy range from 10 GeV down to a few tenth of MeV. With the help of the displacement damage cross section $D(E)$ it is finally possible to define a hardness factor κ allowing to compare the damage efficiency of different radiation sources with different particles and individual energy spectra $\phi(E)$.

It is common practice to define the *hardness factor* κ in such a way that it compares the damage produced by a specific irradiation to the damage which would have been produced by monoenergetic neutrons of 1 MeV and the same fluence:

$$\kappa = \frac{\int D(E)\,\phi(E)\,dE}{D(E_n = 1MeV)\cdot\int \phi(E)\,dE}. \tag{2.1}$$

Here, $D(E_n = 1\,\text{MeV})$ is set to 95 MeVmb [AST94]. The equivalent 1 MeV neutron fluence Φ_{eq} can thus be calculated by:

$$\Phi_{eq} = \kappa\,\Phi = \kappa\int \phi(E)\,dE \tag{2.2}$$

and it is measured in *1-MeV neutron equivalent particles/cm*^{2} or simply (cm^{-2}).

2.4 Conclusion

In this chapter an overview of the different components of the Large Hadron Collider (LHC) project at CERN has been given, with particular emphasis to the complex radiation environment that will be generated during its operation. A mixed radiation field

[4] Also called *damage function*. The NIEL value can also be referred to as the displacement *KERMA (Kinetic Energy Released to MAtter)*. For silicon: 100 MeVmb = 2.144 keVcm^2/g.

composed of broad energies γ's, $e^{\pm}$, n, p, $\pi^{\pm,0}$, etc. has been simulated by Monte Carlo particle-transport codes. Moreover its intensity is expected to be position and time dependent over a range of 5-6 orders of magnitude. This environment, never encountered before in particle accelerator machines with such intensity, represent a danger for all the equipments exposed to it. Therefore, the electronic and the particle detectors at the LHC accelerator and inside its five High Energy Physics (HEP) experiments will suffer from radiation damage over the 10-years of operation.

Focusing on the case of the five HEP experiments of the LHC (ALICE, ATLAS, CMS, LHCb and TOTEM), the energy depositions in the **Ionizing channel (IEL or TID)** as well as in the **Not-Ionizing channel (NIEL or Displacement Damage)** are the main effects that can lead to a loss of performances and to an accelerated aging of the different experimental electronic equipments. Therefore, in the present chapter, the interaction mechanisms with semiconductor materials as well as examples of the different radiation damage effects have been given.

The radiation monitoring in such an environment represent a challenge that has been faced in this thesis work. Various dosimetric technology and devices are existent and have been developed in the last years for different industrial and research applications. In the next chapter, these technologies will be briefly discussed to introduce the radiation monitoring devices that will be characterized and evaluated in the following of this thesis work aiming to fulfill the needs of the LHC experiments.

Chapter 3

Overview of dosimeters and radiation monitoring devices

In Chapter 2 it has been demonstrated that the radiation environment generated during the LHC operation will be very challenging for the electronic equipment and detectors that have to operate in it.

Single Events are *instantaneous effects* that can appear as soon as there is a circulating particle beam. Surface and bulk damage in semiconductors, described in Section 2.3, are instead *cumulative effects* that can be responsible in normal operational conditions for a loss of performance and an accelerated aging of all exposed LHC components. Moreover, there is a risk of accidents or malfunctions that may produce radiation bursts further increasing the above mentioned effects.

Comprehensive Monte Carlo models have been developed in order to predict the LHC radiation field as shown in Section 2.2. Even if the accuracy of these models is constantly improved, it is impossible to fully describe the radiation field in a complex structure like the LHC. Moreover, the physical models used in simulations to describe particle interactions (especially the ones involving very high energy physics processes) haven't been fully validated yet. Because of these reasons, the results of simulation are always intended to be precise within, at least, a factor two.

From all above reasons it is therefore clear that dosimetric measurements have to be performed to cross check the prediction of Monte Carlo simulations and to assess the radiation induced damage in materials, detectors and electronic components during both normal operation as well as after accidental scenarios. For this last purpose, the dosimetric measurement can provide a valuable indication on which element should be replaced to guarantee the reliability of the overall system over time.

The purpose of dosimetry is to quantify the radiation field, to measure the particle fluence and/or the energy imparted to the irradiated material. Many dosimetry methods are available and they can be classified using many different criteria.

For the purposes of this work it is useful to classify them in two categories: *passive dosimeters* or *active dosimeters* depending on how the dosimetric information is read out. Passive dosimeters need to be removed from their measurement locations to perform their readout. Active dosimeters can be remotely accessed while they are positioned in the radiation field. Although calorimetry is the only absolute method to measure the absorbed dose[1], different secondary dosimetric means exist and are used at CERN [Leo93].

Many passive dosimeters, have been already calibrated to radiation of various qualities (particle type and energy) and employed for routine measurements. However, often the existent calibration curves are only valid for tissue-equivalent materials. In such a case, opportune relationships have to be determined in order to convert these dose measurements to the energy deposition in materials more relevant for HEP purposes (Si, SiO_2, etc.). For some others dosimeters, mainly active technologies like the devices studied in this work (solid-state semiconductors and Optically Stimulated Luminescent materials), an appropriate characterization is necessary before their use in the complex LHC environment. It has to be pointed out immediately that the raw OSL material can be the basis for the preparation of both passive and active dosimeter devices. For the purposes of this thesis work, the OSL will be mainly discussed in the framework of the development of active dosimeter systems.

The goal of this chapter is to give an overview of the existing passive dosimetry systems and to describe the active technologies that have been investigated, in the following of this thesis, for the radiation monitoring at the LHC experiments.

3.1 Passive Dosimeters

The following paragraphs list the most important characteristics of various technologies of passive dosimeters. Some of these technologies have been widely employed in this work to characterize the different radiation fields and to benchmark the measurements carried out with the active radiation monitoring devices. At the end of the section the important features of passive dosimeters to be used for TID measurements are summarized in Tab. 3.3.

3.1.1 Polymer-Alanine Dosimeters (PAD)

Alanine is an amino-acid (L-α-alanine: $CH_3 \cdot CH(NH_2) \cdot COOH$) with chemical composition quite close to that of tissue. Among the radical species generated in alanine by ionizing radiation, the stable radical CH_3-$\dot{C}$H-COOH which is predominant at room temperature, gives a prominent pattern when measured by electron spin resonance (ESR) spectrometer. The concentration of this free radical, measured by ESR-spectrometry, grows linearly with the absorbed dose [Wal89].

PADs are produced in form of small cables where the alanine powder (67%) is mixed to a polymer (33%) that act as binder (see for examples the PAD samples currently used at CERN: 4.8 mm in diameter for 30 mm in length as shown in Fig. 3.1(a)). This characteristic makes the alanine easy to be inserted in places difficult to access. The alanine response is tissue equivalent in the range 10 Gy to 100 kGy, it is energy independent for gamma-rays of energies > 120 keV and its neutron sensitivity varies from 1% (low-energy) to about 40% for fast neutrons with respect to gamma-rays [Sch89, Kat86]. No fading is measured at ambient temperature and standard humidity. The

[1] Sometimes Ionization Chambers and Fricke Dosimeters (see Sec. 3.1.5) are also considered as absolute dosimetry methods and recognised as standards

precision achievable in measuring the ionizing dose with such a method is in the order of 10%.

3.1.2 Radio-Photo-Luminescent Dosimeters (RPL)

High energy radiation induces stable radiophotoluminescent centers in silver-activated aluminophosphate glass which emit phosphorescence when exposed to UV light (around 365 nm). The amount of the phosphorescence is related to the amount of radiation absorbed in the glass. The light output increases linearly with the dose up to about 100 Gy, then the calibration curve reverses at about 1 kGy due to the increase of the coloration and the corresponding self-absorption of the glass.

These dosimeters are used at CERN in form of small transparent cylinders of 6 mm length and of about 1 mm diameter (see Fig. 3.1(a)). The response of such devices allows measurements in a broad dose range from 0.1 Gy to 1 MGy, however they present a large overestimation in the measured dose for low-energy gammas ($E < 500$ keV). Their response to fast neutrons is about 0.5% with respect the gamma-ray ones. Small fading, in the order of a few percent over three months, has been measured for RPL a room-temperature. High temperature annealing of RPL can be used to erase the dosimetric information allowing their reutilization.

The precision achievable in measuring the ionizing dose with such a method is on the order of 20% for doses up to some hundred of Gy. At higher doses the reversed behavior of the calibration curve makes the measurement uncertainties bigger for doses in the kGy range. To overcome this problem, a RPL reader based on UV light absorption method is under development at CERN [Fue04].

3.1.3 Hydrogen Pressure Dosimeters (HPD)

Hydrogen is formed and evolves from the irradiated polyethylene (PE). PE films of some tens of micron thickness are thus rolled in a glass capsule of about 6×2 cm as shown in Fig. 3.1(a). The dose is determined by breaking the capsule in a known volume and measuring the pressure of the evolved hydrogen at constant temperature. With this technique, it is possible to perform measurement in the range 10 kGy - 10 MGy with an uncertainty of about 20%.

3.1.4 Thermo-Luminescent Dosimeters (TLD)

Thermo-luminescent dosimeters are inorganic crystals exhibiting a high concentration of trapping centers in the gap between valence and conduction bands. Electrons are elevated from the valence to the conduction band by the incident ionizing radiation and are then captured at one of the trapping centers. Holes can also be trapped in an analogous process. The TLD material functions as an integrating detector in which the number of trapped electrons and holes is proportional on the number of electron-hole pairs formed by the radiation exposure.

After the exposure, the trapped carriers can be measured by heating the TLD. Reaching a certain temperature, determined by the energy levels of the traps, the trapped electrons can pick up enough thermal energy so that they are re-excited back to the

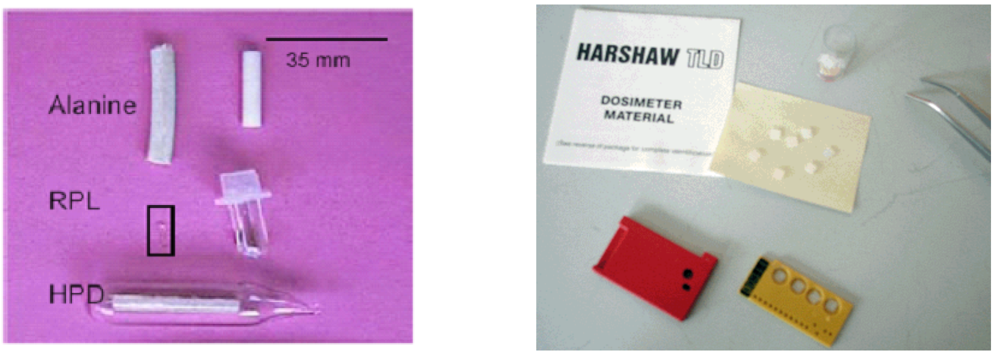

(a) PAD, RPL and HPD (b) TLD from [Sil05]

Figure 3.1: Some passive dosimeters used at CERN.

conduction band. The so liberated electrons migrate to near a trapped hole, where they can recombine with the emission of a photon. Alternatively, if the holes are released, they may migrate to a trapped electron and their recombination also results in a radiated photon [Che97].

The emitted photons are in the visible region of the electromagnetic spectrum and their total number is an indication of the original number of electron-hole pairs created by the radiation. TLD readers derive a signal by heating the dosimeter and reading the light output via a photomultiplier. The light yield is recorded as a function of the sample temperature in a *glow curve* [Fur03].

One common type of TLD material is LiF with trace amounts of Ti and Mg. LiF is usually produced in small pellets of 3×3×1 mm^3 as shown in Fig. 3.1(b). Because natural lithium contains 7.4% ^{6}Li, LiF dosimeters are sensitive to slow neutrons via an (n,α) reaction. The response to neutrons can be enhanced by using lithium enriched in ^{6}Li, or suppressed by using lithium consisting entirely of ^{7}Li. The almost negligible fading at room temperature makes the measurements with these devices very accurate in the range 10 μGy - 10 Gy within an error of 5%.

3.1.5 Fricke Dosimeters

The ferrous sulphate dosimeter, usually called *Fricke*, is based on the chemical process of oxidation of ferrous ions Fe(II) in acid aqueous solution to ferric ions Fe(III) by ionizing radiations. The method can be used for accurate absorbed dose determination using spectrometric measurements of the ferric-ion concentration at 303 nm wavelength in the peak of the absorption spectrum. Even thought this method is quite tedious, it allows tissue equivalent measurements of the dose in the range 20 Gy to 200 Gy with an accuracy of a few percent. For this reason this method is recognized as a standard.

3.1.6 *Dyed* PMMA Dosimeters

This procedure makes use of the radiation-coloration propriety of commercial Polymethylmethacrylate (PMMA or *Plexiglas*) available in the form of sheets. Upon irradiation to doses in excess of 100 Gy the material darken due to the formation of a new

Film type	Configuration	Substrate	Active layer thickness	Dynamic range	Radiation response
XR Type R	three layers	yellow polyester	18 μm	0.1-15 Gy	10-200 keV (γ)
HD-810	Active layer on substrate	clear polyester	6.5 μm	10-400 Gy	>1 keV (γ) >5 keV (e) 150-300 nm (UV)
MD-55	multilayer	clear polyester	2×16 μm	2-100 Gy	>10 keV (γ) >70 keV (e)

Table 3.1: Characteristics of the Gafchromic Films.

absorption band in the visible region of the spectrum. The darkening can be measured in terms of optical density using a conventional densitometer.

Once a calibration curve relating the induced light-absorption to dose is established, the material can be used for dosimetry in the range 0.1 to 50 kGy. The measurements carried out with such devices have been found to be strongly influenced by temperature, humidity and light exposure. Unless corrections are possible, the precision of this method lies around 30%.

3.1.7 Gafchromic Dosimetric Films

Gafchromic radiochromic dosimetry films are self-developing film media used for the measurement of absorbed dose and the mapping of radiation fields. These films develop a distinctive and characteristic color upon exposure to ionizing radiation and become progressively darker in proportion to absorbed dose.

The active component in these media is a micro-crystalline, radiation sensitive monomer (diacetylene) that is dispersed in a gelatine matrix and coated onto a polyester film base. When the active monomeric component is exposed to ionizing radiation, a polymerization reaction is initiated, resulting in the production of a dye polymer (polydiacetylene). The amount of polymer produced, and thus the intensity of the color change, is proportional to the amount of energy absorbed in the active layer. Thus, through the measurement of the color change produced upon exposure to radiation, it is possible to quantify the absorbed dose [Gaf].

Several types of films, in which the sensitive medium is coated with different substrate layers of various materials, are available by *International Specialty Products (ISP) Technologies*. Dosimetric Films XR Type-R, HD-810 and MD-55 have been used in this work and their main characteristics are summarized in Tab. 3.1.

Gafchromic **XR Type R** film is sandwiched between one transparent film substrate and one opaque, white film substrate. The transparent polyester substrate contains a yellow dye. One purpose of the yellow dye is to enhance the visual contrast of the chromatic changes that occur when the film is exposed to radiation. A second purpose is to protect the active layer against exposure by UV and blue light and thereby enable the film to be more tolerant of being handled in the light. These features make this film

Nuclear reaction	Energy Range	Half-life
^{59}Co(n,γ)^{60}Co	thermal	5.3a
^{197}Au(n,γ)^{198}Au	epithermal	2.7d
^{115}In(n,n')^{115m}In	1-14 MeV	4.5h
^{58}Ni(n,p)^{58}Co	2-20 MeV	71d
^{32}S(n,p)^{32}P	4-15 MeV	14.3d
^{27}Al(n,α)^{24}Na	7-27 MeV	15h
^{59}Co(n,2n)^{58}Co	14-50 MeV	71d
^{12}C(n,2n)^{11}C	$>$ 20 MeV	20min
^{59}Co(n,3n)^{57}Co	$>$ 27 MeV	270d

Table 3.2: Main nuclear reactions used for neutron-fluence measurements.

suitable for beam profiling applications.

The films Gafchromic **MD-55** and **HD-810** are instead completely transparent media in which the active layer is coated on thin transparent polyester layers. They develop a characteristic blue color after exposure that can be measured by means of a transmission densitometer with a light of 671 nm wavelength. The color density is thus used to measure the absorbed dose during irradiation in different radiation fields.

The optical density of both film types increases with time reaching saturation less than 24 hrs after irradiation [McL96]. These films allow dose measurements with an accuracy of a few percent if the appropriate wavelength for the readout is chosen and if corrections of the light-absorbance increase after irradiation are carefully taken into account [Kla97].

These dosimetric films have been widely used in this work to calibrate the different radiation environments employed. However, before their utilization, the film batches received at CERN were calibrated. In Chapter 5 the calibration, carried out using a *Nuclear Associates 37-443 Densitometer* in the 23 GeV proton beam available at the IRRAD1 facility will be presented. Examples of how these films are used in the determination of the profile of the same proton beam will be also given there.

3.1.8 Activation foils

This method of absolute particle fluence measurements is based on nuclear reactions that lead to the formation of radionuclides in various high-purity materials (Al, Au, Co, In, Ni, etc.). After particle exposure, the amounts of generated nuclides can be determined by means of γ-spectroscopy analysis.

For neutrons the (n,γ), (n,p), (n,α), (n,xn') nuclear reactions can be selected in accordance with the expected neutron spectrum and the irradiation time. Thin foils of various material are used for this kind of measurement. Their weight and shape is selected with respect to the neutron-flux intensity and irradiation time. The calculation of the specific activities induced in the materials provide then information about the neutron flux in the different energy ranges. In this calculation the irradiation time

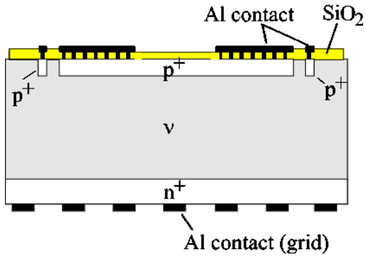

(a) Cross-section

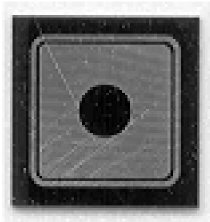

(b) Top view

Figure 3.2: p-i-n particle detector diode structure with a p^+ guard-ring around the active area that consists in a $p^+ - i(\nu)$ junction. Schematic after [Mol99a, Weg98].

and the half-lives of the different isotopes must be taken into account to evaluate the specific activity at saturation. The neutron cross-section curves, being known, allow finally to compute the shape of the neutron spectrum under investigation [Leo93]. The precision of this method is of about 30%. The main nuclear reactions used for neutron-fluence measurements are listed in Tab. 3.2. For charged particles fluence measurements, the above consideration also applies. In Section 5.1.1 the reaction of interest for the measurement of the 23 GeV proton fluence will be given.

3.1.9 Leakage current from reverse-biased silicon detectors

Silicon particle detectors are reverse biased p-i-n diodes with a very high resistivity (several kΩ·cm) n-type bulk of usually 300 μm thickness.

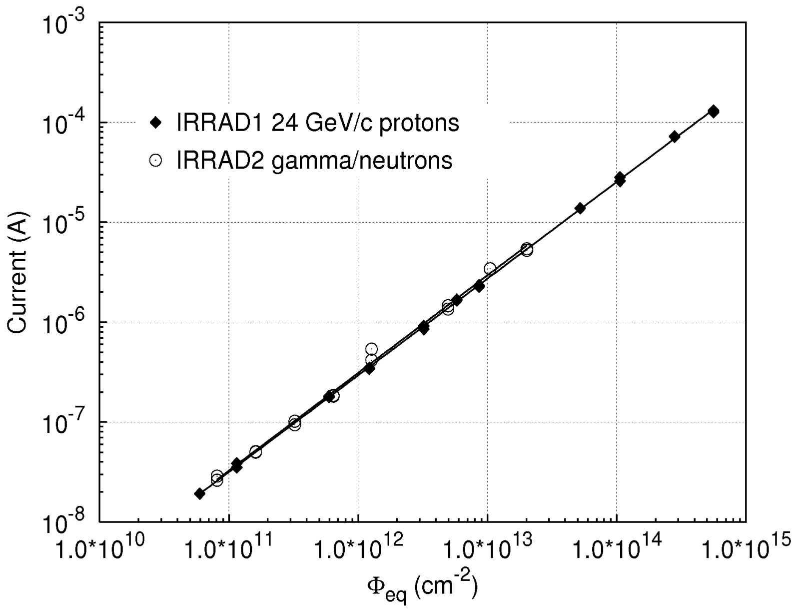

Figure 3.3: Calibration curves for ST p-i-n diodes at the facilities of the CERN-PS Accelerator. Measurements performed after annealing for 4 min at 80°C.

Irradiation of such devices will produce generation/recombination centers in the silicon bulk leading to a fluence proportional increase of the leakage current if the device is kept fully depleted. It has been demonstrated that the increase of the leakage current is independent from the impurity content of the silicon base material [Mol99b]. They can be used as a NIEL proportional damage counter for a wide range of different particles and particle energies if care is taken about the rather complex annealing behavior [Mol02].

For dosimetric purposes usually small "Pad-structures" with an active area in the order of 0.25 to 1 cm^2 protected by one or several guard-rings against edge currents are used as shown in Fig. 3.2.

In this work, 307 μm thick p-i-n detector test structures produced by *ST Microelectronics*, Italy with an active area of 0.25 cm^2 and protected on the front side by a guard-ring have been used. To calibrate them, the detectors were exposed to the different radiation fields at ambient temperature (about 27°C) without biasing them. After irradiation the devices were annealed for 4 min at 80°C and the leakage current at full depletion was measured on a laboratory test-bench and normalized to 20°C [Mol02]. The results are presented in Fig. 3.3 and demonstrate that these devices can be used over a very wide Φ_{eq} range provided that the annealing is performed carefully.

Dosimeter	PAD	RPL	HPD	TLD	Fricke	PMMA	Gafchromic
Dynamic range (Gy)	$10 - 10^5$ Tissue equivalent	$10^{-1} - 10^6$	$10^4 - 10^7$	$10^{-5} - 10^1$	$20 - 2 \times 10^2$	$10 - 10^4$	$10^{-1} - 10^2$
γ-rays energy dependence	underestimation at $E<120$keV	overestimation at $E<500$ keV	negligible	overestimation at $E<100$ keV	overestimation at $E<500$ keV	unknown	negligible
Neutrons Energy dependence	sensibility of 0.4 at 1 MeV 0.6 at 8 MeV 0.7 at 14 MeV	sensibility of 0.9 thermal 0.01 fast		^{7}Li none ^{6}Li thermal			
Fading	none at RT and humidity of 40-60%	1% over 3 months at RT; light sensitive	negligible	negligible	none	important light sensitive	few % of reverse annealing
Readout method	EPR	Luminescence (UV light)	Pressure	Luminescence (heating)	Spectro-photometry	Optical absorption	Densitometry
Advantages	organic	reusable	good for very high doses	reusable	used as standard	cheap and easy to read	very easy to read
Disadvantages		difficult readout in kGy range	not sensitive to low doses	low dose range	difficult to prepare	sensitive to temperature and humidity	

Table 3.3: Summary of the properties of passive dosimeters used for TID measurements (RT = Room Temperature).

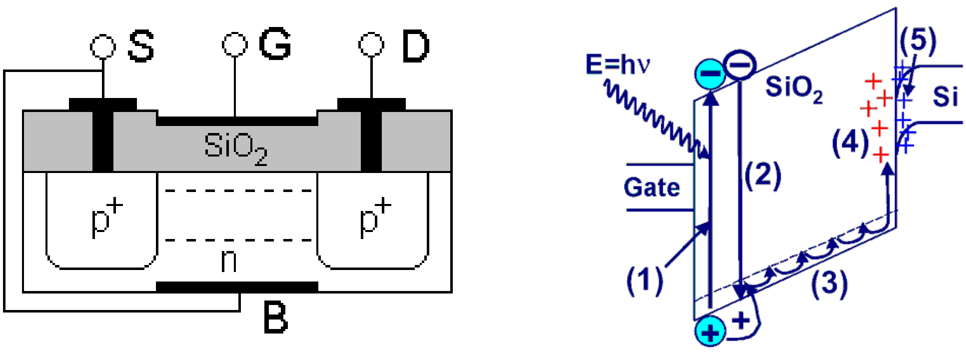

(a) (b)

Figure 3.4: Principle of a RadFET dosimeter. (a) schematic cross-section of the sensor. (b) charge generation in the oxide layer: [1] electron-hole pairs generation, [2] electron-hole pairs recombination, [3] holes transport. [4] holes trapping (red colored '+'), [5] interface states delayed buildup (blue colored '+').

3.2 Active Dosimeters

3.2.1 Radiation-sensing Field-Effect Transistors (RadFETs)

3.2.1.1 Principle of operation

The Radiation-sensing FETs (RadFETs) are p-channel MOS transistors that are used to measure the ionizing dose via build-up of charge in the insulating silicon oxide (SiO_2) layer of the transistor that therefore constitute the sensitive part of the device [Hol74, Hol86]. A schematic cross-section of a RadFET dosimeter is shown in Fig. 3.4(a). RadFETs are integrating dosimeters. They are usually used where regular measurements of integrated doses are required within limited volumes [Con98b].

Ionizing radiation creates electron-hole (e-h) pairs throughout the whole oxide volume. Depending upon the electric field inside the oxide (E_{ox}), the energy (E) and the type of radiation, some (e-h) pairs generated recombine within picosecond with a probability P_r. Due to their high mobility (μ_e = 20 cm^2·V^{-1}·s^{-1}) electrons which escape recombinations are rapidly swept out of the oxide layer via the gate contact (anode). Holes move instead slowly toward the silicon substrate (cathode) with a mobility μ_h = 10^{-8} cm^2·V^{-1}·s^{-1}. The transport of the holes towards the cathode can take several decades in time depending on the temperature, the applied electric field and the processing of the oxide layer [Hug75].

The holes may then be trapped by pre-existing hole traps, generated during the processing of the device [Kum95] and located in a narrow region close to the interface between silicon and the SiO_2. A trapping probability P_t (cm^2) can be defined and it depends on the processing conditions of the oxide layer and the capture cross-section for holes that is a function of the electric field in the insulator E_{ox}.

Therefore, as a result of irradiation, a positive charge (Q_{ot}) develops in the gate oxide near the silicon. Taking into account the parameters introduced before, this charge can be written as [Hol02, Dre89, Hug75]:

$$Q_{ot} = q \cdot g \cdot t_{ox} \cdot P_{nr}(E_{ox}, E) \cdot P_t(process, E_{ox}) \cdot D \quad (3.1)$$

where q is the electron charge, $g = 7.6\text{x}10^{14}$ $cm^{-3}\cdot Gy^{-1}$ is the electron-hole pairs generation rate in the oxide obtained using the parameters of Tab. 3.4, t_{ox} is the oxide thickness, $P_{nr}(E_{ox}, E) = 1 - P_r(E_{ox}, E)$ is the probability of electron-hole pairs to escape recombination and D (Gy) is the dose absorbed in the oxide layer.

The simplified model described in Eq. 3.1 is valid when a constant electric field E_{ox} is applied to the oxide layer via the gate electrode during irradiation ($V_G \neq 0$ V, dosimeter used in biased mode). A positive gate bias is the most favorable case to increase hole trapping, because the electric field is directed from the metal to the semiconductor so that Q_{ot} is stored near the semiconductor-oxide interface. However, E_{ox} continuously lowers its value during the device operation until the dosimeter reaches the saturation. In fact proceeding with charge build-up, the increasing electric field in the trapping region of the oxide reduces the field in the rest of the insulator where the electron-hole pairs are generated. This effect leads thus to a saturation of the response because the electron-hole pairs are no longer separated.

As in the case of this work, the RadFET dosimeters are often exposed to radiation without biasing them ($V_G = 0$ V, dosimeter used in "zero bias" mode [Hol85]). In such a condition, the probability for holes to escape the recombination is very small. A less efficient hole-trapping means thus a reduced sensitivity in detecting ionizing radiations. On the other hand, this condition is advantageous for applications where it is needed to measure high doses (saturation is reached later) and to avoid complex circuitry and external power supply.

From the microscopic point of view, when RadFETs are unbiased (electric field is very small) the situation is more complicated with respect to the model presented above. Several mechanisms such as hole diffusion and space-charge effects have to be taken into account to obtain Eq. 3.1 [Hug85]. Moreover whereas the charge trapping in the region close to the silicon substrate is well established for biased oxides (5-20 nm from the interface with silicon [Hol02]), in the case of unbiased insulators the trapping region has not been demonstrated to be near the electrodes. Hole traps can thus be distributed throughout the SiO_2 volume with, as a consequence, a further decrease of the RadFET sensitivity. Although Q_{ot} cannot be derived anymore from Eq. 3.1 the elements described for the biased mode can be quantitatively applied also to the unbiased case.

The build-up of stable charge in the bulk SiO_2 (Q_{ot}) is not the only phenomenon that occurs once a RadFET is exposed to ionizing radiation. In the interface region between Si/SiO_2 other trapping centers are established during the processing of the silicon oxide. Other charges can be therefore stored in this location ("interface state charges buildup"). In the case of p-MOS transistors these charges are positives and add to the ones trapped in the bulk SiO_2 (Q_{it}). These charge states, being in direct contact with the underlying semiconductor region, are electrically active and can be responsible of several instability mechanisms as will be discussed in Section 3.2.1.4.

Interface states are usually electrically latent before irradiation and they are triggered by radiation exposure or charge injection phenomena. Therefore they develop from a few seconds to thousand of seconds after irradiation. The extent of the Q_{it} build-up period is

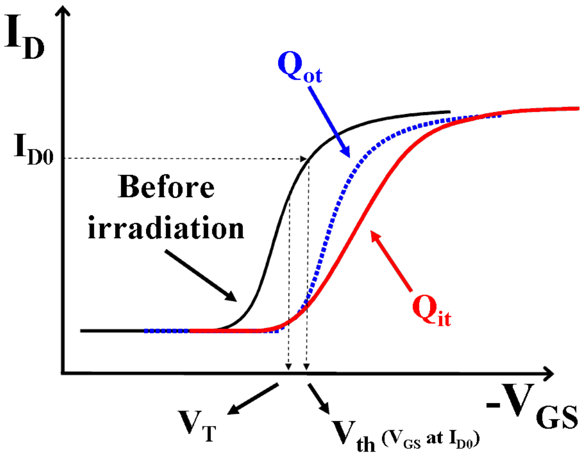

(a)

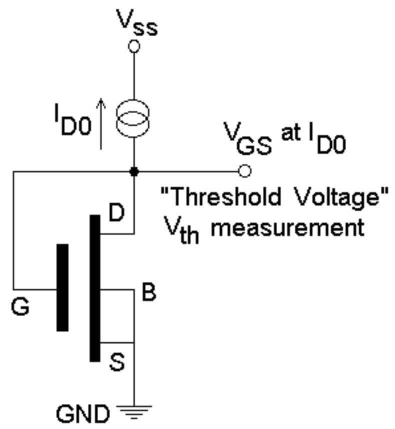

(b)

Figure 3.5: Radiation-induced changes in RadFET dosimeters. (a) shift of the transistor I_D-V_{GS} characteristic curve. The y-axes is here plotted in logarithmic scale (b) Reader circuit for RadFET threshold voltage shift.

highly dependent on the oxide processing conditions. The interface state density growth is higher during irradiation when a bias is applied to the MOS transistor but can be still important also in unbiased conditions.

Fig. 3.4(b) summarizes from (1) to (5) all the steps involved in the deposition, transport and trapping of charges in the forbidden energy gap of the silicon oxide insulator as it has been described in this section.

3.2.1.2 Response under irradiation, sensitivity and dynamic range

Both positive charges Q_{ot} and Q_{it}, generated by irradiation in the gate oxide and at the Si/SiO_2 interface respectively, lead to a shift of the transistor I_D (drain current)-V_{GS} (gate voltage) characteristic curve towards more negative voltages as shown in Fig. 3.5(a). The transistor threshold voltage V_T is defined as the intersection of the linear part of the curve $\sqrt{I_D}$ vs. V_{GS} with the V_G axis when these two quantities are plotted in linear scale. This quantity also shifts under irradiation by an amount ΔV_T following the equation [Sar94, Sar98]:

$$V_T = V_{T,0} - \frac{Q_{ot} + Q_{it}}{C_{ox}} = V_{T,0} + \Delta V_T \tag{3.2}$$

where $V_{T,0}$ is the value of V_T before irradiation and C_{ox} is the gate layer capacitance. The interface charge Q_{it} moreover reduces the slope of the linear part of the I_D-V_{GS} curve due to degradation of the carrier mobility μ in the transistor channel [Zup92] as shown by the red curve of Fig. 3.5(a).

Therefore ΔV_T is the measured dosimetric parameter and it is practically obtained, during or after irradiation, using the basic measurement configuration shown in Fig. 3.5(b). With such a readout circuit, the measured quantity is not V_T that appears in Eq. 3.2, but an equivalent one defined as

$$V_{GS} = V_T - \sqrt{\frac{I_{D0}}{\beta}} \tag{3.3}$$

where I_{D0} is a constant current forced throughout the transistor when it is biased as shown in Fig. 3.5(b). The parameter β is known as the ”transconductance parameter” and is a constant equal to $\beta = \frac{1}{2} \cdot \mu_0 \cdot C_{ox} \cdot \frac{W}{L}$, where μ_0 is the surface mobility of the device, C_{ox} the capacitance of the gate oxide and W/L is the transistor ”aspect ratio” [Sze85]. It is common practice to call the ΔV_{GS} read out from Eq. 3.3 at the same way of ΔV_T (e.g ”threshold voltage shift”). To avoid confusions, to present the RadFET data in this work, the usual nomenclature will be kept and the dosimetric parameter will be indicated as ΔV_{th} to intend the shift of V_{GS} for a constant readout current.

As shown in Section 3.2.1.1, the processing conditions of the silicon oxide and the bias applied during irradiation, are the two parameters that play a fundamental role in the hole-trapping probability P_t parameter and thus in maximizing the RadFET sensitivity.

We have also already seen that in the case of biased devices, neglecting the charge density at the interface, the Q_{ot} is stored very close to Si/SiO_2 interface. The related shift ΔV_T can be thus written, with basic electrostatic considerations, by treating the sensitive oxide layer in the same fashion as a parallel-plates capacitor:

$$\Delta V_T = \frac{t_{ox}}{\epsilon \cdot \epsilon_0} \cdot Q_{ot} \tag{3.4}$$

where ϵ and ϵ_o are the vacuum permittivity and the dielectric constant for the oxide respectively and Q_{ot} is the total charge trapped per unit surface after irradiation in a narrow layer close to the semiconductor interface (see Tab. 3.4 of Pag. 44).

Eq. 3.4 therefore shows that the sensitivity can be further increased over several orders of magnitudes [Sar98] by manufacturing RadFETs with thick oxide layers.

RadFET response depend on the bias applied on the gate (V_G) with respect to the substrate upon irradiation. On the other hand, for oxides produced in same processing conditions, the RadFETs threshold voltage shift as function of the radiation dose (ΔV_{th}) can be kept linear over several dose decades by changing the applied electric field in the insulator. For a fixed V_G the sensitivity of the RadFET to radiation, defined as the slope of the linear part of the ΔV_{th} vs. dose curve, can be also varied by several order of magnitude by varying the oxide thickness. By changing the oxide thickness from 0.69 μm to 2.3 μm a sensitivity increase of more than a factor 10 has been found for RadFETs exposed with a V_G = 20 V [Hol91, Kel91]. Therefore, exposing to radiation a biased thin oxide RadFET ($t_{ox} \sim$ 0.1-0.2 μm), it is possible to cover with a linear response dose ranges up to some kGy with sensitivities in the order of 1-10 mV/cGy [Sar98].

In the unbiased mode (”zero bias” mode) the linear region, if any, extends over a very narrow dose range [Hug86]. In this case, the expected response of the voltage shift ΔV_{th} is better represented by a power-law:

$$\Delta V_{th} = a \times D^b \tag{3.5}$$

where a and b are experimental parameters. Usually it is not possible to find values for a and b which are valid throughout a large dose range; in such cases pairs of a and b are given for different dose ranges. For small doses b is usually close to one while for high doses much smaller values are found. Parameter a in fact contains several constant device parameters such as oxide thickness, number and cross-section of hole-traps in the gate oxide as already shown in Eq. 3.1. Typical sensitivities in the order of 5-10 mV/cGy can be obtained with unbiased thick oxides of some μm thickness.

Another possibility to improve the RadFET dosimeter response is currently under studies and it consist in using several RadFET transistors in a series configuration [Con96, Con98b, Con00, Con98a, Sar01]. It has been shown that stacking n transistors (the source of the device n connected to the drain of the device $n+1$ and so on), the obtained radiation response is more than n times the one of the single device. For a stack of 13 transistors and V_G = 10 V sensitivities of 90-100 mV/cGy can be reached.

3.2.1.3 Influence of radiation type and energy

There are several ways in which the response of the RadFETs can be sensitive to the radiation type and energy.

- *Internal dose enhancement*: This phenomenon is due to the presence of high-Z materials in the metalization of the gate, in the substrate, and in other part of the device [Bru95]. This effect decreases as the insulator thickness increases and it has been found to affect a standard RadFET response by less than 10 % for low-energy (10 keV) X-rays [Sar98].

- *Recombination of electron-hole pairs within the oxide layer*: This contribution, reducing the threshold voltage shift of the RadFETs for a given energy deposition (e.g. dose), is expected to be significant mainly in the case of unbiased dosimeters, with a thick oxide exposed to radiation having high Linear Energy Transfer (LET)[2] [Aug82, Old85, Pea01].

  In zero bias mode the electric field across the oxide layer is only due to the work-function potential and its intensity decreases with increasing oxide thickness [Dea66]. Electron-hole pairs produced by highly ionizing radiations like α, protons and any kind of Minimum Ionizing Particle (MIP), being not sufficiently separated by the existing electric field hardly escape to recombination [Old00]. As a results, the number of holes available for trapping is reduced, as in turn, the RadFET response.

- *External dose enhancement*: This phenomenon is due to scattered electrons produced by the interaction of the radiation with high-Z materials like gold, tungsten and kovar that may be part of the composition of the dosimeter encapsulation (packaging) [Ros95]. In neutron environment also the presence of low-Z (like

[2] The Linear Energy Transfer is equal to the energy dE which a charged particle loses at a distance dl from its path in penetrating the matter. LET is usually indicated in keV/μm and is a term commonly employed in radiation biology. In nuclear physics, for the same quantity, the term *"Stopping Power"* is instead most often used.

Polyethylene and similar polymers) materials can be critical due to the production of proton recoils. Dose enhancement factors from 5-7 (neutrons) to about 20 (low-energy photons) have been registered [Kro95, Rav05b]. Therefore, the packaging required for RadFETs depend upon he application for which the dosimeter is intended.

Neutrons can also interact directly with the oxide layer of the RadFETs. The energy deposition by neutrons in silicon oxide can be calculated and compared with the one deposed by ionization from charge particles and gamma-rays. At energies lower than about 100 keV neutrons transfer only a negligible quantity of energy to secondary particles with respect to photons and charged particles. This is shown in Fig. 3.6 where the energy released in SiO_2 in terms of IEL KERMA [pGy$\times cm^2$] is plotted versus the particles energy. The neutron curve lies several order of magnitude below the others. At higher energies (>100 keV) the difference between neutrons and gamma-ray is reduced to about one order of magnitude because of the contribution of the energy deposition from nuclear reaction fragments. The same happen between neutron and protons but for higher energy values ($\gtrsim$100 MeV).

Once neutrons transfer their energy to charged secondaries, the energy deposition in SiO_2 via ionization processes takes place. However, the produced secondaries have usually high ionization densities and are most likely responsible of enhanced recombination effects. The signal measured upon neutron irradiation of RadFETs result thus reduced with respect to the one measured after exposure to direct ionizing particles or gamma-rays. For these reasons, RadFETs dosimeters are intended to be as not-sensitive to neutrons. For their application at the LHC, a study devoted to the response of RadFETs to high fluences of fast neutrons will be here presented in Chapter 6.

For the purposes of this work, the recombination and the external dose enhancement phenomena listed above have been recognized as main issues. This is due to the composition of the radiation field at the LHC described in Chapter 2: high-energy, mixed-LET radiation field with dominant neutron component in some locations.

Therefore, the recombination within the SiO_2 layer has been taken into account in the selection of the RadFET sensors at the LHC Experiments, while the external dose enhancement phenomena have been considered during the studies of a suitable sensor packaging. These two issue will be widely discussed in the following Chapter 6 and Chapter 10.

3.2.1.4 Instability effects and limiting factors in the dose measurement

The main effects limiting the measurement accuracy and the lowest measurable dose with RadFETs have been identified in the annealing of the trapped charge, the build-up of interface states, the read-time instability, the temperature dependence and the electronic noise.

- *Annealing of the trapped charge*: This phenomenon, compromising the RadFET long-term stability, is due to the neutralization of the charge in the SiO_2 layer (annihilation of the trapped holes) by direct electron tunneling from the nearby silicon layer into the insulator [Hol83].

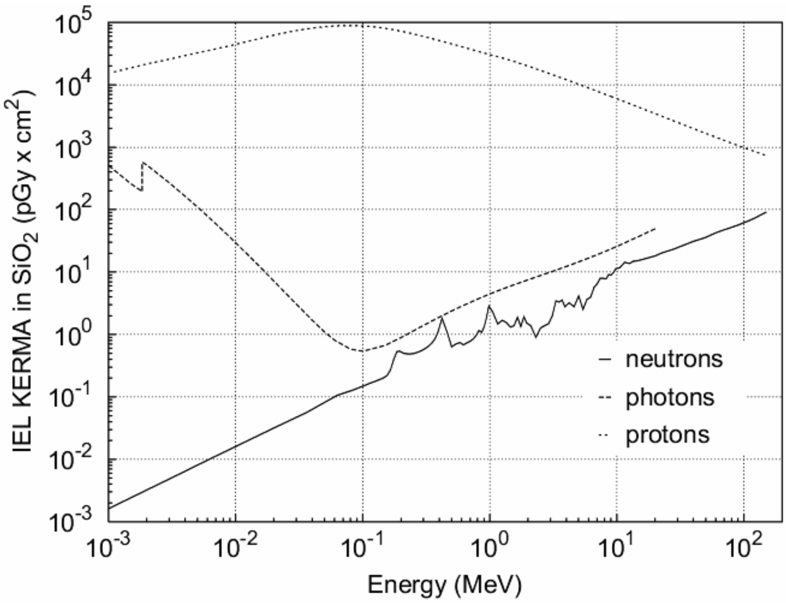

Figure 3.6: Ionizing (IEL) KERMA in silicon oxide calculated for neutron, protons and gamma-rays. The neutron and gamma-ray data are from Ref. [Cha99] and Ref. [Hub82] respectively. The proton data have been calculated by means of the SRIM software [SRI] assuming the composition of the SiO_2 to be 53.3 $\%_w$ oxygen and 46.7 $\%_w$ silicon. The used density is the one reported in Tab. 3.4.

This mechanism, that is usually visible in the RadFET post-irradiation behavior, lead to a reduction of ΔV_{th} in function of the time. Of course the annealing also occurs during irradiation and it can introduce some limitations in the utilization of the RadFETs devices at very low dose-rates.

Annealing is dependent on the gate bias during and after irradiation [Jak02], in processing conditions of the oxide [Kel93, Bla86], in the oxide thickness (annealing decrease drastically as t_{ox} increases) and in the temperature [Kel96]. The temperature effects on the annealing behavior relies in an increased thermal emission of holes from the trap-centers the SiO_2 valence band, leading to an enhanced annealing at high temperature. This latter phenomenon can be considered as a further limitation in the use of RadFETs at higher temperatures.

- *Interface states build-up*: As explained in Section 3.2.1.1 interface states continue to be formed at the Si-SiO_2 interface after irradiation producing an increase in the threshold voltage shift ΔV_{th} [Fle93, Fle95]. Depending on its relative magnitude, the interface build-up can therefore be observed after irradiation whether the formation of interface state is significant. This post-irradiation threshold voltage growth is sometimes referred to as "reverse annealing".

- *Read-time instability*: The threshold voltage of a biased RadFET may drift with time due to a rearrangement of charges formed during processing or irradiation. This mechanism (called also "drift-up" [Cam01, Hol83]) has been explained by some authors with the existence of "slow interface states" called "border states"(Q_{bt})

which lie in the oxide layer very near the Si-SiO_2 interface [Sav95, Fle93]. Charges trapped in these states are very sensitive to changes in the gate potential, which produce a transient escape of charge that, in turn, produce drift up at the instant that the device is accessed by the readout system (RadFET "on").

The drift-up decreases with time after turning the RadFET on, because border states saturate as a logarithmic function of time. The initial rate of drift-up is usually less than 1 mV per decade of time measured in seconds and it increases with increasing oxide thickness. Moreover, the drift-up amplitude increases strongly as a function of irradiation, due to the generation of new border states. However the dynamics of this drift effect can be accommodated by the design of the readout circuit.

- *Temperature dependence*: The ΔV_{th} changes with temperature. Any variation of the threshold voltage is thus the sum of that due to irradiation and that due to temperature variations. The temperature sensitivity of ΔV_{th} increases as t_{ox} increases and depends also on the doping level N_D in the semiconductor layer. However, also this effects can be accommodate by using different measurement procedures that will be described in detail in the following Section 3.2.1.5.

- *Electronic noise*: Some authors [Sar01] identify the signal-to-noise ratio (SNR) as a limiting factor to the minimum measurable dose. This issue is relevant especially for very high sensitivity RadFET devices. Methods to reduce this noise are, for example, to increase the MOSFET gate area and the choice of a thick oxide layer.

3.2.1.5 RadFET temperature dependence

There are three major ways to reduce the effect of temperature on the RadFET threshold voltage [Har04].

The first one involves setting the drain current at the point where minimum effect of temperature fluctuations is expected, i.e., the Temperature Coefficient $T_c = \partial V / \partial T$ is Zero. This point is called the ZTC (or MTC) point [Sul90, Bue93, Vet96, Kim93]. The method relies on the mutual cancellation of the temperature derivatives of threshold voltage and of channel mobility over a specified temperature range [Sul90, Sar94].

The second method uses differential measurement of two devices simultaneously [Mac97, Tho98]. The dosimeter consists of two identical MOSFETs on the same chip operating at two different positive gate biases. Ref. [Sou94] showed that the measured difference between the threshold voltages of the two sensors was representative of the absorbed dose, and the magnitude of this difference per unit dose was constant and independent from temperature variations.

The third way involves assessment and subtraction of the relative contribution of temperature fluctuations to the acquired data [Shi99]. This has been done either by fitting the temperature coefficient and subtracting the temperature fluctuations, or by modeling the temperature dependence based on parameters obtained from laboratory experiments.

3.2.2 High-resistivity forward biased *p-i-n* diodes

3.2.2.1 Forward bias operation of *p-i-n* diodes

A *p-i-n* diode is a *p-n* junction with a doping profile tailored so that an intrinsic layer, the *i* region (or base), is sandwiched between a *p* layer and an *n* layer as shown in Fig. 3.7. In practice however, the *i* region is approximated by either a high-resistivity *p* layer or a high resistivity *n* layer. Because of low doping in the intrinsic region, most of the potential will drop across this region [Sze81].

The *p-i-n* diode has wide applications in microwave transmission because of its constant depletion layer capacitance and the possibility to handle high powers. Moreover *p-i-n* diodes can be used as variable attenuator by controlling the device resistance that varies approximately linearly with the forward current [Sze85].

When a *p-i-n* diode of base-width W is biased in forward conditions, holes are injected from the p^+-i contact and electrons are injected from the i-n^+contact. In these conditions the total voltage drop across the diode is the sum of the voltage drops across both the two junctions (total junction voltage) V_{Fj} and the base V_{Fb}:

$$V_F = V_{Fj} + V_{Fb} \tag{3.6}$$

In **low injection**[3] conditions (e.g low current densities), the carriers density depends linearly on the current density in the base. Therefore the conductivity increases proportionally to the current. The voltage across the base, V_{Fb} is thus independent on the base current and depends only on the W/L ratio and on the mobility ratio $b = \mu_n/\mu_p$. $L = \sqrt{D \cdot \tau}$ is the diffusion length where D is the diffusion coefficient and τ the lifetime of both charge carriers, μ_n and μ_p are the mobility of electrons and holes in silicon respectively. V_{Fj} under these conditions is the usual junction diode equation when the current flow is mainly due to electron-hole recombination processes:

$$J_{Fj} \propto e^{\frac{qV_{Fj}}{2\kappa T}} \tag{3.7}$$

where q is the electron charge, κ the Boltzmann's constant and T is the temperature.

In **high injection** conditions, the carriers density on the base is dependent on the square of the number of the injected carriers. Under these circumstances V_{Fb} depends on the square root of the current density, on b on the ratio W/L as well as on the doping and the length of the contact region. V_{Fj} under these conditions is independent on the base doping and on the carrier lifetime and varies as:

$$J_{Fj} \propto e^{\frac{qV_{Fj}}{\kappa T}} \tag{3.8}$$

3.2.2.2 *p-i-n* diodes behavior under hadron irradiation

The theory of the p-i-n diodes response to neutrons was initially studied by Swartz and Thurston in 1966 [Swa66]. The response was determined for devices with a base manufactured from LOW RESISTIVITY silicon ($\leq$ kΩ·cm). Interaction of particles with the

[3]injected carrier density (n, p) much lower than the doping concentration of the intrinsic region ($n \approx p \ll n_i$).

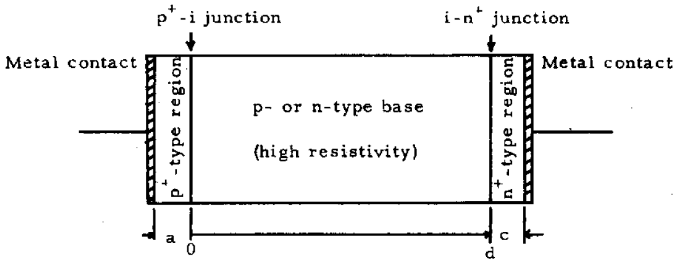

Figure 3.7: Scheme of a forward biased *p-i-n* diode. The distance 0 - d corresponds to the intrinsic base thickness (W).

diode generate stable defects in the silicon lattice which act as recombination sites that have the effect of reducing the minority carrier recombination time and the conductivity of the silicon. The resulting dependence of the minority carrier lifetime (τ) on the particle fluence is given by:

$$\frac{1}{\tau} = \frac{1}{\tau_0} + K_\tau \cdot \Phi \tag{3.9}$$

where τ_0 is the initial minority carrier lifetime, Φ the particle fluence and K_τ is the *minority-carrier lifetime damage constant* function of particle type, particle energy, initial silicon material, injection level and temperature. Typical K_τ values lies in the range of 10^{-5}-10^{-6} $cm^2 \cdot s^{-1}$ [Spe68, Dus04a].

Under conditions of low/intermediate injection (small currents) and where the width of the base (W) is small compared to the diffusion length of the charge carriers L (W/L ratio $\leq$ of about 2), the overall particle sensitivity is negative because the junction voltage V_{Fj} predominates and decreases with decreasing τ. For a large W/L ratio instead, the voltage sensitivity to particles is positive due to the base voltage V_{Fb} that increase with the decreasing of the diffusion length L. For a fixed ratio W/L the voltage sensitivity to particle fluence is calculated by differentiating the Eq. 3.6 containing the expressions of junctions and base voltages valid in low injection conditions. It is thus possible to find:

$$\frac{\Delta V_F}{\Delta \Phi} \sim K_\tau \cdot \tau \sim K_\tau \cdot W^2 \tag{3.10}$$

Under conditions of high injection (large currents) since the total junction voltage V_{Fj} is independent of carrier lifetime a negative particle sensitivity is not found. The total voltage drop across the diode is dominated by the change in V_{Fb} and the particle sensitivity is positive for all values of W/L [Ant77]. In such a case, repeating the above described calculation in case of high injection conditions, for a fixed ratio W/L the voltage sensitivity to particle fluence is:

$$\frac{\Delta V_F}{\Delta \Phi} \sim K_\tau \cdot \tau^{3/2} \sim K_\tau \cdot W^3 \tag{3.11}$$

From the above statements it is possible to conclude that for a low resistivity silicon diode:

- in condition of high injection, independently of the W/L ratio of the diode, the particle sensitivity is always positive due to the decrease of L with increasing Φ.

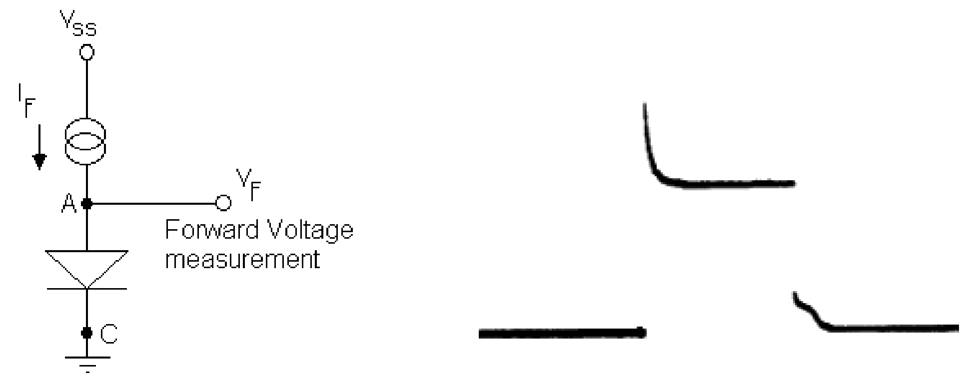

(a) Basic readout circuit (b) Current pulse shape

Figure 3.8: p-i-n silicon diode forward current readout.

However, the effect of the high current heating the junction would be to heat the diode and anneal some of the particle-induced defects;

- in condition of low/intermediate injection and for a high W/L ratio (long-base sensors) the particle sensitivity is again always positive. However, according with Eq. 3.9, τ decreases quickly at the beginning of the irradiation becoming small and almost constant for higher particle fluences. The forward voltage V_F starts therefore to grow with increasing particle Φ but quickly reaches a saturation value. In this condition the useful change in V_F is thus provided only for low Φ range up to about 10^{11} particles/cm^2.

Let's now consider *p-i-n* diodes with a base manufactured from HIGH RESISTIVITY silicon (> kΩ·cm) [Ros90]. In this case, and in conditions of low/intermediate injection, the concentration of carriers in the base region (e.g. the change in resistivity) as a function of the particle fluence must be taken into account. The dependence of the silicon resistivity on the particle fluence, obtained by Buhler, is given by:

$$\rho = \rho_0 \cdot e^{\Phi/K_\rho} \tag{3.12}$$

where ρ_0 is the initial equilibrium resistivity of silicon before irradiation, Φ the particle fluence and the coefficient K_ρ, according to Buhler, has a value between 400 and 3000 cm^{-2} for different silicon materials.

Starting from a silicon material with high resistivity it is so possible to extend the diode dynamic range compensating the V_F saturation by using the increasing resistivity of the base during irradiation according to the Ohm low. The resultant radiation response will be therefore a linear increase of the diode's forward voltage over a broad equivalent particle fluence range.

Concluding, it is clear that the sensitivity of the *p-i-n* diodes to particles irradiation in condition of low/intermediate injection can be determined at the manufacture of the diodes and can be increased making diodes with a **wide** intrinsic base and using **high-resistivity** silicon with a **large** initial carrier lifetime.

3.2.2.3 *p-i-n* diodes readout protocols and methods

The readout of the V_F in a *p-i-n* diode is performed by injecting a forward current throughout it following the scheme presented in Fig. 3.8(a). A number of authors have described readout systems and methods for *p-i-n* dosimetric diodes based on such a method.

Awschalam et al. (FNAL) [Asc85] describe a reader based on a constant current generator, sample and hold circuit and an analog to digital converter with display. The constant current source was set to 25 mA. The voltage across the diode was measured using a single 10 ms pulse of 25 mA during which the forward bias voltage was captured with the sample and hold circuit. A stability of ± 1 mV was obtained with this reader over the course of several days.

Nagarkar et al. [Nag92] investigated a reader which used a series of three to five 10 ms duration pulses of 25 mA each. However they found that this method caused heating of the diode with the consequent annealing of the radiation induced defects. They therefore developed a reader that employed a single 1 ms duration 10 mA pulse.

Other authors [Ant77] in earlier publications conducted experiments more aimed at characterizing silicon damage cross sections employed constant current (non-pulsed) readout circuits with currents of up to 100 mA and as low as 1 mA.

In Ref. [Car00] it has been proven that the readout of the forward bias voltage, with an accuracy within 1 mV, can easily be achieved using a pulsed current source. For a high resistivity *p-i-n* diode with a very large base (W $\sim$ 1 mm), using a pulsed current source and a peak detector circuit, it was shown that is possible the readout of the *p-i-n* diodes with a duty cycle of 0.1.

In all cited references, the minimization of the heating of the diode has been presented as the main issue during the readout. To keep low the temperature increase during the diode's readout is important for two reasons:

- any annealing is avoided;
- changes in the forward bias voltage of the diode due to thermal effects on silicon conductivity are avoided.

The above statement can also be verified with a simple calculation. Before irradiation the typical voltage drop across the base of a *p-i-n* diode with approximative dimensions of $1\times1\times1.2$ mm^3 is in the order of 3 V when it is supplied with a 10 ms forward current pulse of 1 mA. If the power dissipated in the base of the diode is estimated as W $=$ $V \times I$, where V is the voltage drop across the base section and I is the current, then the average power dissipated would be of the order of 3 mW. From this value the energy deposition during the readout of the diode can be calculated using the simple equation for a 10 ms pulse length:

$$Q = P \times t \simeq 3 \times 10^{-5} J \tag{3.13}$$

Now, assuming a specific heat capacity of $c = 0.7\ Jg^{-1}$ °C^{-1} for silicon ($\rho = 2.33\ g/cm^3$) and a mass for the diode of approximately 2.8 mg, it is possible to calculate for a new device that, during the readout cycle, the temperature increase will be of:

$$\Delta T = \frac{Q}{c \times m} = 0.015\ ^{\circ}\mathrm{C} \tag{3.14}$$

Repeating the above calculation after irradiation, assuming the voltage drop across the device increases up to 15 V for an irradiation up to $\Phi_{eq} = 2\text{x}10^{12}\ cm^{-2}$, it easy to see that the temperature inside de diode will increase up to 0.08 °C. Therefore, the temperature in the *p-i-n* diode would be unlikely to rise by more than 0.1 °C during the readout by keeping the current pulse as low as 10 ms. On the other hand, doing the same exercise for a current pulse of 1 s it is possible to estimate that the temperature increases in the diode, will be of about 10 °C during the readout of an irradiated diode.

3.2.2.4 Merits of *p-i-n* dosimetric diodes

The main figures of merit of the *p-i-n* dosimetric diodes have been reported here below as identified in different articles by various authors [Ros94, Oli94, Swa63, Kra66, Spe68, Pro82, Mor95, Asc85]:

- simple readout;
- high spatial resolution;
- wide range of response;
- variable sensitivity;
- response independent of device orientation;
- dose-rate independent;
- small response variation within a batch of devices. If required the device sensitivity can be made more uniform by pre-irradiation with fast neutrons to a fluence of $10^{11}\ cm^{-2}$ followed by a brief high temperature annealing period as reported in Ref. [Ros94];
- devices may be reusable;
- remote recovery using current annealing as proposed in Ref. [Ros94] (advantage for irradiated devices);
- mechanism of response identical to the damage in electronic devices

3.2.2.5 *p-i-n* diodes temperature dependence

The temperature dependence of a *p-i-n* diode is the result of two separate phenomena, the positive temperature coefficient of resistance of the intrinsic silicon and the negative temperature coefficient of the *p-n* junctions. The temperature dependence of the *p-i-n* diodes is a major problem as there is no direct way of differentiating between changes in impedance caused by particle exposure and changed caused by temperature [Nag92].

3.2.2.6 *p-i-n* diodes current-pulse analysis

When a square current pulse is injected through a *p-i-n* diode in the forward direction, the voltage generated across the diode is not a simple square wave, but rather a complex waveform which has three distinct regions. The shape and the amplitude of each of these regions provide valuable information regarding device parameters such as its impedance and the minority charge carrier lifetimes which can be related directly to the incident neutron fluence. A typical diode output waveform is shown in Fig. 3.8(b):

1. The exponential behavior in the beginning is due to the conductivity modulation process which results in lowering the forward resistance of the *p-i-n* diode as the charge carrier density in the device is increased.

2. The steady state region that follows corresponds to constant device impedance. It is this voltage that changes in proportion with the particle flux and is measured as a diode signal. The time required to reach a steady State voltage depends on the resistivity of the intrinsic silicon and the device geometry. This sets the lower limit on the interrogation pulse duration and the power delivered to the device.

3. As soon as the current through the device is interrupted, the steady state voltage drops to a lower value equal to the voltage drop across the junctions of the device. The slope of this portion of the waveform is related to the lifetime of the charge carriers in the silicon crystal, a property known to be affected by absorption of particle and the resulting damage to the lattice. This may be used as an alternative approach to read the device but has extremely low sensitivity.

Thus, there are several ways to read the diode, but the forward voltage drop across the diode offer the higher sensitivity [Nag92].

3.2.3 Optically Stimulated Luminescent materials (OSLs)

3.2.3.1 Principle of operation

Optically Stimulated Luminescence (OSL) phenomena results from processes involving the recombination of trapped charge after irradiation. Trapping phenomena in OSLs are similar to the ones that occur in the oxide layer of a RadFET transistor as we have seen in Sec. 3.2.1.1. Once the charge is trapped, its recombination may be triggered ("stimulated") by different means. For example, the materials can be heated to collect the luminescent signal. This is the case of the TLD dosimeters we described in Section 3.1.4. Another stimulation method is the optical one by flashing the material with an appropriate wavelength. This is what is used in the case of the OSL materials to provide the energy needed for charge recombination.

OSL materials are wide band-gap insulators in which a certain number of energy levels (defects) have been introduced by doping the material during processing. Depending on their position in the insulator band-gap these defects can have the role of trap levels, if they lie close to the conduction band, or they can act as recombination centers, if they are located in the middle of the band-gap [Dus95].

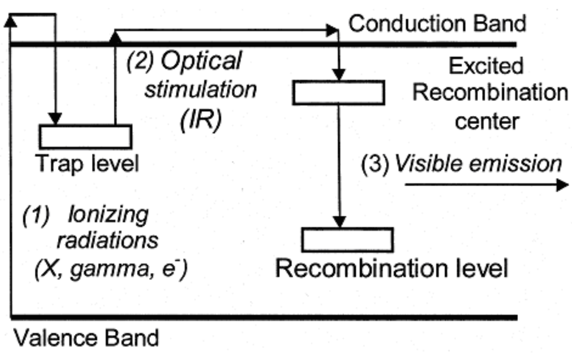

(a)

(b)

Figure 3.9: Operating principle of an OSL dosimeter. (a) Basic mechanism of the optically stimulated luminescence. (b) Raw SrS:Ce,Sm used for this work.

Ionizing radiation creates in the OSL material a large amount of electron-hole pairs. Focusing our attention on the electrons, the effect of the ionization is to excite them to the conduction band of the material as indicted by (1) in Fig. 3.9(a). Some of these free electrons are promptly recombined while some others remain trapped on localized defects (trap levels) for a long time period depending on the temperature and the activation energy of the traps. The activation energy of a trap is defined as the difference between the energy of the trapping center and the energy of the conduction band.

The optical stimulation of the material, with a proper wavelength (2), will provide then the necessary activation energy to release the trapped charge. Once free, the electrons can be trapped again or captured by a recombination center that becomes instable. When the recombination center finally comes back to its fundamental state, a subsequent radiative recombination may be observed (3) as shown in Fig. 3.9(a). Quantifying the amount of emitted light makes it possible to evaluate the energy absorbed by the dosimeter.

Several families of materials have been identified as emitting Optically Stimulated Luminescence. They differ by their chemical and optical properties and not all of them are appropriate for an application in dosimetry. The intrinsic ability to trap charges for long time periods and the efficiency of the luminescence are the major criterion for selecting OSL materials. This efficiency is strongly dependent on the dopants and their concentration. Another important criterion to chose OSL materials is the separation of the stimulation and the emission spectra. An overlap in the two spectra makes it difficult (sometimes impossible) to discriminate the emission from the stimulation.

Rare-earth-doped alkaline sulfides (like SrS, BaS, CaS and others) have been identified by the German physicist Lenard as efficient phosphors. They exhibit both Thermoluminescence and OSL properties. Primarily devoted to infrared-visible conversion, they were later studied intensively for applications in radiation dosimetry. In this work OSL materials based on Strontium sulfide (SrS), processed at the *Electronic and Radiations Research Laboratory* of the University Montpellier II, France have been used (see Fig. 3.9(b)).

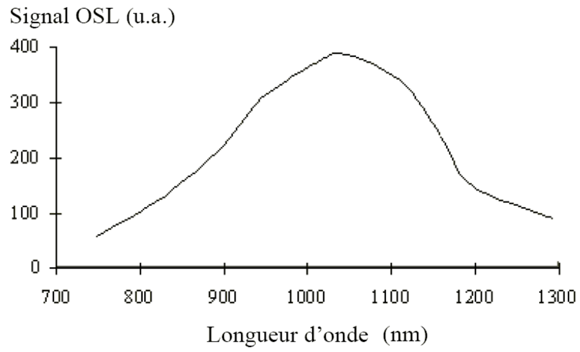

(a)

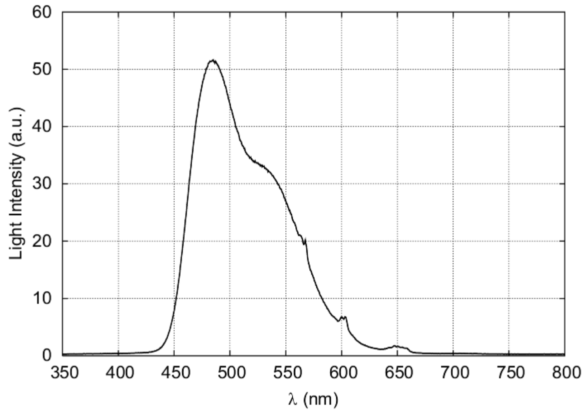

(b)

Figure 3.10: SrS:Ce,Sm characteristic spectra. (a) Stimulation spectrum. (b) Emission spectrum.

The Monpellier SrS is doped with a small concentrations of Cerium and Samarium, impurities of the Lanthanide series (rare-earths). The Cerium (activator) is introduced in the material to give the luminescent emission in the visible part of the electromagnetic spectrum. The Samarium (co-activator) is instead used to define the stimulation spectrum in the infrared (IR) region (750 - 1300 nm). This Sulfide makes it possible to reach a minimum measurable dose in the range of 10 μGy and shows evidence of saturation after exposure to about 100 Gy ensuring a 7 orders of magnitude dynamic range [Mis92]. The characteristic IR stimulation spectrum of the SrS:Ce,Sm is plotted in Fig. 3.10(a). The optimum stimulation wavelength lie around 1 μm. The optical stimulation results thus completely independent and easy to discriminate from the emission spectrum that instead ranges from 450 nm to 650 nm as shown in Fig. 3.10(b) [Dus04b, Dus95].

The full discrimination between the stimulation and emission spectra and the broad measurement range are the two main characteristics that distinguish OSL materials from the others available on the market for dosimetry purposes (α-Al_2O_3, KCl:Eu, etc.). Moreover, the absence of a charge-induced electric field in the OSL (global charge neutrality) avoids any recombination processes described before in the case of the Silicon oxide (see Sec. 3.2.1.4). This feature make the OSL material sensitive to any type of ionization released within it without any dependence on radiation type and energy. The small neutron cross sections of the SrS for neutrons in a broad energy range makes also the OSL sensitivity to neutrons very low. A quantitative evaluation of the neutron sensitivity will be given later in this work in Chapter 8. The above features make therefore the Montpellier OSL a good candidate for the dosimetry at the LHC Experiments.

Limitations in OSL dosimetry can instead come to measure radiations with very high LET. In this case, quenching effects of the emitted luminescence have been reported in literature [Boo98]. Thermally-stimulated fading effects can finally be responsible of a loss of trapped charge that can induce errors in the dose measurement performed with OSL materials [Vai03a]. The charge de-trapping probability ($\frac{1}{\tau}$) follows an *Arrhenius* low as indicated in Eq. 3.15, where A [s^{-1}] is the frequency factor, κ is the Boltzmann

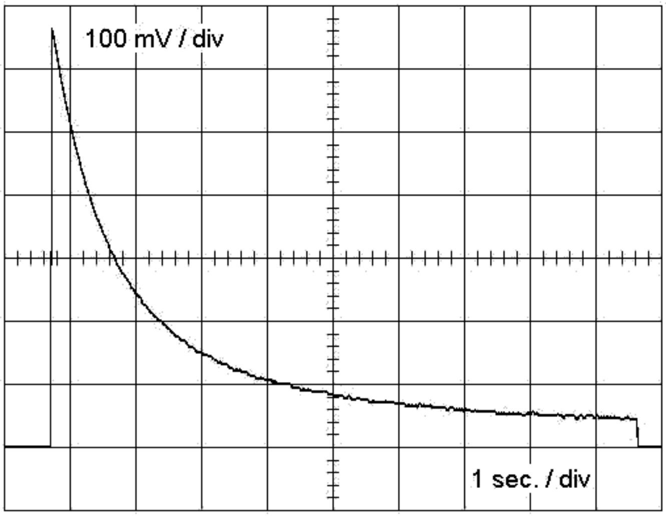

Figure 3.11: Typical shape of an OSL signal as recorded with a photo-sensor by means of an oscilloscope. The stimulation has been provided with a IR LED.

constant, ϕ [eV] is the Activation energy of the trap level and T is the room temperature.

$$\frac{1}{\tau} = A \cdot e^{-\frac{\phi}{\kappa \cdot T}} \tag{3.15}$$

Eq. 3.15 gives therefore the effect of the temperature on the trapped charge. The higher the temperature, the lower the charge storage time of the charges in the trap levels. This effect creates the possibility to reset the OSL material before its utilization by means of a thermal cycle. A preliminary evaluation of the fading of the used OSL materials will be presented here in Chapter 8.

3.2.3.2 The OSL signal

Fig. 3.11 represents the typical shape of an OSL signal of a material exposed to a few mGy dose. In the case presented in the picture, the stimulation were provided by an IR Light Emission Diode (LED) switched on 700 ms after the beginning of the acquisition. The signal show a quick luminescent emission followed by a decay period on second time-scale. The decay of the signal can be easily modeled by considering a simple reaction rate equation providing an exponential solution.

Let now consider irradiated OSL material, in which N charges have been trapped during the irradiation process. The number of charges depends on the dose D so that N(D). Under a constant stimulation flux F, the OSL signal S(t) is observed in function of the time with the shape of Fig. 3.11. Since the response of the OSL to a stimulation is obtained within nanoseconds, the rising time of the luminescence can be considered as negligible. It is then reasonable to assume that the peak value of the signal is obtained for t=0. The decay of the OSL signal is then modeled with an exponential law:

$$S(t) = K \cdot N(D) \cdot F \cdot e^{-\sigma \cdot F \cdot t} \tag{3.16}$$

where K is a constant that depends on both the material and the readout method. σ is the cross section of the stimulated de-trapping process. The time constant of the decay is then purely dependent on the stimulation flux intensity as it is then given by:

$$\tau = \frac{1}{\sigma \cdot F} \tag{3.17}$$

From Eq. 3.16 is then still possible to see that at t=0, the peak value of the signal is given by

$$S_{peak} = K \cdot N(D) \cdot F \tag{3.18}$$

and is directly proportional to the dose D as long as the stimulation flux F remains constant. By integrating Eq. 3.16 it is finally possible to get the expression for the integrated OSL signal:

$$S_{integrated} = \int_0^\infty S(t) \cdot dt = \frac{K}{\sigma} \cdot N(D) \tag{3.19}$$

The value given by Eq. 3.19 is no longer dependent on the stimulation flux but only proportional to the total amount of charge trapped within the material. As a consequence, the dose absorbed by the OSL can be measured from both the peak value of the signal and the integrated luminescence. On the one hand, the measurement of the OSL peak is practical because it only requires the acquisition of a single value instead of a whole curve. On the other hand, the peak value depends on the intensity of the stimulation [Vai03b, Dus04b]. A constant stimulation light became thus the main constraint to guarantee reliable measurements. All the measurements presented in this work where thus obtained by measuring the peak of the luminescent signal.

3.2.3.3 Dosimetry systems based on OSL

The features of the OSL materials described in the preceding sections, can be exploited in many application that goes from the radiography (medical/industrial applications where the OSL is usually shaped in form of passive dosimetric films) to the development of on-line and real-time dosimetry systems (space and nuclear applications). Therefore different IR stimulation sources and photo-detectors can be used in function of the sensitivity and dynamic range required, the space and the power constraints, etc.

In this section only the application principles of direct interest for this work will be described. A more exhaustive list of OSL application can be found in [Mis91, Pla02, Pol00, Vai03a, Idr04] and references therein.

- *Dose cartography with OSL films*: The films used for dose mapping are a 100 μm thick layer of OSL material, silk-screen printed on a kapton foil as the one shown in Fig. 3.12(a). By exposing such a films to a particle beam, the charges get trapped on its surface proportionally to the beam particle intensity [Mis91, Pla02]. After beam exposure, the irradiated foil can be readout using a solid-state laser beam (of about 1.0 μm wave length) focused on it and by positioning the film on a X-Y stage [Pol00]. The laser beam is then stepped over the foil in the two axes and the emitted luminescent signal is collected by means of a photo-multiplier tube. The signal is finally digitized and recorded to get a map of the emitted

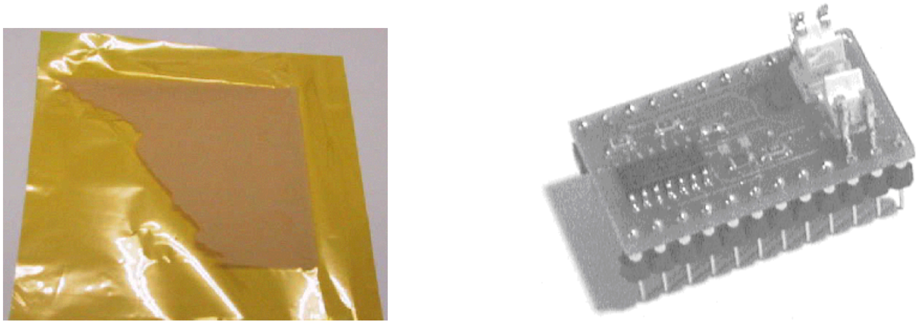

(a) (b)

Figure 3.12: Dosimetry systems based on OSL. (a) Films for dose maps (b) Sensor for space applications.

luminescence versus X and Y-axis that represents the spatial dose distribution. After reading, the material can be completely reset by a 24 hours annealing at 80 °C. The OSL films were used in this work to characterize the proton beam of the IRRAD1 facility at CERN (see Sec. 5.1.2). Their spatial resolution is strongly dependent on the dimension of the laser spot used for the readout and on the film granularity. With the test bench available at the University Montpellier II it is possible to obtain maps of the proton beam with a 250 μm resolution.

- *Integrated OSL sensor for space applications*: The basic OSL sensor cell is designed in a way that a thin OSL layer is directly sandwiched between the IR LED and a visible photodiode. With this principle it is possible to build radiation sensors for PCB-mount like the one shown in Fig. 3.12(b) with a size that fits in a sugar cube volume. The power consumption of such a sensor is limited to the current needed to bias the LED during stimulation. The basic external circuitry needed to operate the sensor consists only of an operational amplifier that converts the current delivered by the photodiode into voltage. The signal is then amplified and digitized. A voltage source, triggered by a logic input is also needed to operate the stimulation source [Vai03a, Vai03b].

  The sensor developed at the *University Montpellier II* includes also a radiation hardening solution that consist, thought a feedback loop, to increases of the forward voltage current in the LED with increasing particle fluence. This has to be done since the LED light emission degrades over time due to displacement damage. The infrared emission is kept constant by measuring it using a second LED/photodiode set installed in parallel to the one used for the OSL readout.

  So far, this OSL Sensor has flown on the International Space Station as a part of the SPICA module designed by the CNES and it has been integrated in several satellite experiments like SET1 (NASA) and CARMEN (CNES). In Sec. 8.3 of this work this sensor will be evaluate with the goal to prove its utilization in the HEP Experiments at CERN.

- *Remote Online OSL Dosimetry using optical fibers*: In the case of the integrated sensor, both the OSL and the electronics for the readout are exposed to radiation,

Property	Si	SiO_2	SrS
Atomic number (Z/Z_{eff})	14	29.9	34.15
Atomic/Molecular weight (A)	28.1	60.1	119.7
Density [g cm^{-3}]	2.33	2.2	3.7
Atoms [$\times 10^{22}$ cm^{-3}]	4.96	–	–
Crystal structure	diamond	various	cubic
Lattice constant [Å]	5.43	–	6.02
Melting point [°C]	1420	1830	> 2000
Thermal expansion coefficient [$10^{-6} K^{-1}$]	2.6	0.4	–
Thermal conductivity [$W m^{-1} K^{-1}$]	1.5	0.14	–
Dielectric constant (ϵ)	11.9	3.8	11.3
Band gap [eV]	1.12	9	4.8
Energy to create e–h pair [eV]	3.86	18	–
Radiation length [cm]	9.4	12.3	–
Average minimum ionizing energy loss [MeV $g^{-1} cm^2$]	1.66	1.69	–
Electron mobility [$cm^2 V^{-1} s^{-1}$]	1410	20	–
Hole mobility [$cm^2 V^{-1} s^{-1}$]	450	1×10^8	–
Intrinsic carrier density (n_i) [cm^{-3}]	1.5×10^{10}	–	–
Intrinsic resistivity [$\Omega \cdot cm$]	2.3×10^5	$> 10^{16}$	–

Table 3.4: Basic properties of Silicon, Silicon oxide and Strontium Sulfide at room temperature (300K) [Sze85, Gro00, Mol99a, Dus95, Sai98].

the problem of the radiation induced damage is supposedly being addressed. It is not always possible or practical to use a sensor integrating both the OSL and the reading circuitry. The reason can be either because of a very harsh radiative environment, or the necessity to minimize the size of the sensor. In some cases the use of long cables until the measurement point can also be a problem for electromagnetic compatibility.

To drive the visible/IR signals from/to the OSL material, the use of optical fibers can provide the solution of the above problems. One application of such a system can be the real-time monitoring of the dose delivered to a tumor during and Intra Operative Radio Therapy treatment. A second application can be also the measurement of very high doses in the environment of the LHC Experiments. This last application has been evaluated in the framework of this thesis and it will be presented in Chapter 8.

3.3 Conclusion

The purpose of dosimetry is to quantify the radiation field and to measure the particle fluence and/or the energy imparted to the exposed materials. Accurate dosimetry measurements are therefore important, especially in the case of the LHC experiments, in order to:

- provide a cross check the prediction of the Monte Carlo models (their accuracy is limited by the complex geometries that have to be modeled to describe the LHC machine and by the knowledge of the physics of very high-energy particle processes);
- assess the long-term radiation damage with the aim to guarantee the reliability of the detector systems over the 10-years of the LHC operation.

Several types of *Passive Dosimeters* are existent and have been described in the first part of this chapter. They were widely used, especially in the previous generation of CERN accelerator machines, for routine measurements. For this reason an important amount of data regarding their calibration (in radiation field of various qualities) is already available in literature.

Although *Passive Dosimeters* will be employed at the LHC, their utilization risk to be limited because of the high level of remanenent radiation in certain location inside the LHC experiments (difficult removal), and because of the impossibility to reach certain measurement positions of interest (difficult access). Moreover, the fact that these devices have been often calibrated to measure the energy deposition in tissue-equivalent materials makes a direct application of the performed measurement, to the evaluation of the damage in electronics and semiconductor devices, difficult.

Active Dosimeters (semiconductor sensors and OSL materials) provide a solution to the above problems allowing to follow in ”real-time” (on-line) the evolution of the radiation field. The characteristics of this second category of devices have been described in details in the second part of this chapter. It is important here to point out that some of these active technologies provide integrated measurements over time because of their capability to store the dosimetric information in a stable way. Some of these sensor can be thus used at the same fashion of a *Passive Dosimeter* with the advantage that their physical dimension can be arranged, with appropriate packages, to be comparable of smaller with respect the majority of the described passive devices.

Before entering in the specific issues concerning the *Active Dosimeters* at the LHC experiments, presented in the Chapters 6 - 8, the experimental equipment used for the characterization of such a devices will be described in the next Chapter 4. Some of the experimental facilities described there (IRRAD1, IRRAD2 and IRRAD6 at CERN-PS) play a privileged role in this thesis work because of their similarity with the LHC radiation environment. The characterization of the *Active Dosimeters* in these radiation fields it is possible only after their accurate calibration by using independent dosimetric means. These calibration issues will be therefore discussed in Chapter 5.

Chapter 4

Experimental equipment for radiation sensor studies

4.1 Irradiation Facilities

4.1.1 PS East Hall irradiation facilities at CERN

To study radiation damage in semiconductors and electronic devices at CERN [Hol02], since 1998 three irradiation facilities are operated in the East Hall Experimental Area of the Proton-Synchrotron (PS) accelerator [Gla99, Gla00]. The facility named IRRAD1, located in the PS-T7 beam-line, allows irradiation experiments with the 23 GeV (24 GeV/c)[1] primary proton beam. In the same beam-line, the IRRAD6 facility allow instead to carry out irradiations in a mixed neutron/charged particles/γ-ray field. The IRRAD2 facility, located at the end of the PS-T8 beam line, allows finally irradiation experiments in a mixed neutron/γ-ray environment produced in a cavity before a beam stopper.

4.1.1.1 IRRAD1

In the T7 beam-line the primary 23 GeV proton beam of the PS accelerator is directed to the irradiation area where the facility named IRRAD1, a remote controlled shuttle system, is located. In this zone the proton bursts are delivered during the 16.8 s super-cycle of the PS machine in 1-3 spills of about 400 ms each (slow extraction) with a maximum beam intensity of 2x10^{11} protons per spill. A defocusing-scanning system is used to spread out the beam in order to produce an uniform irradiation spot over a surface that can vary from 2 to 25 cm^2 [Gla99]. Changing these two parameters, proton fluxes from 8x10^{11} $cm^{-2}h^{-1}$ to 8x10^{13} $cm^{-2}h^{-1}$ can be achieved.

The IRRAD1 shuttle moves on a rail inside a metal conduit of a length of about 15 m and allows transport of the samples to be irradiated directly from the counting room into the irradiation area. The conduit is inserted into a radiation shielding constituted of concrete blocks as shown in Fig. 4.1(a). In the irradiation location, to decrease the

[1] The degree of acceleration of a charged particle is often expressed also as its momentum. Being E the kinetic energy [MeV] of a particle of rest mass M [MeV] and momentum P [MeV/c], it is that $E = \sqrt{P^2 + M^2} - M$. In the case of protons $M = 938$ MeV [Sul92].

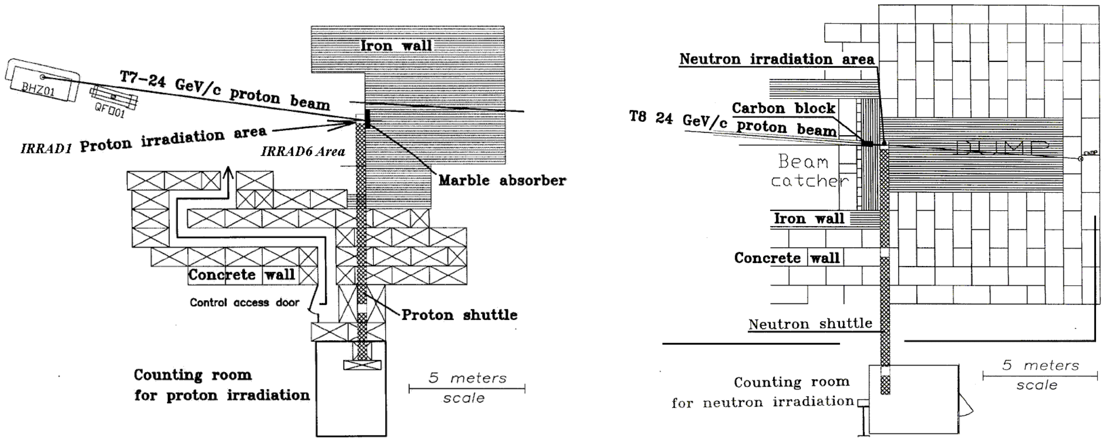

(a) (b)

Figure 4.1: CERN-PS East Hall Irradiation Facilities. (a) Layout of the IRRAD1 facility. (b) Layout of the IRRAD2 facility.

neutron backscattering to a few percent, a marble absorber of 20 cm has been inserted between the shuttle position and the following iron beam stopper. A luminescent screen with a camera is used to display the beam spot and a Secondary Emission Chamber (SEC) [Ber97] provides a measurement of the total beam intensity during irradiations.

4.1.1.2 IRRAD6

The radiation environment generated in the area around the IRRAD1 irradiation position, by the interaction of the 23 GeV proton beam with the beam stopper, is also often used to perform irradiation tests. In this area, named IRRAD6 (see Fig. 4.1(a)), a low rate mixed particle field is then available. The samples to be irradiated there are set in positions identified by means of two coordinates: the distance from the beam-stopper measured along the T7 proton beam (Z) and the radial distance from the beam axis (r).

Several Monte Carlo simulations have been performed [Ler98] to determine the spectral composition of this environment and its intensity. They have been validated by means of activation foil measurements [Bac00]. Fig. 4.2(a) shows the particle spectra simulated for $Z = 20$ cm and $r = 60$ cm in IRRAD6 when 10^5 protons are sent toward the beam-stopper. In this position the environment is dominated by backscattered neutrons and photons of energy around some tens of MeV. For energies higher than 100 MeV the contribution of charged hadrons start to be also important.

Finally, Fig. 4.2(b) shows the radial distribution of the backscattered particles for $Z = 20$ cm. By placing the samples 1 meter away from the beam axis, neutron fluxes of about 10^7 cm^{-2} per proton spill can be reached. At increasing distances from the beam dump, (higher Z values), neutron fluxes as low as 10^6 cm^{-2} per proton spill can be instead obtained.

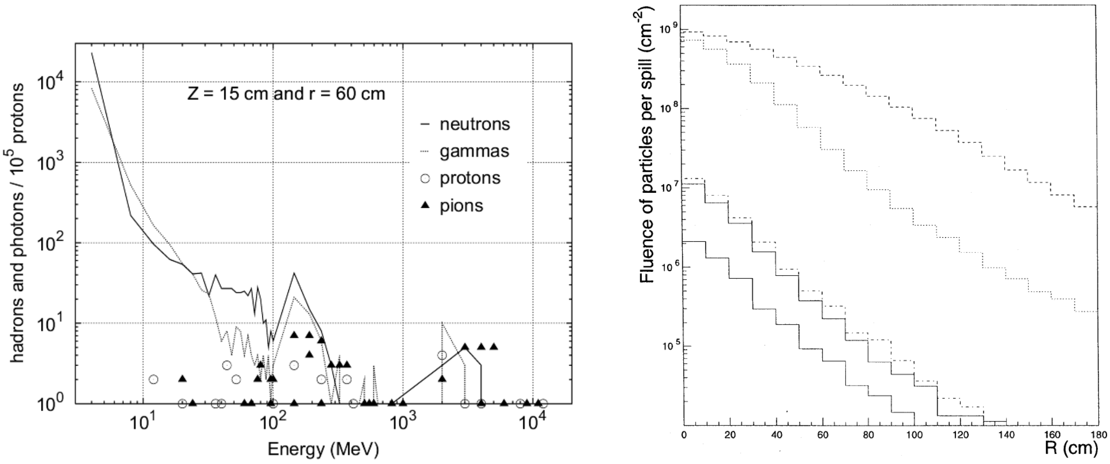

(a) (b)

Figure 4.2: IRRAD6 facility at the PS East Hall. (a) Particle spectra simulated for 10^5 incoming primary protons. (b) Radial distribution of backscattered particles at a distance of 20 cm from the marble absorber (from bottom to top: protons, negative pions, positive pions, gammas and neutrons). The plot is referred to a primary beam intensity of 4×10^{11} protons.

4.1.1.3 IRRAD2

Fig. 4.1(b) shows the layout of the irradiation zone IRRAD2 located at the end of the T8 beam-line. The irradiation is performed in a cavity with secondary particles produced by the primary 23 GeV proton beam after crossing a target constituted of 50 cm of carbon and 5 cm of lead [Gla99].

As for the IRRAD1 facility, a motorized shuttle system allows transport of the samples from the counting room to the irradiation cavity in which a broad spectrum of neutrons, γ-rays and charged hadrons is produced. Fig. 4.3(a) shows the typical spectrum obtained by Monte Carlo simulations with the FLUKA code [Fas01], while in Fig. 4.3(b) the three dimensional particle profile inside the irradiation cavity is shown. The secondary particles intensity in the IRRAD2 cavity shown in Fig. 4.3(b) has been measured by means of activation of Al foils (See Sec. 3.1.8).

With the remote controlled shuttle system it is possible to set the position of the samples in the vertical coordinate Z with respect to the beam axis. Depending on the position Z, the ratio of charged hadrons in the GeV energy range to neutrons and γ can be chosen. It is thus possible to perform irradiations in a pure γ/neutron environment (at positions far from the beam axis, typically Z = 50 cm) or in a charged-hadron rich radiation environment that better represents the one expected for the inner detectors of the LHC experiments (at positions close to the beam axis, typically Z = 10 cm).

The proton bursts delivered in the T8 beam-line have the same time-structure as those of the T7 beam-line. It is therefore possible to reach 1-MeV neutron equivalent fluxes from 0.3x10^{12} $cm^{-2}h^{-1}$ to 1x10^{12} $cm^{-2}h^{-1}$ depending both on the number of spills delivered by the PS and the distance of the sample from the beam axis. As in the case of IRRAD1, a SEC provides finally a measurement of the primary proton beam intensity that hits the target.

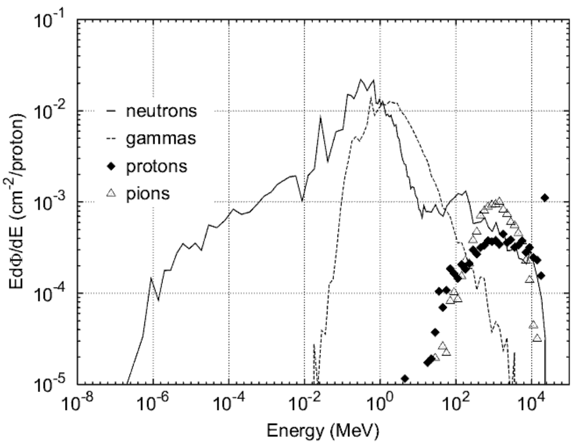

(a) IRRAD2 particle spectra at Z = 10 cm

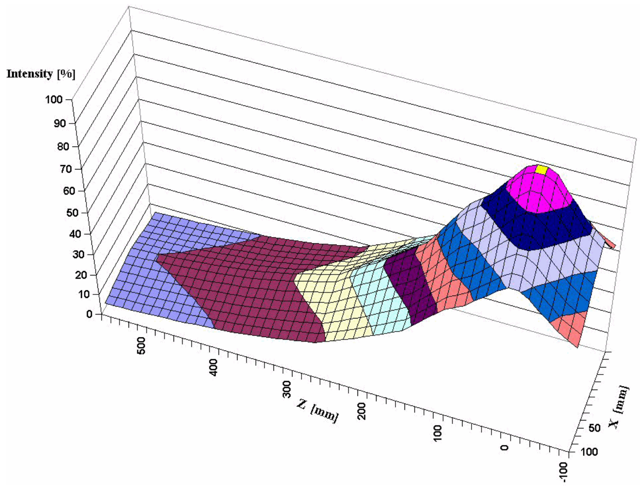

(b) IRRAD2 particle profile in function of Z

Figure 4.3: The IRRAD2 facility. (a) Field composition at 10 cm. from the beam axis normalized to one impinging 23 GeV proton. (b) Secondary particle profile in the whole IRRAD2 cavity, in function of Z and x, determined by means of activation foils technique.

4.1.2 TRIGA Mark II reactor at JSI

The Reactor Research Center at the *Jozef Stefan Institute* (JSI) in Ljubljana, Slovenia has an experimental nuclear reactor of type TRIGA [Rav03a] (see Fig. 4.4(a)). The neutron spectrum of this facility, determined by measuring the activation of foils of different materials, is shown in Fig. 4.4(b) [Kri98].

In this facility, irradiations are performed by placing the samples into the reactor core through two irradiation channels (F19 with a circular cross section of 2.2 cm diameter and the TIC with an elliptic cross section of 7 × 5 cm) that occupy fuel rod positions and enters the reactor core from above. The neutron flux delivered to the samples is linearly proportional to the reactor operating power that ranges from 250 W to 250 kW. The corresponding 1-MeV neutron equivalent flux at the end of the channel F19 is of 1.9×10^9 $cm^{-2}s^{-1}$ at a reactor power of 250 W. In the TIC channel the neutron flux is about a factor 2 higher with respect to the one measured in the channel F19.

In the framework of this thesis, a series of calibration measurements allowed to determine that the accuracy of the neutron flux delivered to the samples under study is better than ± 10% in both F19 and TIC channels. Moreover, a series of experimental measurements have been carried out in order to determine the TID associated to such a neutron flux.

Fig. 4.5 shows the relative dose-rate profile recorded along the TIC irradiation channel. On the x-axis the distance is measured from the center of the reactor core. The measurements presented in the picture have been recorded with the reactor off by measuring the photo-current generated inside reverse biased silicon detectors (same diodes used for NIEL measurements presented in Sec. 3.1.9 of Pag. 22). From the dimensions of the employed diode it is then possible to convert the above mentioned current into ionizing dose in silicon [Dan03]. A second dose-rate measurement, performed with Rad-FET dosimeters, is also shown in Fig. 4.5. The dose profiles measured with these two

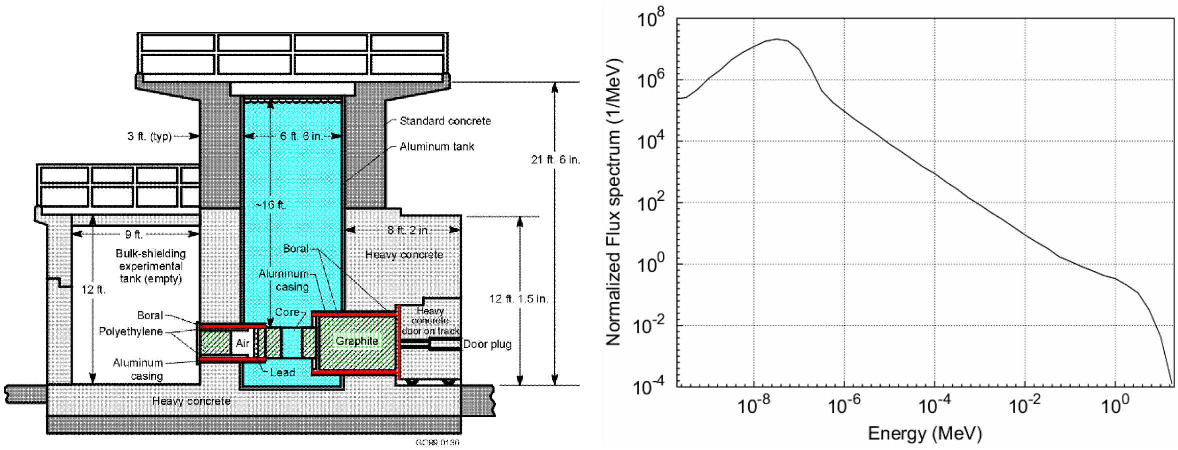

(a) (b)

Figure 4.4: TRIGA Mark II reactor at JSI. (a) Cross-section of the reactor facility. (b) Normalized neutron flux spectrum at 250 kW. The normalization has been done in a way that $\int_{100keV}^{20MeV} \Phi(E)dE = 1$, where $\Phi(E)$ is the neutron flux.

independent means show to be in agreement for less than ± 10%.

In the experimental conditions mentioned above, the dose-rate measured is the remanent one due to the activation of the reactor structure. This contribution to the TID depends on the power at which the reactor has been run before its shut-down. For example, after 1 day of running the reactor at 250 kW, a remanent dose-rate of 0.9 Gy/s has been registered. After 1 week running at the minimum reactor power the dose-rate has been measured to be reduced of a factor 3.5. Repeated measurements with reactor on (e.g. at the presence of neutrons from the nuclear reaction) show a neutron contribution to the TID of about 30 %. These measurements therefore suggest always to calibrate the dose-rate in the irradiation channels of the reactor before the sample irradiations start.

4.1.3 T2 fast neutron beam at UCL

The T2 high intensity neutron beam at the *Cyclotron Research Center* (CRC) of the *Catholic University of Louvain-La-Neuve* (UCL) in Belgium is a secondary beam based on the nuclear reaction ^{9}Be(d,n)^{10}B. The 50 MeV primary deuteron beam of the UCL Isochronous Cyclotron that hits the beryllium target is used to generate a neutron field with an energy spectrum ranging from about 15 to 25 MeV and a maximum that lies at 20.4 MeV [Meu75]. The terminal part of the beam-line that hosts the beryllium target and the samples holder is shown in Fig. 4.6(a).

Deuteron bunches of 4 ns width and with a repetition period of about 80 ns are making the neutron beam quasi-continuous in time. The samples to be irradiated can be positioned at different distances from the target in order to get different neutron fluxes. At a distance of 9 cm from the target, for example, a total neutron flux of $7.3\times10^{10}\ cm^{-2}s^{-1}$ can be obtained. Over the irradiation spot the beam intensity varies smoothly by about 20 %. In terms of fluence, the contamination of the beam with

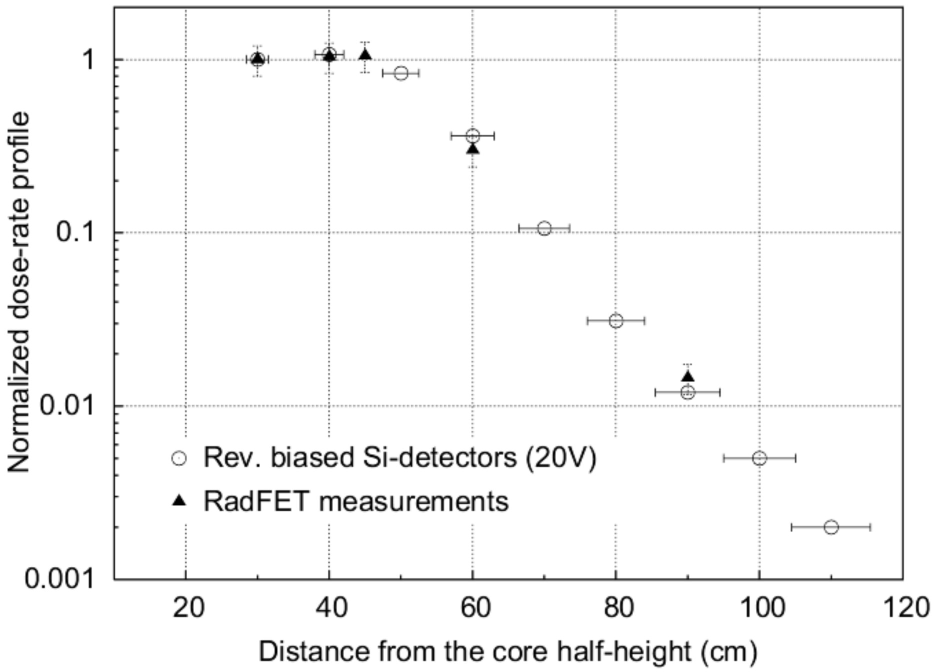

Figure 4.5: Remanent dose-rate profile in the TIC channel of the TRIGA Mark II reactor at JSI. The measurements have been carried out by means of reverse biased silicon detectors (empty markers) and RadFET dosimeters (filled markers).

gamma rays from neutron interactions with the material of the filters surrounding the target has been measured to be 2.4 % [Ber06].

4.1.4 HE-PIF Proton Facility at PSI

The primary proton beam for the High Energy Proton Irradiation Facility (HE-PIF) of the *Paul Scherrer Institut* (PSI) in Villigen, Switzerland is delivered to the test area from the 590 MeV Ring-accelerator by passing through a set of exchangeable copper-graphite blocks (primary degrader), in order to reduce its energy and its intensity. After the primary degrader the proton maximum energy is equal to 254 MeV and the maximum current is restricted to about 1 nA in order to limit the air activation in the experimental area.

The PIF experimental set-up consists of a local energy degrader that allows to further set the proton energy down until about 60 MeV, beam collimators and monitoring devices (ionization chamber and wire chamber) as shown in Fig. 4.6(b). Irradiations are usually carried out in air placing the samples on a movable x-y table that mounts a samples holder perpendicularly to the beam direction.

The maximum flux reachable at 254 MeV is of 2.5×10^{8} protons/($cm^2\times s$) over an irradiation area of 9 cm diameter. The PIF facility is pre-calibrated with accuracy in the flux/dose determination better than 5 %. The contamination due to the neutron background at the irradiation position was calculated to be less than 10^{-4} neutrons/proton/cm^2.

The irradiation is controlled through a set of scalers and a PC-based data acquisition

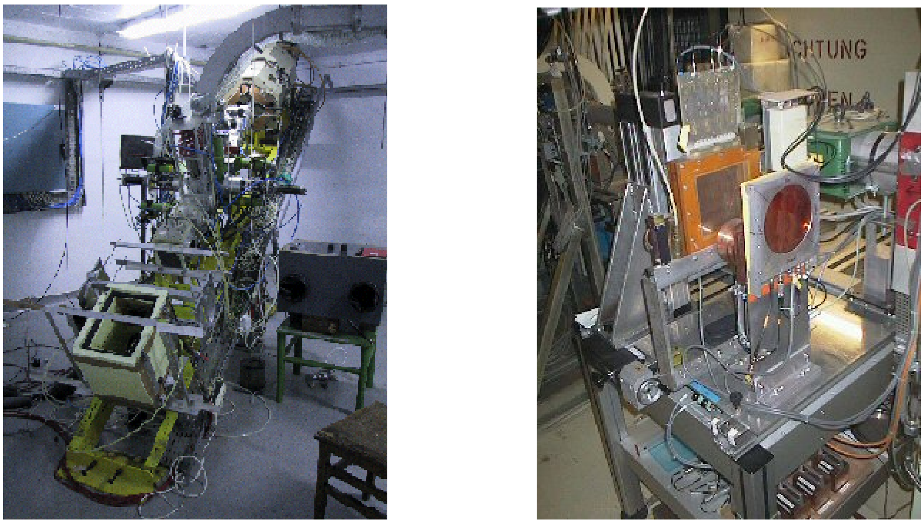

(a) (b)

Figure 4.6: The Irradiation facilities at UCL and PSI. (a) The T2 fast neutrons beam-line at UCL, Belgium. (b) The High Energy Proton Irradiation Facility at PSI, Switzerland.

system. The system monitors proton flux and dose rate, calculates the total deposited dose and controls the position of the sample as well as beam focus parameters. It also allows the setting of the beam energy by changing the layout of the PIF local energy degrader [Haj02].

4.1.5 Gamma sources

The devices studied in this thesis work have been irradiated with different gamma sources depending on the dose-rate needs and the sources availability. Hereafter a brief description of the GIF facility at CERN, the PAGURE facility at CEA of Saclay, France and the gamma irradiator of the University Montpellier II, Montpellier, France will be given.

The Gamma Irradiation Facility (GIF) is installed in a test zone (former X5 beam at the CERN SPS West Area) in which large area high-energy particle detectors were exposed to a particle beam in the presence of an adjustable high background of gamma-rays. This was done with the aim of simulating the background conditions that the investigated detectors will suffer in their operating environment at the LHC[2].

The gamma irradiator is housed in a rectangular container, 400 mm wide and 900 mm high as shown in more detail in Fig. 4.7(a). This source can be also used coupled with a particle beam as described above but it can be used alone to perform pure gamma irradiations. The GIF source is also equipped with a set of attenuation filters that can be set up to decrease the dose-rate. The active element is a radioactive ^{137}Cs source which emits a 662 keV photon in 85% of the decays, with a half-life of 30 years

[2]After the dismantling of the X5 beam-line during 2005 the combined irradiation gamma source/particle beam is no longer operational.

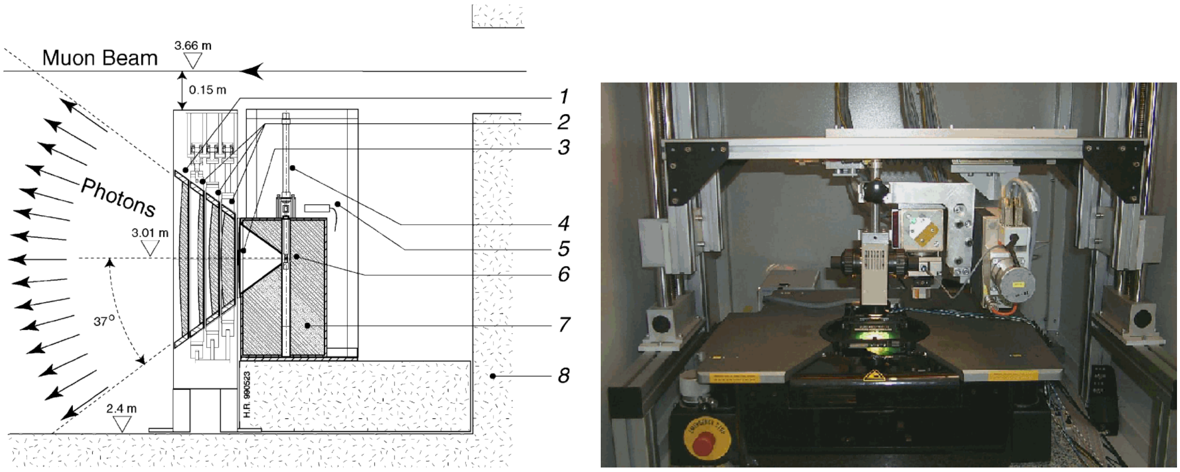

(a) (b)

Figure 4.7: Irradiation sources at CERN. (a) Vertical cut of the GIF source showing the filters [1-3], rod with source at lower end that is lifted to place the source in irradiation position [4], radiation monitor [5], source enclosing [6], lead housing of the source [7] and the concrete shielding [8]. (b) The Seifert X-ray machine in its cabinet.

and a strength of 740 GBq measured the 5 March 1997. The dose rate available in this facility, without using any filter, was of about 45 mGy/h at 1 meter distance from the source in September 2002 [Ago00].

To integrate faster higher TID, some samples were sent to be irradiated to the PAGURE facility of *CIS-bio International*, Saclay, France. The source employed there is a ^{60}Co of activity of about 14 kCi which emits photons at 1.17 and 1.33 MeV. The source is placed in a room of 5×5×3 m^3 In this facility dose rates from 1 Gy/hr to 20 kGy/hr are available depending on the distance from the source (2.5 meters to a few centimeters respectively) [Dim05].

Lower dose rates are instead achievable at the gamma irradiator TECOP SHEPHERN 486 of the University Montpellier II, France. The employed source is a ^{60}Co encased inside an irradiator structure that allows irradiation of samples in a few cubic centimeters volume. In this facility dose rates from 30 to 5 mGy/hr are available moving from 10 to 70 cm from the source respectively [Vai03a].

4.1.6 Seifert X-Ray generator

The set-up available from the CERN Microelectronics group consist of an X-ray irradiation system (SEIFERT RP149), in which a 3 kW X-ray tube uses a tungsten target typical for radiation-effects studies on semiconductors [Pal82]. Depending on the distance, the dose rate achievable with this machine ranges from to 0.1 to 8 Gy/s.

The irradiation cabinet that hosts the X-ray tube is also equipped with a Karl-Suss PA 200 semi-automatic 8-inch wafer probe station, where the X-ray tube and a CCD camera can move via a computer-controlled motorized stepper as shown in Fig. 4.7(b).

The wafer chuck is from Digit Concept and it is thermally controlled over a range of -20 °C to + 200 °C.

4.2 Measurement Equipment

4.2.1 Characterization of semiconductor dosimeters

In Sec. 3.2.1 and Sec. 3.2.2 we have seen that both RadFET and *p-i-n* diodes can be measured in the same way by reading the voltage increases at their terminals upon constant readout current injection. A common readout electronic can be thus used to operate and characterize these devices under irradiation.

Fig. 4.8 schematically shows the system used to readout RadFETs and *p-i-n* diode dosimeters during all irradiation tests presented in this thesis work. The system consists of one *Keithley 2400 Source Meter* and an *Agilent 34970A Switch Unit* equipped with 2 switch module cards (34903A) that allow to connect a maximum of 40 devices simultaneously. Both devices are connected to a PC via IEEE-488 (GPIB) bus interface and are driven via a LabVIEW software. The Source meter can supply a wide range of currents (100 pA to 1 A) with different timing (starting from 1 ms) to bias on 2 wires the different dosimeters under test. The same instrument allows to measure the voltages generated across the device terminals until a maximum voltage of 200 V[3]. With this system, the readout of devices exposed up to 100 meters far away from the readout electronics has been performed [Rav02].

The LabVIEW control panel allows to set up all the acquisition parameters (number of channels, time delays, bias current levels, repetition time, etc.) and record the acquired data on a formatted text file (one for each used channel). The dosimeters are readout sequentially one after the other. The readout time of the whole dosimeter batch is therefore variable depending of the number of devices connected to the system and in the time required to read all devices individually. The *34970A Switch Unit* can finally host a third module, that allows to acquire a counter value that may be used to record the condition of the irradiation beams during the sensor test.

A more detailed scheme of the connection used for the dosimeter readout is given in Fig. 4.9. The devices are connected such that, during radiation exposure, the *Agilent Switch Unit* keeps the devices terminals shorted together to avoid any self-biasing phenomena.

The *Keithley* instruments have been also used as laboratory test-bench (stand-alone mode) to carry out I/V measurements on *p-i-n* diodes after and before irradiation.

For RadFET dosimeters only, a semiconductor parameter analyzer *HP4145B* has also been used to perform the static transistor measurements applying and measuring currents and/or voltages (typically, the MOS drain current (I_d) has been measured as a function of the gate (V_{gs}) and drain (V_{ds}) voltages).

The *HP4145B* instrument is part of the equipment of the CERN Microelectronics group and it can also been used to characterize test structures in die form. Therefore, to measure complex transistor structures, a *Keithley 707 switching matrix* is connected

[3]Sometimes this instrument has been replaced by the *Keithley 2410 Source Meter*. This instruments has the same characteristics of the model 2400 but allow to operate up to a maximum voltage of 1100 V.

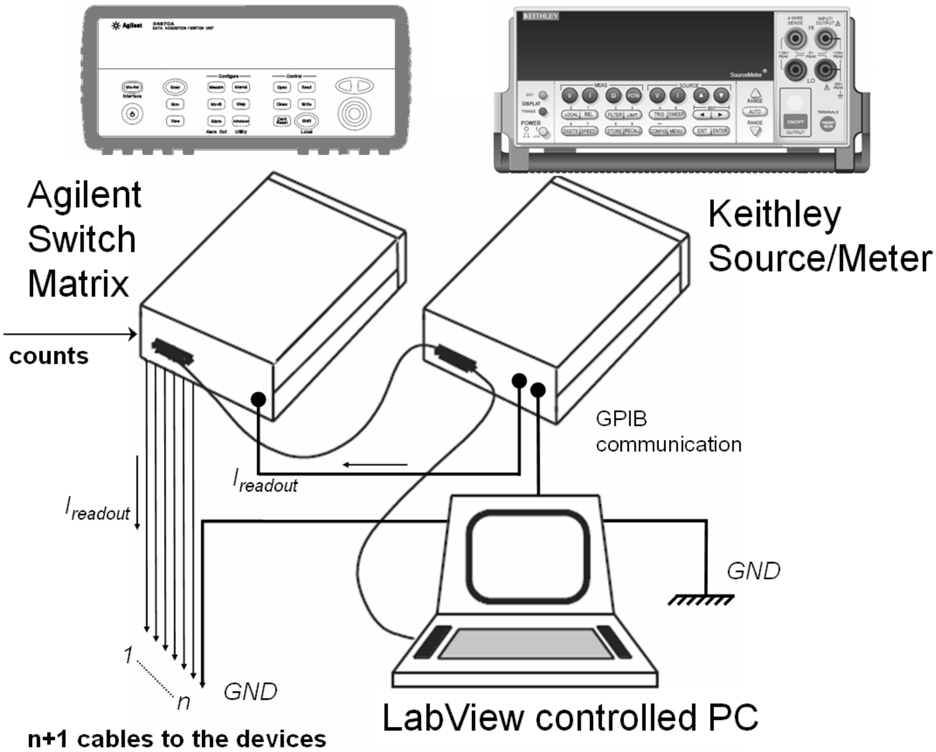

Figure 4.8: Setup for RadFET and p-i-n diode dosimeters real-time measurements.

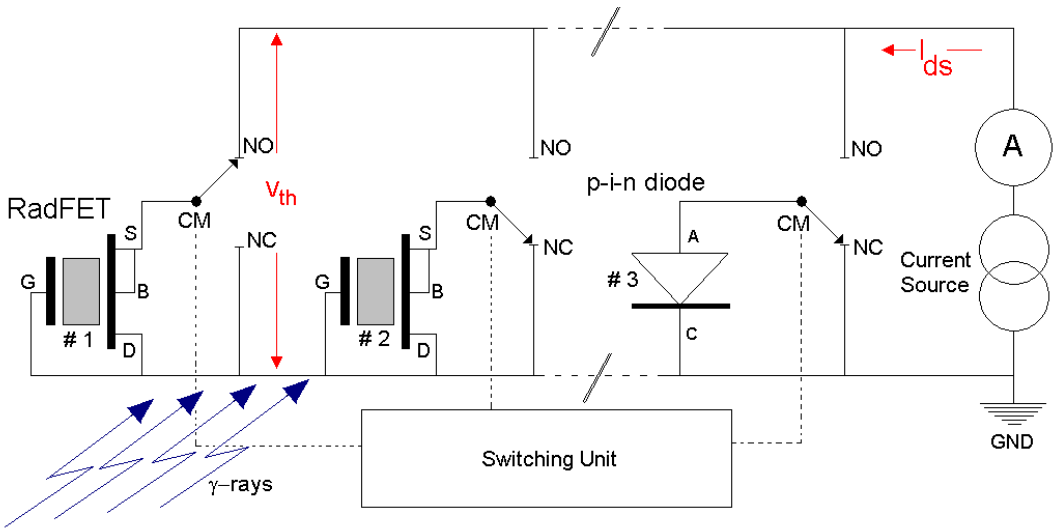

Figure 4.9: Schematic representation of the electrical setup used for the voltage readout of RadFETs and *p-i-n* diodes during irradiation tests. For any channel, the dosimeters are connected between the common (CM) and the "normal close"(NC) terminals of the switch matrix in order to have all the device connections shorted during irradiation. In the picture the device 1 is readout (switch on "normal open" position NO) while the other two are in exposure mode.

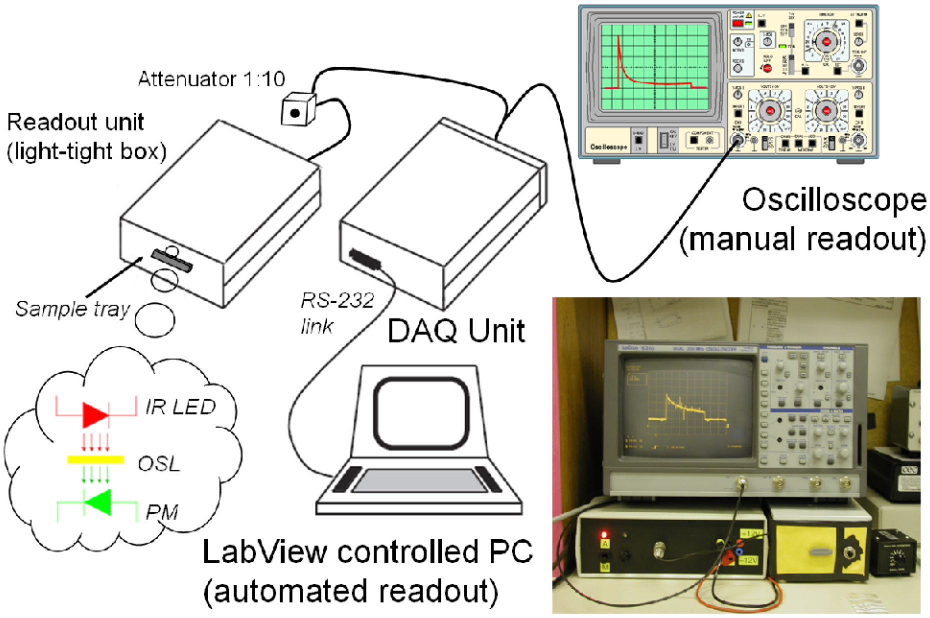

Figure 4.10: Setup used for the characterization of the OSL materials. Insert: picture of the real system. The two boxes located under the oscilloscope are the *DAQ unit* (left-hand side) and the *Readout unit* (right-hand side) respectively. On the extreme right-hand side of the picture, the attenuator module is also visible.

to the measuring channels of the HP semiconductor parameter analyzer [Fac05]. Also in this case, both instruments are controlled by a PC running a LabVIEW program.

4.2.2 Characterization of OSL materials

The characterization of the OSL materials has been done at CERN using a laboratory test-bench developed at the *University Montpellier II*. The OSL reader used in this work is an infrared LED focused on the irradiated specimen that is positioned in a samples holder that slides inside a light-tight box as shown in Fig. 4.10. The emitted luminescent signal is collected by means of a photo-multiplier, then it is send to a DAQ unit where it is digitized and recorded by a PC running a LabVIEW program connected to the test bench via the RS-232 interface.

An oscilloscope has been also connected in parallel to the DAQ unit in order to monitor in real time the evolution of the luminescent signal during the readout procedure. The IR stimulation light is applied typically for 10-20 second in order to get the whole luminescent peak behavior. The DAQ unit supplies also the electrical power needed for the operation of the readout components.

As explained in Sec. 3.2.3.2, the dosimetric signal used in this work is the amplitude (voltage) of the luminescent peak. To allow the investigation of a broad dynamic range, an attenuator has been used in order to avoid the saturation of the amplification chain during readout.

For the readout of the OSL as ”real-time” dosimeter, several prototypes of on-line readout systems have been built and tested in the framework of this thesis work. Therefore, the details of these experimental setups for the OSLs will be given in Chapter 8.

Chapter 5

Dosimetry assessments at the CERN-PS irradiation facilities

Among the irradiation facilities described in Chapter 4, the ones located in the East experimental area of the CERN PS accelerator (see Sec.4.1.1) have a privileged role for this thesis work. The facilities IRRAD1 and IRRAD2 in fact, run particle beams of type and energy close to the real ones expected at the LHC.

The 23 GeV protons of the IRRAD1 facility (see Sec. 5.1) have been used to study the response of the single devices to high energy charged hadrons as it will be shown in the following Chapter 6 and Chapter 7. Moreover, the radiation environment generated around the point in which this energetic beam is stopped (e.g. IRRAD6 facility) has been also used to validate the choice of the devices selected for the LHC in terms of their response and temporal stability as it will be shown in Chapter 9.

The mixed γ/neutron field of the facility IRRAD2 (see Sec. 5.2) is instead a valuable tool to measure the response of the devices in a bi-component radiation field with a relative low radiation rate.

Together with the radiation sensors studies for the LHC experiments, over the last few years the number of irradiation experiments performed annually at these facilities, as well as their complexity, has considerably increased. Experimental assemblies that need on-line readout and experiments performed with non standard beam conditions (high and low intensity, different beam size, etc.) are performed more and more frequently. Along with these experiments comes therefore the request for a more precise characterization of the beam profile, the beam intensity and the particle composition of the radiation field.

To satisfy all above demands, the used dosimetry techniques are continuously improved and optimized. Therefore, some of these dosimetry methods have been studied and validated in the framework of this thesis work and they will be described in the following sections of this chapter. For the IRRAD1 facility a series of beam profile techniques (by using Gafchromic [Gaf] sensitive medias and thin Optically Stimulated Luminescence (OSL) films) will be presented. For the facility IRRAD2, a calibration campaign has been undertaken and the obtained results will be discussed together with their comparison with the predictions from a Monte Carlo simulation.

5.1 Proton beam characterization and dosimetry in IRRAD1

5.1.1 Activation measurements

The basic measurement performed on the 23 GeV proton beam is the determination of the proton fluence by evaluating the ^{24}Na and ^{22}Na activity of Aluminum (Al) foils. A description of this measurement technique has been already given in Sec. 3.1.8. In the case of high-energy protons, the Na isotopes are produced via the nuclear reactions ^{27}Al(p,3pn)^{24}Na and ^{27}Al(p,3p3n)^{22}Na respectively [Leo95].

The cross-sections of these two reactions have been well characterized such that with these activation techniques it is possible to obtain fluence measurements with an accuracy of ± 7 %. The size of the aluminum foils to be used, with a thickness of some hundred μm, is varying from 0.5 to 2 cm^2 according to the size of the samples that have to be irradiated. The half-lives of ^{24}Na and ^{22}Na are about 15 hours and 2.6 years, respectively. According to the time elapsed after irradiation and the irradiation time itself one of the two isotopes is chosen to be measured for the fluence calculation.

Taking into account that ionization is the main contribution to the energy loss of a charged particle and that its mean value, the stopping power dE/dx, is given by the Bethe-Bloch law, it is possible to simply convert the fluence into the dose (Gy) deposited in thin samples, using the following formula:

$$D = K \times (dE/dx)_m \times \Phi \tag{5.1}$$

where Φ is the proton fluence expressed in particles/cm^2, K = 1.602x10^{-10} is a scale factor, and dE/dx_m expressed in $MeV \cdot cm^2/g$, is the minimum ionizing energy loss rate. For 23 GeV protons it has values between 1.6-1.8 $MeV \cdot cm^2/g$ for general semiconductor devices typically irradiated in the facilities. For high-energy charged particles, the contribution of nuclear interactions and the resulting secondaries to the dose in the beam is usually small and can thus be neglected under normal circumstances [Sul92].

5.1.2 Beam profiling with dosimetric films

Gafchromic Dosimetric Films XR, Type-R, HD-810 and MD-55 are currently used for beam profiling, alignment and dose measurements before and during sample irradiation in IRRAD1. The main characteristic of this media have been described in Sec. 3.1.7.

The high sensitivity of the Gafchromic XR Type R film allows an accurate measurement of the proton beam position with only a few spills of particles. The time consumption in the alignment of the IRRAD1 shuttle is thus considerably reduced with respect to the previous procedure which used thin pieces of glass that darkened only after an higher number of proton spills ($\sim$ 250).

The transparent films Gafchromic MD-55 and HD-810, that develop a characteristic blue color after exposure, are instead used to measure the absorbed proton dose during irradiation. Before their utilization in the characterization of the dosimeters presented in the following chapters, several samples of 1 cm^2 have been irradiated in IRRAD1 to obtain the calibration curve shown in Fig. 5.1 that correlates the color "Net Density" (N$_D$) with the absorbed dose.

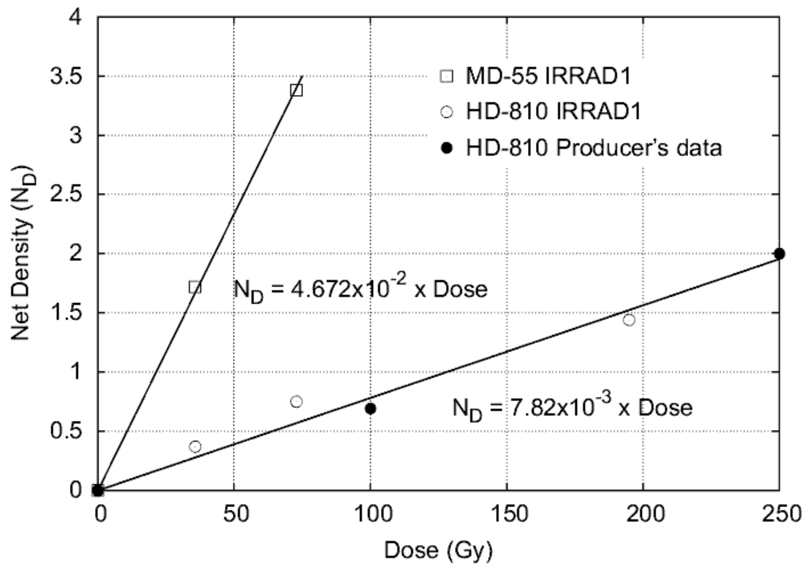

Figure 5.1: Calibration curves for films HD-810 and MD-55. Calibration curves obtained in IRRAD1 (empty markers) compared with producer data (filled markers) obtained with gamma rays.

For this experiment, the films were wrapped in aluminum foils to facilitate handling and they have been irradiated at varying fluences to produce doses from 10 Gy to more than 1 kGy. As the optical density of both film types increases with time reaching saturation less than 24 hrs after irradiation [Kla97], the readings were performed after such time for the present calibration. The change in optical density of the films was measured using a *Nuclear Associates 37-443* transmission densitometer. Un-exposed samples were used to provide a base optical density, which was subtracted from the measured one in order to obtain and plot the N_D as function of the dose.

For the film HD-810, the data obtained in IRRAD1 have been compared with the one from the manufacturer, obtained after γ irradiation, and fitted to obtain a calibration curve (solid lines in Fig. 5.1). The experimental points are in agreement within 20 % with respect to the fit of the experimental data for doses $<$ 100 Gy. At higher TID the agreement increases to better than 10 %.

5.1.3 Beam profiling with OSL films

The OSL materials, in a shape of thin films as used for dose mapping applications and described in Sec. 3.2.3.3, have been also tested to measure the profile of the 23 GeV IRRAD1 proton beam. In the framework of this thesis work, several films were therefore exposed to the IRRAD1 beam with the aim to characterize it before starting the dosimeter studies. After irradiation the films were sent to the University Montpellier II for their readout with a dedicated test-bench.

Fig. 5.2 shows two dose maps obtained with OSLs when the proton beam was run in normal operative conditions. Altought in the two pictures of Fig. 5.2 the beam spots were of two different sizes, in both tests the doses of few Gy have been deposed in the films by several particle spills of 400 ms duration. These profiles, of about 500

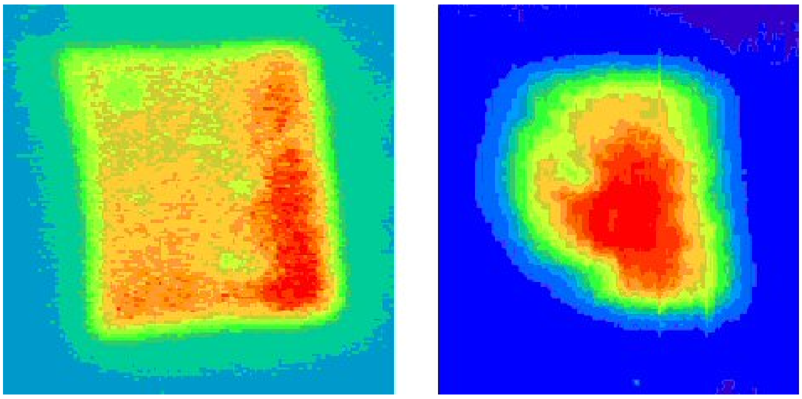

Figure 5.2: High-resolution beam profiles measured by a 100 μm OSL film. Big beam-spot of about 4.5x4.5 cm^2 (left hand side) and standard beam spot of about 2x2 cm^2 (right hand side).

μm resolution can be very useful when a detailed determination of the dose map over the irradiation surface is needed [Dus01].

One of these films has been exposed several times to proton doses of more than 1 kGy (proton $\Phi > 3 \times 10^{12}$ p/cm^2). After a total exposure to particle fluences in the order of 10^{14} p/cm^2 the OSL film doesn't show any degradation of its performance, proving the insensitivity of this material to radiation damage.

From the other side, OSL films have been used also to determine the beam profile in conditions of lower beam intensities. One example has been reported in Fig. 5.3 where the PS proton beam, with an intensity reduced of about three orders of magnitude, was extracted and directed to IRRAD1. In Fig. 5.3(a) the dose map has been measured by OSL after exposure of a few mGy. The performance of the OSL material has to be compared with the same measurement performed with Activation of aluminum foils presented in Fig. 5.3(b).

Apart the clear difference in the resolution of the dose maps obtained with the two techniques, the measurement with aluminum activation took also a large amount of time (hours time-scale) with respect to the OSL one (minutes time-scale), since in the case of the activation technique, it is necessary to reach a proton fluence high enough to activate the material to a measurable level.

5.1.4 Beam profiling using SEE

The need for an on-line method to determine the position and the profile of the IRRAD1 proton beam motivated the feasibility study for an instrument based on the proton-induced Secondary Electron Emission (SEE) from thin metal foils [Pug02]. The foils are required to be made of a low cost and relatively short activity lifetime material. Moreover they have to be on the one hand thin to avoid scattering of beam but on the other hand thick enough to allow easy handling. Aluminum foils were chosen as a good compromise to satisfy most of these requirements. A test setup was realized to verify a set of preliminary calculations and to perform a proof of principle before starting the design of a full Beam Profile Monitor (BPM) system.

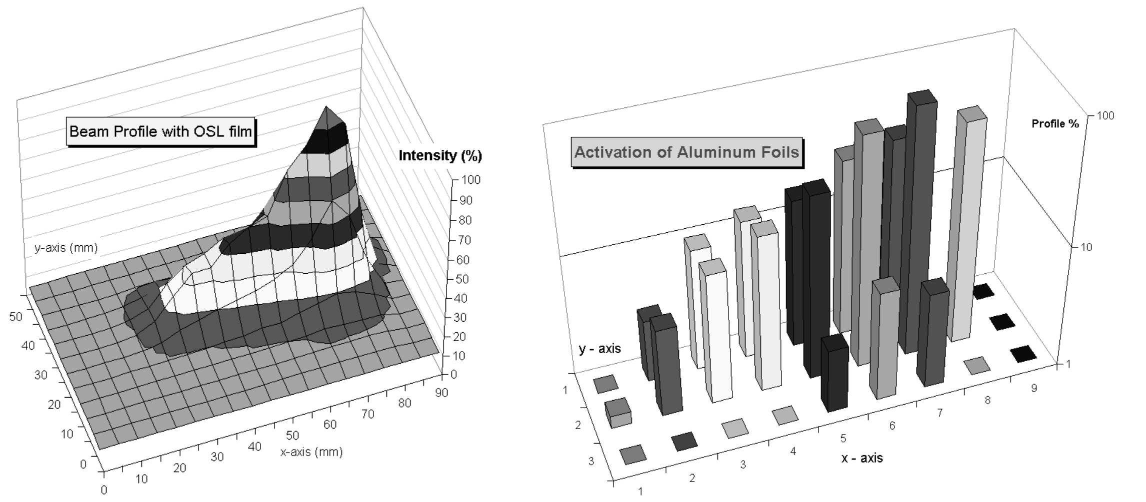

(a) (b)

Figure 5.3: OSL dose map versus activation foil technique. (a) OSL profile with a resolution of 500 μm. (b) dose map obtained by means of activation of aluminum foils. Aluminum foils of 5 mm^2 were assembled in a matrix with a spacing of 5 mm.

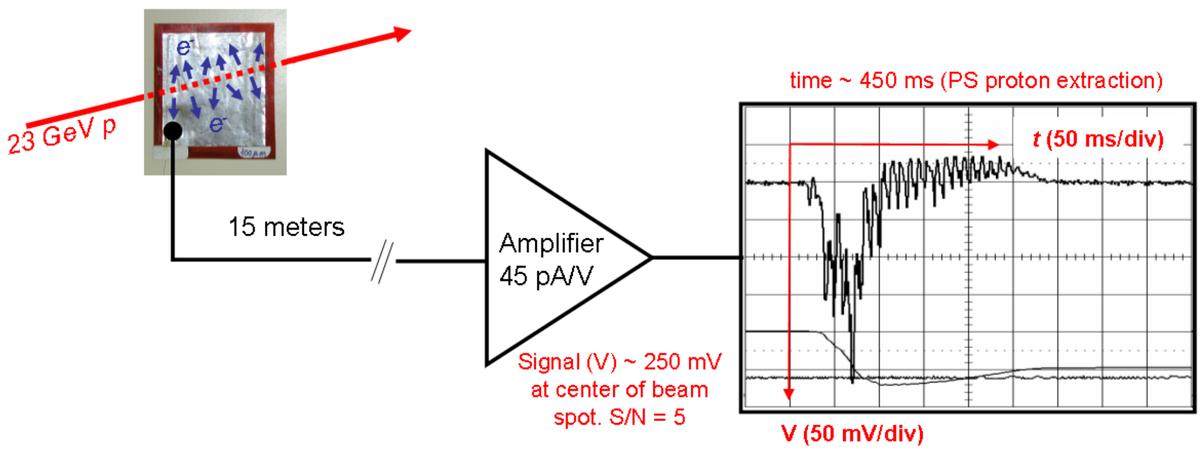

Figure 5.4: Setup used for the validation of the SEE in the IRRAD1 beam. The screen-dump in the picture is referred to the signal acquired while the aluminum foil was placed on the side of the beam spot.

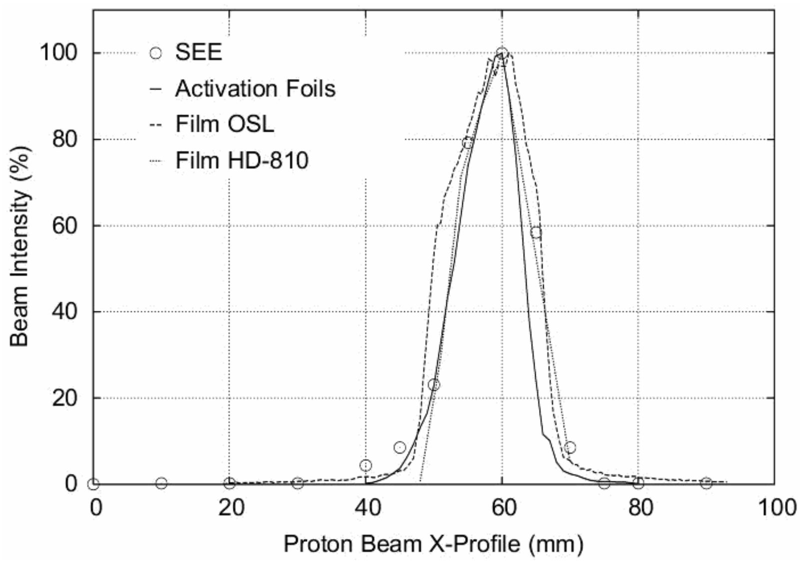

Figure 5.5: BPM measurements (circle marks) compared with the profiles obtained by means of OSL, activation foils and Gafchromic Films (different continuous lines).

The BPM test setup (see Fig. 5.4) consisted of a 3x3 cm^2, 100 μm thick aluminum foil mounted transversally on the IRRAD1 shuttle allowing the beam to pass through the full 3 cm width of the foil. The foil was electrically connected to a high-gain Transimpedance Amplifier located in the counting room via a 15-meter long coaxial cable. The amplified signal was read out with a *LeCroy 9361 300 MHz Oscilloscope*. At a fixed vertical position the foil was displaced to different horizontal positions ranging from 0 to 90 mm and the charge integrated over one particle spill was measured at each step in order to get a horizontal profile. Fig. 5.5 shows the obtained results (circle marks) normalized with respect to the maximum intensity of the beam spot and compared with the same measurement obtained by the profiling techniques mentioned above (various lines). The good agreement of the measurements and the high current collected from the Al foil (a few nA in the center of the beam spot) demonstrated the feasibility of this beam-profiling system and allow to start the design of a multi-pad BPM detector.

5.2 Dosimetry in the mixed γ/neutron environment of IRRAD2

Different dosimetry techniques are used to monitor the neutron fluence and the deposited Total Ionizing Dose (TID) in this complex environment. For radiation hardness tests and solid-state dosimeter characterizations, the environment at 50 cm distance from the beam axis is the mostly used. In this position the radiation field is composed mainly of neutrons (90%) with a small gamma ray contamination (10%). Fig. 5.6 shows the details of the particle spectra in this location [Gla00].

Calculations based on simulations and activation-foil techniques [Vin02] as well as measurements with Polymer-Alanine Dosimeters (PAD), Radio-Photo-Luminescent glasses (RPL) [Con93], Gafchromic films and Silicon detectors [Mol99b] were carried

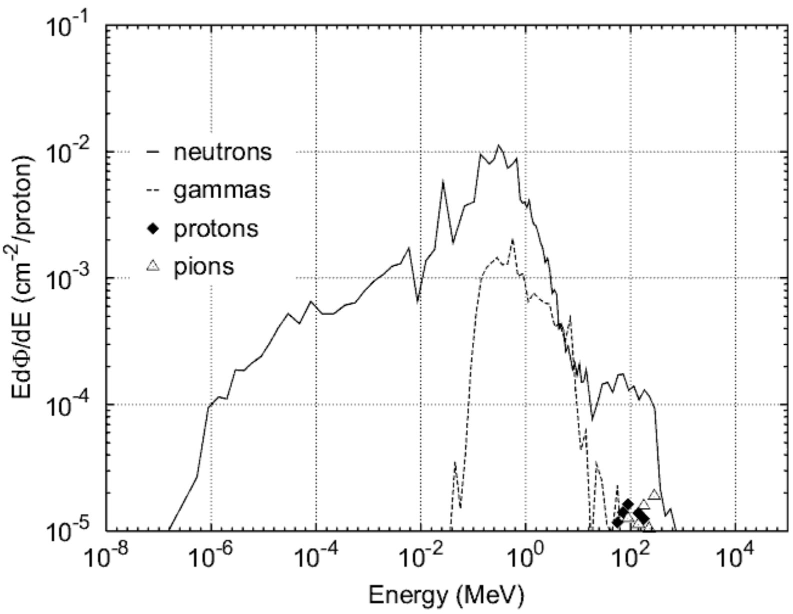

Figure 5.6: Particle spectra in IRRAD2 cavity at 50 centimeters from beam axis normalized to one impinging 23 GeV proton.

out for the calibration of the location at 50 cm distance from the beam axis. In the calibration campaign presented here, samples of each dosimeter type were irradiated to 10 increasing neutron fluences.

Monte Carlo simulations with the FLUKA [Fas01] code have been carried out to predict the hadron flux and the production of ^{24}Na in a thin Al foil placed at 50 cm from the beam axis. The expected delivered dose in the Aluminum, normalized to one proton hitting the target, has also been computed. Measuring the ^{24}Na activity therefore allows calculation of the achieved particle fluence in terms of 1-MeV neutron equivalent fluence (Φ_{eq}) [Gla00].

Fig. 5.7(a) shows the production rate of ^{24}Na per incident proton predicted by simulations in 20x20 cm^2 Al foils (continuous line) compared with the measurements carried out with Al foils placed at different distances from the beam axis ranging from Z = -70 cm to Z = + 20 cm. The measurements (light dotted lines) taken at steps of 5 cm with foils of one square centimeter, have been normalized to the 20x20 cm^2 area (dark dotted line) to allow the comparison with the simulation output. The two sets of ^{24}Na production rates turn out to be in agreement within 20% for all the irradiation positions (i.e. distances from the beam axis). In all the cases the measured ^{24}Na production overestimates the corresponding simulated values by about 20%.

Silicon detectors were directly exposed in the IRRAD2 neutron field at ambient temperature without biasing them. After irradiation the devices were annealed for 4 min at 80°C and the increase of the leakage current at full depletion was measured as explained in Sec. 3.1.9. The leakage current value was then converted to Φ_{eq} following the NIEL scaling in Silicon [Mol02] and the calibration curve of Fig. 3.3. This method was chosen since it is possible to obtain high reproducibility in the fluence measurements even if different batches of detectors are used.

The results of this technique are shown in Fig. 5.7(b). The Φ_{eq} values obtained

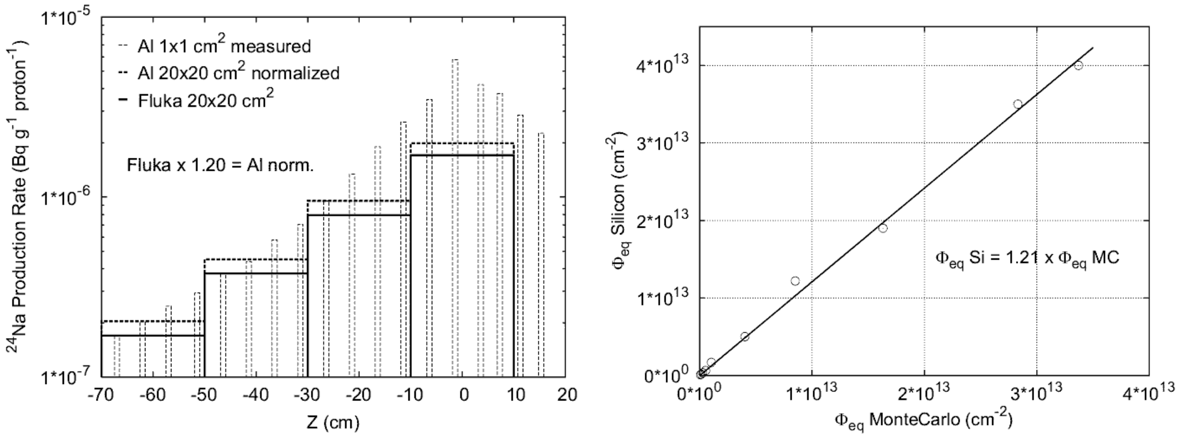

(a) (b)

Figure 5.7: Validation of the IRRAD2 calibration with Monte Carlo simulations. (a) ^{24}Na Production rate at different distances from the beam axis predicted on 20x20 cm^2 Al foils from Monte Carlo simulation (continuous line) and compared with the one directly measured with the Activation-foils technique (dotted lines). (b) Φ_{eq} from Silicon detectors, plotted versus the Φ_{eq} calculated from Monte Carlo simulations.

by the Silicon particle detectors used as NIEL proportional damage counters are there plotted versus the same quantity calculated from Monte Carlo simulations.

With respect to the Monte Carlo simulations the Φ_{eq} as measured by the silicon detectors shows a good linearity but is also overestimated by 21%. The reasons for this difference between measurement and the simulation might be manifold. It wasn't possible, after each irradiation step, to measure the activity of the short-lifetime ^{24}Na nuclide and apply it to normalize the simulation output. For this reason, all the simulated values have been scaled using only a few activation measurements performed during the first irradiation steps. Furthermore, although great care was taken to have stable beam conditions during the one week running of the experiment, small variations can not be excluded. And finally, the simulation itself and the NIEL scaling of the Silicon detector response might also be afflicted by a small error. Nevertheless, Silicon detectors were identified as a good tool for measuring Φ_{eq} and were thus used to plot the experimental data shown in Fig. 5.8.

The Fig. 5.8 shows the comparison between the Total Ionizing Dose in Aluminum estimated by simulations (empty round markers) and the values measured with various dosimeter types (other markers in the plot). The TID deposited by the neutron/gamma environment in thin Aluminum foils is supposed to be equal to the one expected in thin solid-state semiconductors devices.

The values measured with sensitive films, and PAD dosimeters are on average greater by a factor of 7.3±2.7 % than the value predicted from simulations. The RPL technique shows instead a factor 3.2±8.5 % greater than simulations. This difference is expected and is due to the different neutron interactions in the various sensitive materials constituting the employed dosimeters [Van69]. In the IRRAD2 facility the neutron spectrum is dominated by fast and high-energy neutrons (85 % of the neutrons have energies from 10 keV to 1 MeV). In this range, neutrons deposit a significant fraction of their energy

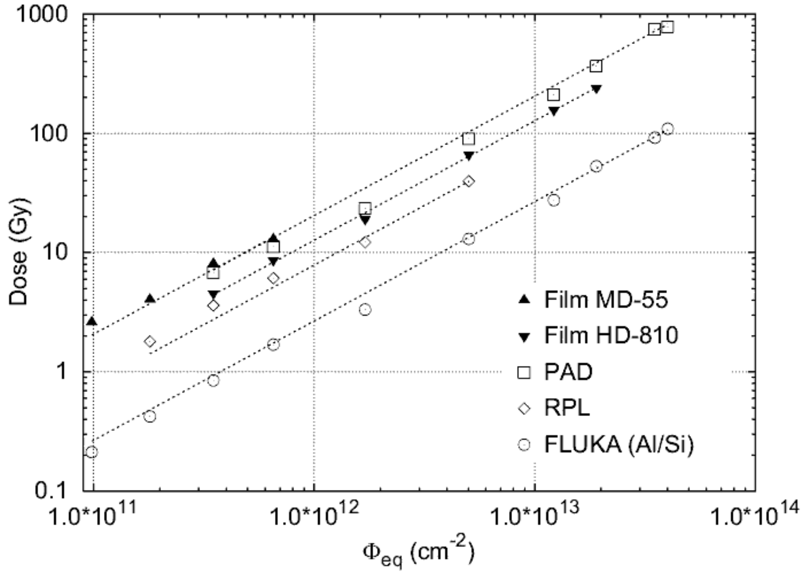

Figure 5.8: Comparison among the different TID measured at 50 cm from the beam axis obtained by different dosimetric means. The dotted lines have been plotted as guidelines within different data sets.

in Non-Ionizing Energy Losses and in inelastic interactions that produce fast and light particles that escape from semiconductor materials. The neutron contribution to the TID in semiconductors with respect to the gamma rays is thus in the order of a few ten percent and results in a TID estimation smaller than the one obtained by other systems. This fact has been also proved in measuring doses in IRRAD2 by means of solid-state Silicon dosimeters [Rav04b].

The most important mechanism responsible for transfer of energy from neutrons to polymeric substances like PAD and Gafchromic films is elastic scattering. The recoil proton generated in this way will move through the material depositing the initial neutron energy via ionization leading to the increased response.

The Films and PAD measurement are therefore in good agreement and lie in an interval of ± 15 %. It has to be noted that the film MD-55 provides almost the same measurement of the PAD with an error of about ± 5 %. The RPL response is a factor 2 lower with respect to the PAD in the IRRAD2 environment and lies thus between the Alanine measurements and the simulation results. This discrepancy, already observed in a previous work [Con93], may be explained with an intermediate neutron interaction mechanism in the different material of the RPL (silver-activated aluminophosphate glass).

For the PAD dosimeters only, the above experimental data were compared to the theoretical calculation of the scaling factors for the TID released in PAD and Silicon that is the base material for solid-state dosimeters.

Fig. 5.9 shows the neutron and photon Ionizing KERMA values simulated for Silicon and PAD calculated from Ref. [Cha99, Hub82]. Folding these coefficients with the neutron and gamma spectra simulated for the IRRAD2 facility of Fig. 5.6 enables calculation of the absorbed dose expressed in Gy normalized to one incident proton. The results of these calculations are reported in Tab. 5.1. The ratio between the dose as

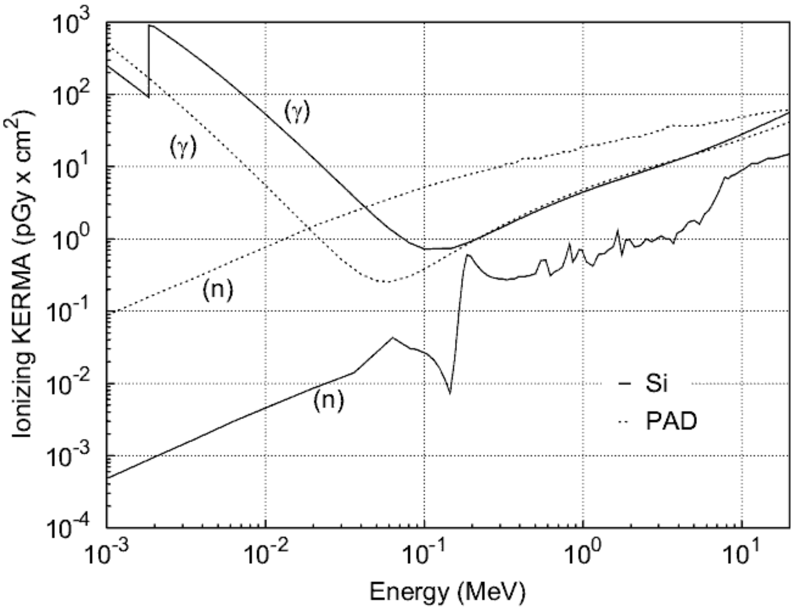

Figure 5.9: Neutron (n) and photons (γ) Kerma factors in Si and PAD for the energy range 1-keV÷20 MeV.

	Dose in Silicon [Gy/proton]	Dose in PAD [Gy/proton]
photons	6.04x10^{-15}	6.10x10^{-15}
neutrons	2.74x10^{-15}	1.52x10^{-13}

Table 5.1: Absorbed dose factors in IRRAD2 calculated from the particle spectra.

measured in PAD and the dose deposed in Silicon as calculated by Monte Carlo is thus given by the following equation:

$$\frac{D_{PAD,measured}}{D_{Si,calculated}} = \frac{D_{PAD,\gamma} + k \times D_{PAD,n}}{D_{Si,\gamma} + D_{Si,n}} \tag{5.2}$$

where the doses D are the ones reported in Tab. 5.1, and the coefficient k is the relative sensitivity of Alanine for neutrons compared to gamma rays [Kat86].

The relative response in Alanine to monoenergetic neutrons ranges from 0.36 to 0.7 compared with the response to ^{60}Co photons in the energy range from 0.5 to 15 MeV [Sch89]. On the basis of the neutron spectrum of Fig. 5.6 a coefficient k = 0.4 has been found for the IRRAD2 facility at the position Z = 50 cm. By substituting all above data in Eq. 5.2, the dose ratio PAD vs. Silicon in IRRAD2 turns out to be equal to 7.6. This is in good agreement with the experimental measurement presented in Fig. 5.8 which gave a factor of 7.3.

5.3 Conclusion

The irradiation facilities (IRRAD1, IRRAD2) in the East experimental area at the CERN-PS accelerator play a privileged role for radiation hardness studies for the LHC components as well as in the radiation sensor studies subject of this thesis work. A precise positioning of the IRRAD1 proton beam and an accurate calibration of the IRRAD2 mixed γ-neutron environment are therefore a prerequisite to guarantee a reliable calibration of the sensors under study. For this reason the improvement of the beam-profiling techniques and the validation of the dose measurement in mixed environment have been addressed in this thesis work.

For the IRRAD1 facility, several beam profile techniques including Gafchromic sensitive medias, OSL films, activation foils, have been described. With such methods it is possible to determine the shape of the 23 GeV proton beam in a μm-scale and to measure the number of particles (and therefore the dose delivered to the different materials) with an accuracy of $\pm$ 7 %. For the facility IRRAD2, in the location at 50 cm distance from the beam axis, the calibration campaign carried out for this thesis work show an agreement of $\pm$ 21 % by comparing the predictions from a Monte Carlo simulation with measurement performed by with Polymer-Alanine Dosimeters, Radio-Photo-Luminescent glasses, Gafchromic medias and silicon particle detectors.

Chapter 6

Characterization of RadFET dosimeters

RadFET dosimeters are p-channel MOS transistors used to measure the ionizing energy deposition (e.g creation of electron-hole pairs in semiconductor materials) by the build-up of positive charge in the gate oxide (SiO_2) layer of the device as it has been described in detail in Chapter 3. The positive trapped charge can be retained for long periods of time at room temperature, leading to a shift of the "transistor gate threshold voltage" V_{th}.

RadFETs are thus integrating devices in which the dosimetric information is retained internally after read-out and they are used when regular long-time dose measurements and low average power consumption are required. These characteristics, together with the fact that these devices have very small dimensions (bare-die chips have a cross-section of a few mm^2), made RadFETs suitable to be installed in accelerator facilities like the LHC experiments for the TID measurement.

The relation between the gate voltage shift and the radiation dose strongly depends on the electric field in the oxide during irradiation (applied gate bias V_G) and on the production process parameters, especially on the thickness of the gate oxide. This relation has to be determined experimentally using a proper calibrated radiation source. All the data reported in this chapter therefore refer to devices exposed to radiation with $V_G = 0$ to benefit from a simple readout circuit configuration.

6.1 RadFETs characterization procedure at CERN

Seven types of RadFET dosimeters, from four different suppliers, have been investigated to evaluate their applicability in mixed hadron radiation environments. This has been realized by studying in detail their responses to the different kind of radiations that constitute the LHC experiments radiation field, as well as evaluating the stability of the dosimetric information over-time (e.g. annealing of the oxide-trapped charge). A summary of the evaluated devices, together with their main characteristics are given in Tab. 6.1.

	National Microelectronics Research Center (NMRC)	Radiation Experiment and Monitors (REM)	Thomson & Nielsen Electronics (T&N)	Laboratory of Analysis and Architecture of Systems (LAAS)
Country / URL	IE / www.nmrc.ie	UK / www.radfet.com	CA / www.thomson-elec.com	FR / www.laas.fr
Device Name	ESAPMOS04	TOT501C TOT504A	TN100P TN250P TN502P	LAAS 1600 LAAS 400
RadFETs/chip	2 same t_{ox}	4 of 2 t_{ox}	2 same t_{ox}	1
Device Type Oxide-thickness (nm)	400 (*implanted gate*)	250 – 850 130 – 1240 (*Type K* – *Type R*)	100 250 500	1600 400
W/L ratio	300/50	440/10	100	9500/37
Readout current (μA)	10	160 160	100 100 100	100 300
Typical initial voltage (V)	1.0±0.4	3.3±0.3 4.0±0.4	2.0 3.2 5.5	2.2±0.3 3.35±0.1
Initial γ-sensitivity (Producer data) mV/cGy([a])	0.46	0.2 – 1.0 0.08 – 3	0.08 0.52 1.7	5 2
Tested packages	bare-die kovar TO-5	bare-die, kovar TO-5 and polymeric carriers	Plastic DIL	bare-die kovar TO-5

Table 6.1: RadFET dosimeters investigated for this thesis work. The readout current has been specified by the suppliers. Data from Ref. [Rav02, Rav03b, Rav05a, Cam03]. Note (a): data for unbiased devices.

RadFET dosimeters are usually supplied encapsulated in different packages of various materials and dimensions. Therefore, when possible, the radiation response studies have been performed on the bare silicon die chip. In the other cases the issue concerning the packages have been taken into account, sometimes with the support of Monte Carlo simulation tools, in the analysis of the dosimeters radiation response.

The radiation response studies for the evaluation of RadFET dosimeters rely on an intense series of irradiation campaigns. A series of irradiation tests presented in this chapter have been carried out in the framework of this work in the experimental facilities described in Chapter 4. For completeness, the results of complementary irradiation tests presented in Ref. [Rav02, Rav03b, Rav05a] compiled by the same author, will be often cited and included in the discussions.

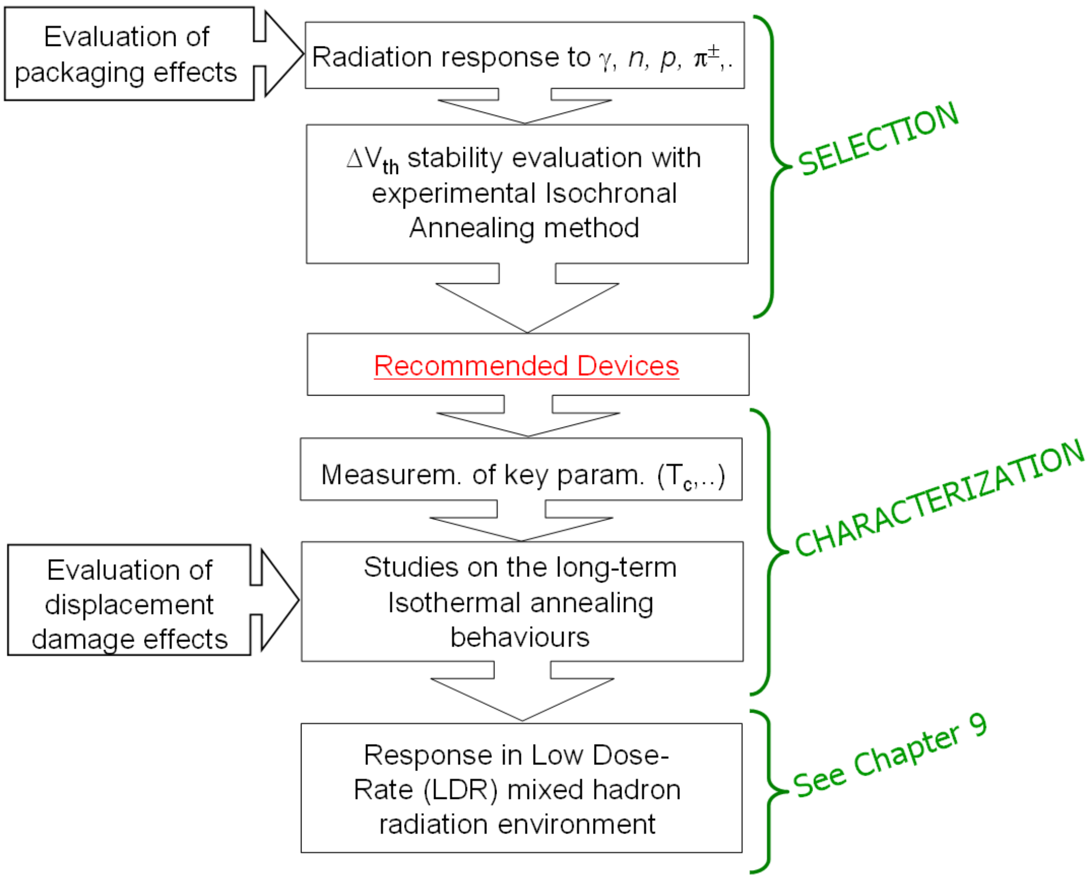

Figure 6.1: Selection/characterization procedure applied to RadFET dosimeters.

The time-recovery evaluation of both Q_{ot} and Q_{it} trapped charge (i.e. annealing of ΔV_{th}) following hadron exposure becomes a crucial parameter to guarantee reliable measurements with RadFETs over the 10-years of LHC [Rav04b]. Since it is not possible to study the annealing of ΔV_{th} over a time-scale comparable with the LHC operation, the components evaluation is based on the experimental isochronal annealing method [Sai97, Sai01]. This technique consists in emptying sequentially a fraction of the defects during a brief annealing period at incremental temperatures. After each annealing step, the effects on ΔV_{th} are then measured at room temperature.

Once the selection procedure is completed and the devices suitable for the LHC experiments identified, a detailed characterization procedure has been started on these devices. In order to provide the required calibration parameters, samples from the batch procured for the LHC, have been measured to quantify the device keys parameters. Finally, measurements and calculations aiming to evaluate the very-long isothermal annealing behavior and the possible influence of displacement damage effects in the RadFETs response after irradiation in hadron-fields have been carried out.

To validate the work presented in this chapter, the operativeness of the selected devices has been afterwards proven under conditions (intensity, field composition, temperature, etc..) similar to the ones expected at the LHC experiments. The results of this "particular" irradiation test, together with the ones of the *p-i-n* diode devices characterized in the following Chapter 7 will be presented later in Chapter 9.

A comprehensive view of the RadFETs selection/characterization procedure applied at CERN in the framework of this thesis work is given in the diagram of Fig. 6.1.

6.1.1 RadFETs charged hadrons response: LET influence

The response of RadFET dosimeters to charged particles has been widely studied for space applications. In this field, the response of the devices to charged particles (mainly electrons and protons) in the energy range 1-100 MeV are of interest [Sai98]. As discussed in Chapter 2, in the case of the LHC experiments, the particle spectra are dominated by charged particles in the 100 MeV range in the outer experiment regions. Moreover, moving toward the interaction point, the charged particle spectra shift toward higher energies in the GeV range.

The different charged particles, interacting with matter, lose energy with a rate (dE/dx) that is given by the *Bethe-Bloch* equation [Gro00]. At certain energies (different for each particle type) this rate reach its minimum value that is around 2 MeV·cm^2/g for the majority of the materials used for physics and electronic purposes. The particles in such an energy condition are usually named "Minimum Ionizing Particles" or MIPs. Protons with momenta ranging from 2 to 30 GeV/c, pions from 0.3 to 5 GeV/c and muons from 0.2 to 3 GeV/c are for example in this condition and show a $(dE/dx) \sim 1.6$-1.8 MeV·cm^2/g when they pass through detector materials. At higher kinetic energies this rate can be practically considered constant up to about 1-5 TeV. However dE/dx slightly increases, because of relativistic effects, to values that are closer to 2 MeV·cm^2/g.

Dependently on the energy, charged particles may be referred as "high-LET radiations" while X-rays, γ-rays and fast electrons are "low-LET radiations". MIPs release about 400 keV/μm while they pass throughout a semiconductor device, therefore they can be considered as very high-LET radiations. Moreover, since only a small fraction of this energy is transferred to secondary particle per event, a narrow ions track is generated along the path of the moving MIPs. According to what was explained in Sec. 3.2.1.3, when electron-hole pairs are generated by ionization in a narrow region, enhanced recombination effects in the sensitive oxide layer of the RadFETs devices can appear. These effects are much more important when RadFETs are operated with low electric field (e.g. "zero bias" mode) as in the case of the LHC experiments. For all these reason the response of RadFETs to MIPs, that frequently populate the LHC radiation environment, has a privileged role in this thesis work.

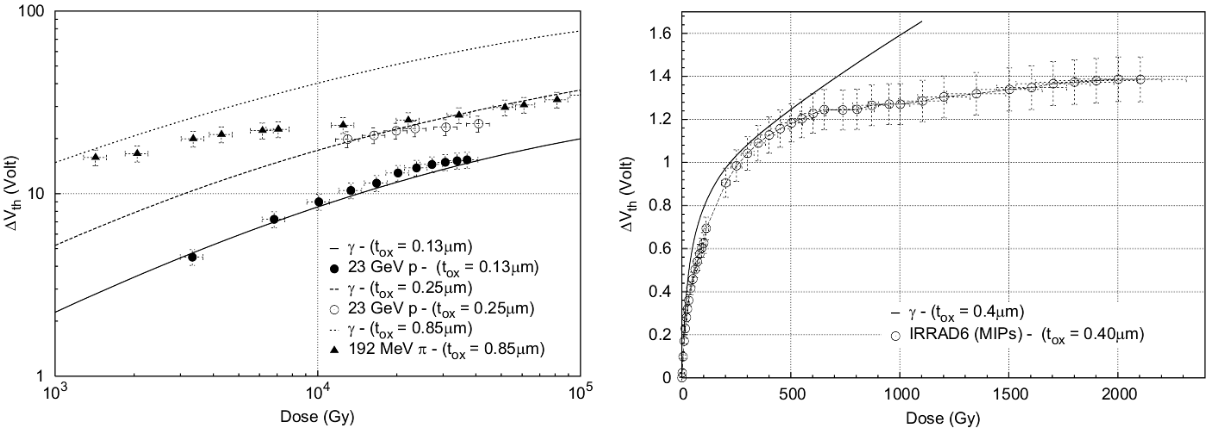

(a) (b)

Figure 6.2: RadFETs sensitivity to MIPs. (a) Response of REM devices with different oxide thickness. In the plot the γ-ray response for the devices TOT-504A (t_{ox} = 0.13 μm) and TOT-501C (t_{ox} = 0.25 μm and 0.85 μm) supplied by the producer have been compared to the ones measured for MIPs. (b) Response to the LAAS 400 device in the IRRAD6 environment. Devices exposed at V_G = 0 V.

The candidate RadFET dosimeters of Tab. 6.1 where irradiated in the 23 GeV proton beam of the IRRAD1 facility and in the environment of the IRRAD6 facility in which p and π of energies ranging from 0.1 to about 10 GeV are simultaneously present. Results from Ref. [Rav02] obtained in a 192 MeV (300 MeV/c) positive pions beam have been added to the presented results.

Fig. 6.2(a) shows the response of three REM dosimeters with three different t_{ox} to MIPs compared to the supplier's reference γ-ray response curves. The measured REM devices have been produced with identical process conditions apart for the thickness of the sensitive gate layer. For the thinnest oxide (lower curve in Fig. 6.2(a)), the experimental 23 GeV proton data follow the reference curve within the experimental error over the investigated TID range. For the intermediate oxide t_{ox} = 0.25 μm, after a TID of 20 kGy, the IRRAD1 data start to diverge from the reference curve. Finally, for the thicker oxide (0.85 μm), the pion data show a reduced response already from 1 kGy and to 100 kGy were the pion signal result is lowered by a factor 3 with respect to the γ-ray one.

These experimental data prove how the enhanced recombination within the SiO_2 layer can affect the RadFETs response and clearly underline the influence of the gate oxide thickness. For sensors made with the same process the recombination effects appear at low TID for thick oxides. In these conditions in fact, the electric field within the gate oxide, already relatively weak before irradiation, becomes quickly too week to prevent e/h ionization pairs from recombination.

The trapping probability P_t defined in Eq. 3.1 also depends on the manufacturing process of the silicon oxide layer as shown in Fig. 6.2(b) where the response of the LAAS 400 (t_{ox} = 0.4 μm) in the IRRAD6 environment has been plotted and compared with the γ-ray one. In IRRAD6 the dose deposition in the transistor oxide is driven by the MIP component of the radiation field as will be extensively explained later on in

Chapter 9. In Fig.6.2(b) the LAAS 400 signal measured in IRRAD6 starts to deviate from the reference one already at a TID of 0.5 kGy while for the ticker oxide of REM RadFETs (triangular markers in Fig. 6.2(a)), the derive start at a higher TID exceeding 1 kGy.

Significative is finally the case of the device LAAS 1600 (t_{ox} = 1.6 μm) irradiated in IRRAD1 and presented in Fig. 6.5 of Pag. 78. This device shows a response for 23 GeV protons already reduced of a factor 2 at a dose of 2 Gy.

The above finding demonstrates that recombination effects have to be taken into account in the interpretation of the signal measured with unbiased RadFETs used in high-LET radiation fields. Although this can be taken easily into account when the radiation field under measurement is composed by a single particle type, in the case of the LHC experiments the reduced response due to enhanced recombination became a limiting factor. Several solutions can be proposed to account for this effect, namely:

1. parametrize the devices response curves to MIPs in order to correct the measured signal;

2. apply a bias ($V_G \neq 0$ V) during radiation exposure;

3. use devices with thin oxide layers in order to reduce the recombination effects.

The first solution implies intensive irradiation campaigns based on predictions from the Monte Carlo simulations of the unknown radiation environment that has to be measured. The second solution is feasible only by making the readout circuitry more complicated. Moreover dedicate series of irradiation tests with biased devices will be required to prove the effectiveness of this solution in the LHC high-LET radiation fields. The third solution appears therefore the more appropriate for the measurement of an unknown mixed high-LET radiation field.

It has to be noted here that the utilization of thin-oxide devices won't allow to detect radiation doses with a very high sensitivity. However in the conditions expected at the LHC experiments this doesn't represent a serious constraint as will be explained later in Sec. 6.2.

6.1.2 RadFETs response to high energy neutrons

As mentioned in Chapter 2, high-energy neutrons will be present everywhere in the radiation field of the LHC experiments. Close to the interaction region an intense neutron background ($\sim 10^{13} - 10^{14}\ cm^{-2}/y$) is expected to join the high flux of charged hadron coming directly from the interaction point. In the outer part of the experiments, neutron levels of $\sim 10^{10} - 10^{12}\ cm^{-2}/y$ are instead expected to be the main component of the radiation environment.

In a first experiment presented in Ref. [Rav02, Rav03b], significant differences in the response of unpackaged (i.e. bare die) and packaged RadFETs were observed in the mixed γ/neutron environment of the IRRAD2 facility. In particular the RadFETs from T&N, available only encapsulated in a plastic packaging, showed a very high "neutron" sensitivity that was attributed to the neutron interactions with the packaging of the device itself. The other exposed RadFET devices (from REM and NMRC) showed instead a reduced neutron sensitivities but with complete different response behaviors.

For the above mentioned reasons, the study of the RadFETs neutron response over a wide Φ_{eq} range has been extended and detailed in this section. The influence of the packaging in a fast neutron field became therefore a crucial issue which will mainly influence the integration of the RadFET sensors at the LHC experiments.

The experimental study presented here has been carried out in the T2 pure neutron source of the *Catholic University of Louvain-La-Neuve (UCL)* described in Sec. 4.1.3 that provides a pure and mono-energetic neutron beam of an energy of 20.4 MeV and with a very low γ-ray contamination. The neutron response of RadFET chips available in bare-die form (REM TOT-501C $t_{ox} = 0.25\ \mu$m and NMRC $t_{ox} = 0.4\ \mu$m) was thus investigated as well as the one of the same chips covered with Polyethylene (PE) slabs of different thicknesses. This second test has been done in order to simulate the chip's plastic packaging. The results of this experiment has been compared here to the predictions of a Monte Carlo simulation using the GEANT4 package [Col03].

6.1.2.1 Experimental setup for the neutron irradiation

The samples were mounted with the sensing surface perpendicular to the T2 beam and exposed to a flux of $1.96\times10^{13}\ cm^{-2}\cdot h^{-1}$ corresponding to a total neutron fluence (Φ) of $3.04\times10^{14}\ cm^{-2}$ cumulated in 15.5 hours of irradiation. Over the irradiation spot of 4.0 cm radius used for the described experiment, the beam intensity varied smoothly by about 20 %.

Four thin Printed Circuit Boards (PCBs), of 4.2 cm^2 area containing six bare die RadFETs each, were produced and assembled as shown in Fig. 6.3(a). The six devices (three REM and three NMRC) were mounted in an area of a few square millimeters in one corner of a metallised square as indicated by *(a)* in Fig. 6.3(b). Care was taken to position the four PCBs at the same distance from the center of the beam. The device-to-device response for all the dosimeter series varied only by a few percent, proving a good reproducibility of the measured results.

One board was exposed directly to the neutron beam while the other three were covered with polyethylene (PE) slabs of different thicknesses (2 mm, 5 mm and 10 mm) in order to simulate different plastic packaging. Fig. 6.3(b), taken during the assembly, shows two PE slabs already positioned on top of two PCBs (right hand side) and the uncovered PCB. The assembly of four boards was inserted into a cavity worked into a block of lithium-doped polyethylene (*LiPE*). The dimensions of the *LiPE* block and the cavity were 20 cm × 20 cm × 6.5 cm and 11 cm × 9 cm × 1 cm, respectively (see Fig. 6.3(a)).

The *LiPE* material, developed as neutron shielding for the ATLAS detector at CERN [Pos95], was used to shield backscattered neutrons generated by interaction of the primary neutron beam with surrounding materials in the irradiation area. The Hydrogen contained in PE is slowing down neutrons, while the Lithium is capturing them via the reaction ^{6}Li(n,α)^{3}H, that is not accompanied by gamma ray emission [Pos97]. Although the gamma background present in the facility was very low, for the presented experiment an independent determination of the gamma ray contamination of the beam has been carried out. These measurements (for details see Ref. [Rav05b]) revealed that

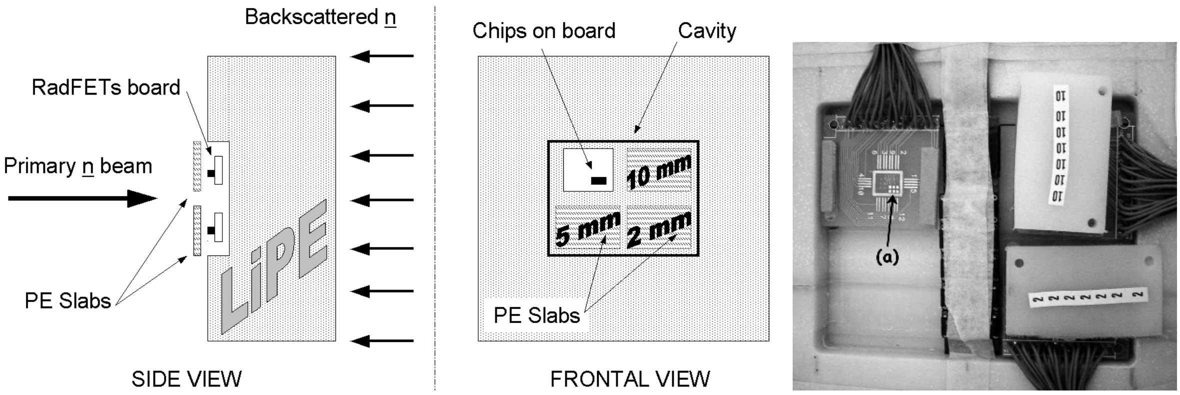

(a) (b)

Figure 6.3: Experimental setup as installed in the T2 beam-line. (a) Sketch of the dosimeter assembly. *LiPE* stands for "lithium doped polyethylene", used as shielding against back-scattered neutrons in the beam-line (b) Six RadFET dies can be seen in the lower right-hand corner of a metallised square indicated by *(a)*.

in the irradiation position the sensor received a dose of 5.62 Gy due to γ-rays. The RMS variation on this measurement was ś 3 %. All readings were taken in "zero bias mode" during irradiation with the experimental equipment described in Sec 4.2.1.

6.1.2.2 Response of bare die RadFETs to the pure neutron beam

To allow the calculation of the RadFET neutron responses, a calibration describing the device response to gamma radiation is needed. RadFETs response to ^{60}Co gamma-rays is the most frequently used calibration to convert the RadFET signal into absorbed dose. For the presented calculation the ΔV_{th} versus dose curves for gamma rays were obtained combining the data of an irradiation carried out at the CERN GIF facility and ^{60}Co data provided by the manufacturers.

Taking into account the measurements of the gamma-ray contamination described in the precedent section, the REM and NMRC RadFET responses to the 20.4 MeV neutrons were calculated as follows. The neutron spectrum of the T2 beam [Ber06] was folded with the absorbed ionizing-dose factors $d_f(E)$ simulated for thin semiconductor devices in a similar high-energy neutron field [Ale94] resulting in an averaged $d_f(E)$ of $2.47\times10^{-12}\ Gy\cdot cm^2$. In this way the cumulated total neutron fluence of $3.04\times10^{14}\ cm^{-2}$ was converted into a dose in Silicon of about 744 Gy.

Using the parameterization of the gamma-ray response and the measured gamma ray background, the expected shift of the threshold voltage due to gamma rays for the NMRC and the REM devices were calculated for each reading. By subtracting these values from the measured threshold voltage shift measured in the T2 beam it was possible to obtain the RadFET response to neutrons.

In Fig. 6.4 the markers are the neutron responses obtained with the above procedure for the bare die devices. For comparison also the gamma ray responses of the same devices, have been plotted as lines (dotted line for REM, solid line for NMRC). The curves of Fig. 6.4 are plotted as function of both absorbed dose in Silicon (lower x-axis) and total neutron fluence (upper x-axis). Tab. 6.2 summarizes then the measured

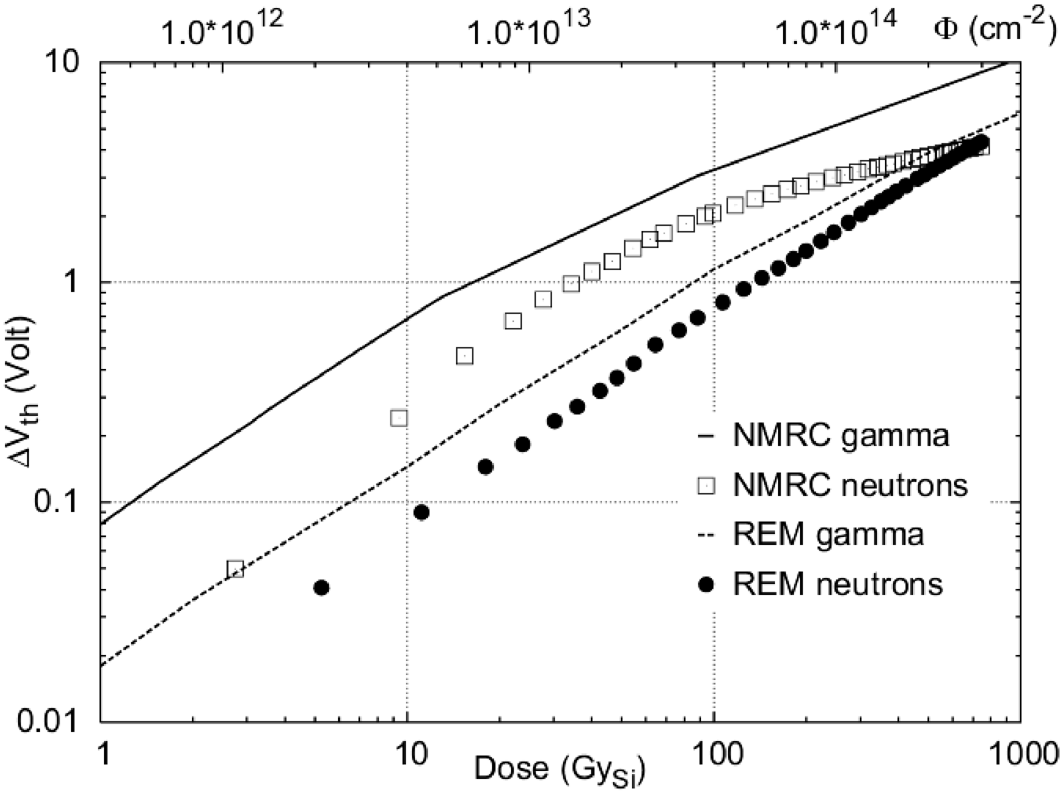

Figure 6.4: Responses of bare-die RadFETs exposed to the 20.4 MeV UCL neutron beam (markers) compared to the gamma response (lines). The open data points refer to NMRC devices, while the filled ones are referred to REM samples. Data plotted as function of both absorbed dose in Silicon (lower x-axis) and total neutron fluence (upper x-axis). Devices exposed in "zero-bias mode".

REM	Low dose-range (1-50 Gy) mV/Gy	High dose-range (600-744 Gy) mV/Gy
neutron	7.64	4.7
gamma	12.3	4.9
NMRC	Low dose-range (1-50 Gy) mV/Gy	High dose-range (600-744 Gy) mV/Gy
neutron	26.9	1.6
gamma	66.8	8.5

Table 6.2: Neutron sensitivities of bare-die RadFETs. Devices exposed in "zero-bias mode".

sensitivities (mV/Gy) for low (1 to 50 Gy) and high (600 to 744 Gy) doses for gamma rays and neutrons.

These experiments confirm what others have predicted [Aug82] and demonstrated [Kro95] namely that the RadFET will indicate any ionization which is released within the oxide layer, whatever the nature of the particle which releases it. However, it has been shown in the previous section that RadFETs respond less to particles having high Linear Energy Transfer (LET) such as knock-on protons [Old00]. Sensitivity to the T2 neutron beam in mV per unit dose is at least 1.5 times lower than sensitivity to gamma rays. In the low dose range up to about 50 Gy the reduction is 1.6 (REM) and 2.5 (NMRC). Similar reduction factors in the order of about two have been reported for similar dose ranges in other works [Kro95, Pea01]. The products of (n,p) and (n,α) reactions, have LET values well above the level required to give enhanced recombination. As a result, the number of holes trapped per Gy - and hence the RadFET signal in mV per Gy - is reduced.

The above statements can be verified taking into account that, in the thick oxide of the NMRC devices exposed in "zero-bias" mode, the electric field (E) across the oxide layer due to the work function potential [Dea66] is about a factor 2 lower with respect to the REM devices. It has been demonstrated [Car00] that in a thick oxide the MOSFETs sensitivity is proportional to $E^{0.7}$. So, in our situation, the reduction factor (ratio of sensitivities to gamma rays versus neutrons) for the NMRC devices is expected to be a factor $2^{0.7} \sim 1.6$ higher with respect to the REM samples. This is in good agreement with the measurements performed here on two Al-gate devices with different oxide thickness values as it is shown in Eq. 6.1.

$$\frac{Ratio_{\frac{\gamma}{n}}(NMRC)}{Ratio_{\frac{\gamma}{n}}(REM)} \sim 1.6 \tag{6.1}$$

A notable difference between neutron and gamma responses, as plotted in Fig. 6.4, is the difference in curve shape under the different types of radiation. For the REM devices (thinner oxide) the absolute threshold voltage shifts for neutron and gamma rays are only slightly different. However, for the NMRC devices (thick oxide) the response curve

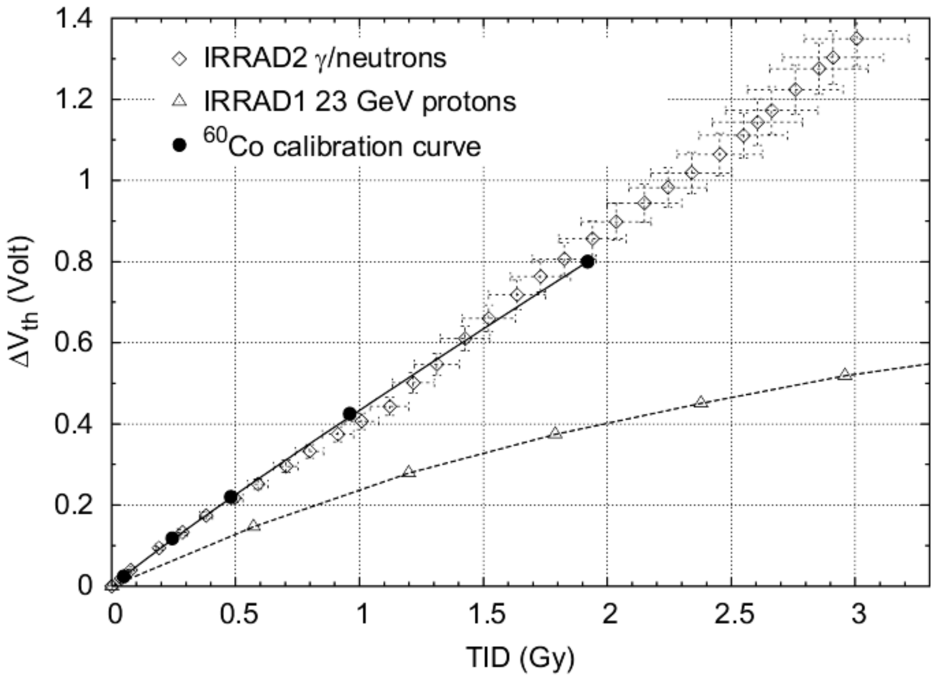

Figure 6.5: Response of LAAS 1600 devices to irradiation in the facilities of the CERN. With diamond and triangle markers, the response in the IRRAD2 and IRRAD1 facilities have been plotted. The filled circular markers are instead the calibration curve supplied by the manufacturer.

for the neutrons starts to saturate earlier than for gamma rays and the response above 100 Gy is near saturation. Given a proper conversion of fluence to dose, we would expect curves from the two types of radiation to coincide quite closely, so there is no obvious mechanism for the mismatch.

A possible explanation for differences in curve shape lies in the profiles of oxide trapped charge in the four cases. This profile can be modified for example by the introduction of new radiation defects in SiO_2 by high neutron fluences. Differences in charge profile lead to differences in the profile of the internal field. In turn, these apply different restraining forces on electrons attempting to leave the oxide. In the thinner oxide of the REM devices this effect will be observed later as its initial electric field is 2× higher. Clearly, the use of RadFETs for neutron dosimetry at high dose requires careful calibration.

For the LAAS devices, their neutron sensitivity has been evaluated in the mixed γ-neutron field of IRRAD2. Bare-die LAAS 1600 devices have been exposed to a Φ_{eq} of 1.1×10^{12} cm^{-2} and to a TID of about 3 Gy. Due to their very thick gate-oxide layer, these RadFETs provide a very high sensitivity. The log-log plot of their ΔV_{th} function of the TID for shows that ΔV_{th} varies linearly up to about 10 Gy. Although it is still possible to measure TID increases for higher doses, ΔV_{th} becomes strongly sub-linear moving quickly toward saturation above 500 Gy. The results of this irradiation test have been plotted in Fig. 6.5 where the TID measured in IRRAD2 (diamond markers) has been compared to the γ-ray calibration curves supplied by the manufacturer (filled circular markers).

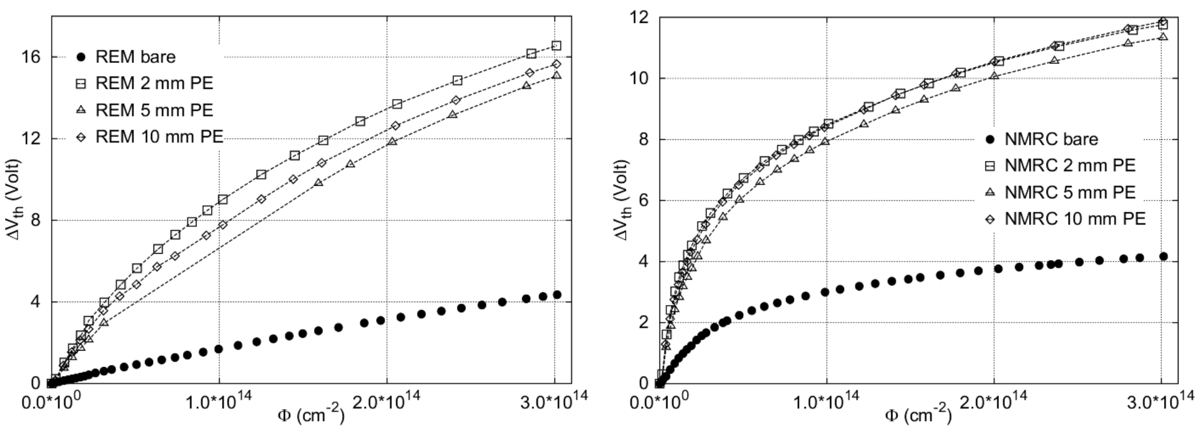

(a) (b)

Figure 6.6: Responses of the REM and NMRC devices covered with different PE slabs (see Sec. 6.1.2.4 for the comparison of these experimental results with the GEANT4 simulations). In the pictures the device signals are plotted as function of the total neutron fluence. (a) Comparison between bare die and PE covered REM devices. (b) Comparison between bare die and PE covered NMRC devices. Devices exposed at $V_G = 0$ V.

In the range measured in the irradiation test, the LAAS 1600 response fits exactly the calibration curve indicating that the device is essentially sensitive only to the photon component of the radiation field being thus neutron-insensitive. This is in agreement with the fact, at the reached exposure level, the neutron contribution to the ionizing KERMA can be estimated, from Ref. [Cha99] to be within 10 % well within the experimental error that affects the measurements. In addiction to that, such a low level of neutron irradiation has been proven to not induce any measurable changes in the I_{ds}-V_{gs} MOS characteristics that could deviate its signal behavior from the pure γ-ray response, as found in Ref. [Bho97] and articles cited therein.

6.1.2.3 Packaging influence on RadFET response

The data for the PE covered samples were treated as for the bare die samples presented in Sec. 6.1.2.2. In Fig. 6.6(a) and Fig. 6.6(b) the responses of the REM and NMRC devices covered with different PE slabs of increasing thicknesses from 2 mm to 10 mm are plotted in linear scale as a function of the total neutron fluence.

Square, diamond and triangular empty markers represent in both pictures the PE slabs of 2 mm, 5 mm and 10 mm thickness respectively. To compare the influence of the slabs on the device's response, the data of the uncovered bare die devices are also plotted in the figures (filled markers). Finally, in Tab. 6.3 the sensitivity enhancements measured for the devices covered by PE slabs, with respect to the bare-die samples, are summarized. In analogy with Tab. 6.2, the relative sensitivities for low (0.5-3$\times10^{13}$ cm^{-2}) and high (2.5-3$\times10^{14}$ cm^{-2}) total neutron fluences are given.

REM	Low Φ-range ($0.5\text{-}3\times10^{13}\ cm^{-2}$)	High Φ-range ($2.5\text{-}3\times10^{14}\ cm^{-2}$)
2 mm PE	7.1	2.5
5 mm PE	5.2	2.7
10 mm PE	6.4	2.6
NMRC	**Low Φ-range ($0.5\text{-}3\times10^{13}\ cm^{-2}$)**	**High Φ-range ($2.5\text{-}3\times10^{14}\ cm^{-2}$)**
2 mm PE	2.5	3.0
5 mm PE	2.3	3.2
10 mm PE	2.7	3.3

Table 6.3: Neutron sensitivities of bare-die RadFETs. Devices exposed in ”zero-bias mode”.

Particle	PE thickness		
	2 mm	5 mm	10 mm
e^- (%)	2.7×10^{-4}	1.2×10^{-3}	3.4×10^{-3}
e^+ (%)	4.3×10^{-5}	1.5×10^{-4}	4.6×10^{-4}
p^+ (%)	0.64	1.0	1.1
γ (%)	0.035	0.085	0.167

Table 6.4: Abundances of ejected particle except neutrons in forward direction from GEANT4.

6.1.2.4 GEANT4 simulations for RadFET packages studies

To model the influence of the PE absorbers, the particle production from polyethylene slabs was calculated using the GEANT4 simulation tool [Col03]. In the model, a neutron beam of infinitesimal radius hits perpendicularly polyethylene blocks of 5x5 cm^2 surface and with several thicknesses in beam direction. The neutron energy was varying according to a Gaussian distribution of a width of 5 MeV around the mean value of 20 MeV.

Tab. 6.4 shows the calculated relative abundances of all particles except neutrons ejected from the polyethylene in forward direction as a function of slab thickness. These data were obtained with a statistics based on 10^8 neutrons launched on the three different slabs.

In Fig. 6.6(a) and Fig. 6.6(b) the enhancement of dose due to a PE cover, simulating polymeric RadFET packaging, is vividly demonstrated. The PE slabs act as a neutron converter producing recoil protons with energies up to 30 MeV, confirming the work of Kronenberg and Brucker for different oxide thicknesses, neutron energies and fluences [Kro95]. The GEANT4 simulation demonstrates that the γ fluence is about 10 times lower than the proton fluence while the electron/positron production is negligible. In these experiments the addition of the PE slabs in the range 2 to 10 mm increases the neutron sensitivity on average by a factor of 6.2 for the REM devices and by a factor of

2.5 for the NMRC RadFETs for fluences lower than 3×10^{13} cm^{-2}. At higher fluences, the observed differences in the sensitivities of the two device types are possibly driven by the different degree of saturation. However the enhancement of sensitivity lays around a factor 3.0 for both devices. The weak dependence on the thickness of the PE slabs was not expected. While GEANT4 predicts over 40 % variation from 2 to 10 mm, the variations observed were instead 15 % for the REM devices and 8 % for NMRC. This unexpected behavior suggests a repeated experiment.

These results finally confirm the plastic packaging as responsible of the enhanced neutron sensitivity what was found in the case of the T&N devices in the mixed γ-neutron field of IRRAD2. However, further GEANT4 analysis, using more accurate representations of MOSFET structures may clarify this apparent effect of sensor-layer thickness on charge yield. New simulations should also be based on the full real neutron spectra, with better accuracy in the spectrum below 15 MeV produced by the Be(d,n)B reaction. Such adjustments will give a better figure for the effectiveness of the PE converters [Cor04].

6.1.3 Stability of the dosimetric information: Isochronal Annealing studies

The stability of the dosimetric information (annealing of the Q_{ot}/Q_{it} trapped charge) over time is the most important parameter that has to be evaluated to guarantee reliable measurements with RadFET devices over the 10 years of the LHC experiments. The spontaneous recovery of the trapped charge [Bla86] occurs in competition with the build-up of charge induced by radiation. Annealing effects on the employed dosimeters can therefore be important during both shut-down and operation periods of the LHC experiments.

In the first case (shut-down), the loss of signal can be easily detected and corrected before the forthcoming particle run. During operation periods instead, especially when the devices are exposed to low dose-rates, the annealing of the trapped charge convolute with the radiation build-up and can strongly affect the dosimeter accuracy. In this situation the response curve starts to differ from the one determined in the calibration phase (usually results of "fast" irradiation runs) becoming a source of error in the measurement. In extreme cases, the excess of annealing can even bring the RadFETs signal to decrease when the devices are exposed to very low dose-rates [Rav02].

The testing of the RadFETs stability for the LHC cannot obviously be done on the time-scale of the machine operation. For this reason, an "accelerated" testing procedure is required to evaluate the devices behavior in order to determine the suitability for the LHC application. The prediction method used in this chapter, is based on the measurement of experimental isochronal annealing curves [Dus97]. This technique, considering only the oxide-trapped charge and the thermal annealing of it, consists in emptying sequentially a fraction of the defects during a brief annealing period at incremental temperatures and it has been demonstrated, under certain conditions, to allow prediction in a few hours of the year time-scale annealing of irradiated MOS devices [Sai00].

The isochronal annealing studies carried out for in this work were all performed using a 20 °C temperature step staircase function and a 360 sec. dwell time [Sai97]. No bias was applied during irradiation and following isochronal annealing. When possible, the annealed components were mounted on metal packagings, with the aim to maximize the thermal exchange during the heating and cool-down steps. After each annealing step the signal from the devices (V_{th}) has been measured, and its un-annealed fraction

$$U_F = \frac{V_{th} - V_{th}(\text{before irradiation})}{V_{th}(\text{after irradiation}) - V_{th}(\text{before irradiation})} \tag{6.2}$$

is used to quantify the annealing process. From the isochronal annealing curve, characteristics temperatures T* can then be extracted, as well as the proportion of defects annealing at a given temperature [Sai01]. T* corresponds to transition temperatures associated to different activation energy levels. Using the activation energy levels calculated from T*, it is then possible to evaluate the annealing of defects at any temperature for any time without performing isothermal annealing experiments.

In the present section the isochronal annealing behaviors measured in the different radiation fields for the REM, NMRC, T&N and LAAS devices are discussed and used as indication to identify the components that fulfill the stability requirements for the LHC experiments.

The irradiations of the components analyzed in this section were performed with γ-rays, in the 23 GeV protons of IRRAD1 and in the secondary radiation environment of IRRAD6 that consists of high-energy photons, broad-spectrum neutrons and charged particles in the GeV energy range as explained in Sec. 4.1.1.2. At the irradiation position used for the presented experiments (Z = 15 cm and r = 60 cm), the contribution of charged particles is always two orders of magnitude lower with respect to the neutrons component; thus, discussing the data recorded in IRRAD6, only neutron fluences will be quoted in the following.

Fig. 6.7 shows three experimental annealing curves in the hundred Gy range for the REM TOT-501C Type K (t_{ox} = 0.25 μm) devices. The experimental data following irradiations with different kind of particles show the same behavior: the charge stays stably trapped up to 120-140 °C and then starts smoothly to recover. At temperatures close to 300 °C, the radiation-induced charge build-up has been completely annealed. According to Ref. [Sai00, Dus97, Sai97] this behavior corresponds to a constant recovery due to the thermal detrapping of the Q_{ot} which is net positive. The isochronal annealing curves for the other MOS structures present on the same die (Type R with t_{ox} = 0.85 μm) show similar behaviors.

Similar results are visible for the device TN250P shown in Fig. 6.8. The trapped charge doesn't start to recover for temperatures lower than 200 °C and at the maximum temperature reached on the presented experiments (300 °C), 40 % of the charge lies stably trapped in the device proving their high trapping capability. Equal behaviors have been measured for the devices TN100P and TN502P where the charge starts to recover always between 180 °C and 200 °C. For these devices, supplied in plastic chip carriers, the irradiation in a neutron field has not been performed. The neutron-to-proton conversion in plastic lead to an enhance of the deposed dose difficult to quantify in term of dose as shown in Sec. 6.1.2.3. For this reason only data for γ-rays and 23 GeV protons have been measured.

Fig. 6.9 shows the results of the test performed on the NMRC devices. Here the isochronal annealing curves for γ-rays and in mixed fields at low doses show unusual

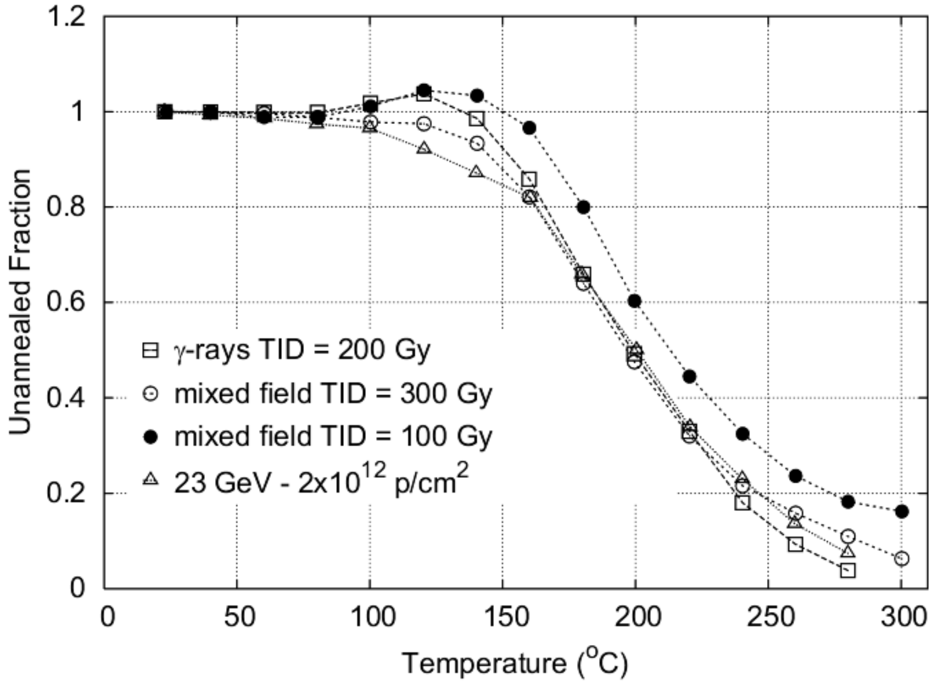

Figure 6.7: Experimental isochronal annealing curves for REM TOT-501C Type K RadFETs ($t_{ox} = 0.25$ μm). Examples of measured isochronal annealing curves following irradiation with γ-rays (square markers), in the mixed hadron field of IRRAD6 (circular markers) and in the 23 GeV proton beam of IRRAD1 (triangular markers).

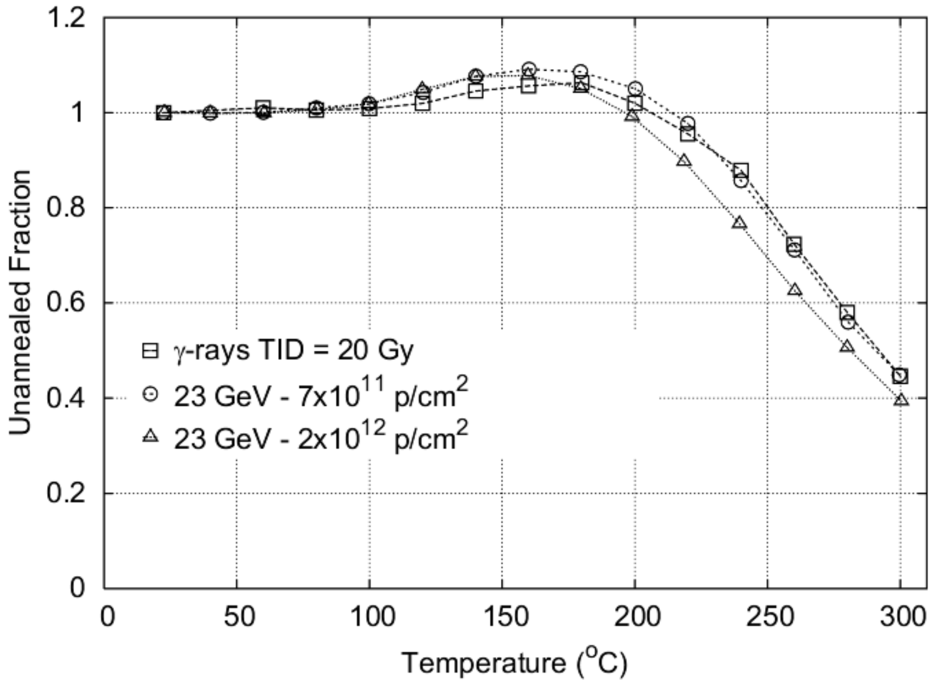

Figure 6.8: Experimental isochronal annealing curves for TN250P RadFETs. Examples of measured isochronal annealing curves following irradiation with γ-rays (square markers) and in the 23 GeV proton beam of IRRAD1 (triangular and circular markers).

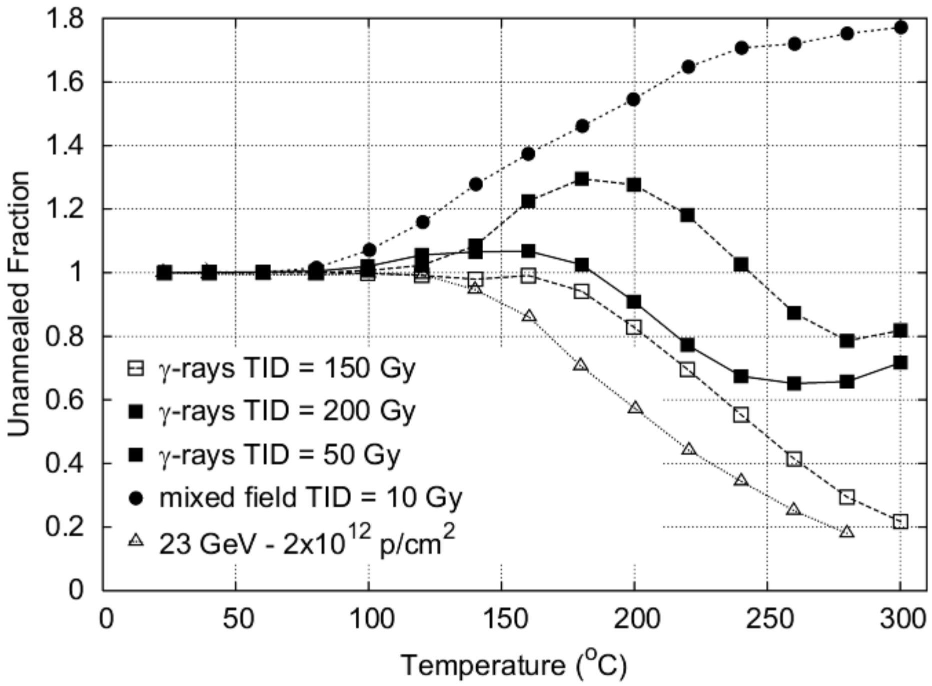

Figure 6.9: Experimental isochronal annealing curves for NMRC RadFETs. Examples of measured isochronal annealing curves following irradiation with γ-rays (different square markers), in the mixed hadron field of IRRAD6 (circular markers) and in the 23 GeV proton beam of IRRAD1 (triangular markers).

behaviors. The γ-ray curve measured after exposure to 50 Gy shows an additional degradation between 140 °C and 200 °C. Moreover after a period of recovery up to 260 °C, in the final part of the isochronal experiment, the curves start again to degrade. In the case of the hadron field irradiation for a TID of 10 Gy, one part continuously degrades over the investigated temperature range without showing any recovery signs. In the NMRC devices, where degradation evidences occur during annealing, more complex phenomena than the trapped charge recovery has therefore to be assumed. However, it should be pointed out that, in the case of the component irradiated in IRRAD6, the Φ_{eq} level associated to the absorbed TID is too low to claim its possible influence inducing any other radiation effect mechanism than charge-trapping phenomena [Aub72].

In the case of the NMRC devices, the isochronal annealing cannot be used to extract parameters that will allow to predict the long-term behavior at room temperature. Here in fact, the isochronal annealing method is used as a screening procedure to identify the devices with thermal behaviors difficult to evaluate. The NMRC RadFETs are one of these devices in which the measured behavior can be interpreted as a warning of complex phenomena that can play an important role in the evolution of the trapped charge over time. As a consequence of this, these devices have been identified to be a possible source of problems when used for long-time in real isothermal applications.

For a "preliminary evaluation" of the LAAS 1600 sensors, the curve determined at low TID ($\sim$ 10 Gy) in pure γ-ray and in IRRAD6, plotted in Fig. 6.10, can be considered. As in the case of the T&N devices of Fig. 6.8 these devices show a very high stability of the trapped charge, with a measured $U_F \sim 1$ up to 240 °C. In the same Fig. 6.10

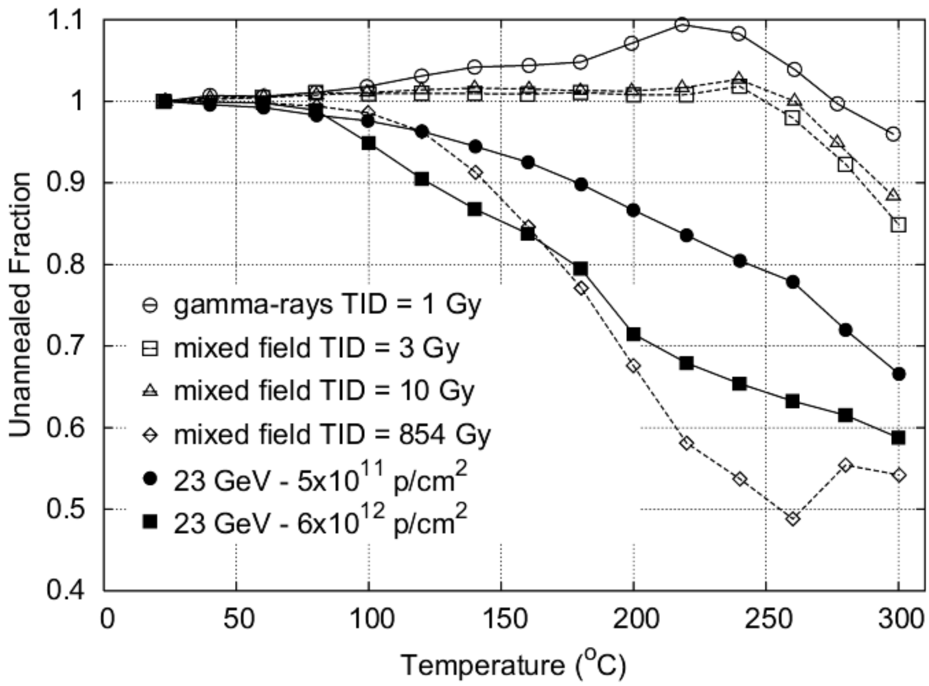

Figure 6.10: Experimental Isochronal annealing curves for LAAS MOSFETs irradiated in mixed-hadron field (empty markers) and with 23 GeV protons (filled markers). The round markers-continuous line curve shows the isochronal annealing behavior of a device that was irradiated with gamma-rays.

isochronal annealing curves at higher TID level are also shown. A detailed discussion taking into account this second data set will be given later in Sec. 6.3.2.

Finally, isochronal annealing curves were measured also for the LAAS 400 device. In this case some unusual behaviors were also found. However, because of the few number of devices tested, at the moment it is not possible to give a reliable evaluation of these devices based on the isochronal annealing technique.

Tab. 6.5 summarizes the results of the presented isochronal annealing tests. According to Ref. [Dus97] when the MOS devices show regular isochronal annealing behavior it is verified that the same net charge is trapped within the SiO_2 transistor layer either with a short annealing time at high temperature, or with a long annealing time at low temperature. Therefore, if as figure of merit the experimental isochronal temperature at which the RadFET signal loses 20 % is determined, an estimation of the RadFET isothermal annealing can be done by using the factor of thermal acceleration A. Therefore assuming $A = 1{\times}10^7\ s^{-1}$ [Sai98], it is possible to calculate the time at 28 °C when the different investigated devices are expected to lose 20 % of their signal. The result of this calculation has been reported in the last column of Tab. 6.5.

6.2 Selection of the RadFET dosimeters for the LHC

The results of the previous sections can be summarized as follows:

- The presence of high-LET particles at the LHC experiments suggest the utilization

Device type	t_{ox} (μm)	Observed behavior	Reference T when $\lvert U_F \rvert \sim 20$ %	Equivalence T $\leftrightarrow t$ at 28 °C
NMRC	0.40	unusual	prediction not possible	
REM TOT-501C	0.25	regular	170 °C	$\lessapprox$ 1 year
TN502P	0.50	regular	220 °C	$\geq$ 10 years
TN250P	0.25	regular	240 °C	$>$ 10 years
TN100P	0.10	regular	240 °C	$>$ 10 years
LAAS 400	0.40	a few devices measured: evaluation not possible		
LAAS 1600	1.60	regular	300 °C	$\rightarrow \infty$

Table 6.5: Summary of the isochronal annealing test on the candidate devices.

of unbiased thin oxide devices (0.1-0.2 μm) in order to avoid enhanced recombination effects over the TID range of interest that extends up to some tens of kGy. Increasing the t_{ox}, reduced response behaviors may appear after certain TID values that will depend on the oxide production processes.

- The responses of different RadFET dosimeters over the range of fast-neutron fluences of interest for the LHC, showed a reduced sensitivity by a factor of 2 with respect to γ-ray response for doses up to 50 Gy. At higher TID it was also found that strong saturation effects can appear in the RadFET devices with different gate oxides.

- In the neutron irradiation test it was shown that the presence of a plastic package (simulated by slabs of polyethylene) on the beam entry side can significantly increase the response to neutrons (a factor of up to 7 was found in this work). While RadFETs are thought of as "neutron-insensitive", introducing a hydrogenous material gave neutron sensitivity values which were higher than the sensitivity for gamma rays. Using polyethylene slabs of 2, 5 and 10 mm, it was found that even the thinnest layer was sufficient to increase the sensitivity with respect to the one measured for γ-rays.

- Concerning the stability studies, apart for the NMRC RadFETs and the LAAS 400 devices for which a complete set of measurements is not available, all the other devices show regular degradation behavior of the dosimetric signal and a satisfactory stability over years time scale.

Cross checking these results, the device REM TOT-501C appeared to be the best device for monitoring the most hostile environments of the LHC experiments. On the other hand, as it as been explained in Chapter 3, with thin-oxide devices the minimum achievable sensitivity is limited so that a unique device cannot be sufficient for LHC applications.

However, the locations at the LHC experiments where high sensitivity measurement (mGy) are required are generally far away from the interaction regions. The radiation field expected in these locations will be composed mainly of neutrons and γ-rays, while MIPs constitute a small background. Therefore, the TID cumulated there rarely exceed the tens of Gy over 10 years of LHC operation. The monitoring of this environment can be so performed with a thick oxide. From the above measurements, the RadFET LAAS 1600 is therefore the best device as it combines an high-sensitivity together with an high stability over time.

In the next two sections of this chapter, a detailed analysis of these two devices will be presented.

6.3 Characterization of the LAAS 1600 RadFET

6.3.1 Calibration curves and operational parameters

The devices LAAS 1600 supplied by the *Laboratory of Analysis and Architecture of Systems* in France have been irradiated in different particle fields with the goal to determine calibration curves and the operative parameters to be used at the LHC experiments. The LAAS 1600 die contains only one RadFETs structure with an oxide gate thickness of 1.6 μm.

This RadFET has been operated with a readout current of 100 μA as indicated by the manufacturer following measurements of the MTC point as indicated in Ref. [Kum95]. Using the LAAS 1600 RadFET at such current level, the sensitivity to temperature associated to ΔV_{th} is in the order of 0.1 mV/°C, so that sensitivity in the mGy range can be provided. This value slightly increases with irradiation to 3 mV/°C at a TID of 10 Gy. The temperature induced variations to the dose measurement are therefore kept in the order of 0.1 % at the maximum dose of 10 Gy [Rav05a].

To determine the readout protocol for the calibration runs, measurements of the "read-time" instability (or "drift-up") have also been performed [Rav05a]. For an unirradiated device, the ΔV_{th} has been found to increase in the range of 0.3-0.7 mV from 1 to 5 seconds after the injection of the readout current. After a TID of 10 Gy, this value increases to about 10-20 mV, corresponding to less than 1 % with respect the ΔV_{th} reached at 10 Gy. These measured values, together with other independent results found in literature [Kum95], suggest to perform the readout of the RadFET ΔV_{th} after 1 second from the start of the current injection.

Fig. 6.11 shows the results of the different irradiation tests performed on the LAAS 1600 device exposed in "zero bias" mode with the above described readout protocol. Experimental data from γ-rays, 23 GeV protons, as well as for two different neutron environments are presented. The log-log plot of ΔV_{th} as function of the TID shows that ΔV_{th} varies almost linearly up to about 10 Gy. Although it is still possible to measure TID increases at higher doses, ΔV_{th} becomes strongly sub-linear moving quickly towards saturation after 500 Gy (this last only slightly visible in Fig. 6.11).

For doses exceeding 10 Gy, Fig. 6.11 shows that the radiation response curves change in slope, and the degree of saturation appears to be different under exposure to different radiation fields. Although this finding suggests to limit the operational range of the devices to a maximum TID of 10 Gy, at higher doses, this feature has been found to be of interest in the case of the LHC as it will be explained later on in Sec. 9.2.3.

All the experimental data in the range 0.01-10 Gy can be conveniently fitted with Eq. 3.5 to obtain the following parameterization:

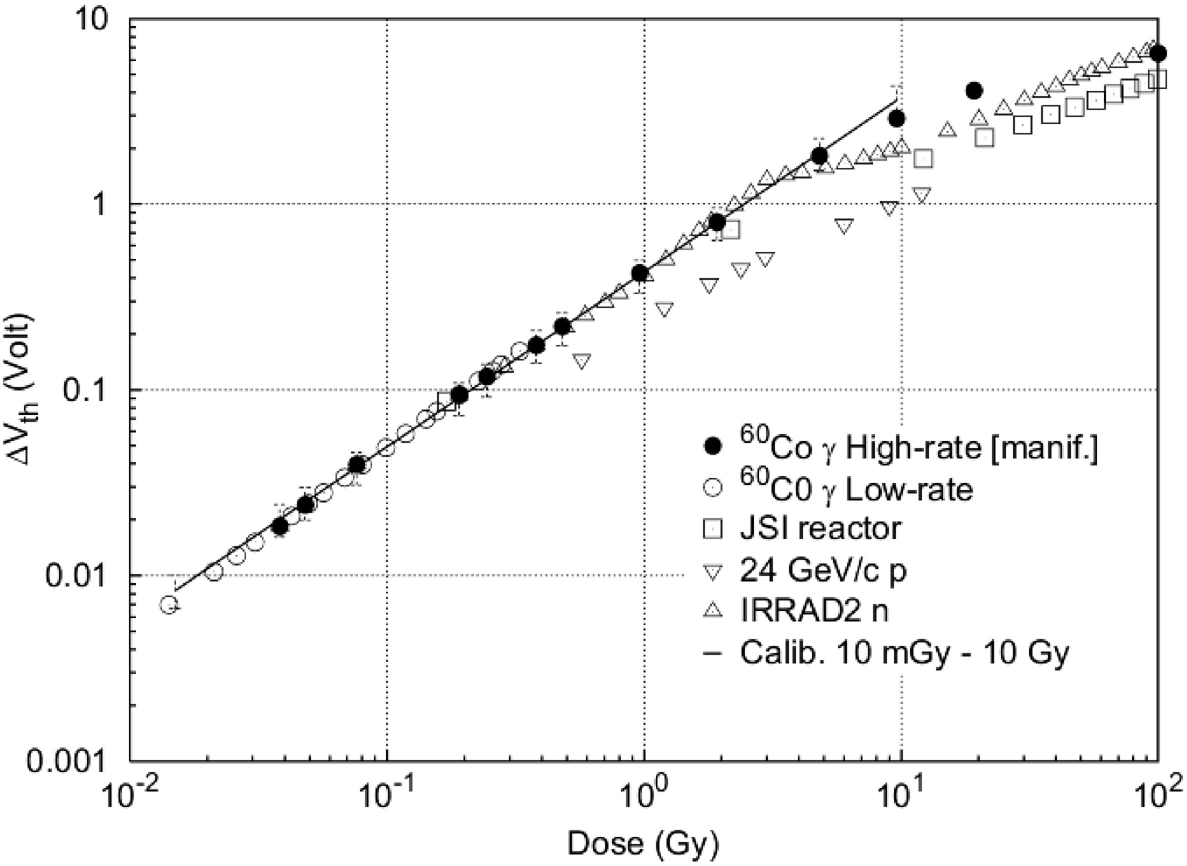

Figure 6.11: Radiation response of LAAS 1600 RadFETs. The RadFET threshold voltage shift at 100 μA is plotted versus the TID. The readout time was comprised between 1 and 5 sec. The experimental ^{60}Co data plotted here come from the producer and from one irradiation at the *Montpellier University II*. The neutron data are from the TRIGA reactor at JSI and from the IRRAD2 facility at CERN. Finally, the 23 GeV beam of the IRRAD1 facility has been used to determine proton data. Devices exposed in ”zero-bias mode”.

$$\Delta V_{th} = a \times D^b \qquad \text{with} \qquad \begin{array}{c} a = 0.432\ V/Gy \\ b = 0.9404 \\ for\ 10^{-2}\ Gy\ <\ D\ <\ 10\ Gy \end{array} \tag{6.3}$$

The accuracy of the presented fit is of ± 10 % up to doses of 6 Gy. Even if in the range from 6 to 10 Gy a more accurate fit can be determined, Eq. 6.3 can be still used if a bigger error in the measured TID is allowed.

6.3.2 Annealing behavior and displacement damage in hadron field

Isochronal annealing studies carried out on the LAAS 1600 devices have been already presented in Sec. 6.1.3. In this section, these data will be re-discussed with particular emphasis to the application of the LAAS 1600 at the LHC experiments. The isochronal annealing results will be also compared here with a set of experimental isothermal annealing data recorded over 14 months after irradiation in the secondary radiation environment of the IRRAD6 facility at CERN (see Sec. 4.1.1).

The dotted curves in Fig. 6.10 plotted with squared and triangular markers represent isochronal annealing behaviors for two devices irradiated in the mixed-hadron field at dose levels of 3 Gy and 10 Gy respectively discussed in Sec. 6.1.3. It is here useful to remember that in the annealing curves presented in this section, ΔV_{th} has been normalized to unity and its un-annealed fraction has been used to quantify the annealing processes [Sai01]. As already pointed out, the two devices show a remarkable stability of ΔV_{th} that does not start to recover until temperatures exceeding 250 °C. A similar behavior has been measured from a third device exposed to 1 Gy of pure ionizing gamma rays from Cobalt source (round markers in Fig. 6.10).

It is possible then to consider that these first three measured behaviors are mainly due to the Q_{ot} and Q_{it} annealing. Applying the isochronal method on these data sets it is possible to estimate a room temperature recovery of ΔV_{th} less than 1 % over 10^4 hours (taking always $1{\times}10^7\ sec^{-1}$ as factor of thermal acceleration). This prediction is in excellent agreement with experimental data presented in Ref. [Kum95, Ges93], for the same devices exposed to tens of Gy in a pure ionizing radiation environment. The neutron fluence that has hit the device exposed to 10 Gy does not exceed $1.5{\times}10^{11}\ cm^{-2}$. In agreement with a previous work [Bho97], this level of neutron irradiation is not expected to induce any measurable changes in the I_{ds}-V_{gs} transistor characteristics.

The curve plotted with diamond markers in Fig. 6.10 shows instead the isochronal annealing behavior of a fourth MOSFET irradiated up to a TID of 854 Gy. In this case the device has been exposed in parallel to a high neutron fluence of about $2{\times}10^{13}\ cm^{-2}$. For this sample the ΔV_{th} recovers about 50 % at a temperature of 250 °C. Clearly at this irradiation level, an overlapping phenomenon that recovers in the presented data must be taken into account. It is then possible to consider that, for such neutron fluence, the number of displacement damages generated by the parallel particle exposure is high enough to induce an I_{ds}-V_{gs} modification: the observed annealing can then be assumed to correspond to displacement damages recovery.

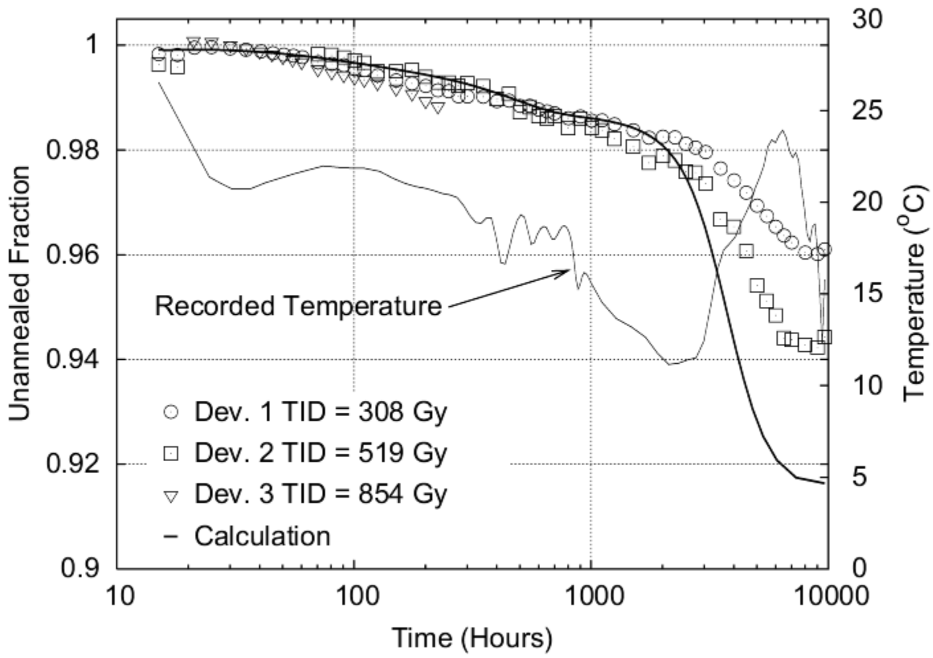

Figure 6.12: Experimental isothermal annealing curves (different markers) for LAAS devices measured following irradiation in the mixed-hadron field at CERN. The light solid lines represent the temperature recorded during the isothermal measurements, while the heavy line show the results of the isothermal annealing calculation based on the recover of silicon radiation-induced defects taking into account the real temperature profile during the fourteen months experiment.

According with Sec. 3.2.1.2 the dosimetric signal V_{th} readout from RadFET devices is in reality a voltage V_{gs} obtained, for a "real" MOS transistor, from the equation:

$$I_d = \beta \cdot (V_{gs} - V_T)^2 \cdot (1 + \lambda V_{ds}) \tag{6.4}$$

when a constant current I_d is forced within the transistor *source-drain* connections. The constant λ only depends on the MOS channel geometry and on the channel carrier mobility (μ).

Atomic displacements [Lin99] in the bulk semiconductor layer can be responsible for the degradation of the transistor channel mobility [Gaw74] that in turn may increase the MOS channel resistance [Bal92]. Via the parameter λ the bulk damage can thus degrade the dosimetric signal measured through Eq. 6.4. Therefore, in order to assess whether the additional degradation in the ΔV_{gs} recovery can be related to the occurrence of displacement damage, a second series of devices was exposed to the pure 23 GeV proton beam of the IRRAD1 facility. The annealing measurements related to this second irradiation test are plotted with filled markers in Fig. 6.10.

From these last data sets, it is possible to identify a common series of transition temperatures [Dus97] (inflection point of the experimental isochronal annealing curve) $T_1^* = 130$ °C, $T_2^* = 180$ °C and $T_3^* = 280$ °C that may correspond to the temperatures at which the different types of radiation-induced defects spontaneously dissociate in silicon [Hol02]. According to Ref. [Cor75] these T^* may indicate the recovery of

Defect Type	Recovery T* (°C)	i	A_i (s^{-1})	$E_{A,i}$ (eV)	B_i
V-P	130	1	7×10^8	0.94	0.25
V-Sb	180	2	1×10^{10}	1.28	0.25
V-V	280	3	1×10^9	1.47	0.5

Table 6.6: Parameters of the radiation-induced defects in Si extracted from the LAAS isochronal annealing test.

radiation-induced centers formed by vacancy defects (V) in the silicon lattice with impurities atoms or with other vacancies. To verify the above hypothesis, the bulk damage characteristics extracted from the proton isochronal annealing curves can be used now to predict the isothermal annealing behavior of ΔV_{gs} for the heavy irradiated devices. ΔV_{gs}(t), normalized to its initial value $\Delta V_{gs}(0)$, is so computed taking into account that the time-dependence of the defects dissociation is described by a first order process [Mol99a]:

$$\frac{\Delta V_{gs}(t)}{\Delta V_{gs}(0)} = \sum_{i=1}^{3} B_i \cdot \exp(-\sigma_i \cdot t) \tag{6.5}$$

$$\sigma_i = A_i \cdot \exp\left(-\frac{E_{A,i}}{k_B T}\right)$$

where: t is the annealing time, σ_i is the probability per unit time for the defect i to dissociate (s^{-1}) and B_i is the fraction of ΔV_{gs} that recovers with the dissociation of defect i (experimental parameter from the curves of Fig. 6.10). The temperature dependence of σ_i is given by an *Arrhenius* relation where A_i is the factor of thermal acceleration of defect i (s^{-1}), $E_{A,i}$ is the activation energy for dissociation of defect i (eV), k_B is the *Boltzmann*'s constant and T is the annealing temperature (K).

According to Ref. [Cor75, Mol99a, Elk68] the characteristic temperatures T_1^*, T_2^* and T_3^* could correspond thus to the recovery of the V-P, V-Sb and V-V centers respectively. Tab. 6.6 details the microscopic parameters of the identified defect found in the above mentioned references. These parameters are the ones that appear in Eq. 6.5.

Fig. 6.12 shows finally the comparison between the curve from Eq. 6.5 and the experimental annealing, recorded over 14 months, for three MOS transistors independently irradiated in the same IRRAD1 secondary radiation field. The three devices where exposed to different TIDs and to high neutron fluences ranging from 4.5×10^{12} cm^{-2} to 2×10^{13} cm^{-2}. It has to be noted that the calculation with Eq. 6.5 takes into account the real temperature profile recorded during the measurement of the data. It is then possible to follow the thermal annealing of the defects at any time of the experiment. The prediction, evaluated on the real temperature profile (see secondary y-axis of Fig. 6.12), fits the experimental data better than 1 % up to about 3×10^3 hours. The accuracy of the calculation is still very good (4-5 %) after fourteen months.

The calculation and the hypothesis presented in this section is also confirmed by the measurement performed on the drain diode curve. This measurement has been carried out by measuring the $I_{ds} - V_d$ characteristic curve of the RadFET, between the *drain*

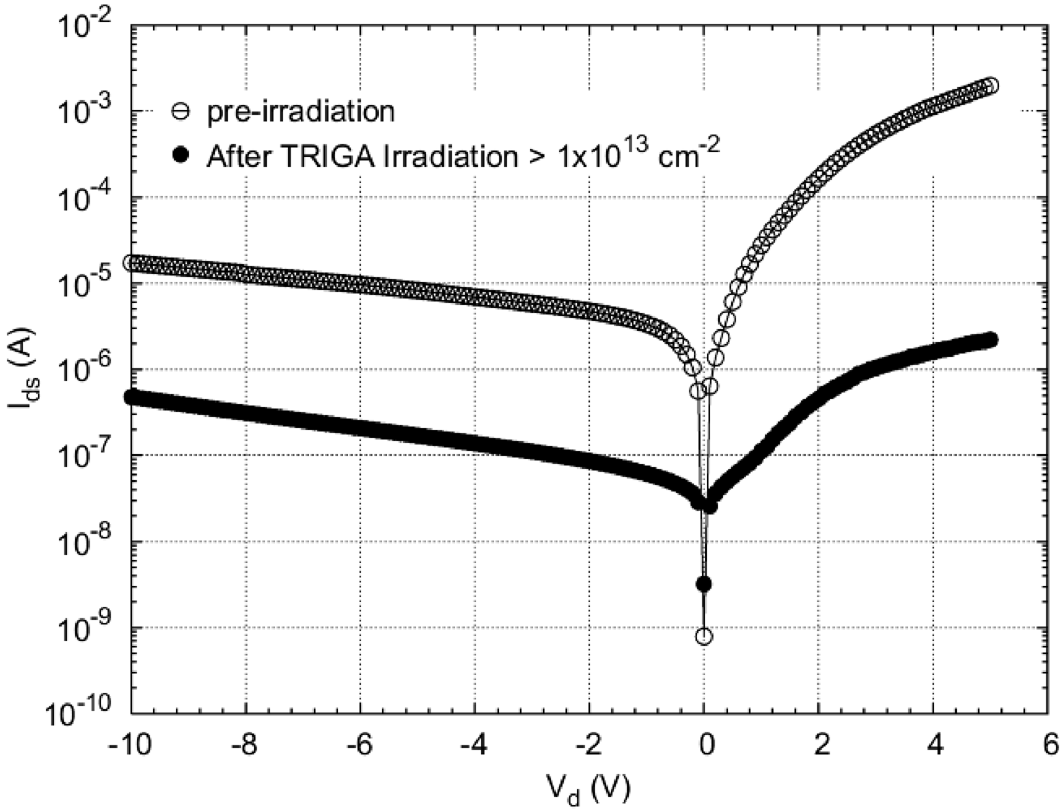

Figure 6.13: *Drain* current-voltage characteristics of a LAAS 1600 RadFETs. I/V for a un-irradiated transistor (empty round markers) and following irradiation to Φ_{eq} of about $2{\times}10^{13}$ cm^{-2} (filled round markers)

terminal and *source, body* and *gate* terminals shorted together. The results of this test have been plotted in Fig. 6.13 where the I/V drain characteristic before irradiation (empty markers) has been compared to the same curve measured after heavy neutron irradiation in the JSI TRIGA Mark II reactor (filled markers). In the forward part of the curves, for a given voltage (see for example V_d = 2V), the drain current results reduced of more than two orders of magnitude for a Φ_{eq} of about $2{\times}10^{13}$ cm^{-2}.

As mentioned before, even if the principal effect in the MOS device remains the charge trapping in the oxide and at the Si-SiO_2 interface, the parallel exposure to neutrons (and fast hadrons in general) induces carrier removal in the silicon substrate, thus causing the substrate resistivity to increase [Bal92] at the same fashion as the *p-i-n* silicon devices described earlier in Sec. 3.2.2.

Normally, the increase in the substrate resistivity has only small effect on the *drain* current since a MOSFET device carries current in an inversion layer at the surface and the inversion layer conduction is rather insensitive to the substrate doping level. However, the increase in substrate resistivity would be expected to increase the width of the *drain* space-charge region, eventually allowing it to directly contact the source. "Punch-through" between *drain* and *source*, would then occur. From the data of Ref. [Aub72] and references therein, this can become a serious effect when $\Phi_{eq} \gg$ substrate doping concentration.

Coming back to the ΔV_{gs} measurement, it can be still pointed out that the measurement of the "real" ΔV_T of the transistor will be probably immune to this effect due to its independence in the transistor's channel mobility degradation.

The isochronal annealing procedure has been used in the case of the LAAS 1600 devices, also to evaluate the displacement damage annealing and then their long time behavior. The comparison between the annealing prediction and a set of experimental data recorded over 14 months is found to be very accurate. It is then shown that in this kind of device, defects induced by harsh radiation environment characteristic of CERN-LHC experiments can be evaluated using the isochronal annealing method. Bulk damage effects can therefore induce additional errors in the ΔV_{gs} measurement. This has been found here to be as low as 8 % over 14 months of thermal annealing for absorbed doses up to the kGy range, proving that the tested LAAS devices fully comply with the LHC stability requirements even under extremely high radiation levels.

6.4 Characterization of the REM RadFET

6.4.1 Calibration curves and operational parameters

The devices REM TOT-501C supplied by the *REM Oxford Ltd (REM = Radiation Experiment and Monitors)* in United Kingdom were irradiated in particle fields with the goal to determine a calibration curve and the operational parameters to be used at the LHC experiments. Although the device's chip contains four RadFET structures with different gate-oxide thickness, only the structures having a "thin" gate oxide thickness (Type K) were considered for the LHC experiments. For this reason, a selection procedure was used to select the best "Type K" samples (see Appendix A), and only these with $t_{ox} = 0.25$ μm were investigated in detail.

These RadFETs were operated, following the manufacturer indications, with a readout current of 160 μA. However this value was not verified by the producer to be corresponding to the MTC point of the RadFET. For this reason, an evaluation of the transistor MTC has been carried out by measuring the transistor *drain* current as function of V_{gs} for temperatures ranging from 12 °C to 90 °C. Fig. 6.14(a) shows the current-voltage characteristics of the MOS with the temperature as parameter. The working point region in which the sensitivity to temperature is reduced virtually to zero for the REM 0.25 μm RadFETs has been found here to be between 70 and 90 μA. Although the readout current used is twice such measured values, for coherence with previous measured data [Rav02, Rav03b] and with the data from the producer, 160 μA has been kept as standard readout current. Moreover, as confirmed by Fig. 6.14(a), the sensitivity to temperature associated to the REM ΔV_{th} at 160 μA is slight, being less than 0.05 mV/°C, so that dosimetry in the cGy range is not hampered by keeping the above mentioned readout current.

The magnitude of the temperature dependence increases with irradiation reaching about 50 mV/°C at a TID of 20 kGy as shown in Fig. 6.14(b) where the temperature dependence has been evaluated from data recorded during X-ray and mixed hadron field (CERN-IRRAD6) irradiations. The error on the presented data has been evaluated to be ± 20 % in both T_c and TID measurements. The temperature-induced variations

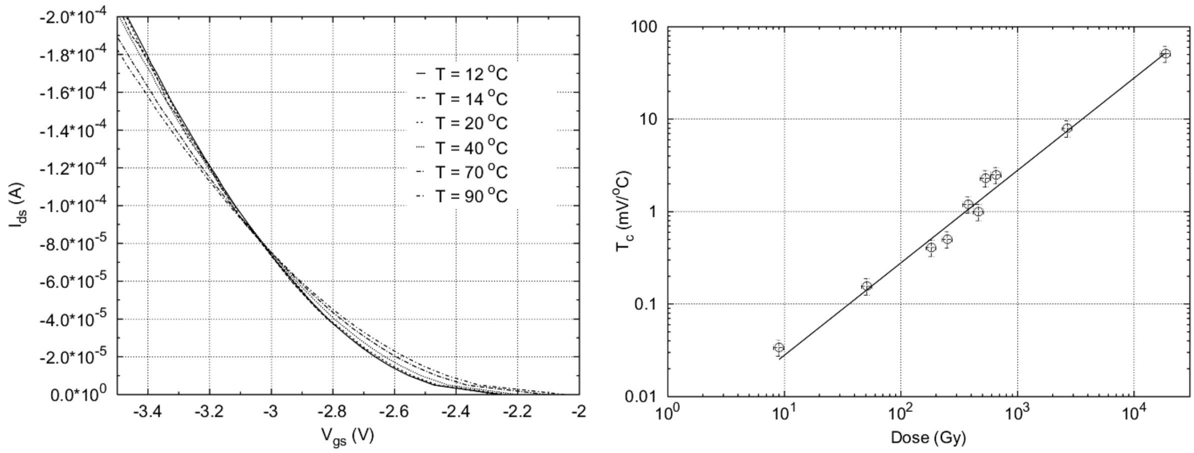

Figure 6.14: Temperature sensitivity of the RadFET REM TOT-501C Type K. (a) Determination of the MTC point. (b) Temperature coefficient T_c in mV/°C measured at increasing TID for 160 μA. Experimental points from X-ray and mixed hadron field (CERN-IRRAD6) irradiation. The best-fit of the experimental data show a $|T_c| = 2.8{\times}10^{-3}\ mV/°C\cdot\ Gy^{-1}$. Devices exposed at $V_G = 0$ V.

of the dose measurement are therefore in the order of 0.2 % at the maximum dose of 20 kGy. By fitting the data of Fig. 6.14(b) the following temperature dependence as function of the TID can be found:

$$|T_c| = 2.8 \times 10^{-3}\ mV/°\mathrm{C} \cdot\ Gy^{-1} \tag{6.6}$$

For "megarad" and "kilogray" dosimetry, this degree of temperature sensitivity change is a problem which demands a temperature compensation of some sort as indicated early in this work in Sec. 3.2.1.5.

Measurements of the "read-time" instability (or "drift-up") have also be performed for the REM 0.25 μm devices [Rav05a]. For an unirradiated RadFET, the ΔV_{th} has been found to increase in average of 0.7 mV from 5 to 10 seconds after the injection of the readout current. After a TID of some tens of kGy, this value increases to about 500 mV, representing thus a few % of the ΔV_{th} measured at such doses that is in the order of 30 V. These measured values, suggest to apply for the device's readout a DC current at least for 5 second before the ΔV_{th} is measured. In these condition the REM "drift-up" can be kept as low as the experimental error in the overall TID range of interest for the LHC of some tens of kGy.

Fig. 6.15 shows the results of the different irradiation tests performed on REM TOT-501C devices with the above readout protocol and with the samples exposed in "zero bias" mode. Some of the plotted data comes from Ref. [Rav02, Rav05a]. Experimental data from nine different test-beams have been plotted there (see details on Fig. 6.15 caption). The log-log plot of ΔV_{th} as function of the TID shows that ΔV_{th} varies almost linearly up to about to 4 kGy. Although it is still possible to measure TID increases at higher doses, ΔV_{th} smoothly rise toward saturation that appear after a TID of 100 kGy.

For TID lower than 4 kGy, all the experimental data from photons, MIPs and mixed field are in very good agreement following the same response behavior. As shown in

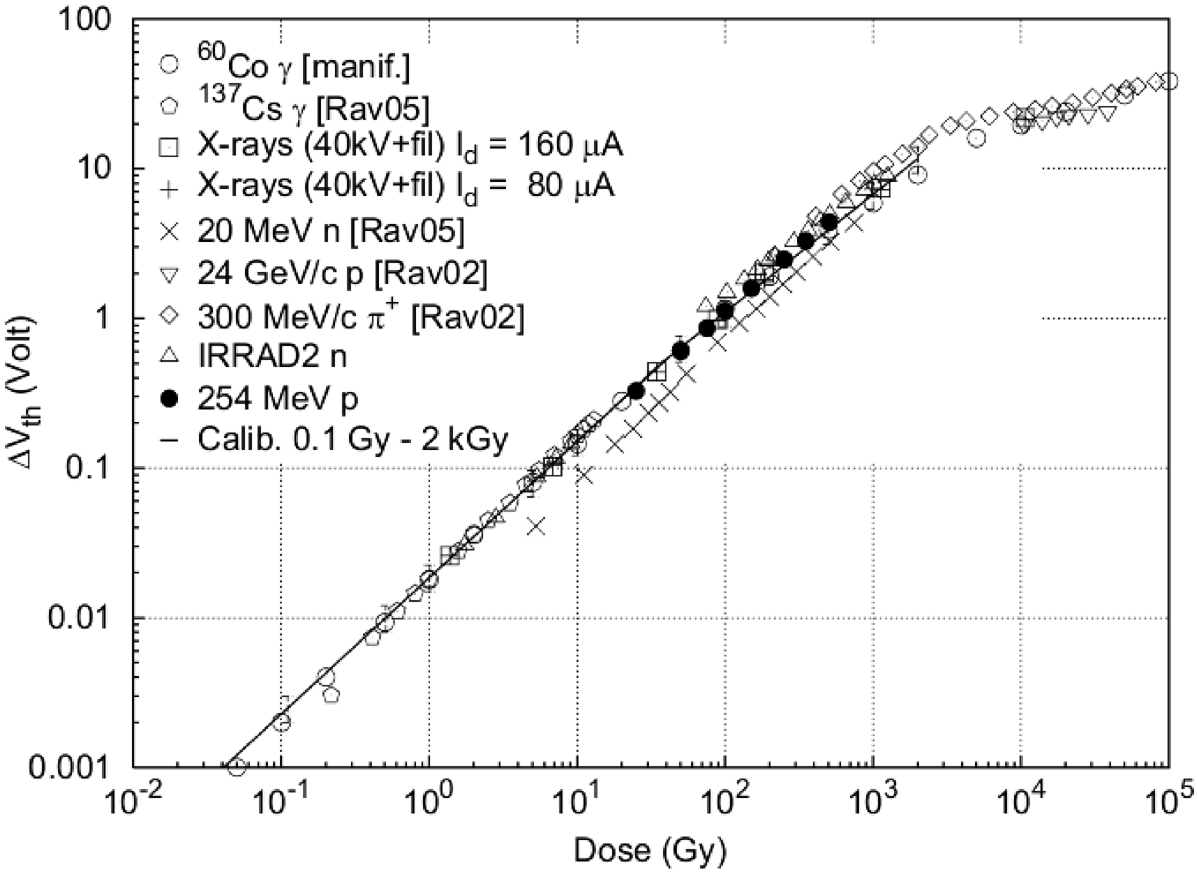

Figure 6.15: Radiation response of REM-501C Type K RadFETs (t_{ox} = 0.25 μm). The RadFET threshold voltage shift at 160 μA is plotted versus the TID. The readout time was set to be between 5 and 10 sec. The experimental ^{60}Co data plotted here come from the producer and from one irradiation at the CERN-GIF facility. The neutron data are from the IRRAD2 facility at CERN and the T2 facility at UCL. The 23 GeV beam of the IRRAD1 facility and the 254 MeV of the PIF facility at PSI where used for proton irradiations. Data for positive pions from older irradiations (see text) has been also plotted there. Finally the sensitivity to X-rays (tungsten target filtered with 3 mm of Al) at two different readout currents have also been plotted. Devices exposed in "zero-bias mode".

detail in the previous Sec. 6.1.2.2, the response of the REM devices to a pure neutron beam (cross markers in Fig. 6.15) is clearly reduced by a factor of about two as expected. This confirms the strongly reduced response of this devices to neutrons, apart for the contribution that these particles give to the ionizing KERMA. In the Irradiation test with X-rays, the V_{th} increases as function of the TID has been measured for the operational current of 160 μA (empty square markers) as well as for the MTC current of 80 μA (+ markers). The results of these two irradiation tests show that the relative radiation response is the same for the two operating currents. This result suggest, using REM devices where important temperature variations are expected, that they can be operated at the MTC current (70-90 μA) value by keeping valid the set of calibration curves presented in Fig. 6.15. Moreover, apart from the reduction of the devices temperature dependence, by operating it at a lower current, the initial voltage of the REM devices is reduced by some hundreds of mV. As consequence of this, the measurement range of the sensor can be slightly extended.

The experimental data in the range 0.1-2 kGy (with exclusion of the neutron "×" set) can be therefore fitted with Eq. 3.5 to obtain the following parameterization for the REM devices:

$$\Delta V_{th} = a \times D^b \qquad \text{with} \qquad \begin{array}{c} a = 0.01854\ V/Gy \\ b = 0.91072 \\ for\ 10^{-1}\ Gy\ <\ D\ <\ 40\ Gy \\ (0\ <\ \Delta V_{th}\ <\ 0.5343) \\ \\ a = 0.02921\ V/Gy \\ b = 0.78778 \\ for\ 40\ Gy\ <\ D\ <\ 2 \times 10^3\ Gy \end{array} \tag{6.7}$$

The accuracy of the presented fit is of ± 10 %. In the range from 2 kGy to 10 kGy a more accurate fit can be determined, however, Eq. 6.7 can be still used here, if a bigger error (± 20 %) is tolerated in the measured TID.

6.4.2 Annealing behavior and displacement damage effects in hadron field

Isochronal annealing studies carried out on the REM TOT-501C devices have been already presented in Sec. 6.1.3. In this section, these data will be compared with a set of experimental isothermal annealing data recorded over 14 months after irradiation in the secondary radiation environment of the IRRAD6 facility at CERN (see Sec. 4.1.1).

Fig. 6.16 shows the result of this long-term annealing period. The un-annealed fraction has been calculated by dividing the shift of the threshold voltage of the transistor recorded at any time step $V_{th}(t)$ by the one measured immediately after the irradiation at $t = 0$, $V_{th}(0)$. The devices exposed to purely ionizing radiation in the order of some hundred of Gy show a remarkable stability by loosing less than 2 % of the initial threshold voltage. The device exposed to a higher dose of purely ionizing radiation lose a bit more signal in the order of 7 % over 14 months. Following the indications of

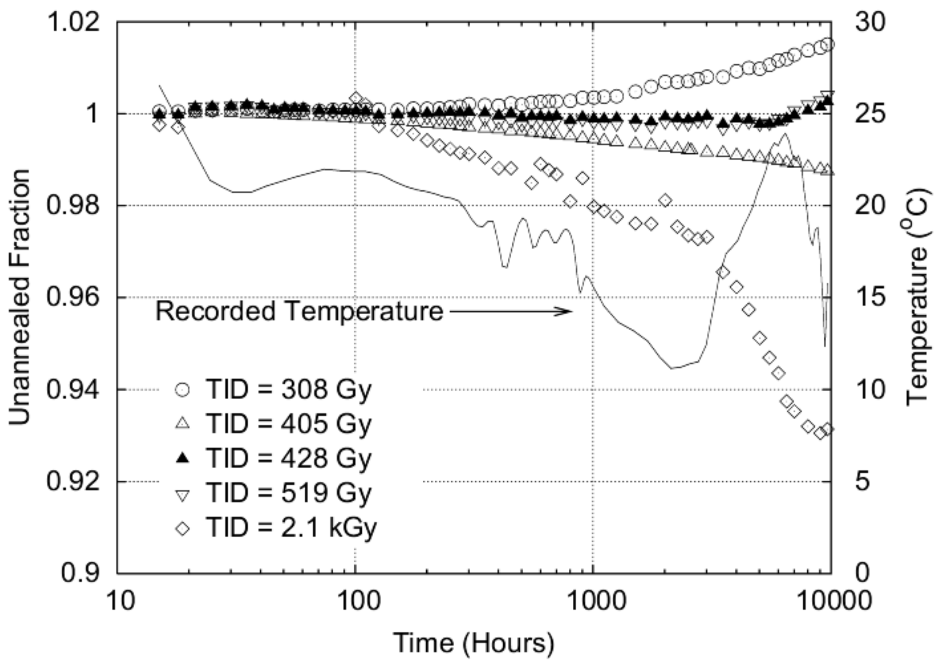

Figure 6.16: Experimental isothermal annealing curves (different markers) for REM TOT-501C Type K devices measured following irradiation in the mixed-hadron field at CERN. The light solid lines represent the temperature recorded during the isothermal measurements and is referred to the secondary y-axis. Devices exposed in "zero-bias mode".

Sec. 6.1.3 and the data measured in Fig. 6.7, the prediction of the isothermal annealing behavior of the REM devices at T = 20 °C , would have given a loss of about 20 % after 1 year annealing-time. The real results appear to be lower by a factor of two with respect the isochronal annealing estimation.

The prediction based on isochronal annealing seems thus to be overestimated but conservative in the framework of a selection procedure as it was been used in this first part of the chapter. A possible explanation about these two discordant sets of annealing data for the REM devices can be manifold and may be attributed to a delayed buildup of interface-trapping states. As explained in Chapter 3, the sites where positive charges can be trapped are usually electrically latent before irradiation and they are triggered by radiation exposure. Moreover they develop from a few seconds to thousands of seconds after irradiation. In the case of p-MOS transistors they give therefore a contribution that adds to the one of the trapped charge in the bulk silicon oxide.

The interface state density growth can be important when the transistors are exposed in unbiased conditions. This has been verified on one REM RadFET device after "zero bias" mode exposure to increasing doses of X-rays up to 33 kGy. By applying the *Winokur method*[1] [McW86] on the set of $I_{ds} - V_{gs}$ curves measured after any irradiation step, it has been found that the contribution of the Q_{it}, on the recorded V_{th} from the

[1] Characterization technique which allows a threshold voltage shift in an MOS transistor to be separated into shifts due to interface traps and trapped oxide charge. This method is based on the determination of the whole $I_{ds} - V_{gs}$ characteristic of the MOS for a given V_{ds} after irradiation. For further details see: [McW86]

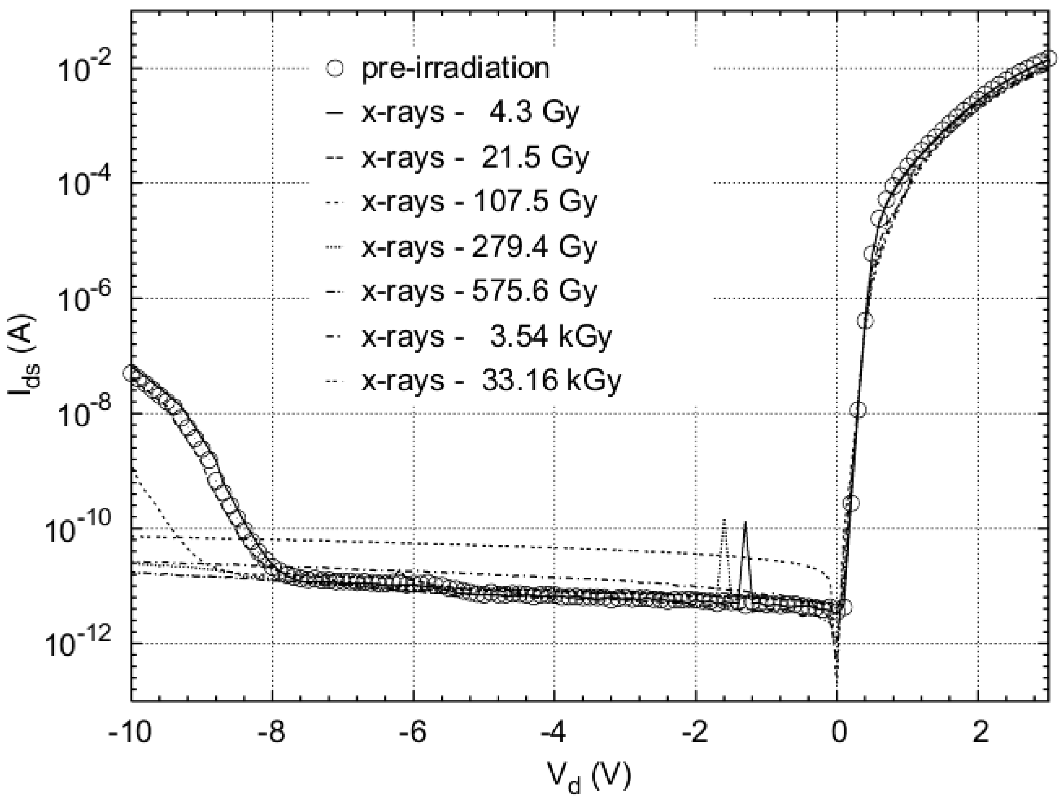

Figure 6.17: *Drain* current-voltage characteristics of REM TOT501C Type K (t_{ox} = 0.25 μm) RadFETs. Devices exposed in "zero-bias mode" to increasing doses of X-rays to study the effects of the TID on the *drain* voltage.

irradiated transistor, is about 10 % for doses of 100 Gy and quickly increase to more than 50 % for doses exceeding the kGy.

In this way, the 50 % of interface states already developed in the irradiated transistors (Q_{it}) can slowly continue to grow increasing the V_{th} over time. This signal increase can thus partially compensate the loss of the Q_{ot} measured and predicted with the isochronal annealing technique. Being the isochronal annealing procedure not able to account the behavior of the Q_{it}, this can explain the differences observed between the two annealing procedures.

The REM TOT-501C devices at the LHC will be devoted to the measurement of high-dose levels in the location of the LHC experiments where the radiation environment is the most hostile. In analogy to what has been done for the LAAS 1600 devices in Sec. 6.3.2, the measurement of the $I_{ds} - V_d$ characteristics curve has been carried out by running I/V measurements of the irradiated RadFETs, between the *drain* terminal and *source, body* and *gate* terminals shorted together. This was done with the goal to investigate possible modifications in the silicon substrate.

Fig. 6.17 shows the results of a series of irradiations carried on a REM device in pure ionizing radiation environment with increasing dose of X-rays. The presented data have been measured on the same REM chip. After any irradiation step a complete $I_{ds} - V_d$ characteristics has been measured (different lines) and compared with the characteristic measured for the un-irradiated device (empty round markers). Taking as figure of merit

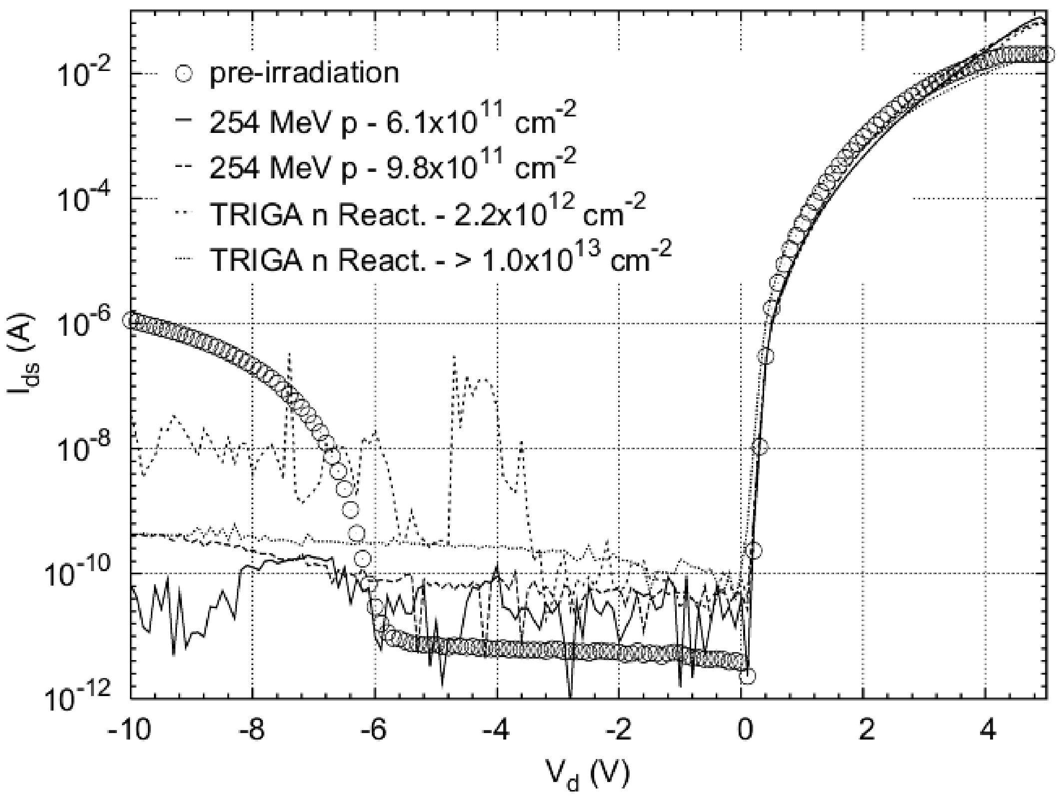

Figure 6.18: *Drain* current-voltage characteristics of REM TOT501C Type K (t_{ox} = 0.25 μm) RadFETs. Devices exposed in "zero-bias mode" to increasing hadron fluences to study the effects of the displacement damage on the *drain* voltage. The experimental data comes form 254 MeV proton irradiation ad PIF and from neutron exposure at the JSI TRIGA Mark II reactor.

an I_d of 160 μA, the *drain* voltage has been found to change less than 10 % in the TID range of more than 33 kGy. Being the measured variation within the experimental errors and considering the very low damaging power achievable with photons, the effect of the TID on the substrate can be neglected.

Finally Fig. 6.18 shows the measurement of the results $I_{ds} - V_d$ characteristics for a series of devices irradiated with fast hadrons. The data presented in this plot comes from different REM RadFETs measured after exposure to the 254 MeV protons in the PIF facility and after neutron exposure at the JSI TRIGA Mark II reactor. Taking again as figure of merit an I_d of 160 μA, the *drain* voltage has been found to change for about 15-20 % in the Φ_{eq} range exceeding $1{\times}10^{13}$ cm^{-2}.

This second result shows a bigger variation in the *drain* forward voltage than the previous one. An increase of the transistor leakage current of about one order of magnitude has been also observed in the investigated Φ_{eq} range. However, the effect on the leakage current has no influence on the high injection level used for the dosimetric RadFET readout. Accounting the device-to-device differences on the initial $I_{ds} - V_d$ curves, it is not thought that the regular operation of these devices at the LHC experiments is going to be compromised in any way by the small bulk-induced perturbations in the leakage current observed for exposure to high levels of JSI reactor neutrons and protons.

6.5 RadFET packaging issues for the LHC experiments

Especially for RadFET dosimeters, the use of inappropriate materials located close to or around them can modify the radiation response inducing errors in the TID measurements. For example, as it has been shown before in Sec. 6.1.2 for neutrons, these particles can interact with the sensors packaging and significantly enhanced the measured dose. Similar effects can be also found for low energy photons as documented for example in Ref. [Ros95]. Contrary, charged hadrons can loose a big fraction of their energy inside the package materials leading to an underestimation of the radiation dose. These considerations clearly apply to the case of the two RadFET devices characterized here for LHC Experiments.

Therefore, the commercially available transistor packaging could not satisfy the requirements in terms of dimensions and employed materials. Thus, a custom-made packaging has been specially produced for the CERN applications. In the first part o this section the studies carried out for the development of this CERN-custom package will be described.

Rough calculations of the effects of packaging materials are straight forward. However, in order to take rigorously into account all different effects of the materials inside the complex LHC field and in order to optimize the sensor packaging, the use of simulation tools is indispensable.

A Monte Carlo model, based on the GEANT4 [Col03, All06] Simulation Toolkit, has therefore been developed to study the effects of the packaging on the RadFETs response. The simulation model exploits GEANT4 advanced capabilities to describe the sensors in detail, and a rich set of physics processes to study the effects induced by a complex radiation environment, such as expected at LHC.

Before the Monte Carlo models can be accurately applied to the complex simulation of the full mixed LHC environment, they need to be validated using a set of experimental data from "simple" (in terms of particle spectra, boundary conditions, etc.) irradiation experiments. Although these first experiments and simulations will not match the full complexity of the LHC environment, they might already be used to provide a guideline for the choice of suitable sensor packaging materials for the LHC. The GEANT4 model described in this chapter has been entirely developed by the I.N.F.N.[2] of Genova, Italy. In the framework of this thesis work, the first experimental campaigns devoted to its validation will be presented and the measurements compared with the first simulation runs.

These irradiation tests where performed by measuring the response of RadFET dosimeters mounted inside the chip carrier and covered with lids of different thicknesses and various materials.

6.5.1 Packaging design studies

Several materials have been evaluated including Alumina (Al_2O_3), Aluminum Nitride (AlN), Graphite (C), Epoxy-glass (G10, FR4), Teflon (C_2F_4) and Beryllium Oxide (BeO)

[2] I.N.F.N. stand for *Istituto Nazionale di Fisica Nucleare*

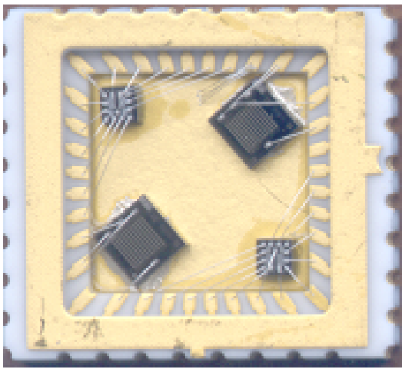

Figure 6.19: SM chip carrier recommended for the RadFET devices to be used at the LHC experiments. In the picture four RadFET dies (2× REM and 2× LAAS) are mounted and wire-bonded in it.

in order to find the one suitable for the packaging of the REM and LAAS devices to be used at the LHC experiments.

Without entering in details all these candidate materials have been evaluated following different criteria as for example:

1. the results of analytical calculations involving the transport inside matter of neutrons [Exf], photons [Shl02], electrons and protons [SRI];

2. the evaluation of mechanical proprieties like the materials thermal conductivity, thermal expansion, resistivity, etc.;

3. the availability of the selected material and the possibility to build a chip package out of it;

4. the costs of the material and the package manufacturing.

Alumina (Al_2O_3 or most commonly "ceramic") turned out to be the material that provides the best compromise among the above requirements. Moreover, a series of Surface-Mount (SM) ceramic carriers was found to be already available in thousand parts inhouse at CERN. The choice went then to this packaging model. The selected RadFET packaging is shown in Fig. 6.19 already fully equipped with sensors. Its dimensions are about 1 cm^2 surface and 1.3 mm thickness.

The available space inside it allows a maximum of 4 transistor dies (2 REM and 2 LAAS devices) to be mounted. The electrical connections are made via an Au/W metalization backplane and wire-bonding pads of about 3 μm width. As the chip mounting inside the package is custom-made, the number of devices that equip the package can vary from 1 to 4 upon user requests. However, the internal connections of the four dies have been "standardized" in order to define once for all the pin-out of the dosimeter package. Details on the connections can be found on the wiring scheme of Fig. 6.20. A thin foil will be glued on the top of the carrier in order to protect the RadFET dies from dust and mechanical damage during handling. Different kinds of materials are suitable as lids for such a carrier. However the choice of the lids constitutes one of the parameters

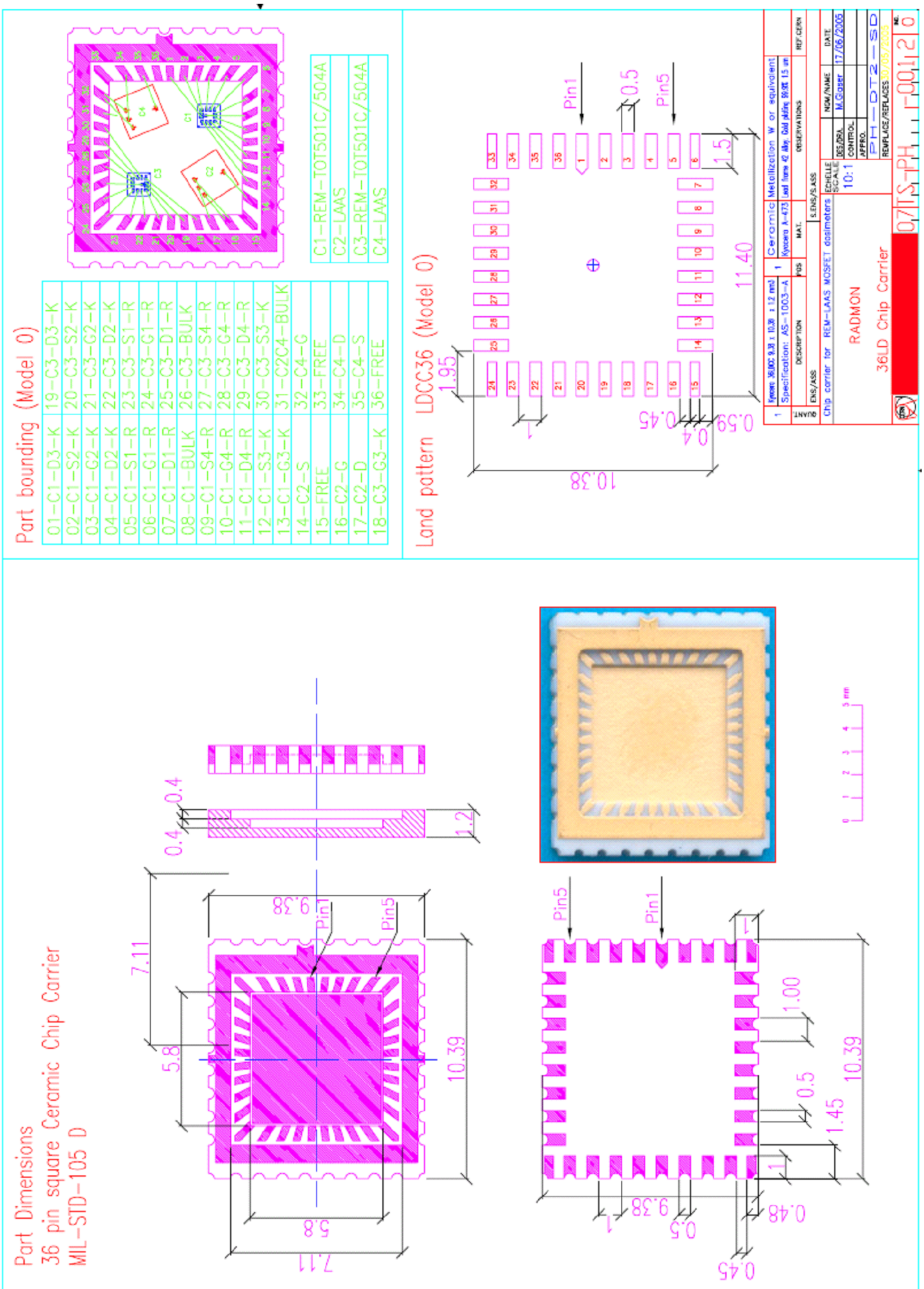

Figure 6.20: Detailed connection layout for the SM chip carrier recommended for the RadFET devices to be used at the LHC experiments.

	unit	value
radiation length	mm	70.3
electrons cut-off	keV	550
protons cut-off	MeV	10
photon transmission	keV	20
neutrons attenuation	%	2-3

Table 6.7: Analytical calculations of the radiation transport characteristics for the RadFET packaging. These calculation have been carried out assuming a simplify carrier-geometry made by a 0.4 mm slab of alumina.

for the optimization of the sensor carrier design. For this reason, the material choice will be discussed in detail later in this section.

Once the RadFET packaging was defined, a new series of analytical calculations involving the radiation transport throughout the packaging material were done. These calculations are made on a simplified geometry (ceramic slab 0.4 mm thick), and their results are summarized in Tab. 6.7. The effects of the Au/W metalization has been also considered adding to the above calculations two supplementary layers of 1.5 μm of Gold and Tungsten respectively. The effects of these heavy metal layers on the above calculations have been found to be in the order of 2 %. The obtained results are very satisfactory for neutron and photons. The package is transparent to neutrons and completely filters low energy photons that are often responsible of enhancement dose effects as documented in Ref. [Ros95]. Higher are instead the energy cut-offs determined for electron and protons. To reduce this values a proper choice for the lid should be therefore taken.

6.5.2 The GEANT4 model of the LHC experiments RadFET packaging

A GEANT4-based simulation application has been developed to study the effects on the sensors when exposed to different radiation environments. A detailed description of the geometry of the sensors has been implemented in the simulation as can be seen from the three-dimensional model of Fig. 6.21 and in the detail of Fig. 6.22(a).

Various packaging options can be selected for the study of specific configurations. For example (see Fig. 6.22(b)) slabs of different thicknesses and of different materials can be placed as SM carrier lid, in order to take their effectiveness into account in the Monte Carlo simulation.

The simulation uses a selection of physics processes out of those available in the GEANT4 Toolkit for each particle type: models of the Low Energy Electromagnetic package for photons and charged particles, and a set of hadronic models covering different ranges from the very high energies typical for LHC down to intra-nuclear transport, pre-equilibrium and nuclear de-excitation. Moreover, various options of alternative physics models are available in the simulation to evaluate possible systematic effects.

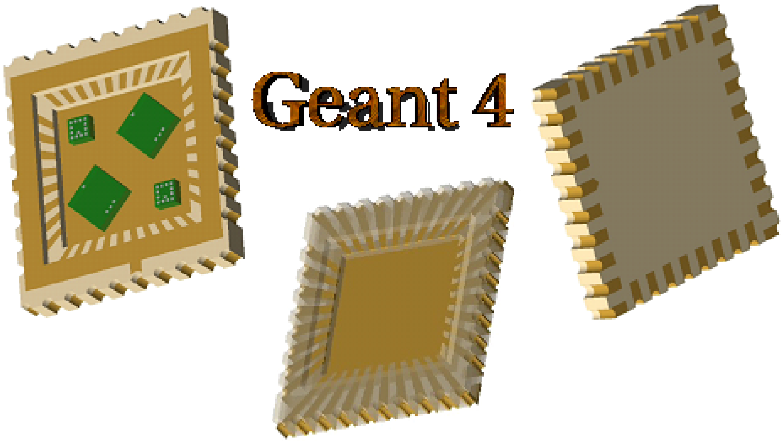

Figure 6.21: 3-dimensional view of the GEANT4 model of the chip carrier hosting the RadFETs.

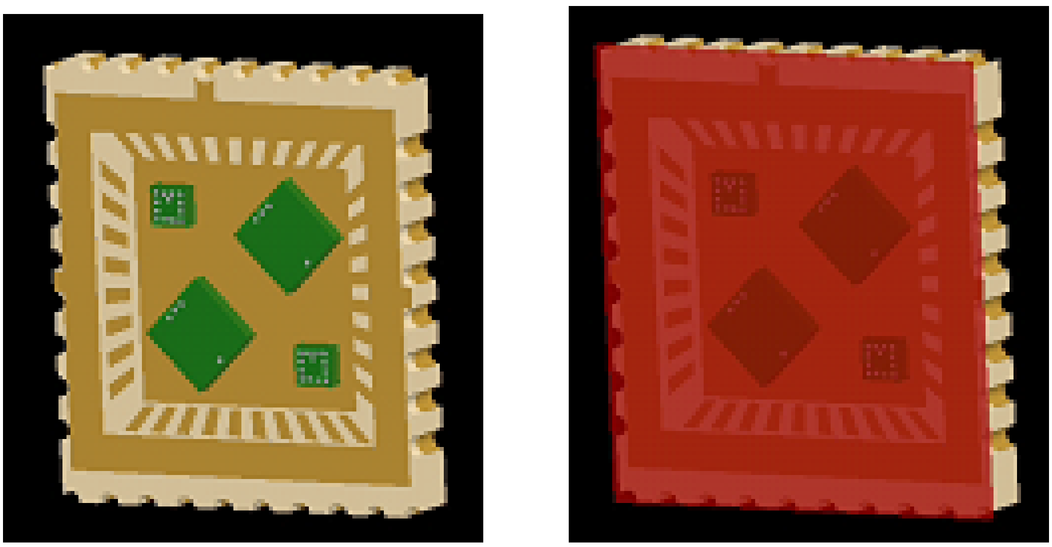

(a) (b)

Figure 6.22: Frontal view of the GEANT4 model of the chip carrier hosting the RadFETs. (a) The SM carrier hosting four semiconductor RadFET dies. (b) packaging configuration covered with a simulated lid.

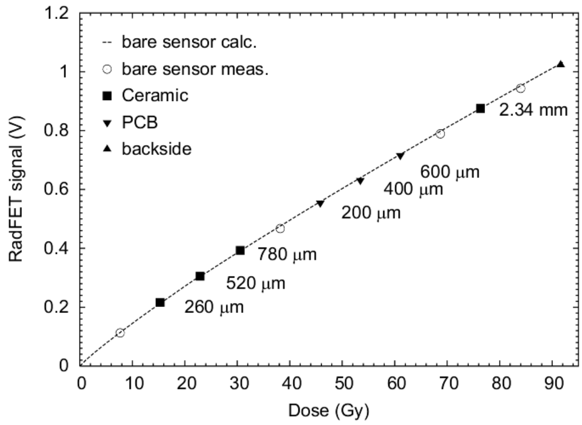

(a)

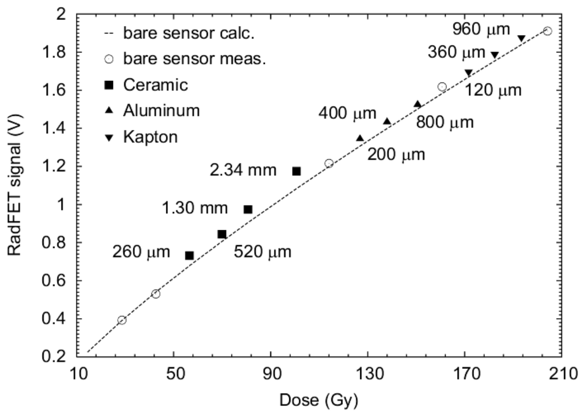

(b)

Figure 6.23: Experimental validation of the GEANT4 Monte Carlo model by means of proton and neutron experimental data. (a) Experimental results obtained at PIF facility (254 MeV protons) (b) Experimental results obtained at the JSI facility with reactor neutron-spectrum.

6.5.3 Packaging experimental validation and comparison with GEANT4 simulations

The two radiation fields selected for the first validation studies were the High Energy Proton Irradiation Facility (HE-PIF) at PSI (see Sec. 4.1.4) and the neutrons from the JSI TRIGA Mark II reactor (see Sec. 4.1.2).

The RadFET sensor carrier were irradiated at PIF with 254 MeV protons at an average flux of about $1{\times}10^8$ $protons/s/cm^2$. The samples were mounted in a frame and exposed perpendicularly to the beam-axis. At JSI, the carrier irradiations were performed placing them into the reactor core through an irradiation tube that occupies a fuel rod position and enters the reactor from above. For the presented experiment the reactor power was set to 250 W. During the exposure in the nuclear reactor, the samples were also exposed to an important gamma-ray component. Although the 1 MeV equivalent neutron flux and the TID were previously calibrated in the channel, additional measurements have been performed in parallel during this irradiation test in order to increase the precision of the comparative dosimetry.

The RadFET model used to carry on the validation experiments was the REM TOT-501C. In the two cases the irradiations were executed step-by-step exposing the samples to increasing particle fluence. After any exposure a readout cycle was started to record the sensor's voltage increases. During the irradiation steps the chip carrier was covered with different thicknesses of various materials, in order to simulate different lid options. The covering materials selected were alumina, Al, FR4 (e.g. Epoxy-glass, the common printed-circuit board material) and Kapton. From time to time the carrier was exposed bare in order to verify the measured signal to be consistent with the theoretical RadFET calibration curve.

Fig. 6.23(a) and Fig. 6.23(b) show the experimental results obtained with 254 MeV protons and in the mixed γ/neutron field of the nuclear reactor respectively. In the case of the 254 MeV protons, the effect of the different materials on the RadFET response

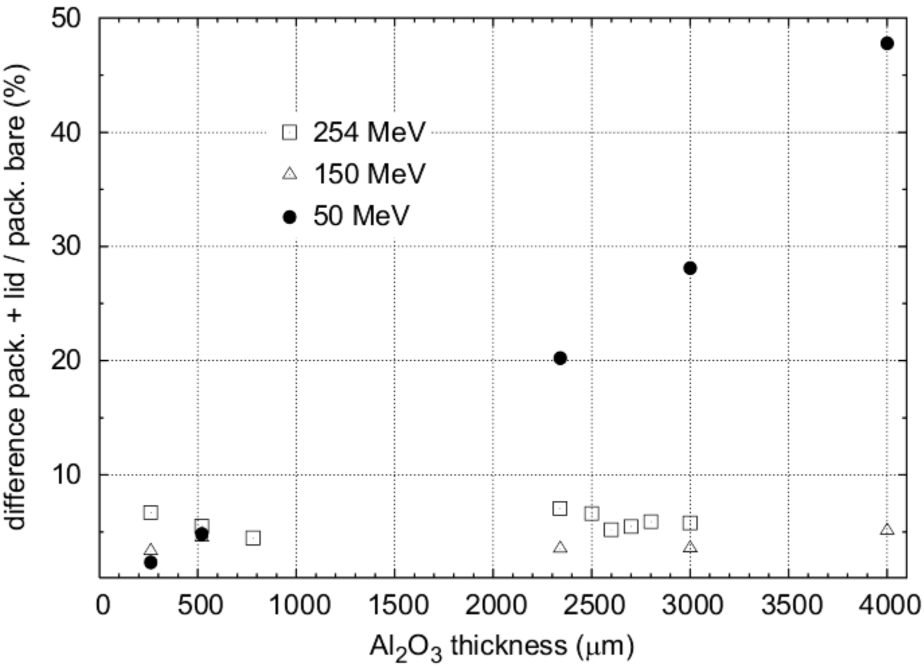

Figure 6.24: Energy deposit in the sensors as a function of the alumina lid thickness, resulting from simulated irradiation with protons at various energies (254, 150 and 50 MeV).

curve was negligible for all material employed of any thickness. The data of Fig. 6.23(a) show in fact that all points lie on the calculated radiation response of the uncovered device within the experimental error of ± 5 % in the measurement of the proton fluence (e.g. proton dose). It has to be noted that even placing the RadFET package with the backside in the direction of the incoming protons (see filled triangular marker of Fig. 6.23(a)) no effects have been detected confirming thus the negligible contribution of the metalization layers deposed on the chip carrier.

Almost the same situation has been found for the neutron data of Fig. 6.23(b). Aluminum and Kapton lids show to be transparent to the reactor field in a range of thicknesses going from 0.1 to about 1 mm. Different is the situation for the ceramic lids. For ceramic slabs exceeding 1 mm thickness, the RadFET response results enhanced of about 8-10 %.

As first step, the simulation model described in Sec. 6.5.2 has been run for pure proton beams of different energies that hit perpendicularly the carrier lid, simulated by increasing thicknesses of different materials. The energy deposited in the sensors, resulting from primary and secondary particle interactions, is calculated by the simulation. Fig. 6.25 details the energy deposed in the target volume (4 silicon dies simulating the RadFET chips) when protons of 254 MeV and 50 MeV are launched toward the chip packaging as function of the ceramic lid thickness. Fig. 6.24 shows a selection of these data obtained with Al_2O_3 lids. The run at 254 MeV confirms the experimental results showing that protons of such an energy can penetrate up to 3 mm of ceramic without to interfere with the dose measured by the devices within the 5 % error. By reducing the energy of the protons from 254 MeV to 150 MeV the same result is obtained. For 50 MeV protons a strong dose enhancement is predicted by the simulation reaching a

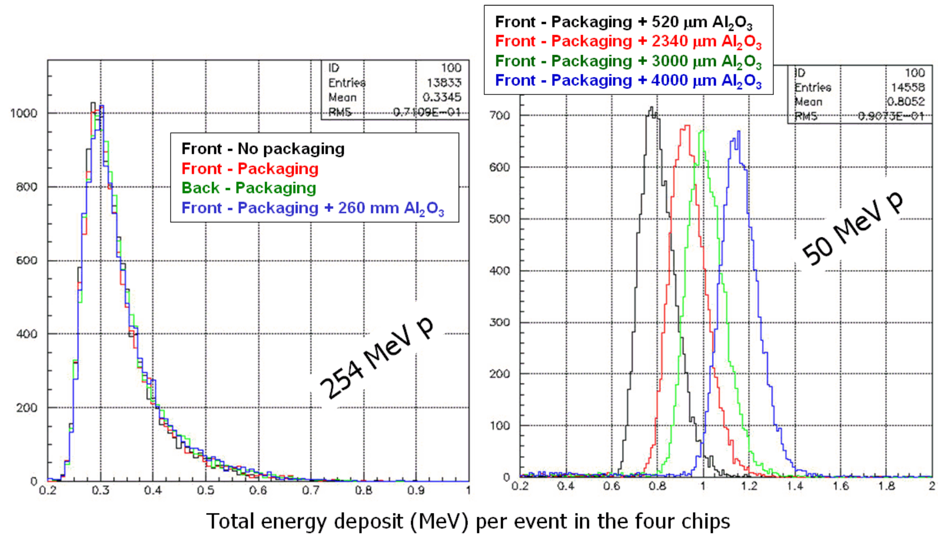

Figure 6.25: Energy spectra obtained with monoenergetic protons (50 MeV and 254 MeV) with different packaging lids configurations.

50 % TID increase for a 4 mm thick ceramic lid.

These results show that, by changing materials, thicknesses and energies, the simulation with protons can be used as predictive tool, even where experimental results are not available, to optimize the lid to be mounted on the sensor carrier installed at the LHC experiments. The simulations for the mixed reactor field are currently ongoing. In this second validation study care is taken in the simulation of the reactor γ-rays background that, together with the secondaries from neutron interaction, is responsible of a big fraction of the TID deposition in the gate-layer of the RadFET devices.

6.6 Conclusion

In the first part of this chapter, the selection of the RadFET dosimeters suitable for the operation in the radiation environment of the LHC experiments has been addressed.

From the selection procedure discussed in this chapter, it can be stated in general that the choice of a thin oxide RadFET ($t_{ox} \sim 0.1$ μm range) allows measurements over several decades of dose up to tens of kGy, but does not offer the sensitivity to measure very small doses (< cGy). Unbiased thin-oxide devices show a built-in gate electric field strong enough to minimize the recombination effects that may be responsible for RadFETs reduced responses in radiation fields with different LET as the ones expected at the LHC experiments. Moreover, by using thin oxide RadFETs, the sensitivity to high-energy neutrons is kept low, while possible RadFET saturation effects due to high neutron fluences are avoided.

The opposite situation can be observed with thick oxide RadFETs ($t_{ox} \sim$ 1-2 μm) that provide much higher sensitivities (mGy). In this case the gate voltage shift per unit dose is much higher, thus limiting the measurable dose range up to tens of Gy. At higher doses, even if it is still possible to measure TID increase, the device responses in a mixed field show to be driven by different degrees of saturation for the different particle types. These devices are therefore suitable for measurements in low-intensity γ-n fields where the contribution of MIPs is negligible as it is the case in the radiation environment expected in the external detector layers of the LHC experiments.

Annealing effects can introduce major errors in the measurements performed by RadFETs over long-term periods (e.g. years). A detailed knowledge of the devices annealing behavior is thus an essential element for the device selection. Because of the impossibility to study annealing effects on the same time-scale as the LHC experiments operation, an accelerated method to characterize the devices annealing behaviors has been used in this work. Isochronal annealing experiments were thus carried out and their results utilized to identify devices with anomalous annealing behaviors.

From the selection procedure it resulted that two RadFET devices are needed to fulfill the radiation monitoring requirement of the LHC experiments. These two devices, with two completely different oxide thicknesses are the LAAS 1600 (t_{ox} = 1.6 μm for the measurement of "low-LET, low intensity" mixed γ-neutron field) and the REM TOT-501C Type K with t_{ox} = 0.25 μm for the measurement in "high-LET, high-intensity" hadron fields.

For the selected devices, the annealing studies have been detailed by comparing the isochronal annealing results with a series of isothermal annealing data recorded over more than one year following the exposure of the devices to the mixed hadron environment of the IRRAD6 facility.

For the LAAS 1600 devices it has been found that their annealing behavior in a harsh radiation field may show a component due to the recover of radiation-induced displacement damages in the n-type silicon bulk of the transistor. This appears when the hadron component of the mixed radiation field exceeds some 10^{12} cm^{-2} and it is most likely due to the employed RadFET's readout procedure: measurement of the transistor ΔV_{gs} under irradiation for a fixed *drain* current. These findings were also confirmed here by the determination of the transistor *drain* characteristic that showed a clear increase of the substrate resistivity after high-level neutron irradiation. However after both low and high TID exposure level in a hadron field, the LAAS devices have shown satisfactory annealing properties that guarantee their stability for the LHC applications.

For the REM TOT-501C, the isochronal annealing prediction results are overestimated by a factor of two with respect to the measured isothermal data over 1-year. The measured isothermal annealing shows a degradation of the dosimetric signal of less than 10 % for TID in the range of kGy. The difference in the two annealing procedures has been manifold and it has been attributed to the contribution of the interface-states that are not accounted in the prediction based on the isochronal annealing procedure. For these RadFET devices the substrate resistivity has been found to be unaltered (within 10 %) after exposure to TID exceeding 30 kGy in pure ionizing environment, but also after hadron irradiation exceeding the Φ_{eq} of 1×10^{13} cm^{-2}.

Dosimetry measurement with RadFET devices rely on the homogeneity of the procured batches of devices. In fact, the response of a few devices is used to determine the radiation response curve (e.g. calibration) and then it is assumed to be equal to the one of all the other devices used in the unknown radiation field. For this reason the control of the pre-irradiation parameters of the devices is of fundamental importance. The LAAS 1600 devices were supplied in homogeneous batches pre-characterized from the manufacturer. For the REM devices, the remnant stock of the wafer TOT-501C were bought from the producer. A testing procedure and a set of selection parameters have therefore been drawn in order to select the REM RadFETs with characteristics which satisfy CERN applications. This selection and testing procedure is reported in Appendix A.

The experiments presented in this chapter show that, in the context of the LHC, the mounting of dosimeter-surrounding materials have a significant influence on their response to neutrons. Analog result were also found in literature in the case of low-energy photons. For the development of a radiation sensor this means that, while preliminary calibrations of single dosimeters in individual hadron beams have been used to select operational dosimeters in LHC, dose calibration of the radiation sensor to high accuracy can only be performed with its final design and using the material environment in the array position of the LHC experiment.

Another approach is to develop a sensor packaging that minimizes the particle interaction with it. This solution was discussed in this chapter where the results of the irradiation experiments were used in the study of a custom-made RadFET packaging.

To study in detail the compatibility of this packaging with the LHC radiation environment, a detailed Monte Carlo Code has been prepared. In this chapter this model has been described, the irradiation experiments devoted to its validation were presented and their results finally discussed.

Chapter 7

Characterization of p-i-n diodes

In Chapter 2 it has been shown that the particle fluences expected over 10-years in the four experiments of the LHC accelerator (mostly hadrons, e.g. n, p, $\pi^{\pm}$, etc.) will cover a broad dynamic range of more than five orders of magnitude from 10^9-10^{10} to 10^{14}-10^{15} particles/cm^2. *Active* semiconductor dosimeter types used for particle fluence measurement are the high-resistivity forward bias *p-i-n* diodes described in Sec. 3.2.2. To cover such a broad dynamic range together with a high sensitivity in a low fluence range, one single device is clearly not enough.

The *p-i-n* diodes show a hadron-dependent increase of the voltage between their terminals when they are supplied with a constant forward current. Even if some of these devices have been extensively characterized for neutron detection, the response of *p-i-n* diode devices in a hadron environment similar to the one expected at the LHC experiments has to be still studied in detail as pre-requisite for their utilization in this type of application.

High-sensitivity *p-i-n* diodes have been developed mainly for medical and military purposes in the field of neutron measurement[1] [Sop91, Pro89, Ros03]. For the purposes of this work, two types of *p-i-n* diodes have been selected and investigated for the LHC needs. The first device is manufactured by the *Center for Medical Radiation Physics* (CMRP) of the University of Wollongong, Australia, the second one are two diodes distributed by the *Czech Metrology Institute* of Praha, Czech Republic. They are known under the commercial name of *Long Base Silicon Diode* (LBSD Si-1 and LBSD Si-2).

As it will be discussed in detail later, the dosimetric response from these high-sensitivity devices can cover a maximum Φ_{eq} range of the order of 10^{12} cm^{-2} before saturation phenomena appear. To extend the measurement range to the level of the LHC (several 10^{14} cm^{-2}) another device is therefore needed. From preliminary studies carried out at CERN in the nineties, a good candidate for such purpose seems to be the commercial *p-i-n* diode model BPW34F [Tav91].

The aim of this chapter is thus to present in detail the characterization of this commercial diode BPW34 and to prove its applicability as fast-hadron dosimeter in the high fluence range of interest for the LHC. Moreover the measurement of the key parameters of the high-sensitivity CMRP and LBSD diodes will be also presented here.

[1] This is the reason why sometimes these devices are identified with the name of "neutron diodes".

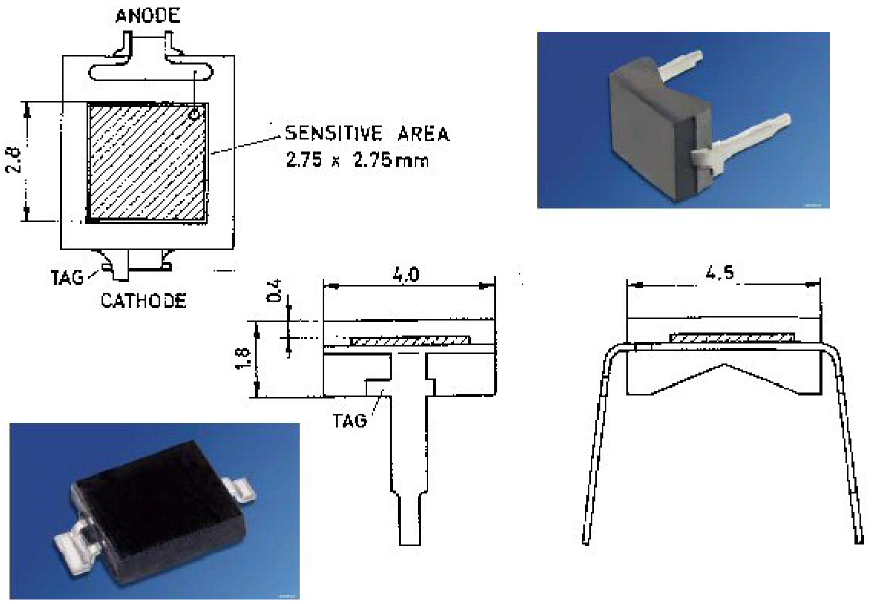

Figure 7.1: The *p-i-n* diodes BPW34F as commercially supplied in DIL (right-hand side top corner) and SMD (left-hand side bottom corner) packages.

7.1 The commercial BPW34F p-i-n diodes

The BPW34 diodes are produced by several semiconductor companies like OSRAM, SIEMENS, TELEFUNKEN, etc. The applications of these diodes are mainly in the field of photo-interrupters and IR remote controls. A list of typical electrical and optical characteristics for this device can be found in Ref. [Bpw]. According to the electronic nomenclature, the part number "BPW34" means the following: B is the material used for the active region of the device (B = silicon), P indicates the circuit function (P = radiation sensitive diode) and W34 is the serial number [Tel97]. The fact that these devices are commercially available in large numbers at a relatively low cost (1-2 €), makes the possibility of using them as neutron dosimeter an attractive prospect.

This diode consists of a small 3x3 mm^2 silicon die (the active part of the component) encased in a plastic packaging which allows an easy handling as shown in Fig. 7.1. This component is available in three different packagings labeled as following:

- BPW34: transparent plastic DIL packaging that allows the device to be sensitive to light from 400 nm to 1100 nm;
- BPW34F: plastic packaging DIL with a daylight filter that limits the light sensitivity of the device to about 950 nm to 1100 nm (see right-hand side of Fig. 7.1);
- BPW34FS: like the previous one but in SMD plastic packaging (see left-hand side of Fig. 7.1).

Because of their lower sensitivity to light and their dimensions that allows an easy-handling, unless indicated, all the samples used for his study were packaged diodes of the type BPW34F.

7.1.1 Conclusions from previous studies

The study of the BPW34F diode (produced by SIEMENS) as neutron sensor was addressed at CERN since 1992. The results of irradiation tests in the neutron field of the PSAIF facility at CERN [Tav91] were summarized in a CERN Report from Malfante [Mal92] and were the following:

- the devices are presented having a base thickness W = 210 μm and a resistivity ρ = 2.5 kΩ·cm;
- the diodes were measured in condition of intermediate injection (1 mA) applying a constant forward current after the radiation exposure;
- the response of the diodes to neutrons were sometimes far from the linearity;
- the measured sensitivity to neutrons (E > 140 keV) were of about 35-50 mV/10^{12} cm^{-2}. The lower particle fluences measured in the Malfante study lied around some 10^{12} cm^{-2} not giving any clear information about the diodes behavior at lower neutron fluences;
- irradiation with γ-rays were performed on these diodes and their response was found to be very low compared to their neutron sensitivity. For 100 kGy of ionizing dose, a V_F shift of about 100 mV was measured. This corresponds to a neutron sensitivity of about 2x10^{12} cm^{-2}.
- Following a neutron irradiation of $\Phi_{(>140keV)}$ = 2.5x10^{13} cm^{-2} a room temperature annealing of V_F of about 0.5 % was measured after 21 days.

7.1.2 Response of BPW34F to neutron and proton irradiation

From 2002, several irradiation campaigns were carried out exposing the BPW34F diodes to the direct 24 GeV/c proton beam of the IRRAD1 facility and to the neutron environment of the IRRAD2 facility at CERN.

A selection of these preliminary results has been summarized in Fig. 7.2 [Rav04b], where the measurements performed during radiation exposure (on-line) have been plotted as function of Φ_{eq} for the two facilities. To allow a comparison of the IRRAD1 data with the results obtained in the IRRAD2 facility, proton fluences were converted into Φ_{eq} by means of the hardness factor κ = 0.62 [Mol02].

The on-line proton data were obtained from different irradiation tests performed with various fluxes ranging from 1.1x10^8 to 1.1x10^{10} protons/(cm^2 $\times$ s) and the ones with neutrons were obtained at an equivalent flux of 8.3x10^7 neutrons/(cm^2 $\times$ s). All plotted data have been measured at an intermediate injection level (1 mA) with a forward current pulse ranging from 100 ms to 700 ms duration. In this condition no significant differences regarding the response of the devices to the two different particles were observed. Both data set follow the same trend represented by the dotted line in Fig. 7.2 within an error of $\pm$ 20 %.

More in detail, after an initial flat region up to Φ_{eq} $\sim$ 2x10^{12} cm^{-2}, in which the devices are not sensitive to fast hadrons, the response is linear and in agreement with the

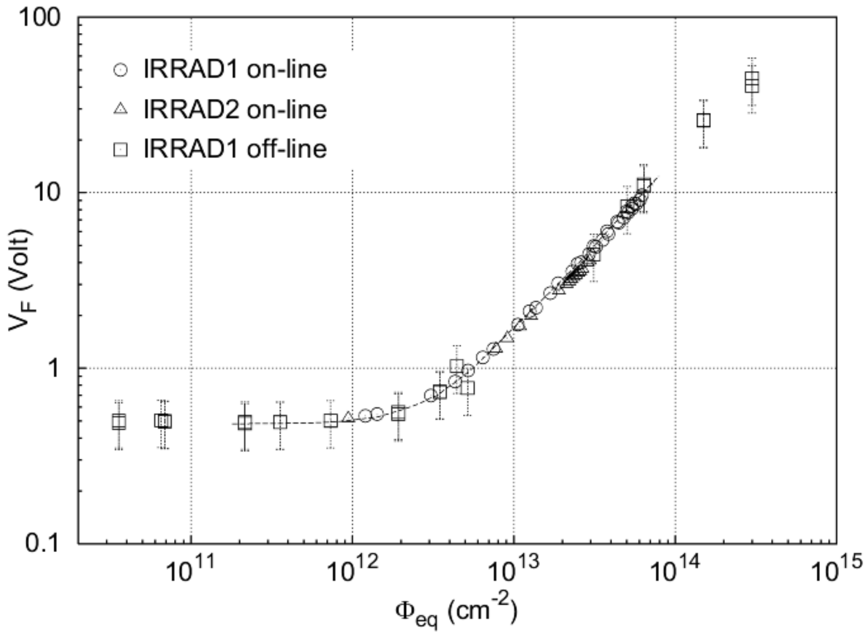

Figure 7.2: BPW34F on-line vs. off-line measurements at the IRRAD1 and IRRAD2 facilities at CERN.

displacement damage scaling in silicon (NIEL hypothesis see Sec. 2.3.3) up to several 10^{14} cm^{-2} proving that this device is suitable to measure high particle fluences. A forward voltage shift ΔV_F of 1.1 V was measured for a neutron equivalent fluence of 1x10^{13} cm^{-2}. Taken into account the difference in the readout methods and in the particle spectra, this particle sensitivity is in agreement with the early values measured by Malfante [Mal92].

In Fig. 7.2, the on-line measurements are also compared with a series of data taken immediately after irradiation (off-line) without performing any annealing procedure before their readout [Hel03]. While the on-line data represent the V_F increase from the same device, the off-line measurements come from different samples, each of them exposed to a different particle fluence. For the off-line data presented in Fig. 7.2 the initial distribution V_F was unknown. Nevertheless, the agreement of the un-annealed data lies around ± 30%.

In parallel with the tests presented in Fig. 7.2, a series of room temperature annealing measurements were performed. They showed, following protons irradiation of 1.2x10^{14} cm^{-2} a decrease in V_F of more than 20 % after 300 hours. This first result thus revealed that for this device, long-term annealing phenomena can be an issue for the precision achievable in the particle fluence measurements.

One of the proton response curves presented in Fig. 7.2 has been zoomed in the low fluence range and shown in Fig. 7.3 in linear scale. The analysis of the behavior of this curve confirms what was theoretically predicted by *Swartz and Thurston* [Swa66] for a low-resistivity, small W/L ratio, *p-i-n* diode operating at intermediate injection level as described in Sec. 3.2.2.

The forward voltage across the diode starts to decrease under irradiation due to the

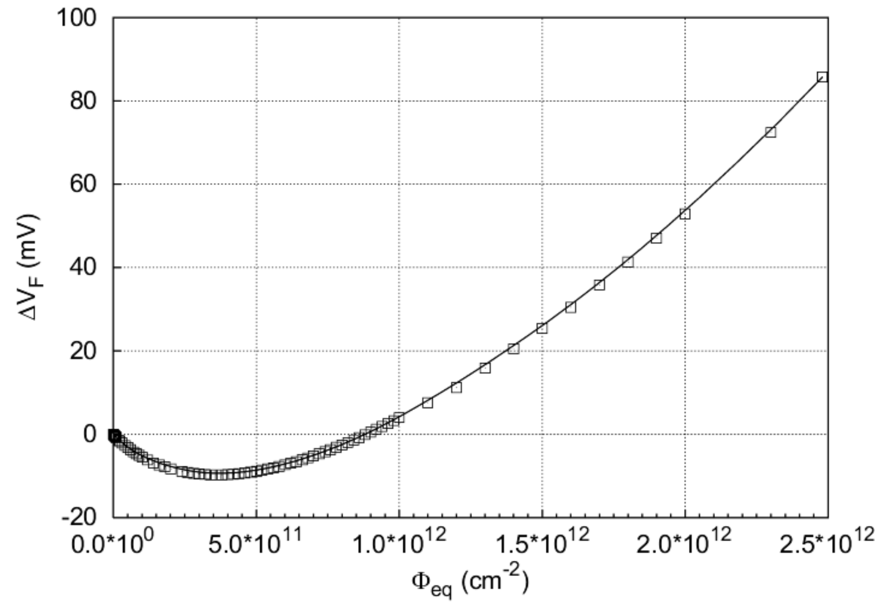

Figure 7.3: BPW34F radiation response behavior at low Φ_{eq}

predominant decreases of V_{Fj} caused by the decrease of the minority carrier lifetime. Increasing the irradiation level, the voltage sensitivity to particles becomes positive due to the diffusion length (L) decreases (e.g. V_{Fj} increases) and the base resistance V_{Fb} that starts also to increase with increasing Φ_{eq}.

The devices to be tested at CERN were procured from different sensor batches produced by various manufacturers in different production sites and in different time periods. Before starting a systematic study of the BPW34 sensor, a batch of 155 diodes has been procured and measured [Hel03, Tem04] with the aim to insure the homogeneity of the devices under study. The diodes measured in the following of this chapter, with C-V and I-V techniques in both forward and reverse bias mode, were therefore selected from this batch [Mol99a].

Tab. 7.1 summarizes the measured diode used to build the homogeneous sensor batch. As figure of merit, the initial voltage under 1 mA constant current injection has been measured. The temperature recorded during the measurement was 23.5 ± 1.7 °C. From this preliminary screening it was possible to identify that the oldest series of devices produced by SIEMENS presented an initial voltage $V_{F,0}$ lower of about 15% with respect to the OSRAM ones. Independently on the packaging type, the other diodes, resulted to be homogeneous within ± 11% with an average $V_{F,0}$ of 0.531 V. Thus, after rejecting the SIEMENS components, all the other devices were accepted to be used in the following investigations.

7.1.2.1 Reverse bias measurements

After several steps of proton irradiation in the IRRAD1 facility, the determination of the diode leakage current has been done by means of I-V and C-V measurements. The radiation-induced increase of the leakage current ΔI is given by the difference between

Company	Package type	Production site	Year of procurement	Number of pieces	Average $V_{F,0}$ at 1 mA (V)
OSRAM	BPW34F	USA	2004	75	0.527±0.011
OSRAM	BPW34F	Malaysia	2003-2004	50	0.525±0.010
OSRAM	BPW34FS	Malaysia	2004	10	0.564±0.055
OSRAM	BPW34F	Malaysia	2004	10	0.533±0.004
SIEMENS	BPW34F	-	1993	10	0.492±0.002

Table 7.1: BPW34 diodes for the studies carried out at CERN.

the current measured after and before irradiation [Mol99a]. In Fig. 7.4(a) the leakage current increase of the BPW34F diodes has been plotted vs. Φ_{eq} after being normalized to 20°C. In the picture, each point corresponds to an individual diode irradiated with protons in a single exposure to a given fluence. Moreover, before measurement the samples were brought to the same annealing state by heating them for 4 minutes to 80°C [Mol99a].

From Fig. 7.4(a) it is possible to see that the leakage current increase is proportional to Φ_{eq} in the range from 10^{10} cm^{-2} to 10^{13} cm^{-2} and after 10^{14} cm^{-2}. In the intermediate region the measured ΔI was much higher with respect the foreseen linear behavior. A similar result has also been found in a second series of diodes irradiated with neutrons at the IRRAD2 Facility [Hel03]. For $\Phi_{eq} < 10^{13}$ cm^{-2} the diodes can thus be used as NIEL counter in the same way of the particle detector diodes presented in Sec. 3.1.9. The data of Fig. 7.4(a) were finally linearly fitted (continuous line in the picture) and the proportionality factor $\Delta I/\Phi_{eq}$ was calculated to be 5.17x10^{-20} A·cm^2.

The above data can be conveniently used to estimate the base thickness (W) of the BPW34F devices. In the proton beam, independent particle flux measurements were carried out in parallel by using a series of calibrated particle detector diodes (see Sec. 3.1.9). As the volume of these reference devices is well known, from these independent measurements done in comparable experimental conditions, it was possible to determine a *current related damage rate* α = 2.27x10^{-17} A/cm. By comparing α with the factor calculated before for the BPW34F diodes, it is then possible to estimate the BPW34F diodes volume (2.28x10^{-3} cm^3). Therefore, knowing from Ref. [Bpw] that the BPW34F surface is 0.0702 cm^2, it is finally possible to calculate a thickness W about 324 μm. This value results to be in agreement with the one reported in Ref. [Mal92].

Once the value of W is determined for the BPW34 diodes, it is still possible to estimate the material resistivity by using the depletion voltage determined from the C-V curve of a non-irradiated BPW34F diode as the one presented in Fig. 7.4(b) [Mol99a]. As a first approximation, in condition of full depletion it is valid that:

$$V_{dep} = \frac{q}{2\epsilon\epsilon_0} N_{eff} W \tag{7.1}$$

where ϵ_0 = 8.85x10^{-14} F/cm, ϵ = 11.9 for silicon and q, the elementary charge, is equal to 1.602x10^{-19} C. Measuring a V_{dep} = 110 V and assuming W = 300 μm, it is possible to calculate an *effective doping concentration* of the silicon material (n-type) N_{eff} =

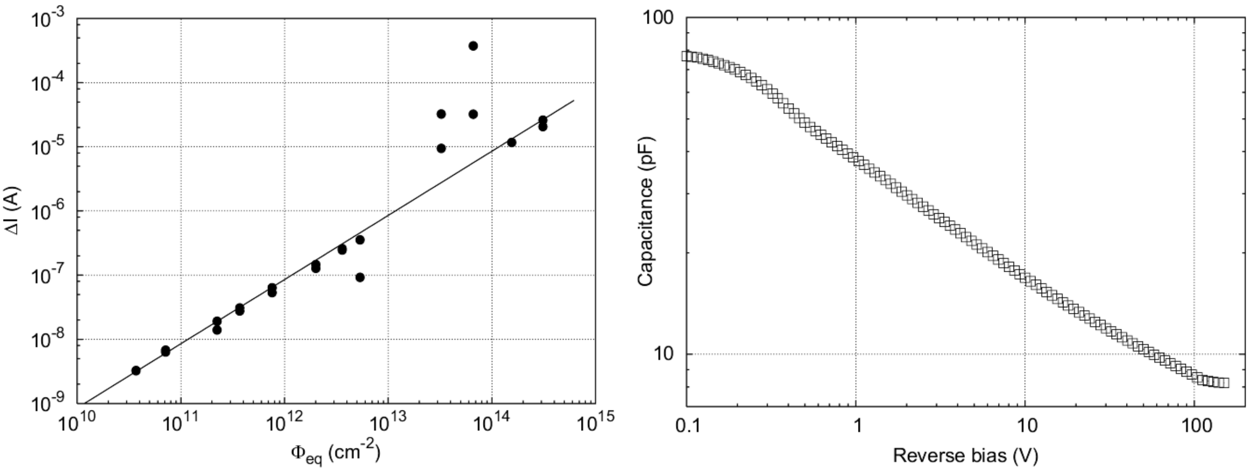

(a) (b)

Figure 7.4: BPW34F characteristics in reverse bias normalized to 20°C. (a) Leakage current measurement and increasing irradiation levels with 23 GeV protons. (b) Capacitance measurement of an unirradiated diode.

1.607×10^{12} cm^{-3}. Now, knowing the electron mobility in n-type silicon (μ_n = 1450 cm$^2V^{-1}s^{-1}$) it is finally possible to evaluate the material resistivity:

$$\rho = \frac{1}{q\mu_n N_{eff}} \simeq 2.7\ k\Omega \cdot cm \tag{7.2}$$

This value, again in good agreement with the one reported in Ref. [Mal92], became a further confirmation of what has been stated in Sec. 7.1.2 during the analysis of the radiation response behavior of the BPW34 diodes observed in Fig. 7.3.

7.1.2.2 Forward bias measurements

The characterization of the BPW34F diodes in forward bias has been done by measuring the whole forward I-V curves for samples irradiated to different Φ_{eq} levels with 23 GeV protons and in the neutron field of IRRAD2 at CERN. A total of 24 diodes were exposed to protons and other 20 to neutrons. For a given fluence step, two devices were exposed in order to get redundancy in the results. The measurements were carried out after irradiation using a test-bench based on a stand-alone *Keithley 2400* by injecting increasing 100 ms-wide currents pulses and recording the following forward voltages across the diode terminals. All the experiments were carried out in a light-tight box.

Fig. 7.5 and Fig. 7.6 display the results of the measurements following proton irradiation in both linear and logarithmic scale respectively. Each curve corresponds to the average of the two I-V curves measured for the two devices exposed to the same fluence. For $\Phi_{eq} < 1\text{x}10^{13}\ cm^{-2}$ the I-V curve of the diode shift in the positive direction with increasing particle fluence. At higher fluences the curve start to bend back toward smaller V_F when forward currents in the order of 100 mA are reached. From that point the BPW34F I-V assume a "thyristor-like" behavior. Altought a rigorous explanation for this phenomena has not been found, it has been reported in literature [Hol02] that

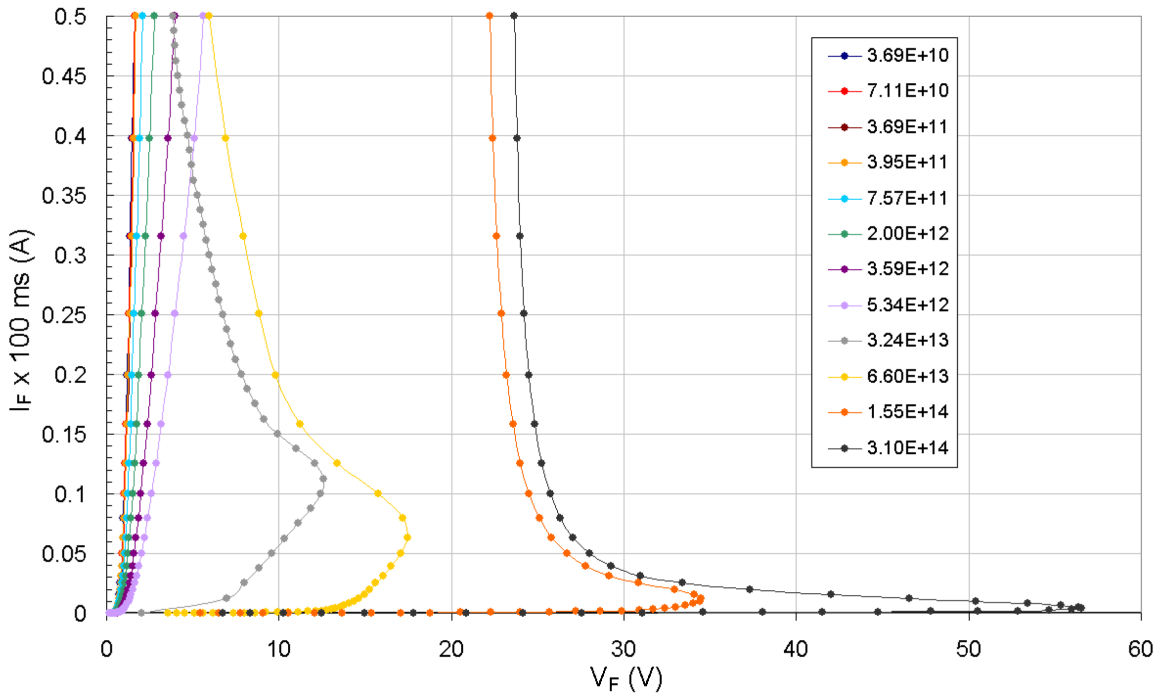

Figure 7.5: Forward I-V curves after 23 GeV proton irradiations (linear scale). In the y-axis the current (A) upon 100 ms forward voltage bias is plotted. Each curve corresponds to a different Φ_{eq} as indicated in the legend.

radiation induced changes in silicon conductivity can lead to the formation of *p-n-p-n* thyristor structures in devices powered in forward bias as in the case of the devices under studies.

The set of devices irradiated with neutrons in IRRAD2 confirm the above behavior and the change in the shape of the I-V curve for Φ_{eq} exceeding 1x10^{13} cm^{-2}. Thanks to these observation it is possible to define in 25 mA the upper limit for the injected forward current with which the BPW34F diode can be used in dosimetric applications.

For the proton irradiated samples, a second I-V curve was measured after 4 minutes of annealing at 80°C. At low and high Φ_{eq} ranges, the effect of the annealing treatment is very low on the measured data as shown in Fig. 7.7(a). Variations in the ΔV$_F$ on the order of 2% to 11% have been measured for samples irradiated to 3.6x10^{12} cm^{-2} and 3.1x10^{14} cm^{-2} respectively.

In the Φ_{eq} range of 10^{13} cm^{-2} the heating of the samples is instead very effective inducing a recover of the I-V curve of more than 50% as shown in Fig. 7.7(b).

The above finding suggests to avoid, particularly in the fluence range 10^{13} cm^{-2}, to heat the diode as this would enhance annealing phenomena. This finding definitively confirms I$_F$ = 25 mA as the upper limit for the currents that can be used in the diode's readout.

Taking into account all the above measured curves, the values of V$_F$ for three selected currents have been extracted and plotted as function of Φ_{eq} in order to determine the variation of the hadron sensitivity at different forward currents. The three selected

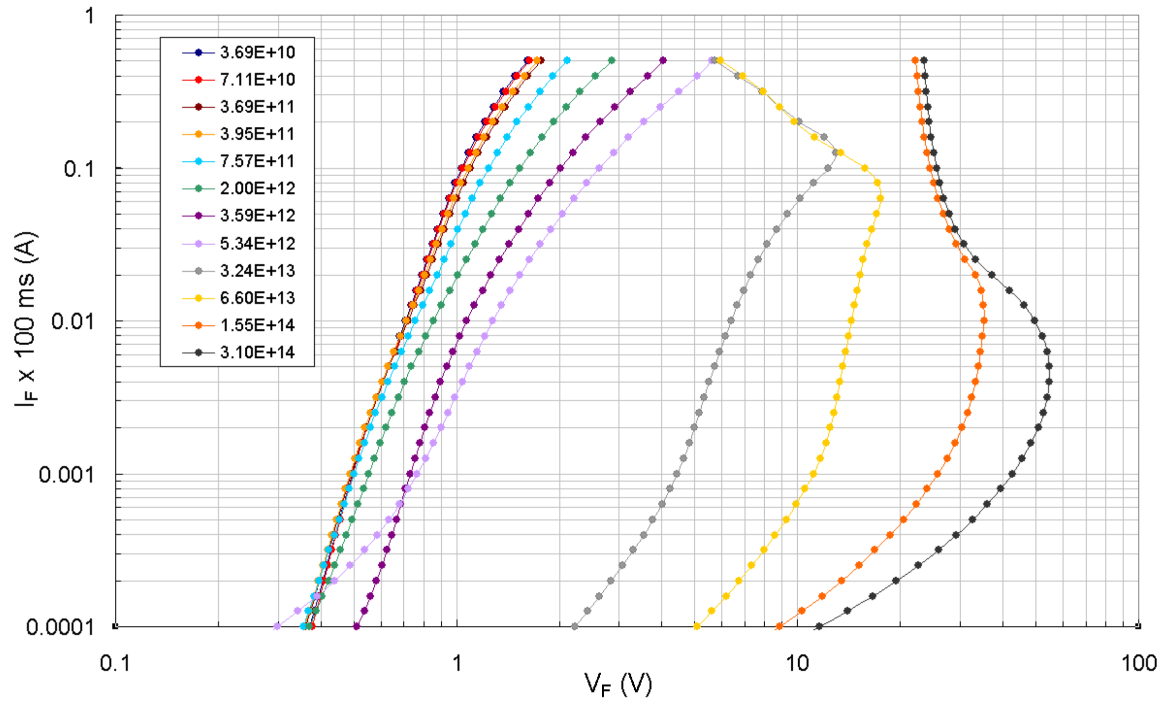

Figure 7.6: Forward I-V curves after 23 GeV proton irradiations (logarithmic scale). In the y-axis the current (A) upon 100 ms forward voltage bias is plotted. Each curve corresponds to a different Φ_{eq} as indicated in the legend.

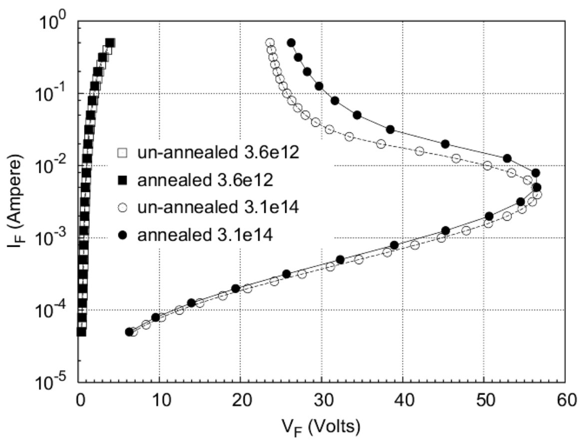

(a) $\Phi_{eq} < 10^{13}$ and $> 10^{14}\mathrm{cm}^{-2}$

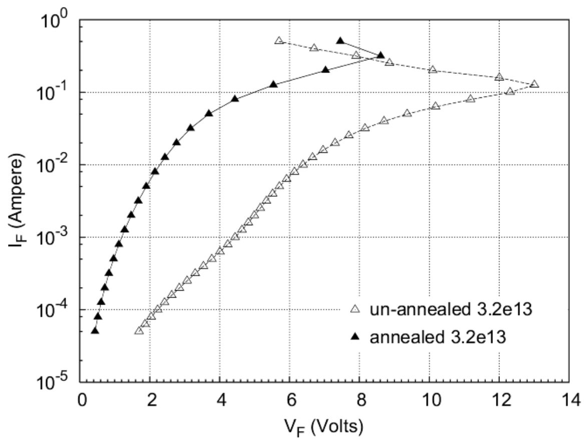

(b) Φ_{eq}in the decade of $10^{13}\mathrm{cm}^{-2}$

Figure 7.7: I-V curves for proton-irradiated BPW34F before and after annealing 4 min. at 80°C.

currents where 1 mA (usual readout current), 25 mA (maximum level allowed from the observation of the I-V behavior) and 10 mA. This last value has been intentionally selected in between the two fixed lower and upper limits according to the electronic standards for commercial current sources.

Following the theoretical indications of Sec. 3.2.2 the radiation response of forward

Forward current (mA)	$\Delta V/\Delta\Phi_{eq}$ Experimental (mV/cm^{-2})	$\Delta V/\Delta\Phi_{eq}$ ratio to 1 mA	Dynamic range Φ_{eq}(cm^{-2})
1 mA	1.09x10^{-10}	1	$\geq$ 4x10^{14}
10 mA	1.54x10^{-11}	0.14	< 2x10^{14}
25 mA	3.96x10^{-11}	0.36	< 1x10^{14}

Table 7.2: BPW34F sensitivities and dynamic ranges at different injection levels.

biased *p-i-n* diodes to particle irradiation is expected to be improved at higher injection levels. For this reason, forward currents lower than 1 mA have not been considered in this study.

Fig. 7.8 shows the BPW34F forward voltage shifts for the injected currents of 1, 10 and 25 mA respectively. In these plots both data from proton and neutron irradiation have been used. The plotted points have been extracted from the complete I-V curve of Fig.7.5 where the different diodes have been measured "off-line" after irradiation.

For $\Phi_{eq} < 2\text{x}10^{12}\ cm^{-2}$, independently on the forward current used, the devices did not show sensitivity to fast hadrons. For $\Phi_{eq} > 2\text{x}10^{12}\ cm^{-2}$, the linear part of the characteristics has been fitted and the sensitivity (ΔV/$\Delta\Phi_{eq}$) increase at 10 and 25 mA have been measured with respect to the one determined at 1 mA. The results of this calculation are reported in Tab. 7.2.

At the higher current the gain in sensitivity is 36%. However, under this high injection conditions, the dynamic range is reduced by about a factor 4. Although the readout current can be chosen by the user to select the device sensitivity, from the presented results it appears that 1 mA remains the readout condition that insure the best compromise between the achieved sensitivity and the measurable hadron fluence range.

7.1.2.3 Analysis of the forward current pulse

The study of the temporal behavior of the signal of irradiated BPW34F diodes has been carried out on three samples irradiated at increasing equivalent particle fluences ranging from $9\times10^{12}\ cm^{-2}$ to $1\times10^{14}\ cm^{-2}$. The samples have been measured after irradiation recording, on a ms time-scale, the values of the forward voltage during the injection of a 3 seconds square current pulse. This has been realized by means of a laboratory test-bench based on a *Keithley 2400* Source-Meter.

Fig. 7.9 and Fig. 7.10 show the evolution of the forward voltage variation (e.g. the increase of the V_F with respect the first recorded values at $t=0$) upon forward current injections of 1 mA and 25 mA respectively. The measurements have been performed directly after irradiation (empty markers) as well as after a brief annealing period of 4 minutes at 80 °C (filled markers). The continuous lines present on the plots are the best fit made on the data series while the voltage value given into brackets are the V_F recorded at $t=0$.

All the curves recorded immediately after irradiation present a logarithmic behavior with the time. This differs from what explained in Sec. 3.2.2.6 where the evidence of the conductivity modulation process was expected. The behavior recorded for the BPW34F

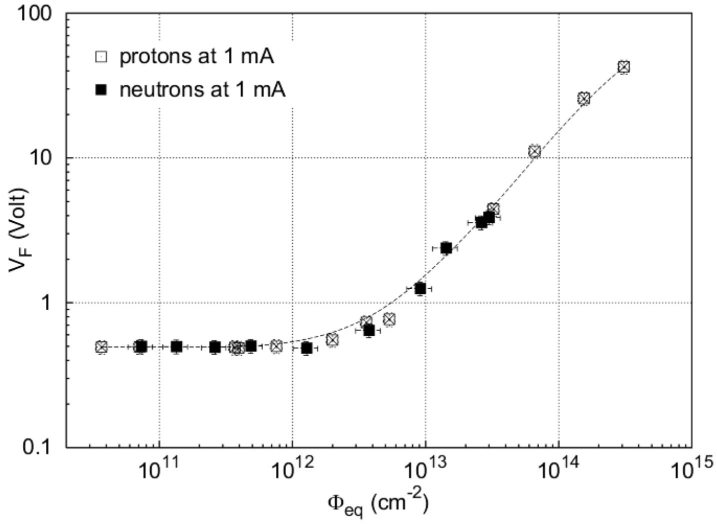

(a) I_F = 1 mA

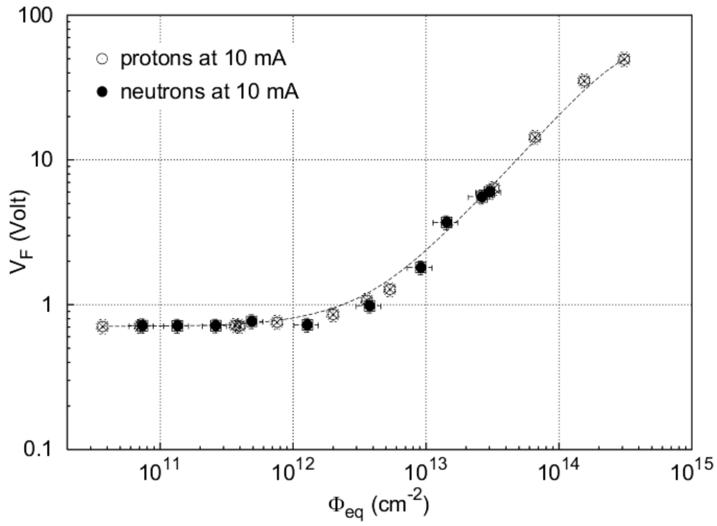

(b) I_F = 10 mA

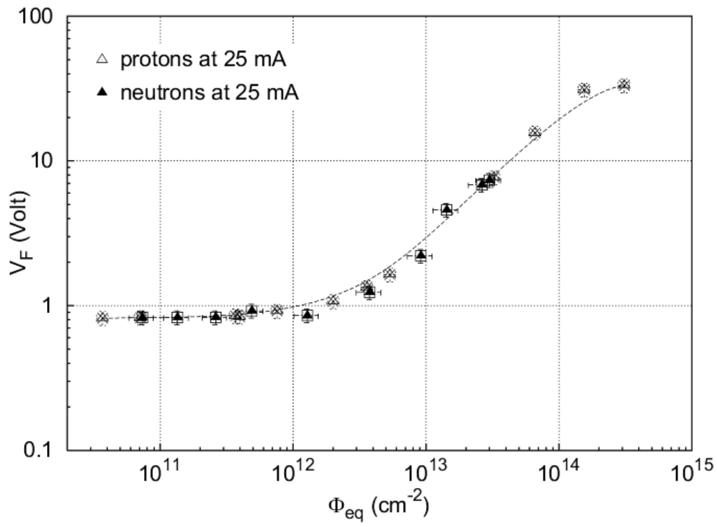

(c) I_F = 25 mA

Figure 7.8: Hadron sensitivity of BPW34F devices at different injection levels.

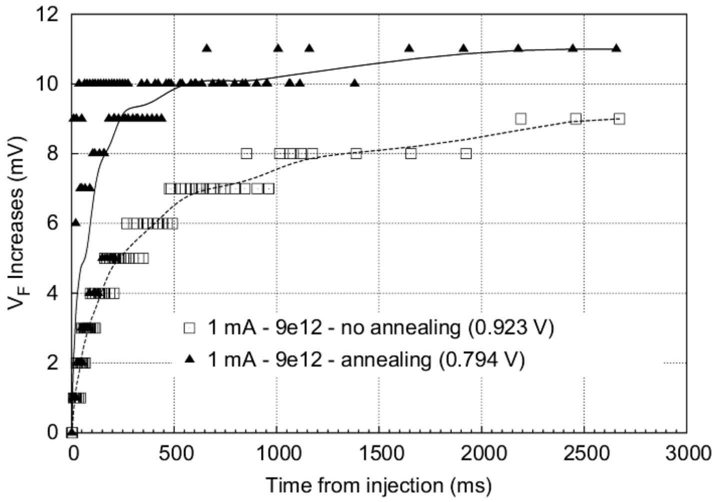

(a) $\Phi_{eq} = 9{\times}10^{12}cm^{-2}$

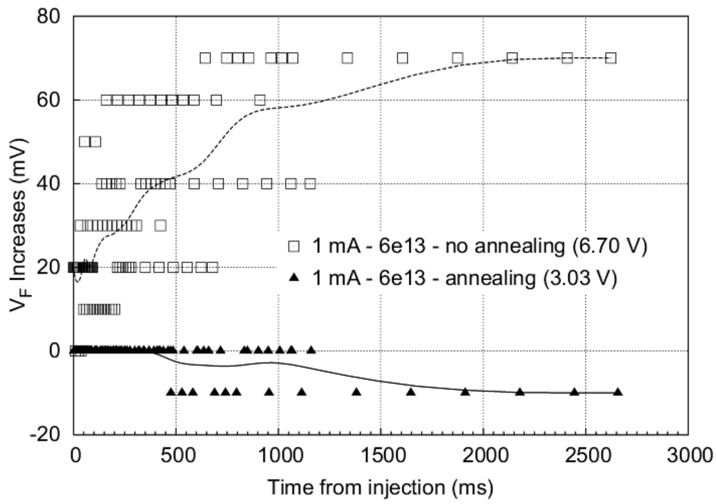

(b) $\Phi_{eq} = 6{\times}10^{13}cm^{-2}$

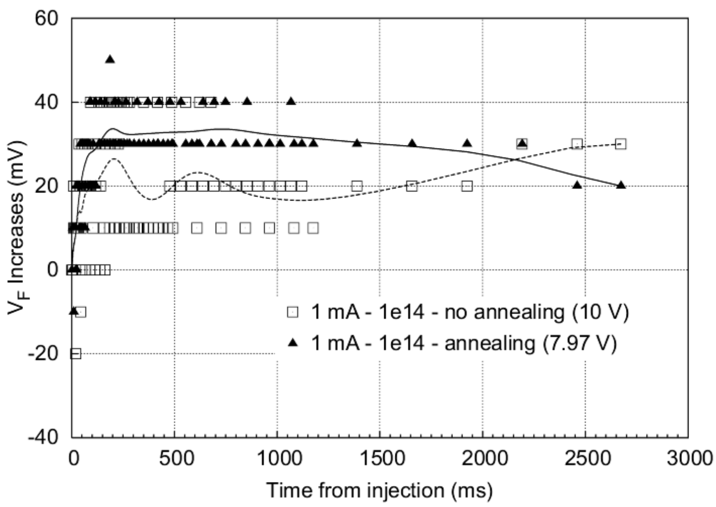

(c) $\Phi_{eq} = 1{\times}10^{14}cm^{-2}$

Figure 7.9: Signal from irradiated BPW34F diodes at different times after injection. Forward current of 1 mA.

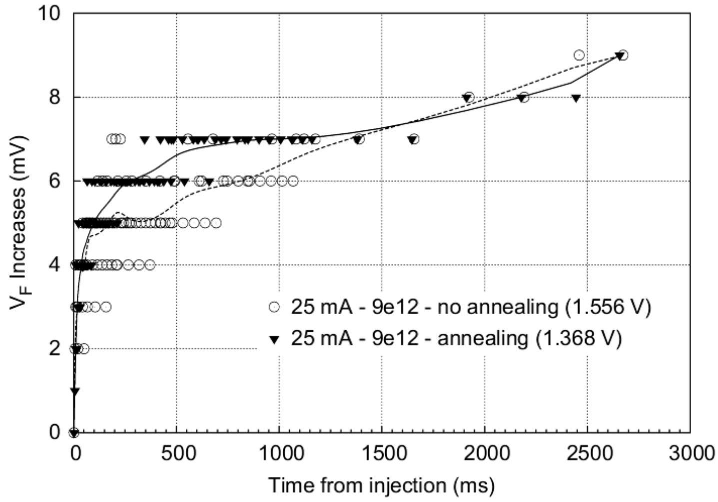

(a) $\Phi_{eq} = 9{\times}10^{12}cm^{-2}$

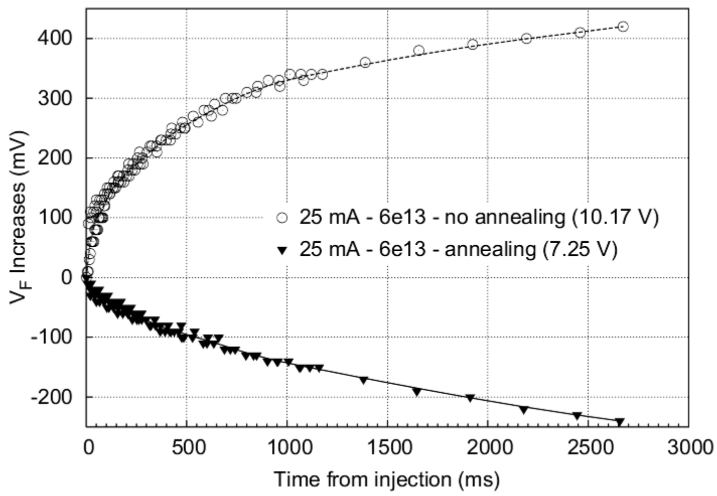

(b) $\Phi_{eq} = 6{\times}10^{13}cm^{-2}$

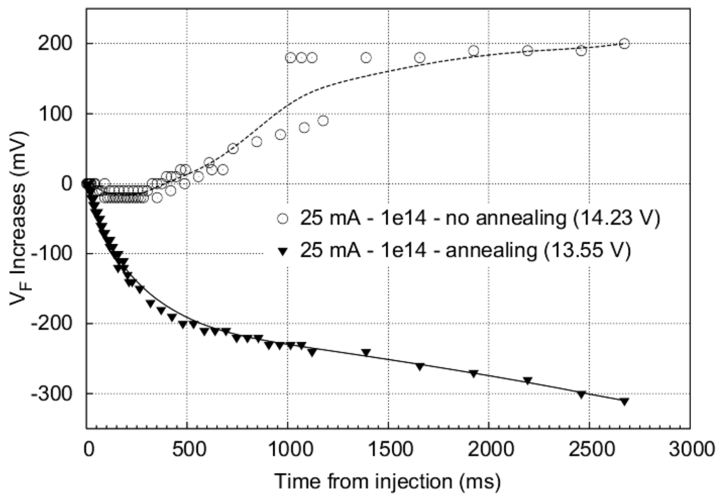

(c) $\Phi_{eq} = 1{\times}10^{14}cm^{-2}$

Figure 7.10: Signal from irradiated BPW34F diodes at different times after injection. Forward current of 25 mA.

remind instead, in shape and characteristic time, the *read-time* instability that affects RadFETs dosimeters (see Sec. 3.2.1.4). In such a case, the "border states" lying in the insulator layer of the device, produce potential variations that modify the temporal behavior of the sensor's voltage.

Although the exact layout of the BPW34F it is not known, silicon dioxide can be present on the diode structure as passivation or isolation layer. The origin of this effect remains unknown, however if isolation layers are present on the devices, charge trapping phenomena can take place and may effectively produce this logarithmic increase of V_F over time.

From the practical point of view, before the annealing, the logarithmic growth of the forward voltage reaches the saturation about 1 second after the current pulse injection in all presented cases of Fig. 7.9 and Fig. 7.10 for both investigated currents. If the time before current injection it is not taken into account, the growth of V_F has been evaluated to affect the measured values by about 0.5 %.

Repeating the experiment after annealing, in some cases the logarithmic growth of the signal is replaced by a monotonic decrease in the diode's voltage over time, as plotted with filled markers in Fig. 7.9(b) relative to the device exposed to a fluence of $6{\times}10^{13}$ cm^{-2}. The signal starts to constantly decrease about one second after the current injection. The fact that this phenomenon is enhanced at higher forward currents (see Fig. 7.10(b) and Fig. 7.10(c)) lead to think that the device starts to heat-up and the radiation-induced defects start to anneal. To avoid this inconvenience it is thus suggested to keep the width of the current pulses for the readout lower than 1 second.

The readout of these devices can thus be performed with current pulses that don't have to exceed one second. As lower limit the current pulse has to be chosen according to the characteristics of the transmission line from the diode to the source that provides the readout pulse in order to adapt the impedance of the transmission line. The results presented in the following sections were thus obtained by using current pulses ranging from 50 ms to 700 ms.

7.1.3 Calibration Curves for BPW34F devices

Taken into account the restrictions in the readout parameters determined in the previous section, the current pulse adopted for the study of the BPW34F particle sensitivity was set to 1 mA $\times$ 700 ms. The forward voltage growth curves have been therefore determined during irradiations carried out in different particle beams. The data presented in this section for the BPW34F diodes were recorded by means of the system described in Sec. 4.2.1.

Fig. 7.11 shows the increase of the forward voltage versus the Φ_{eq} recorded during five different proton irradiation runs and in the neutron environment of the IRRAD2 facility at CERN described in Sec. 5.2. In the same plot the sensitivity to γ-rays has also been reported with cross markers. For the gamma irradiation, four diodes were exposed to increasing doses from the ^{60}Co source of the PAGURE facility (see Sec. 4.1.5). The four samples were thus exposed to TID of 0.1, 2, 10 and 22.6 kGy respectively as indicated in the upper x-axis of Fig. 7.11. The conversion between γ dose and photon fluence has been done with the KERMA factor for 1.3 MeV photons in Silicon equal to 4.45 pGy·cm^2. For the photon data, the x-axis therefore corresponds to the number of γ-

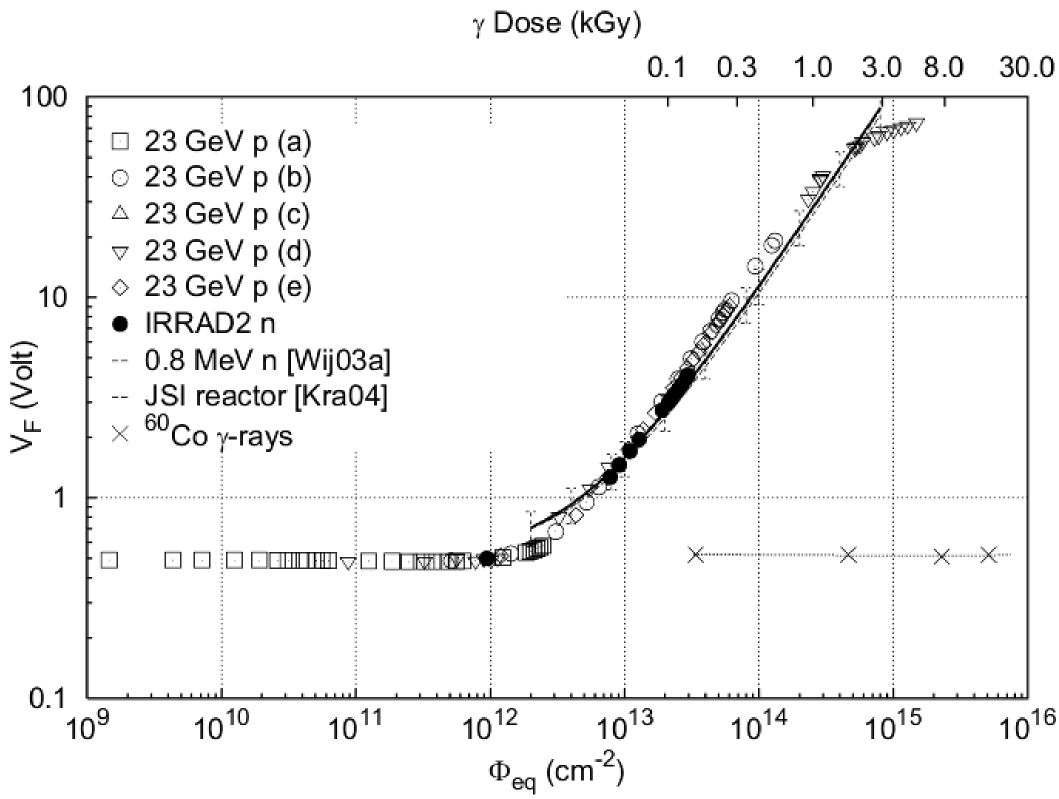

Figure 7.11: Radiation response of BPW34F diodes. The diode's forward voltage at 1 mA is plotted versus the Φ_{eq}. The width of the readout current pulse was of 700 ms. The experimental data taken in the 23 GeV beam of the IRRAD1 facility at CERN has been recorded at different proton rates: (a) $2.4\times10^{11} cm^{-2}\cdot h^{-1}$, (b) $3.7\times10^{12} cm^{-2}\cdot h^{-1}$, (c) $8.1\times10^{12} cm^{-2}\cdot h^{-1}$, (d) $2.0\times10^{13} cm^{-2}\cdot h^{-1}$, (e) $2.5\times10^{13} cm^{-2}\cdot h^{-1}$. In the upper x-axis the TID employed during the exposure to γ-rays have been also reported. The conversion between γ dose and photon fluence has been done with the KERMA factor for 1.3 MeV photons in Silicon equal to 4.45 pGy·cm^2.

photons/cm^2. Finally, in this calibration plot, the results of two independent irradiations carried out with 0.8 MeV neutrons [Wij03a] and in the broad neutron spectrum of the TRIGA reactor at JSI [Kra04] (see Sec. 4.1.2) have also been included.

By fitting the different data set, it is then possible to determine the calibration factor c of the linear relationship that links the growth of the forward voltage (ΔV_F) with the Φ_{eq}, so that:

$$\Delta V_F = c \cdot k \cdot \Phi = c \cdot \Phi_{eq} \text{ where } \frac{1}{c} = 9.1 \times 10^9 \text{ cm}^2/\text{mV} \quad (7.3)$$

The best fit of the data show to be in agreement within ± 20 % with respect to the measured experimental data. Fig 7.11 confirm also that the BPW34F diodes doesn't show sensitivity to γ-rays in the fluence ranges of interest for the LHC.

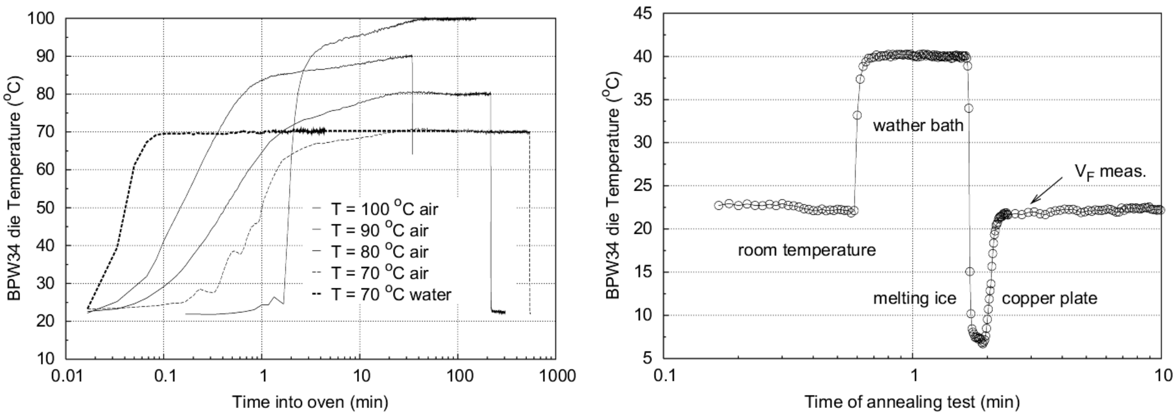

(a) (b)

Figure 7.12: Annealing protocol for BPW34 devices. (a) Time employed from the silicon die to reach the thermal equilibrium in different heating condition. (b) Experimental procedure adopted for the annealing of the BPW34 devices.

7.1.4 Long-term annealing and temperature dependence for BPW34F devices

The first room temperature annealing test performed of the BPW34F devices [Rav04b] showed that after 1 week the signal of the irradiated diodes ($\Phi_{eq} = 2{\times}10^{14}\ cm^{-2}$) decreases of about 25 %. Long-term annealing of these devices has been so considered as an issue to be studied in detail to guarantee reliable measurement with the BPW34F devices.

Before starting a detailed annealing study, an investigation on the influence of the packaging in the thermal behavior of the BPW34F diodes has been performed. For this purpose, one unirradiated BPW34F diode has been used as thermometer and heated up in different experimental conditions. During these experiments, the evolution of its I/V have been corresponding recorded on-line. The variation of the forward voltage upon 10 μA current injection has been chosen as figure of merit. Fig. 7.12(a) show therefore the variation of the diode's forward voltage, supplied with a current of 10 μA, as a function of the time. In the picture the V_F variation has been converted in temperature growth by using a linear scaling.

The continuous lines in Fig. 7.12(a) refer to the diode kept in contact with a metal plate heated up to different temperatures ranging from 70 °C to 100 °C. The signal from the BPW34F devices appears to reach stably the wanted temperature between 10 to 100 min. after the beginning of the heating procedure. This long time needed to reach the thermal equilibrium, clearly indicates that the thermal exchange between the device (e.g. silicon die) and the oven needs to be improved to carry on a precise annealing study.

The solution has been found by heating up the component at the desired annealing temperature by putting it into a volume of warm water. As shown by the dotted line in Fig. 7.12(a) in the case of 70 °C, with this method the annealing temperature can be reached 5 to 10 seconds after the beginning of the thermal cycle.

Therefore, in order to guarantee the temperature stability over time and to be able to perform reproductive annealing measurements, the annealing study presented in this section has been performed by following the protocol shown in Fig. 7.12(b). More in detail, the measurement procedure consisted of three phases:

- to dip the diode in water at the desired annealing temperature (40 °C in Fig. 7.12(b));
- to quickly cool the diode down in water with melting ice for 10 seconds;
- to keep the diode in contact with a copper plate for 1 minute in order to reach back the room temperature conditions before starting the diodes readout.

A series of irradiated BPW34F diodes has been thus submitted to this annealing procedure in order to characterize the annealing dependence of the forward voltage as function of the temperature and the Φ_{eq}. The BPW34F samples used for this studies were irradiated with protons at Φ_{eq} ranging from 6.4×10^{11} cm^{-2} to 1.0×10^{14} cm^{-2} and they were annealed at four selected temperatures (20 °C, 40 °C, 60 °C and 95 °C) with the above described procedure. In the three pictures of Fig. 7.13, the experimental data at the different annealing temperatures are plotted with different markers. This set of annealing data has been obtained by reading out the diode voltages with 700 ms forward current pulses.

From Fig. 7.13(a) it is possible to see that, for Φ_{eq} lower than 2×10^{12} cm^{-2} the signal doesn't show any evidence of annealing as confirmed by the measurement at 20 °C (empty square markers) and 95 °C (filled circular markers). For Φ_{eq}>2×10^{12} cm^{-2}, clear annealing behavior instead appear. In the temperature range from 20 °C to 60 °C, the annealing has the following behavior: for the first 100 minutes the dosimetric signal show only a small degradation. For t greater than 100 minutes the degradation speed increases as shown in Fig. 7.13(b) and Fig. 7.13(c). In the investigate annealing time of more than 10^5 minutes (e.g. 70 days), evidences of saturation phenomena have not been found.

In analogy to what has been done for the leakage current related damage rate in silicon particle detector structures [Mol99a], the long-term annealing of the forward voltage for the BPW34F diodes seems to follow a logarithmic function of the time. Thus the annealing of V_F at room temperature, as well as at higher temperatures, was chosen to be described by one exponential and a logarithmic term. The first part of the annealing curves measured at 95 °C for $t <$ of 100 minutes, differs with respect to the one at lower temperature. For this reason, only the data measured from 20 °C to 60 °C, have been considered for such a parameterization. Finally, in the same annealing function the temperature dependence has been also introduced so that:

$$V_F(t) = A - \alpha \cdot \exp\left(-\frac{t}{\tau}\right) - \beta \cdot \ln\left(\frac{t}{t_0}\right) - (|T_c| \times \Delta T) \tag{7.4}$$

$$\text{where} \qquad \Delta T = T - T_{ref}$$

For each temperature, and for each Φ_{eq}, the data were fitted according to Eq. 7.4 with t_0 set equal to 1 min and T_{ref} = 20 °C. The temperature coefficient (T_c) used in

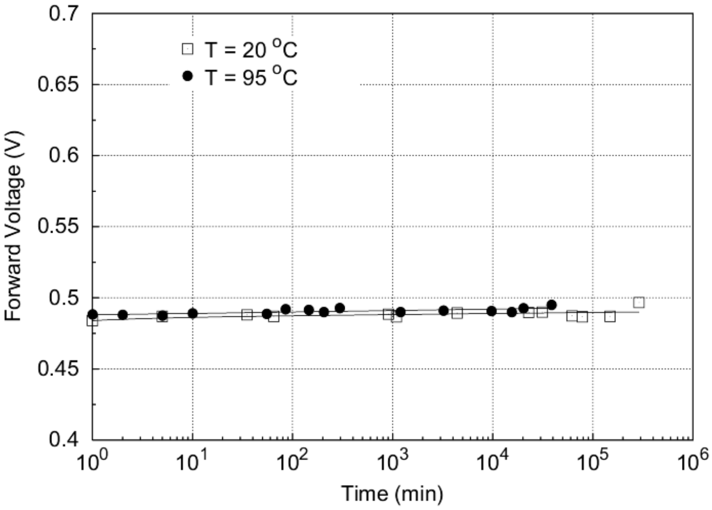

(a) $\Phi_{eq} = 6.4{\times}10^{11} cm^{-2}$

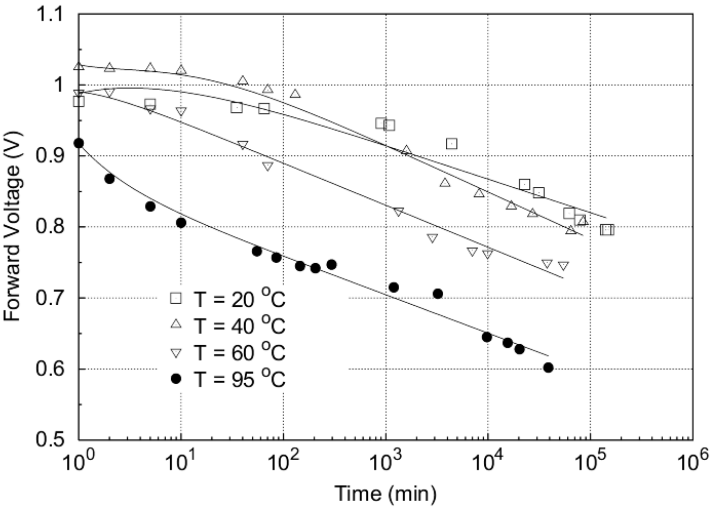

(b) $\Phi_{eq} = 6.3{\times}10^{12} cm^{-2}$

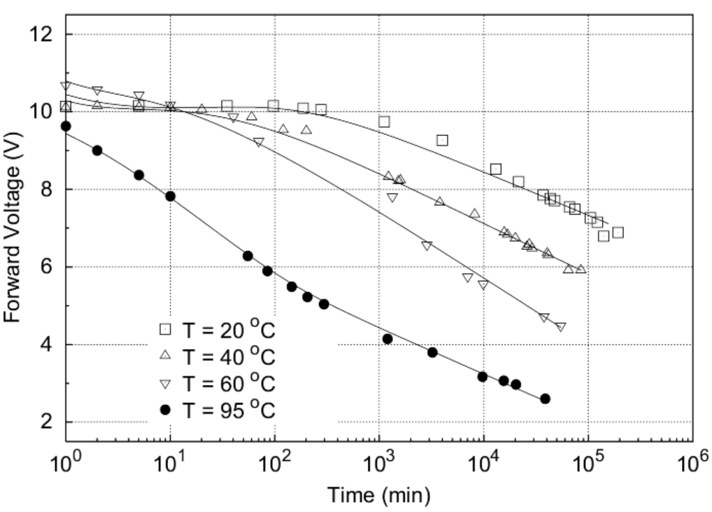

(c) $\Phi_{eq} = 6.8{\times}10^{13} cm^{-2}$

Figure 7.13: Experimental data used for the annealing parameterization of the BPW34 diodes. From (a) to (c) the data refer to diodes irradiated at increasing particle fluences. The continuous lines are the data fits done to extract the parameters to be used in Eq. 7.4.

Eq. 7.4 has been instead measured from a different set of diodes that were irradiated and annealed in various conditions. The T_c for the BPW34F diodes is a function of Φ_{eq}. Its value before irradiation is of -2.3 mV/°C as it was determined by fitting the experimental measurements presented with empty square markers in Fig. 7.14(a). The Φ_{eq} dependence of this parameter is instead shown in Fig. 7.14(b) where the experimental data have been fitted with the following linear function:

$$|T_c(\Phi_{eq})| = 8.315 \times 10^{-13}\ cm^2 mV/°\text{C} \cdot \Phi_{eq} + 2.3\ mV/°\text{C} \tag{7.5}$$

The other parameters A, α (amplitude of the exponential term), and β present in Eq. 7.4 have been found to be temperature independent, while their Φ_{eq} dependence can be described by the following first and second order relations:

$$A(\Phi_{eq}) = (1.99 \pm 0.2) \times 10^{-13}\ cm^2 V \cdot \Phi_{eq} - (0.46 \pm 0.05)\ \text{V} \tag{7.6}$$

$$\alpha(\Phi_{eq}) = (4.23 \pm 0.4) \times 10^{-28}\ cm^4 V \cdot \Phi_{eq}^2 + (4.51 \pm 0.45) \times 10^{-15}\ cm^2 V \cdot \Phi_{eq} + + (0.051 \pm 0.005)\ \text{V} \tag{7.7}$$

$$\beta(\Phi_{eq}) = (9.66 \pm 0.5) \times 10^{-29}\ cm^4 V \cdot \Phi_{eq}^2 + (2.42 \pm 0.12) \times 10^{-15}\ cm^2 V \cdot \Phi_{eq} + + (0.003 \pm 0.0001)\ \text{V} \tag{7.8}$$

Finally, the *Arrhenius* plot of the time constant τ revealed that:

$$\frac{1}{\tau} = k \times \exp\left(-\frac{E_A}{k_B T}\right) \quad \text{with} \quad E_A = 0.236 \cdot \exp(1.966 \times 10^{-14}\ cm^2 \cdot \Phi_{eq})\ \text{eV}, \quad k = 1.706 \cdot \exp(3.274 \times 10^{-13}\ cm^2 \cdot \Phi_{eq})\ \text{s}^{-1}$$

again dependent on Φ_{eq}. It has to be noted that the given parameterization holds only for the time indicated in the data series of Fig. 7.13, for temperature ranging from 20 °C to 60 °C and in the Φ_{eq} range from $2\times10^{12}\ cm^{-2}$ to $1\times10^{14}\ cm^{-2}$. The validity of the above parameterization has been tested on a series of diodes irradiated in the same conditions with respect to the ones used for the parameterization. As shown in Fig. 7.15, the calculation is in agreement within ± 7 % with respect to the different experimental data sets in the above mentioned temperature and fluence range.

7.2 High sensitivity p-i-n diodes from CMRP

The high sensitivity CMRP devices to be characterized for the LHC experiment have been developed and manufactured by the *Center for Medical Radiation Physics* (CMRP) of the University of Wollongong, Australia. They are ion-implanted bulk *p-i-n* diodes with a base length of 1 mm and a cross section of p^+ and n^+ of 1.2 mm^2. These devices were fabricated from high-purity n-type silicon of $\rho \sim 10\ k\Omega{\cdot}cm$ [Rav05a, Ros03]. These devices show an initial forward voltage of about 3.4 V when biased with a DC current of 1 mA.

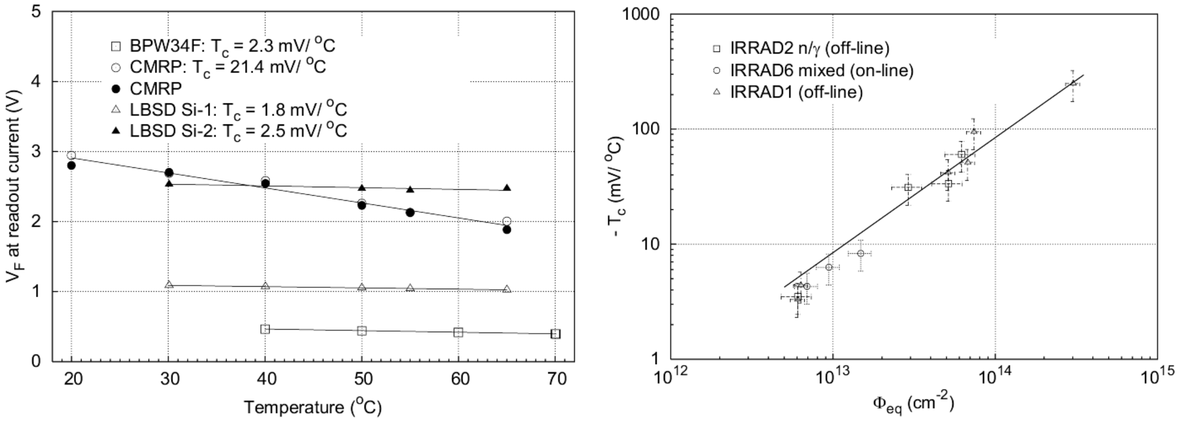

(a) (b)

Figure 7.14: *p-i-n* diodes temperature coefficients. In the legend the $|T_c|$ have been reported (a) Pre-irradiation temperature coefficients of *p-i-n* diodes BPW34F (□), CMRP (○), LBSD Si-1 (△) and LBSD Si-2 (▲). (b) Φ_{eq} dependence of the temperature coefficient for the BPW34F diodes only.

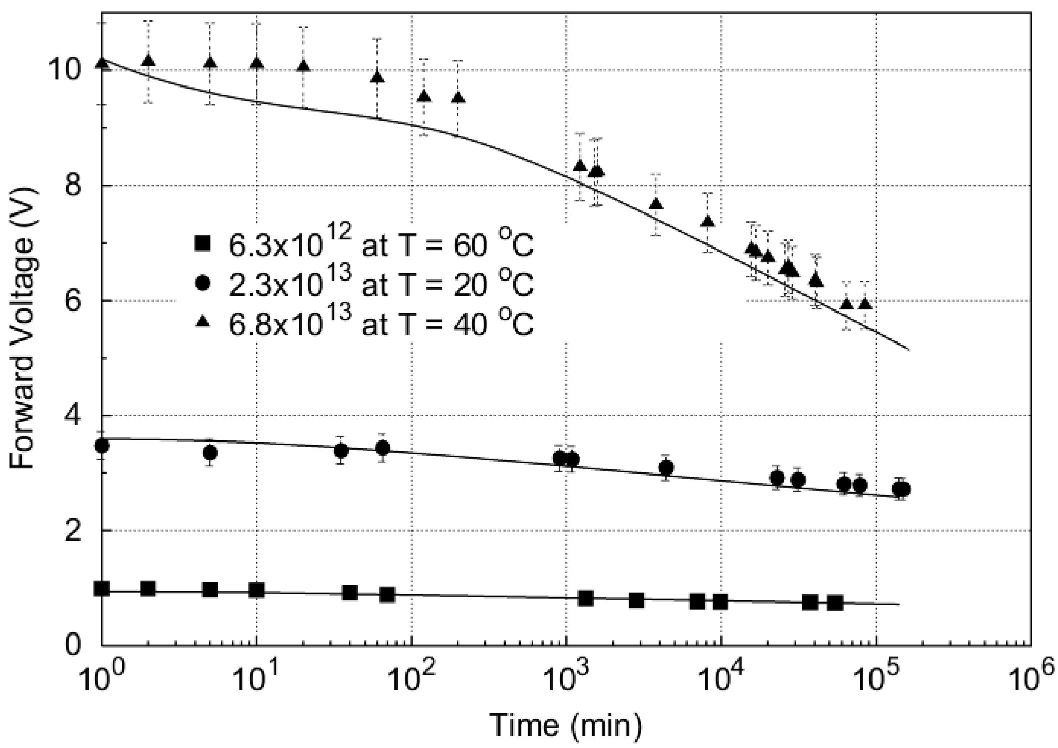

Figure 7.15: Validation of the annealing parameterization for the BPW34 diodes.

7.2.1 Calibration Curves for CMRP devices

Fig. 7.16(a) shows the increase of the forward voltage versus the Φ_{eq} recorded during five different irradiations carried out in the experimental facilities described in Chapter 4 and from Ref. [Rei03, Rav02]. The response curve from Ref. [Rei03] has been measured in the epithermal neutron beam at the High Flux Reactor (HFR) of the *European Commission Joint Research Center* (JRC) while the one from Ref. [Rav02] has been measured in the 300 MeV/c π^+ beam (πE1 facility) at the *Paul Scherrer Institut* (PSI), Villigen, Switzerland [Wal94]. As it has been shown by experimental measurements in Ref. [Rav02], for $\Phi_{eq} > 2\times10^{12}\ cm^{-2}$, the response of the CMRP devices start to increase exponentially as the dependence of V_F on the silicon resistivity (see Eq. 3.12) starts to dominate. The behavior of the V_F growth as function of Φ_{eq} begins thus to deviate from linearity. For this reason, the curves presented in this work end at the above mentioned Φ_{eq} level.

By fitting the different data from neutron, proton, pion and mixed field irradiations in the operational range of the device, it is then possible, in analogy with what has been done in the case of the BPW34F diodes (see Eq. 7.3), to determine the calibration factor c in the linear relationship that links the growth of the forward voltage (ΔV_F) with the Φ_{eq}, so that:

$$\Delta V_F = c \cdot k \cdot \Phi = c \cdot \Phi_{eq} \text{ where } \frac{1}{c} = 1.7 \times 10^8 \text{ cm}^2/\text{mV} \quad (7.9)$$

The best fit of the data shows to be in agreement within ± 13 % with respect to the measured experimental data sets as it has been also indicated by the error-bars of Fig 7.16(b). The measurements presented in these calibration plots have been carried out with 1 mA current pulses of variable width from 50 ms to 700 ms.

In Fig. 7.16(a) the sensitivity to γ-rays has also been plotted with cross markers. The three experimental points corresponds to three doses from the ^{60}Co source of the PAGURE facility (see Sec. 4.1.5): 2, 10 and 22.6 kGy respectively. The best fit of these data show a gamma sensitivity of 0.014 mV/Gy.

7.2.2 Annealing and temperature dependence for CMRP devices

The annealing has been measured following irradiation of CMRP diodes. Fig. 7.17(a) shows for example a short annealing period (∼ 20 hrs.) measured at 20 °C, for a diode irradiated at the Φ_{eq} of $1\times10^{12}\ cm^{-2}$ in the IRRAD6 environment (Z = 15 and r = 60 cm, see Sec. 4.1.1.2). The recorded annealing is found to be less than 2 % over such a period. This result has been confirmed and extended until 1800 hours after neutron irradiation to the maximum Φ_{eq} level, at the JSI reactor facility of Ljubljana, Slovenia, by *Mandic et al.* [Kra06]. Fig. 7.17(b) presents the long-term annealing behavior of the CMRP devices. After 2.5 months of room temperature annealing after irradiation to the maximal fluence, the forward voltage shift lost 13-15 % of its initial value. This value is in the same order of the accuracy determined in the calibration curves presented in Fig. 7.16 (± 13 %), therefore the annealing correction hasn't been considered as an issue for these devices.

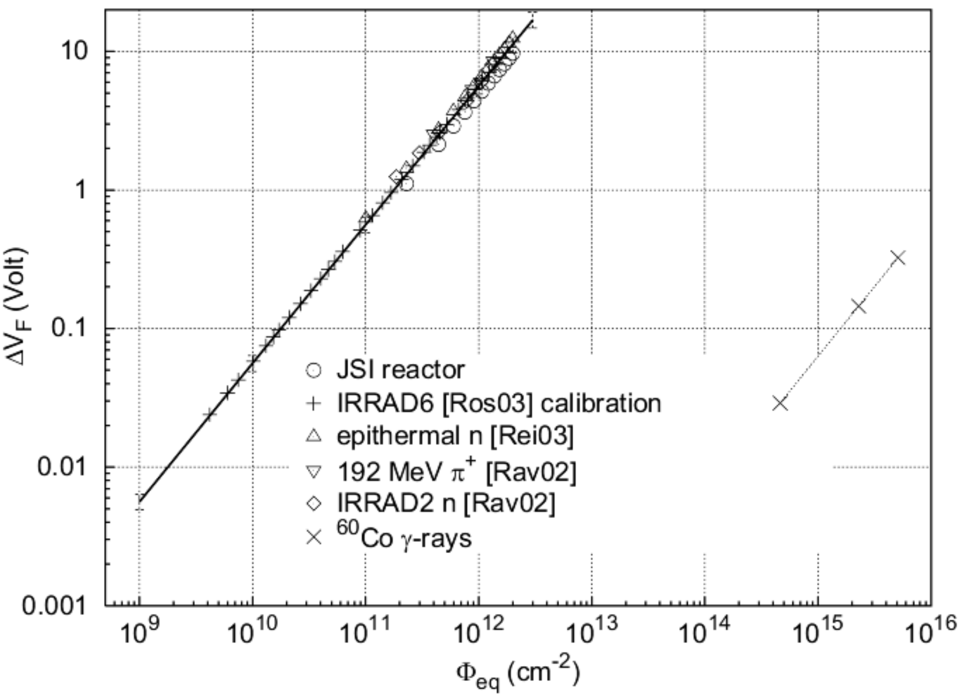

(a) logarithmic scale

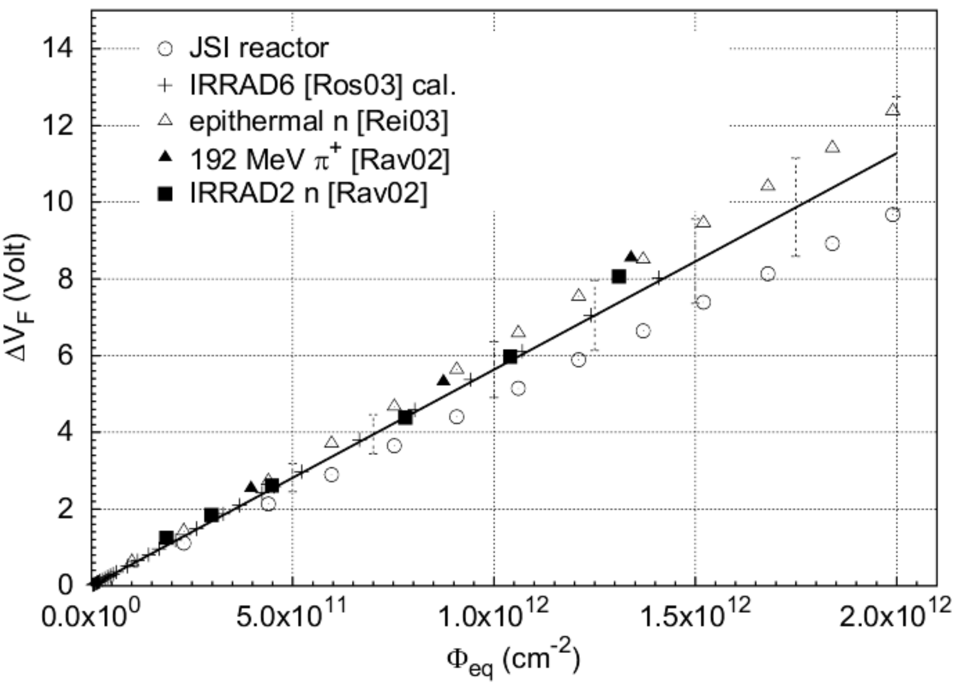

(b) linear scale

Figure 7.16: CMRP diodes calibration curves at 1 mA in different hadron fields. Current pulse width from 50 to 700 ms. Neutron data from JSI TRIGA Mark II reactor, CERN-IRRAD2 and JRC-HFR facility. Pions data from PSI-πE1. Mixed-hadron field data from CERN-IRRAD6. (a) Data plotted in logarithmic scale. In the figure the sensitivity to γ-rays is also shown. The conversion between γ dose and photon fluence has been done with the KERMA factor for 1.3 MeV photons in Silicon equal to 4.45 pGy·cm^2. (b) Data from (a) plotted in linear scale. The linear fit is in agreement by $\pm$ 13 % (error-bars) with respect to the experimental data.

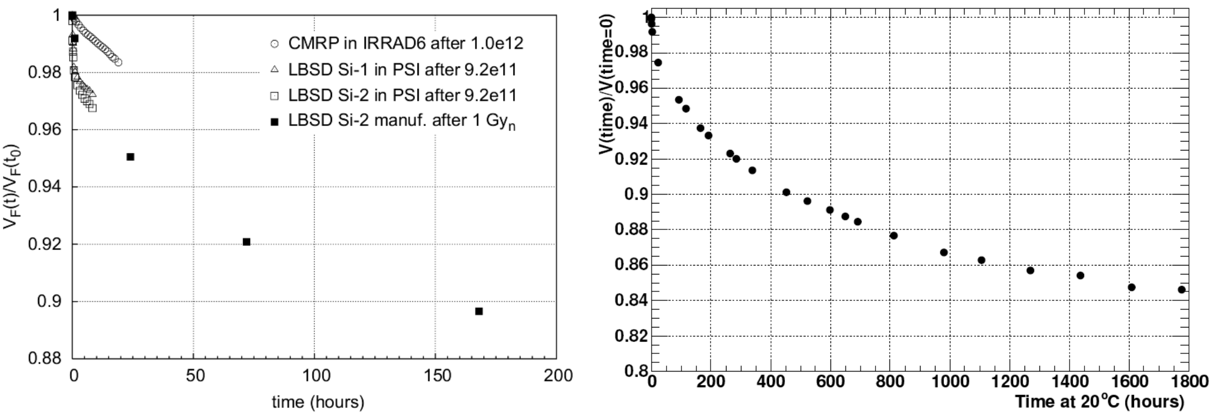

(a) Annealing of CMRP and LBSD diodes (b) Long-term annealing of a CMRP diode

Figure 7.17: Annealing of CMRP and LBSD *p-i-n* diode devices. (a) Annealing behaviors for both CMRP (T = 20 °C) and LBSD Si-1 and Si-2 devices (T = 25 °C). The data for the diodes LBSD Si-2 have been compared with independent measurements from the producer recorded after 1 Gy_n neutron exposure from a ^{252}Cf source. According with Ref. [Hol02], 1 Gy_n in tissue is equivalent to a $\Phi_{eq} \sim 4.4\times10^{10}\ cm^{-2}$ or a $\Phi_{eq} \sim 9.1\times10^{11}\ cm^{-2}$ in silicon. (b) Long-term annealing for CMRP devices measured at the JSI TRIGA Mark II after exposure to $\Phi_{eq} = 2\times10^{12}\ cm^{-2}$ from Ref. [Kra06].

The temperature dependence of the CMRP devices has been determined and plotted in Fig. 7.14(a). As for the case of the BPW34F (see Sec. 7.1.4), this measurement has been done by dipping the packaged devices into a water bath heated to different temperatures. At any temperature the diode's V_F has been measured by injecting a 50 ms long current pulse of 1 mA intensity. A T_c of -21.4 mV/°C has been determined. This value has been found to quickly decrease with the irradiation due to the shift of the Fermi level to the center of the semiconductor band gap [Ros06]. In the investigated Φ_{eq} range up to $2\times10^{12}\ cm^{-2}$, this value has been found to decreases up to 0.8 mV/°C.

7.3 LBSD p-i-n diodes

The high sensitivity LBSD devices have been manufactured by the *Institute for Research, Production and Application of Radioisotopes* (IRPAR) in Prague [Pro89]. These devices were prepared by ion implantation of boron and phosphorus into the initial n-type silicon single crystal using the floating zone method. The specific resistance of the initial material is $\rho \sim 100\ \Omega \cdot cm$. A complete list of technical parameters for both LBSD Si-1 and LBSD Si-2 devices is available in Tab. 7.3 [Sop91, Pro89, Met05].

7.3.1 Calibration Curves for LBSD devices

Fig. 7.18 shows the LBSD increase of the forward voltage versus the Φ_{eq} recorded during two different irradiations carried out in the PIF facility (254 MeV protons) and in the JSI TRIGA reactor described in Chapter 4. The measurements presented in these calibration plots have been carried out with 25 mA current pulses with the width of 50

Description	Type Si-1	Type Si-2
Radiation detected	neutrons with E > 300 keV	
Dimensions (S)×t_{base}	(1.8×1.8)×1.2 mm	(2.0×2.0)×2.5 mm
Neutron KERMA range	0.1 - 30 Gy	0.01 - 5.0 Gy
Neutron KERMA energy dependence	less than ± 15 %	
Fast-neutron sensitivity	128 mV/Gy	1 V/Gy
γ sensitivity	< 0.01 mV/Gy	< 0.4 mV/Gy
Encasing	plastic	
Initial voltage at 25 mA	0.9 - 1 V	1.8 - 2.5 V

Table 7.3: Technical parameters of LBSD Si-1 and Si-2 diodes. Table from Ref. [Met05]. The neutron KERMA plotted in this table is referred to the dose delivered to human tissue. According to Ref. [Hol02], 1 Gy_n in human tissue is deposed by a $\Phi_{eq} \sim 4.4\times10^{10}$ cm^{-2} of 1-MeV neutrons.

ms as indicated in the devices data sheet. A set of measurements has also been carried out by injecting the 25 mA biasing current with a pulse length of 700 ms. This last measurement series shows to be in agreement with the 50 ms ones for about 13 % (Si-1) and 11 % (Si-2).

By fitting the different data of Fig. 7.18 for broad spectrum neutrons and 254 MeV protons, it is possible to determine the calibration factor c in the linear relationship that links the growth of the forward voltage (ΔV_F) with the Φ_{eq}, so that for the type LBSD Si-1:

$$\Delta V_F = c \cdot k \cdot \Phi = c \cdot \Phi_{eq} \text{ where } \frac{1}{c} = 1.6 \times 10^8 \text{ cm}^2/\text{mV}, \tag{7.10}$$

while for the for the type LBSD Si-2:

$$\Delta V_F = c \cdot k \cdot \Phi = c \cdot \Phi_{eq} \text{ where } \frac{1}{c} = 2.7 \times 10^7 \text{ cm}^2/\text{mV}. \tag{7.11}$$

The best fit of the data, for the two devices, show to be in agreement within ± 15 % with respect to the measured experimental data. Always from the experimental curves of Fig. 7.18 it is possible to determine the operational range of the two devices as the maximum Φ_{eq} value at which the devices response still follows a linear behavior. Therefore a Φ_{eq} range of about 1×10^{12} cm^{-2} and 2×10^{11} cm^{-2} has been determined for the diodes Type Si-1 and Si-2 respectively. These results are in very good agreement with the data of Tab. 7.3 where a range of 1.3×10^{12} cm^{-2} (30 Gy) and 2.2×10^{11} cm^{-2} (5 Gy) is indicated in terms of neutron KERMA in tissue.

7.3.2 Annealing and temperature dependence for LBSD devices

Annealing curves have been measured following 254 MeV proton irradiation for the two types of LBSD diodes. Fig. 7.17(a) shows the measurements recorded over about 10 hrs. at a room temperature of 25 °C. Both diodes have been irradiated to a Φ_{eq} = 9.2×10^{11} cm^{-2}. On the same plot, annealing data measured by the manufacturer after exposition to a Φ_{eq} of 9.1×10^{11} cm^{-2} has been also reported. The recorded annealing is

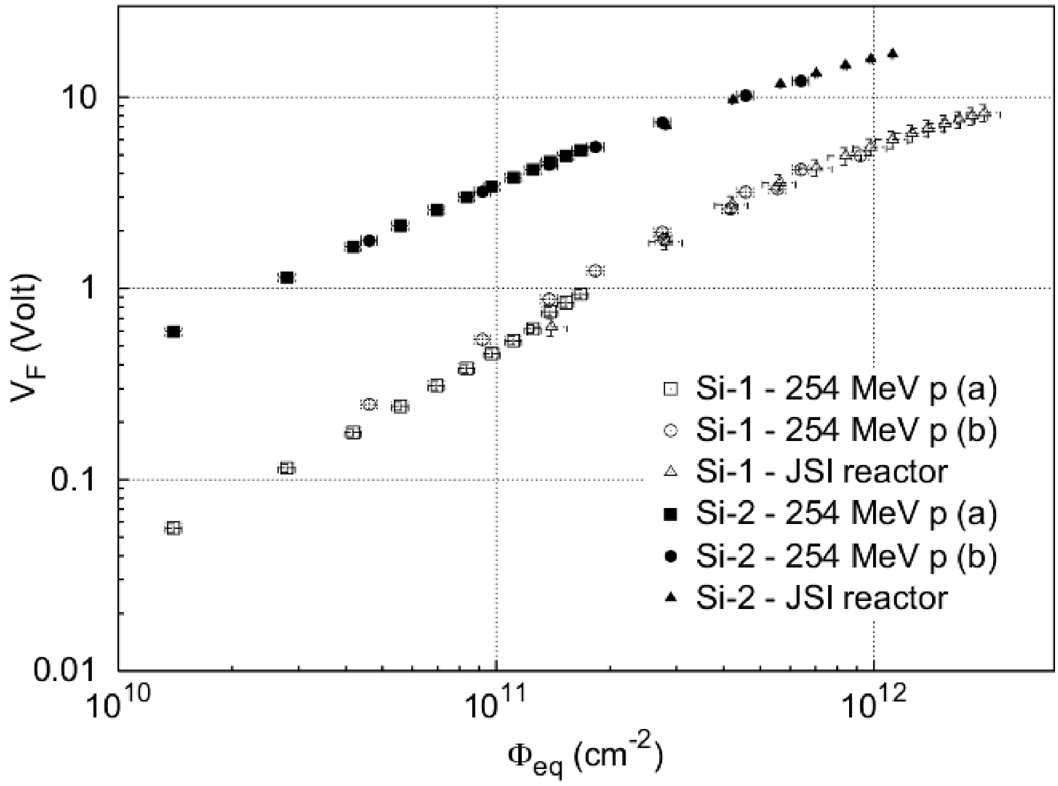

Figure 7.18: Radiation response of LBSD diodes. The diode's forward voltage at 25 mA is plotted versus the Φ_{eq}. The width of the readout current pulse was of 50 ms. The experimental data taken in the 254 MeV beam of the PIF facility at PSI have been recorded at different proton rates: (a) $1\times10^8 cm^{-2} \cdot s^{-1}$, (b) $2.5\times10^8 cm^{-2} \cdot s^{-1}$.

found to be about 10 % over a period of 200 hrs. This result is in good agreement with Ref. [Pro89] and other references cited therein.

The temperature dependence of the LBSD devices has been determined with the same experimental procedure employed in the previous cases and plotted in Fig. 7.14(a). Temperature coefficients T_c of -1.8 mV/°C and -2.5 mV/°C have been determined for the diode Type Si-1 and Si-2 respectively. This value has been found in very good agreement with Ref. [Pro89] that mentions absolute temperature dependencies of 1.1 mV/°C and 2.3 mV/°C respectively with an accuracy of ± 30 %. These values are expected to be roughly constant in the Φ_{eq} operation range of the devices. However a detailed investigation for the Φ_{eq} dependence after irradiation wasn't carried out in the framework of this thesis work.

7.4 Conclusion

In this Chapter, three types of *p-i-n* diodes have been investigated for the needs of the LHC experiments.

To cover the required broad dynamic range up to several 10^{14} cm^{-2}, the commercial devices from OSRAM BPW34F, already subject of preliminary investigations at CERN in the nineties, have been characterized in detail. For dosimetric purposes the series of measurements carried out with different types of particles and energies, suggests to supply these devices with a forward bias current pulse of 1 mA of a width that doesn't have to exceed 1 sec (current pulses from 50 ms to 700 ms are the optimum choice for the readout of such a device). In this way enhanced annealing and self-heating phenomena are avoided within the diode's operative range. The calibration curves presented here reveal that the devices is not sensitive at Φ_{eq} levels $< 2\times10^{12}$ cm^{-2}. A sensitivity of 9.1×10^{9} $cm^{-2}/mV \pm 20\%$ is instead measured in the following part of the response curve.

The long-term annealing of the ΔV_F has been identified as the limiting factor for such a devices. For this reason a parameterization to correct the time behavior of ΔV_F as function of the operational temperature and the cumulated Φ_{eq} has been here proposed. Moreover, the absence of annealing phenomena for $\Phi_{eq} < 2\times10^{12}$ cm^{-2} (see Fig. 7.13(a)), suggests to **pre-irradiate** such devices before their utilization. In this way the initial "insensitive" region can be eliminated without altering the characteristics of the diode's radiation response as it has been shown in Ref. [Rav04a].

Diode type	Sensitivity	Maximum Φ_{eq} range	Annealing
CMRP	1.7×10^{8} $cm^{-2}/mV \pm 13\%$	2×10^{12} cm^{-2}	$<$ 15 % after 1800 h.
LBSD Si-1	1.6×10^{8} $cm^{-2}/mV \pm 15\%$	$\sim 1\times10^{12}$ cm^{-2}	$\sim$ 10 % after 200 h.
LBSD Si-2	2.7×10^{7} $cm^{-2}/mV \pm 15\%$	$\sim 2\times10^{11}$ cm^{-2}	$\sim$ 10 % after 200 h.

Table 7.4: Summary of the performances of high-sensitivity forward-biased silicon diodes.

To provide the LHC experiments with *p-i-n* diode sensors with an high sensitivity, three devices have been tested in the framework of this thesis work. The test on these devices has been carried out powering them with forward current pulses from 1 mA (CMRP) to 25 mA (LBSD) and of a width ranging from 50 to 700 ms. Their annealing behavior, as well as their temperature dependence have been also measured and presented here. Tab. 7.4 gives an overview of the main characteristics measured for the three tested devices.

From Tab. 7.4 results that the diode type LBSD Si-2 has the highest sensitivity which is about a factor 6 greater than the one of the LBSD Si-1 and the CMRP devices. However, the high current required to powered the LBSD devices, at the moment constitutes a limiting factor in the integration of such devices into the LHC. The CMRP device, supplied with 1 mA forward current, turn out to have instead the same readout protocol as the one defined for the BPW34F. Moreover the two LBSD devices start to saturate before reaching the Φ_{eq} of 2×10^{12} cm^{-2}, needed to fully cover the LHC experiment range. For these reasons the CMRP devices were preferred to the LBSD ones and therefore have been selected, together with the BPW34F diodes, as Φ_{eq} monitor to fulfil the LHC experiments needs.

Chapter 8

OSL dosimetry for the LHC Experiments

Radiation sensors using Optically Stimulated Luminescence (OSL) have been presented in Chapter 3. The development of such devices was focused to address the concern of the dose measurement aboard spacecrafts [Dus04b]. The OSL-based sensors, like the one described in Sec. 3.2.3.3 can exploit the OSL material dosimetry properties in order to achieve:

- a sensitivity of the order of the 1 mGy;
- a dynamic range of four orders of magnitude (mGy to 100 Gy);
- a power consumption close to zero except for the few seconds reading time.

During the OSL reading process, the trapped carriers are released producing a reset of the sensor itself. As a consequence, it is always possible to choose a reading cycle that prevents the sensor from saturating [Vai05]. The above features make the OSL an interesting candidate, not only to measure the dose received orbit-by-orbit aboard spacecrafts but also to monitor the environment in large radiation facilities, like reactors and particle accelerators. Moreover, among the other advantages cited above, the independence of its response in the ionizing radiation type and energy, make higher the interest of using the OSL material in mixed radiation environments as the one expected at the LHC experiments.

An evaluation of the OSL material properties and of several OSL-based sensor has been thus conducted at CERN as a part of this thesis work and it will be developed in the present chapter aiming to demonstrate the feasibility of an ”real-time” system that can integrate also the OSL technology. In particular, with a fully integrated system including OSLs, the long-term Total Ionizing Dose (TID) is monitored with RadFETs, forward biased *p*-*i*-*n* diodes provide information on the cumulative displacement damage effects and the OSL sensor, reset after each reading, has to contribute to the measurements of the periodical variations of the dose [Rav04b].

In this chapter, for the first time the study of the sensitivity of the OSL material under GeV charged particles and neutrons will be presented as well as different methods to enhance the OSL material sensitivity to thermal and high energy neutrons. Moreover,

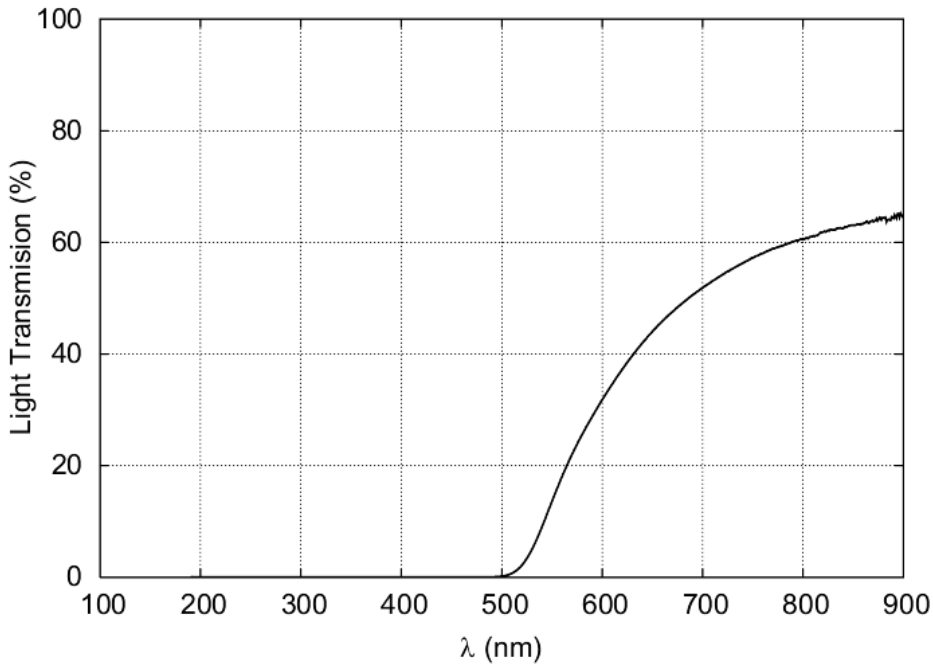

Figure 8.1: Light-transmission spectrum for a 100 μm foil of kapton material.

the experimental campaigns carried out at the CERN IRRAD1 and IRRAD6 facilities on an integrated sensor developed for space applications will be also presented. Finally, preliminary tests with a prototype of "real-time" fibered OSL system will be also described in this chapter.

8.1 Samples used for CERN studies

The OSL samples employed for this thesis work, used to study the response of the sensitive material to different kind of radiations, were obtained from a 80 μm thick OSL layer silk-screen printed on a 100 μm thick kapton foil. These OSL foils, prepared at the *University Montpellier II*, were cut in small squares with the size of 5×5 cm^2. Kapton has been chosen as substrate for the sensitive material because of its transparency to the IR light as visible from the transmission spectrum of Fig. 8.1 that has been measured at CERN before the OSL samples production. Moreover these samples were found to be easy to handle and measure with the laboratory test-bench described in Sec. 4.2.2. As described in Sec. 4.2.2, for the readout the specimens were placed in the samples tray with the kapton side facing the IR LED and the "material" side facing the photomultiplier window.

The OSL samples so prepared were also easy to protect from the daylight sensitivity. A set of 10 samples were tested by exposing them directly to the light. Other 10 samples were instead exposed by placing them upside-down so that the kapton layer was facing directly the light. After 4 days, all samples were measured and the firsts series of samples showed a luminescent background signal about a factor 3 higher with respect to the second series that showed signals lying close to the offset level of the readout system.

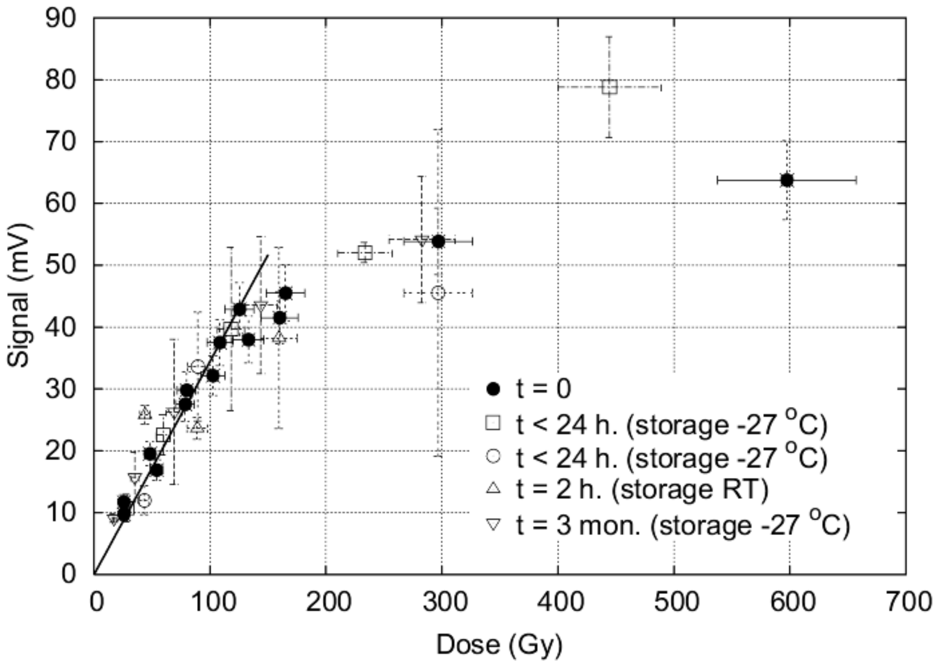

Figure 8.2: OSL material sensitivity to 23 GeV protons. The different symbols in the picture correspond to different OSL sets read out at different times t after irradiation. (•) samples readout immediately after irradiation. (□,○) samples from different OSL batches stored at -27 °C and readout within 1 day. (△) samples stored at room temperature and readout 2 h. after irradiation. (▽) samples stored at -27 °C and readout after 3 months.

This test confirms the choice of such a preparation method for the OSL material to be investigated.

8.2 OSL Sensitivity to 23 GeV protons

To determine the sensitivity of the OSL material to the high energy protons different series of OSL samples, prepared as described in Sec. 8.1, have been exposed to increasing proton fluences in the IRRAD1 facility at CERN. At any fluence level, from 3 to 5 identical OSL samples were irradiated at the same time. The proton fluence at any step was determined by activation of Al foils with the same dimensions as the OSL samples under test. The fluence-to-dose conversion has been done using Eq. 5.1 and results are accurate within ± 10 %.

The results of these irradiation tests are reported in Fig. 8.2. The filled circular markers are data coming from the same set of materials exposed to increasing proton fluence and readout immediately after particle exposure (t=0). The OSL measurement points follow a linear behavior in the range 0-100 Gy with an accuracy better than 10 %. At higher doses, the response becomes sub-linear due to saturation of the trapped charge. These results are in agreement with the data of other OSL and TL materials irradiated with charged particles [Dus01].

To confirm this first data set, other OSL samples have been irradiated to increasing proton fluences and read out following different storage periods at various temperatures.

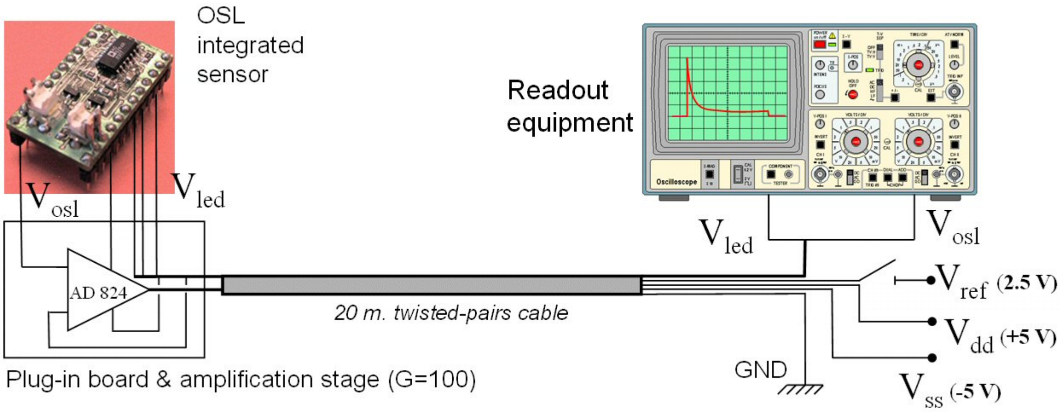

Figure 8.3: Experimental setup for the irradiation test of the on-line sensor for space applications. In the schematics the signals that were driven from/to the sensor are detailed as well as the output amplification stage.

All these following data points have been measured from various single OSL samples irradiated separately at any dose step. These measurements are shown in Fig. 8.2 plotted with different empty markers. Altought the shape of the radiation response is confirmed, the experimental error that affects the measurements became much higher as visible in the vertical error bars of all these data sets. In the linear region agreement of the data points goes down to about ± 30 %.

The increase of the uncertainty among the different measurements may indicate that other phenomena, as for instance the fading of the OSL material, should be taken into account when the OSL readout is performed after long times and in not well controlled temperature conditions. OSL fading curves will be discussed in more detail in Sec. 8.4.3.

8.3 Test of an integrated sensor for space applications

The first step toward the conception of a real-time sensor based on OSL for the LHC experiments, was to evaluate the performances of the existent OSL integrated sensor developed for space applications at the *University Montpellier II* previously described in Sec. 3.12.

The sensor tested at CERN was a version build with commercial electronic components (COTS), radiation hardened by compensating the radiation-induced damage in the IR LED. The compensation of the LED emission loss has been realized via a feedback loop that increases the LED operative current while the light emitted decreases. Such a sensor version was meant to be sensitive to doses as low as 10 mGy and it was proven to be immune up to a Φ_{eq} of $5x10^{11}cm^{-2}$ (irradiation with 12 MeV electrons) [Vai03b]. The tested sensor mounts a Siemens IR LEDs SFH425 and a Hamamatsu visible GaAsP photo-sensors G2711-01. Before starting the irradiation test, the sensor was connected to an external transimpedance amplifier stage with a gain of 100. This external circuit has been realized by using the JFET input stage AD824 quad-amplifier equal to the one mounted on the sensor board that was also proven to be hardened at the particle fluence level of interest [Vai03a].

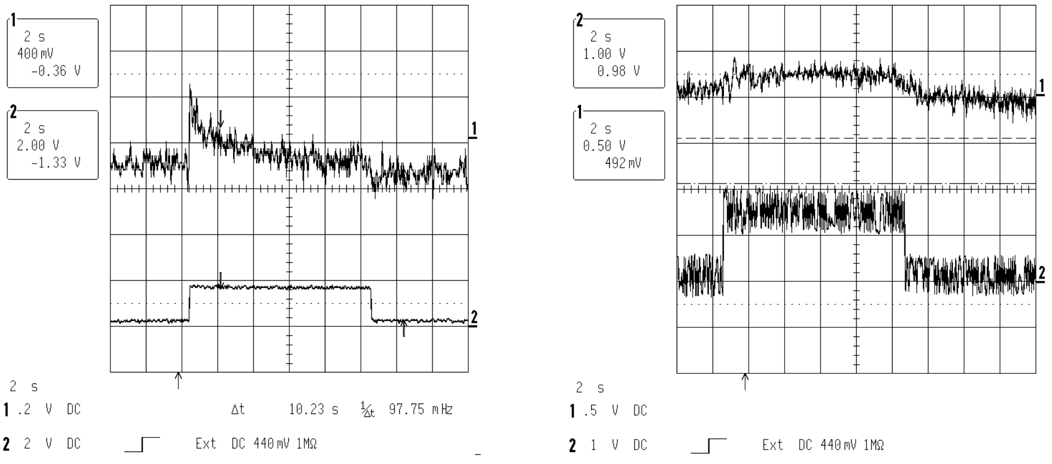

(a) (b)

Figure 8.4: OSL integrated sensor response in mixed hadron field of IRRAD6. OSL peak (trace 1) and LED current monitoring (V_{led} on trace 2) as readout from the oscilloscope. (a) Signal recorded after 9 day exposure. (b) Signal recorded after 4 days exposure.

Fig. 8.3 shows the experimental setup used for the irradiation test. The sensor was plugged on a PCB containing the amplification stage to collect the luminescent peak from the OSL material (V_{osl}) during the IR stimulation. The stimulation is provided by applying for a certain time a reference voltage (V_{ref}) that corresponds to a forward current injected in the LED. The sensor provides also a second output (V_{led}) that can be used to monitor the degradation of the LED current. These signals are driven to the readout equipment via a 20 meter twisted-pairs cable.

The external equipment consisted of an oscilloscope to monitor both (V_{osl}) and (V_{ref}) signals. A power supply was then needed to bias the electronics on boards and to trigger the readout (V_{ref}) by using a manual interrupter as shown in the right-hand corner of Fig. 8.3. A V_{ref} of 2.5 V was then applied for 10 seconds to readout the exposed OSL material. The sensor was installed in the radiation environment of the IRRAD6 facility at CERN at the location Z = 130 cm and $r = 80$ cm, where a ϕ_{eq} of about 1.5x10^{10} cm^{-2} per day was integrated. Neutrons, protons and charged hadrons delivered a TID in the sensor location that was recored by means of PAD dosimeters.

During the first days of exposure it was not possible to observe a signal emerging from the noise level that was of some hundred of mV. The first measurable signal was observed after about 9 days exposure to a dose of about 4.5 - 5 Gy. This signal (peak of about 600 mV) is shown in the first oscilloscope trace (1) of Fig. 8.4(a) while the emission of the LED V_{led} was monitored on the trace number 2 and it was equal to 1.33 V.

The experiment was repeated 4 days later (after a TID of about 7 Gy) without success (see Fig. 8.4(b)). The OSL peak was hardly distinguishable from the background of about 250 mV and the V_{led} stimulation signal, although it was still of about 1.3 V, was affected by a noise of 1 V. At that point the sensor was exposed to a particle fluence value about 40 % greater with respect the one to which it had been tested for space applications.

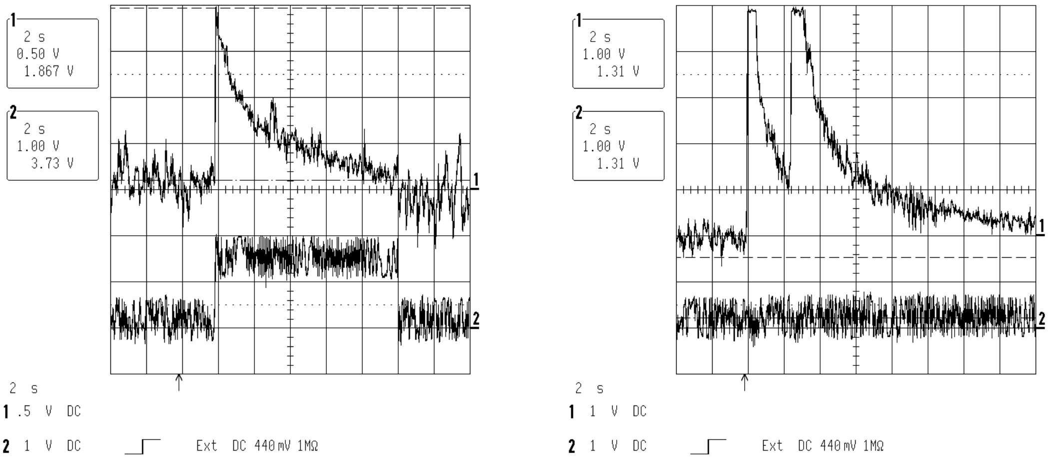

(a) (b)

Figure 8.5: OSL integrated sensor response in the 23 GeV protons of IRRAD1. (a) Signal recorded after one 23 GeV proton bunch. (b) on-line signal recorded after the integrated sensor failure.

To verify if the sensor was still operational it was decided to test it directly with a 23 GeV proton burst in the IRRAD1 facility. In this condition the dose delivered to the sample in one shot was of about 15-16 Gy in about 400 ms time. The result of this test is shown in Fig. 8.5(a) where for the same intensity of stimulation (1.3 V) a peak of 1.8 V has been measured. This result is in agreement with the previous one since the signal obtained was about three times bigger for three times the deposed TID.

After this first proton irradiation the sensor started to fail. The energetic protons passing through the sensor structure were able to trigger the readout sequence. Fig. 8.5(b) shows the two luminescent peaks, corresponding to two consequent proton spills recorded during the radiation exposure. Therefore, the OSL material was already completely reset when the external trigger (voltage V_{ref}) was given after the exposition to the proton spills.

The results presented in this section brought to evidence that the tested sensor assembly, although it was working in the hostile IRRAD6 environment, was not able to properly accomplish its task in measuring the radiation dose with the expected sensitivity. These first experiments underlined a series of constraints that the development of a OSL integrated sensor must face to account the specificity of the LHC environment:

1. The sensitivity of the readout cell (sandwich LED/OSL/photodiode) should be improved;

2. The "on-board" sensor output stage was not able to drive electrical signals out to long distances (20-30 m.). The electromagnetic perturbations, inducing hundreds of mV of noise on the transmission line, were the main factor reducing the SNR and thus the minimum detectable dose;

3. The radiation hardness of the electronic components on-board has to be extended since the design limit of the tested sensor developed for space applications were

rapidly reached. Moreover the LHC-like radiation field strongly differs to the spatial one and resulted to be more effective in damaging the sensor's electronics.

4. The fading of the OSL material was suspected also to be responsible of the sensitivity loss. This because in the HEP facility the readout cycles were performed over long times (e.g. several days) and the operative temperature in the experimental areas was around 27 °C;

5. The operation in radiation environment with high LET particles may induce current spikes that in turn can accidentally trigger the readout process. Protection against these effects maybe also foreseen. This problem has been not faced in this thesis work, however an advanced version of the space sensor has been produced at the *University Montpellier II* where this problem has been solved in the design of the sensor by introducing a validation switch that avoids accidental readouts cycles. Further details about this new sensor architecture can be found in Ref. [Vai05].

8.4 Prototype of an integrated sensor for CERN applications

In order to follow up the irradiation tests on an integrated sensor OSL structure, a new prototype optimized following the indications listed in Sec. 8.3 was built at CERN. A picture of this prototype PCB of an OSL integrated sensor is shown in Fig. 8.6(a). The components were assembled on a test PCB and the signals routed out via a 9-pin cannon plug that allowed to connect the remote sensor board to a receiver unit placed at 20 m distance from the irradiation position. The cable has to drive the signal lines as well as the power lines to supply the on-board electronic and to control of the IR LED for the optical stimulation.

8.4.1 System description and performances

To address the point (1) raised in Sec. 8.3, the OSL readout cell was modified by direct deposition of a thin layer of OSL material on the sensitive surface of a Hamamatsu GaAsP visible photodiode type G1126-02 [Ham]. These sensor heads, prepared at the laboratory of the *University Montpellier II*, are shown in detail in Fig. 8.6(b). These new OSL heads have been developed in order to maximize the light collection from the stimulated OSL material. The Hamamatsu photodiode has been chosen because of its high sensitivity in the visible range and because of its good cut-off in the IR region of the electromagnetic spectrum.

The sensor cell for the CERN prototype was then build by using such sensitive photodiode and coupling it to an OSRAM GaAs IR LED SFH415 [Osr]. The coupling has been realized by using an empty aluminum cylinder to allow the relative centering of the couple LED/photodiode. The full assembled OSL sensor cell is shown in Fig. 8.6(a).

The readout circuitry implemented for the CERN integrated sensor prototype is shown in Fig 8.7. The circuit has been designed in order to transmit the current signal

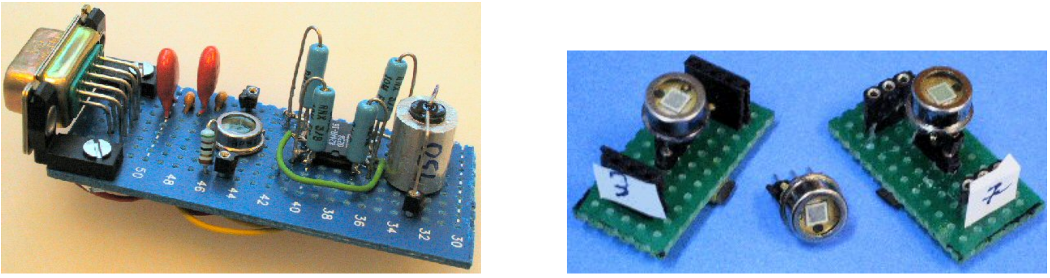

(a) (b)

Figure 8.6: The prototype of an integrated OSL sensor built at CERN. (a) Picture of the prototype as assembled on the test PCB. (b) GaAsP photodiodes with OSL material deposed on the sensitive surface.

over long distances reducing the effects of the electronic noise on the transmission line. The output stage of the sensor has been realized with two current amplifiers that split the photo-current generated in the photodiode G1126-02 (during OSL stimulation) toward a twisted pair cable to the receiver unit. The noise generated in the transmission line is then split into equal components and suppressed when the signals are merged at the readout stage.

The differential amplifier, mounted as input stage of the receiver unit, recombines the luminescent signal that is then treated by a pick detector in order to measure the OSL peak amplitude that constitutes the dosimetric parameter. The circuit has been dimensioned in order to get a linear response over a broad current range generated in the photodiode (>4 orders of magnitude), starting from currents of 10 pA as shown in Fig. 8.8 that represents the output of a SPICE simulation [Tui95].

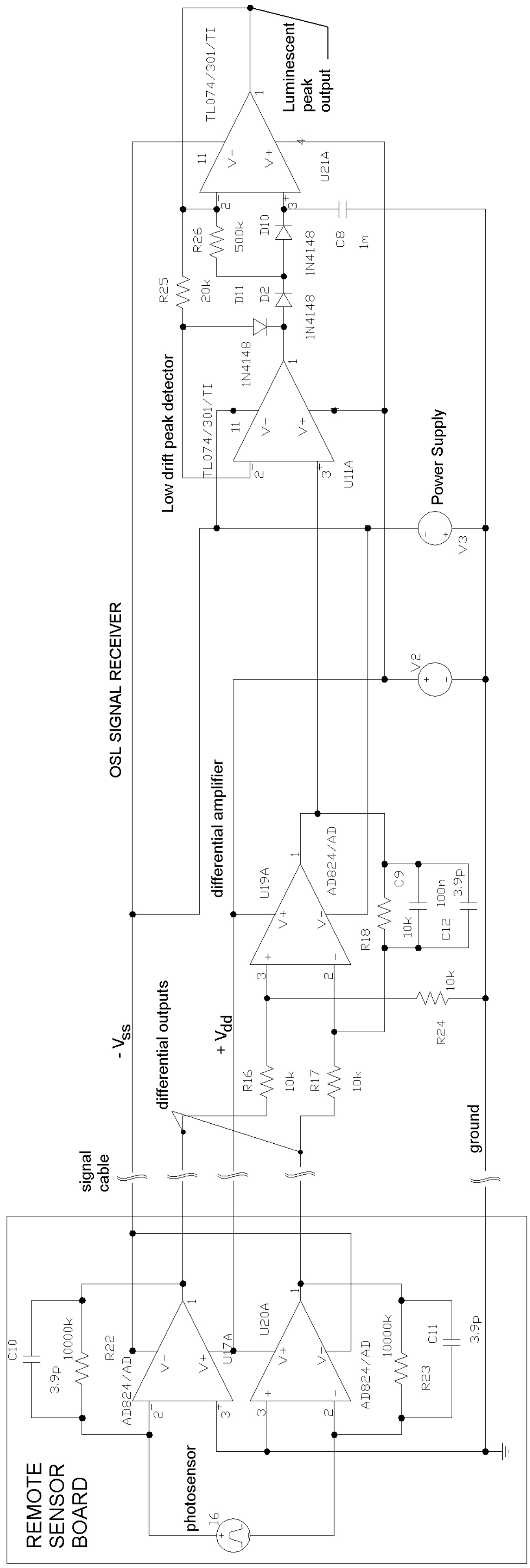

Figure 8.7: Electrical Scheme of the OSL integrated sensor developed at CERN. The encased part in the left-hand side represents the circuit mounted on the remote sensor's PCB (see Fig. 8.6(a)). The photo-sensor, simulated in the circuit as a variable current generator, represents the OSL-sensitive cell. In this picture the details of the circuit used to pilot the IR LED have been omitted. The remanent part of the circuit has been assembled on the receiver unit placed 20 meters away from the integrated sensor and not exposed to the radiation field.

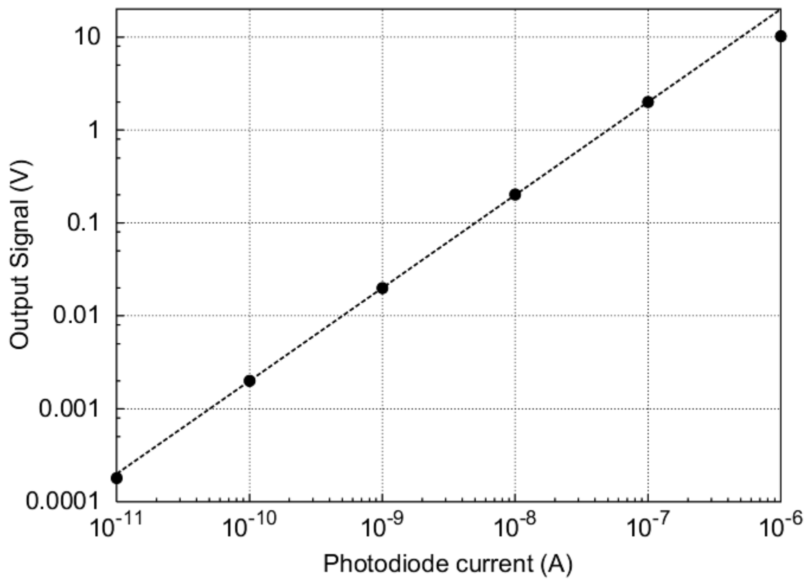

Figure 8.8: SPICE simulation for the output of the OSL integrated sensor.

The above mentioned circuitry scheme is implemented twice in the CERN sensor prototype. The second sensitive cell mounts a simple BPW21 visible photodiode without sensitive OSL material deposed on it in order to evaluate the loss of performances of the IR LED SFH415 used for the optical stimulation.

The sensitivity to radiation of this new prototype has been tested with X-rays by using the CERN irradiator described in Sec. 4.1.6. The irradiation was carried out at an operative voltage of 60 kV$_p$ with the addition of a 3 mm Al absorber in order to cut the very-low energy part of the photons spectrum ($<$ 20 kV). In such conditions, the dose-rate achievable at 3 cm distance from the tube was of 1.72 Gy/min.

Fig. 8.9 shows the response curve of the OSL (net peak amplitude) as function of the radiation dose by using a stimulation current of 50 mA. The prototype shows a sensitivity of 2.3 mV/cGy so that the measurement of doses in the range of 0.1 Gy shall be possible. The response of the prototype behaved linearly up to 2 Gy. At higher doses the response became quickly sub-linear. This "early saturation effect" was not expected and has been identified in the mounting of the photodiode that has been done without biasing it during the luminescent signal readout. The operation with a weak electric field may enhance recombination effect giving in turn saturation of the luminescent signal response.

The optimized CERN prototype was then placed inside the radiation environment of the CERN IRRAD6 facility in order to evaluate its performances in hadron environment. The prototype was thus exposed during several weeks and its readout was performed cyclically several times per day. Although the new output stage allows a reduction of the noise of about a factor 10 down to tens of mV it was difficult, since the beginning, to measure a clear luminescent peak out of the background noise on the transmission line. The operation of this simplified prototype allows to understand that the loss of performances of the overall system were most likely dominated by a quick decrease of the performances of the optical components.

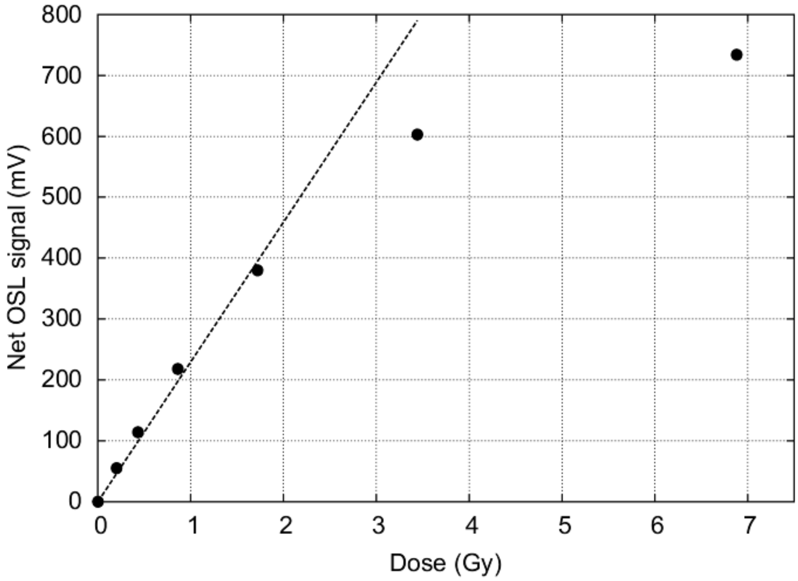

Figure 8.9: Sensitivity of the CERN integrated sensor prototype to 60 kV$_p$ Al-filtered X-rays.

To verify the above hypothesis, a series of IR LED and visible photodiodes were exposed to different levels of radiations in order to check their tolerance to the hadron environment. The results of these studies will be presented in the next Section.

8.4.2 Radiation hardness of integrated sensors optical components

The IR LEDs used in both two integrated sensors (OSRAM SFH425 and SFH415) and the visible photodiodes (Hamamatsu G2711-01, G1126-02 and SIEMENS BPW21) have been exposed to different radiation levels in the IRRAD6 environment at Z = 15 cm and r = 60 cm. The irradiated components have been exposed together with PAD dosimeters (see Sec. 3.1.1) and reverse biased silicon detectors (see Sec. 3.1.9) in order to measure the radiation dose and the Φ_{eq} respectively. In this position the measured ratio Dose in PAD/Φ_{eq} was equal to $8\times10^9\ cm^{-2}Gy^{-1}$.

Fig. 8.10(a) shows the irradiation test of Hamamatsu G1126-02 GaAsP photodiodes used to build the sensitive OSL cell in the CERN integrated sensor prototype. The measurements were performed by illuminating the photodiodes with an increasing intensity of red light (635 nm) emitted by a LED and recording the corresponding photo-current. For doses below 100 Gy variations of about 7 % have been measured. These variations, being comparable with the experimental error that affects the measured points, indicates that the performances of the components are unchanged. The tested components show instead a decrease of 12 % in their performances when the radiation level exceeds 110 Gy and about 20 % after 0.5 kGy exposure.

For this photodiode, measurements have been performed with and without the quartz windows that protect the sensor die inside the TO-5 package. This measurement shows that the degradation occur in the device since the sensor windows doesn't change the measured results. The same results have been found for the Hamamatsu G2711-01

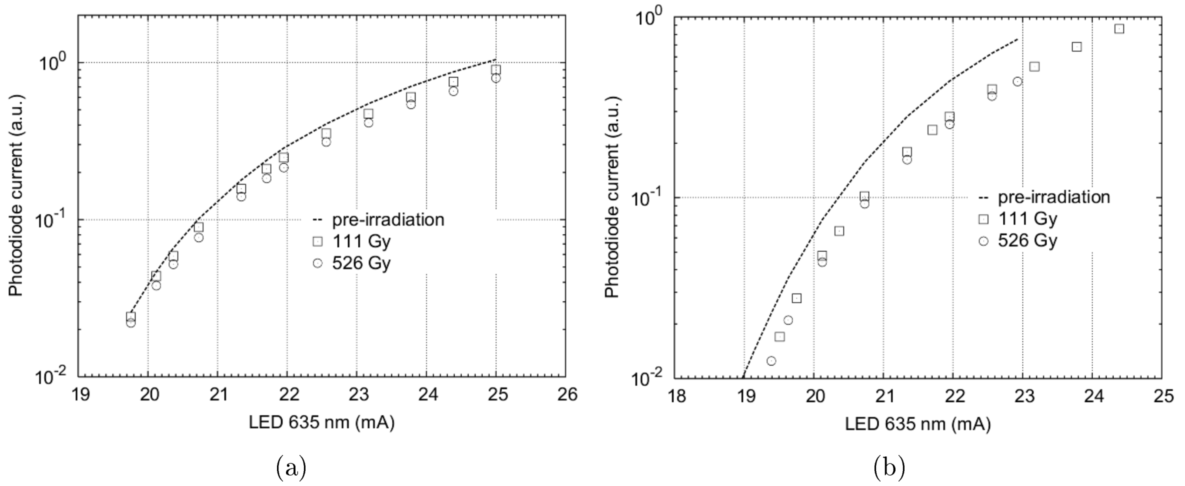

Figure 8.10: Radiation Hardness tests of photodiodes used for the OSL sensors in the IRRAD6 environment. (a) Hamamatsu G1126-02 GaAsP photodiode. (b) SIEMENS BPW21 silicon photodiode

GaAsP photodiodes mounted in the *Montpellier* sensor confirming thus the results published in Ref. [Vai03b].

Different is the situation for the SIEMENS BPW21 Si photodiode. The detection level for this component result to be reduced of more than 40 % at 111 Gy and of about 50 % at 0.5 kGy as it is shown in Fig. 8.10(b). The above results confirm the choice of using GaAsP photodiodes as sensitive elements for the OSL integrated sensor.

The two commercial IR (950 nm) LED mounted in the OSL sensors (OSRAM SFH425 and SFH415) were identical apart for their packaging type. Therefore their radiation hardness in hadron field has been studies by irradiating in IRRAD6 several samples of SFH425 device only.

Fig. 8.11 shows the measured results by means of a calibrated optical transceiver InGaAs photodiode that was used to measure the IR emission from the irradiated LED. The current was sent to the LED by means of a pulse generator in order to avoid possible self-heating phenomena due to a DC forward current flow. For the typical operational current of 50 mA the IR emission was already reduced by a factor 3 after the dose of 25 Gy. The most sensitive element to radiation damage in hadron environment result to be the commercial LED component used in both integrated sensor assemblies. This result is in good agreement with the one published in Ref. [Vai03b] for the *Montpellier* sensor.

To replace this radiation sensitive equipment, a survey has been done in order to find a LED device better adapted to the harsh hadron environment at the LHC. In terms of radiation hardness, suitable components for this application have been identified in InGaAsP LEDs [Lis93]. Thus the Epitex L1050-35T52 High Power InGaAsP NIR LED [epi] has been selected as candidate for the OSL integrated sensor. Moreover this LED emits light in a wavelength band of 1050 nm that better matches the OSL stimulation spectrum as shown in the curve of Fig. 3.10(a).

The results of several irradiations performed on the Epitex diode has been plotted in Fig. 8.12. Different Epitex L1050-35T52 samples have been exposed to the ^{60}Co gamma

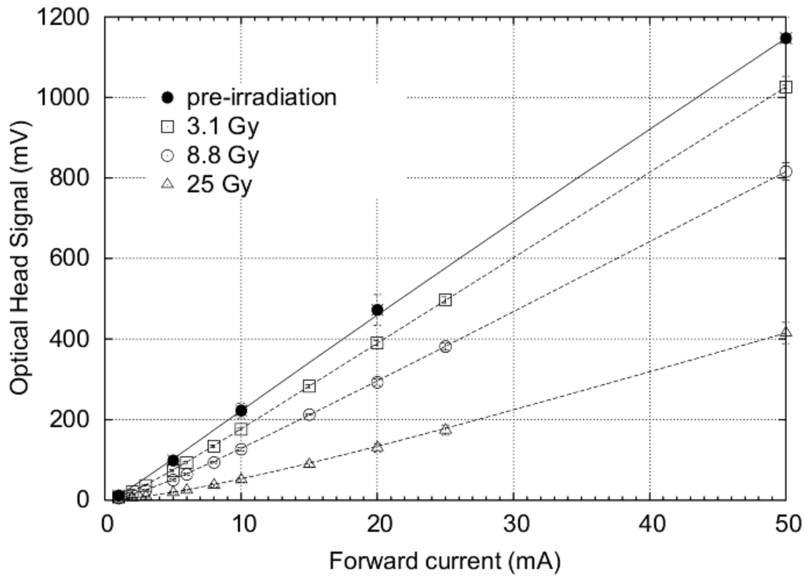

Figure 8.11: Radiation Hardness tests of LEDs used for the OSL sensors. Irradiation test carried out at the IRRAD6 facility (see text).

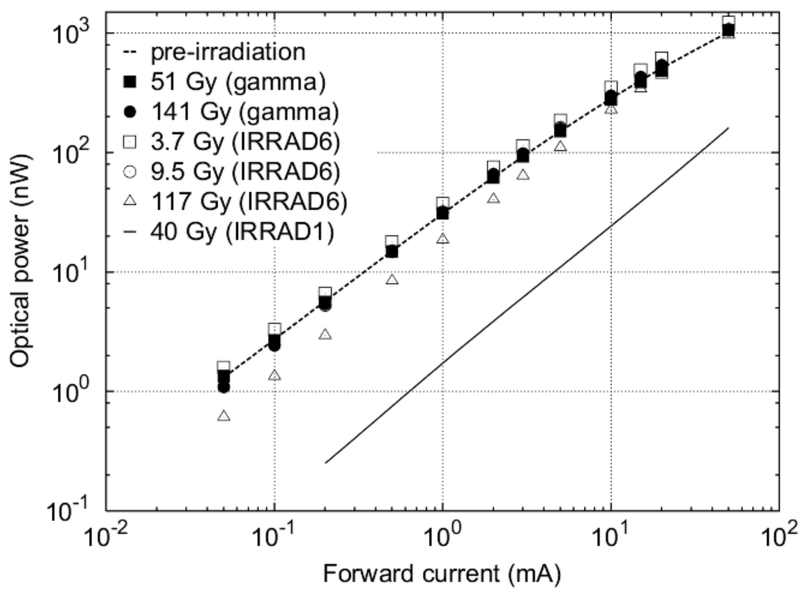

Figure 8.12: Radiation Hardness tests for the Epitex L1050-35T52 High Power InGaAsP NIR LED.

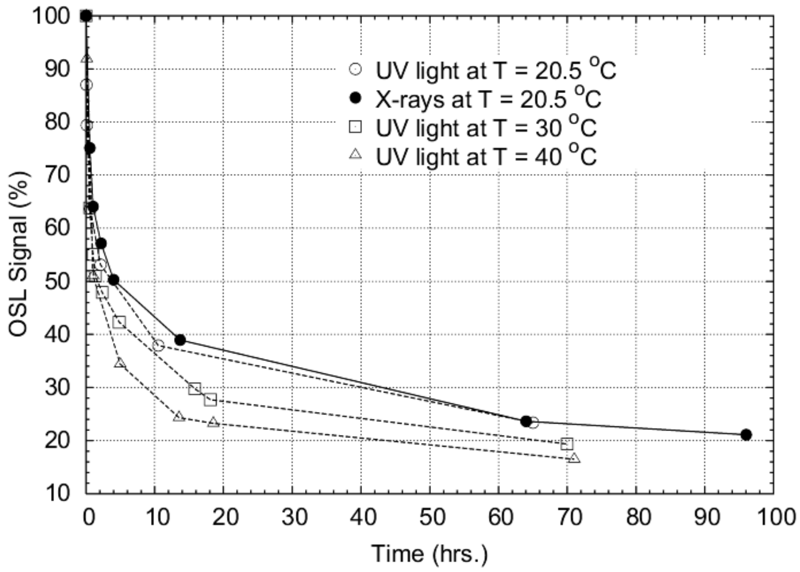

Figure 8.13: Fading curves for the OSL annealing employed at CERN.

radiation at the Pagure Facility (see Sec. 4.1.5), to the mixed environment of the CERN IRRAD6 as well as to the direct proton beam of IRRAD1. The characterization of these components has been again performed by measuring the light emission at increasing pulsed forward currents.

This LED proved to be insensitive to TID levels up to 141 Gy upon gamma irradiation. In the mixed hadron field of IRRAD6 and working at forward current higher than 10 mA, the light emission results attenuated for less than 10 % after a dose of 117 Gy. One diode has been also exposed directly to the 23 GeV proton beam of the IRRAD1 facility. In this condition the light output of the LED has been found to be attenuated of about a factor 10 after a few proton spills ($\sim 10^{11}\ p/cm^2$) that deposed a dose of 40 Gy. Although this component shows better radiation hardness in hadron environment (especially if powered with higher forward currents), this last result brings to evidence the sensitivity of this optical equipment to displacement damage effects.

8.4.3 OSL material fading

The integrated sensor prototype built at CERN has been also used to quantify, in a pure ionizing radiation field, the fading of the OSL material used at CERN. The fading of the material reduces, with the time, the amplitude of the luminescent signal for a given radiation dose. Therefore, it has a direct impact on the sensitivity and on the minimum detectable dose achievable from dosimetric systems based on the OSL. The fading measurements are shown in Fig. 8.13 where the OSL signal amplitude, normalized to the value obtained at t = 0, is plotted as function of the time after irradiation.

The first annealing curve at room temperature (RT) has been measured following 2 minutes irradiation to 60 kV$_p$ X-rays at a dose-rate of 1.72 Gy/min. This curve is plotted with filled circular markers in Fig. 8.13. A second fading curve has been determined following 254 nm UV light irradiation. The dose deposed by UV light has been fixed by exposing the OSL material for a time enough to have the same OSL peak amplitude at t = 0 with respect to the previous X-rays exposure.

The same procedure has been repeated following UV light exposure, at T = 30 °C and T = 40 °C. These fading results reproduce what was measured in Ref. [Dus95] for a similar OSL material. The luminescent signal reach about 20 % of its value after some tens of hours from the irradiation. This stable signal level is reached faster when the temperature increases as predicted in Sec. 3.2.3.1.

By measuring OSL samples at different time after irradiation the amplitude of the signal may be affected by significant reductions due to the fading. This is what happened in the determination of the 23 GeV proton sensitivity where, as shown in Sec. 8.2, the different data sets are in agreement within about 30 % when the OSL are measured two hours after irradiation. As expected before, the fading of the material revealed to be crucial parameter that has to be taken into account in the design of an integrated sensor as well as in its calibration and utilization.

8.5 Real-time monitoring with fibered OSL system

In the previous sections it has been shown that although the electronic architecture of the integrated sensor has been improved, the sensitivity of such sensor layouts, in the operative conditions typical of HEP facilities, is mainly limited by two factors:

1. the radiation hardness of the IR LEDs used for the OSL stimulation that rapidly degrade in hadron environment;

2. the proper fading of the sensitive material that quickly reduces the luminescent signal for a given dose;

The first issue can be faced for instance by replacing the stimulation source with a component with enhanced radiation hardness (see the Epitex diodes tested in Sec. 8.4.2). However these components being more expensive and more difficult to procure that the ”standard” commercial LED may lead to a decrease in the interest of such a integrated sensor scheme.

The second problem can be faced partially compensating the signal loss by improving the efficiency of the detection cell or by increasing the stimulation power. One method to increase the light collection efficiency is, for example, to improve the OSL material deposition on the sensitive head. Some tests have been performed in that direction as shown in Fig. 8.14. In this plot the OSL sensitivity to UV light for different OSL sensor cells (like the ones shown in Fig. 8.6(b)) has been plotted in function of the exposure time. By increasing the granularity of the OSL materials, the sensitivity has been enhanced by a factor 50.

A second method to increase the detection efficiency could also be to replace the photodiode with a more sensitive photomultiplier (PM) device. However, this last solution will increase the encumber and the weight of the overall integrated sensor assembly.

Another concept of OSL sensor structure can be built by replacing the stimulation LED with a IR Laser. Moreover, to avoid to expose this component to the radiation environment and thus, to avoid any degradation of the stimulation source over time, the light signal can be driven to the OSL crystal by means of an optical fiber. By collecting

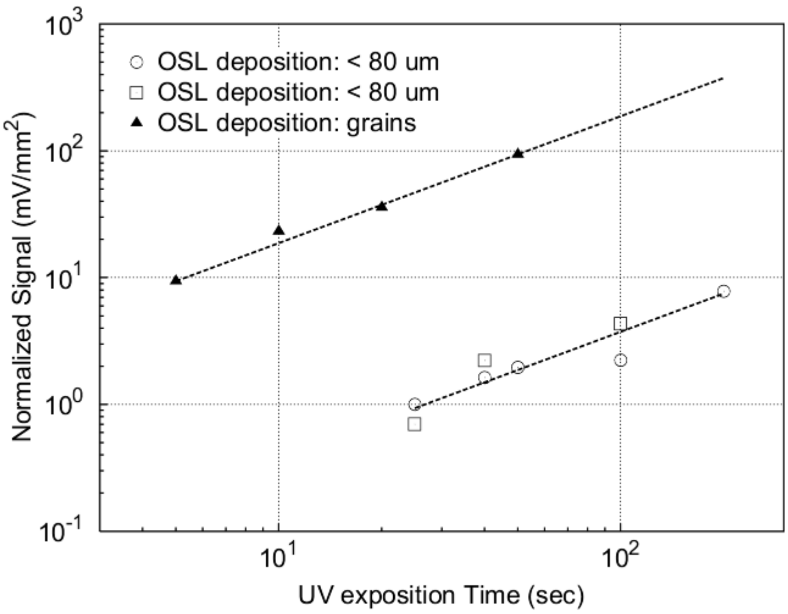

Figure 8.14: Sensitivity to UV light of the OSL sensitive cell based on G1126-02 photodiodes.

the luminescent signal using the same principle (second optical fiber), all the electronic needed to readout the OSL material can be kept outside the irradiation area. Therefore a PM device can be employed maximizing at the same time the stimulation/detection source capabilities.

Following the above layout also the OSL sensor head get profit of it. The OSL sensitive head is in fact now reduced to a small capillary probe of a few cubic millimeters. The two optical fibers, with at the edge an OSL crystal, are therefore guided to the measurement point while all the readout electronic lay several meters away form the irradiation site. This concept of real-time OSL dosimetry has been also tested at CERN. The details of the developed measurement system, as well as the first results are described in the following sub-sections.

8.5.1 Layout of the system

Altought the radiation hardness of the readout electronics doesn't constitute a problem with this readout scheme, to insure reliable measurements with the real-time OSL in the harsh CERN environment, the radiation tolerance of the optical fibers that carry both the laser and the OSL signals became instead fundamental. For this reason, the system designed at CERN takes advantage on the R&D performed in optical fibers used in the HEP Experiments of the LHC [Dum02, Mer05].

Fig. 8.15 shows the layout of the first prototype of real-time OSL tested for radiation monitoring in hadron facilities. Two quartz fibers from *Polymicro Technologies, LLC*, Phoenix, AZ, USA, of 20 m. length and 0.6 mm core diameter were inserted into a light-tight capillary pipe of about 3 mm diameter. At one side (sensor head), the fibers were polished and a 0.5 mg OSL crystal was coupled by means of EPO-TEK 310 optical glue. A detail of the optical head is visible in the insert of Fig. 8.15. Finally, the sensor

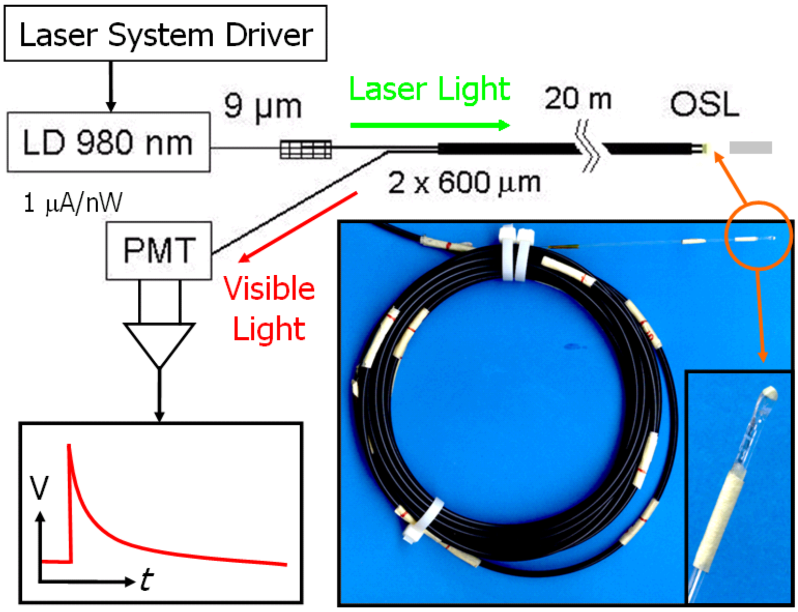

Figure 8.15: Prototype of Real-time OSL system designed for the monitoring in HEP facilities.

head was wrapped-up using a light-tight material. At the readout side one fiber was connected to a 980 nm InGaAs pump laser to provide the IR optical stimulation, while the second one was coupled to a photomultiplier tube to collect the OSL visible emission. For the prototype used in this work, the optical stimulation can be provided in a power range up to 200 mW.

It has to be noted here that the maximum optical power reachable with the LED mounted in the previous integrated sensors devices was about an order of magnitude lower when the LED are powered to very high forward currents (typically 100 mA). Considering that, to avoid self-heating problems in DC operation, the LED are usually powered at less than half of the maximum current rated, this make clear the choice and the benefits in using a laser stimulation source.

The employed fibers were specified for the Hadron Forward (HF) calorimeter of the CMS Experiment (see Sec. 2.2). They were previously tested at CERN-LIL facility using 500 MeV electrons up to 1 MGy (equivalent to $\sim 10^{16}$ electrons) [Dum02] and with 23 GeV protons at the CERN-IRRAD1 irradiation facility reaching 12 MGy (equivalent to more than $4{\times}10^{16}$ p/cm^2) [Mer05]. These irradiation tests show that the radiation damage exhibits the same behavior for both electrons and protons tests: high light attenuation below 380 nm and in the band 550-680 nm. Moderate attenuation has been found in the band 400-520 nm and no attenuation has been instead measured above 700 nm. Fig. 8.16 show, with dotted lines, the fiber attenuation spectra before after exposure to 1 MGy electrons from Ref. [Dum02]. In the picture the OSL emission and stimulation spectra are also reported.

The above mentioned radiation hardness studies have been done for wavelengths (λ) from 200 nm to 800 nm. In this range, the radiation-induced attenuation after exposure to 1 MGy is minimal in the region in which the maximum of the OSL emission spectrum lies. No data are available at wavelength higher than 800 nm. However, even thought

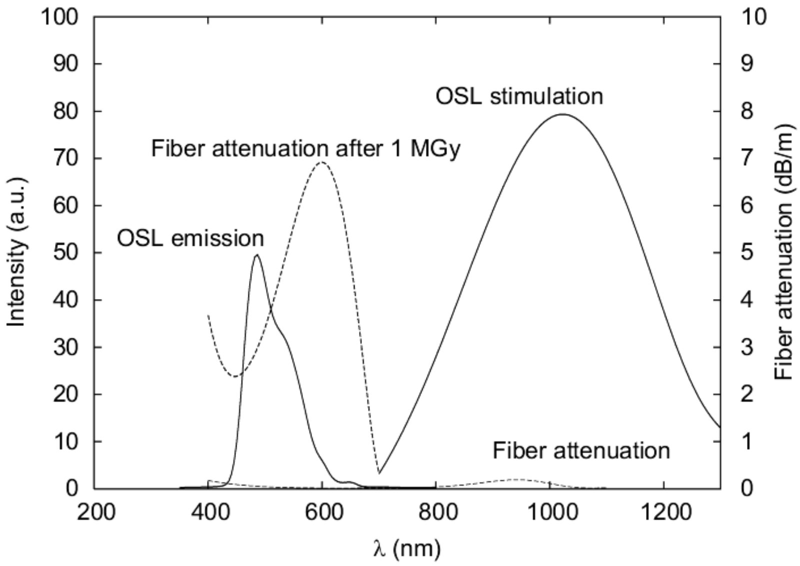

Figure 8.16: Radiation-induced attenuation in the optical fiber used for the real-time OSL. In the picture, the OSL spectra are referred to the left-hand side y-axis, while the attenuation in the fibers light transmission (dB/m) are referred to the secondary y-axis. In the picture the OSL emission and stimulation spectra are also reported. The attenuation spectra of the not-irradiated fiber labeled with *"fiber attenuation"*, being very small, lie close to the x-axis and is hardly visible.

that a big attenuation peak might appear for λ around 1000 nm, the high power-range of the laser light can allow to increase the stimulation power for increasing radiation doses to compensate for possible radiation induced losses.

The above consideration thus indicate the CMS-HF fiber as a good candidate to carry the OSL signals for the real-time system.

8.5.2 Performances of the OSL fibered prototype

The first irradiation experiment for the assembled prototype has been performed in the TRIGA MARK II reactor of the *Jozef Stefan Institute* in Ljubljana, Slovenia described in Sec. 4.1.2. The OSL real-time sensor was irradiated by placing it into the reactor core through the TIC irradiation tube. Several measurement points were taken, moving the real-time OSL by 10 cm steps, inside the irradiation channel in order to measure the dose profile along it.

At the reactor power of 250 kW the dose-rate was of about 1 Gy/s at the starting position situated half-length in the reactor core (labeled 30 cm in Fig. 8.17). At the same position, the neutron flux delivered to the sensor head, and measured by means of reverse biased silicon detectors, was of 1.4×10^{10} n/cm$^2 \cdot s$. The OSL measurements were performed during neutron irradiation by recording the amplitude of the luminescent peak emitted during 4 sec. laser stimulation. Before each OSL readout cycle, the sensor head was exposed for 6 seconds to the radiation field in order to accumulate charges.

The prompt Radio-Luminescence (RL) light emitted by the OSL material during irradiation can also be used for dose-rate evaluations in the same fashion as the lumi-

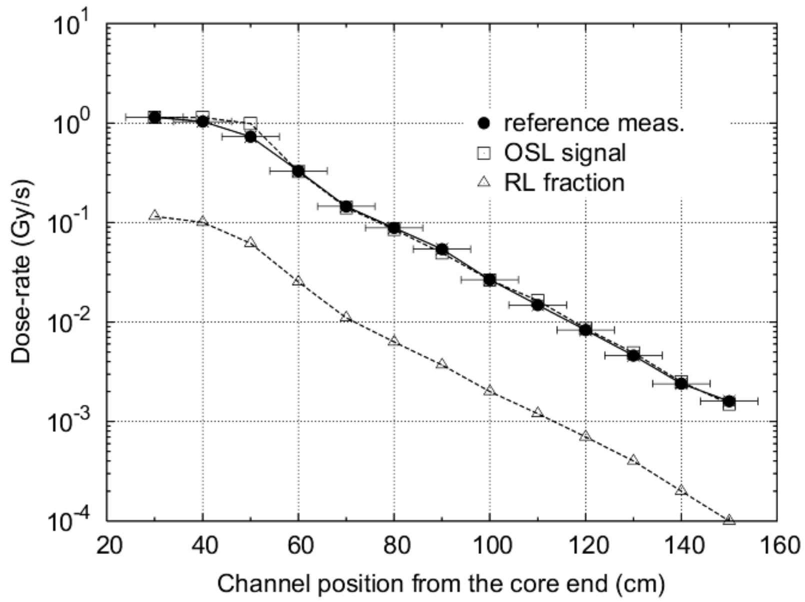

Figure 8.17: Real-time OSL measurements in the TRIGA reactor. In the picture, the OSL and RL measurements carried on with the real-time OSL have been compared with the dose-profile recorded independently by means of semiconductor dosimeters.

nescence from scintillator [Pol04]. Performing OSL measurements during irradiation, this amount of light has to be taken into account and subtracted from the OSL peak amplitude. In the present case, the fraction of measured RL signal represents about 10 % of the recorded luminescence as shown in Fig. 8.17.

Fig. 8.17 finally compares the dose-rate profile measured with the OSL technique (squared markers) with reference measurements obtained using silicon dosimeters (filled circular markers). The OSL measurements are in very good agreement with the reference ones over a range of four dose-rate decades. Moreover, the RL behavior matches the OSL one, confirming thus the capability of the real-time system to use both luminescence techniques for radiation measurements during (RL) and after (OSL) radiation exposure [Gaz04]. The series of OSL measurements in the different channel positions were repeated several times. A measurement repeatability better than 6 % has been obtained. This value is comparable with the uncertainty in the absolute positioning of the sensor head inside the reactor irradiation channel. For each measurement point, precision better than 1 % has been obtained after ten consecutive measurements. All above tests confirm thus that the employed optical fibers don't show significant evidences of radiation damage in the neutron fluence range up to $5{\times}10^{13}$ cm^{-2} to which they were exposed in total during the different irradiation tests.

The design of the CERN real-time OSL prototype is currently under optimization in both the sensor head and the readout side, with the goal to extend the sensitivity range of the system of at least one order of magnitude in dose.

8.6 Neutron detection with OSL materials

OSL materials have been successfully used for HEP applications to measure the dose delivered by high-energy charged particles as it has been shown in the previous sections. Since there is a lack of on-line neutron dosimeters for HEP applications, especially for thermal neutron energies, the possibility to make OSL material sensitive to neutrons is a very attractive prospect. However, the response of "pure" OSL to neutron irradiation has still to be studied in detail, as a prerequisite to a possible use in the CERN radiation environments. This will be the topic discussed in this section. Moreover in this section, for the first time, the manufacture of "specially prepared" OSL materials will be presented together with the qualification process aiming to evaluate their neutron sensitivity and their energy dependence.

Neutrons do not produce direct ionization in materials; however, a little amount of ionizing energy is deposited via secondary particles generated by neutron interactions. The total neutron cross-sections for the elements constituting the used OSL material are in the order of a few barns for neutron energies ranging from thermal to several MeV. The resulting energy deposition is expected to be not sufficient to generate a measurable quantity of electron-hole pairs in pure OSL.

For this reason, to increase the OSL sensitivity to neutrons, different additives have been mixed with the standard OSL material. In particular: Boron (B) was added to increase the OSL sensitivity to thermal neutrons and polyethylene (PE) was added for fast neutron detection.

Boron is responsible for thermal neutron capture via the nuclear reaction:

$$^{10}B + n \rightarrow ^7 Li + \alpha + \gamma + 2.3 MeV. \quad (8.1)$$

This reaction has a very large cross-section σ_r = 3840 barns for thermal energies that decreases down to a few barns for energies above some tens of keV as shown in Fig. 8.18 [Exf]. The alpha particles and the lithium ions generated by the neutron capture loose their energy via ionization in the sensitive SrS material. The ranges of the two reaction products in the SrS were calculated with the SRIM software [SRI]. Taking into account that the 2.3 MeV released in the reaction contributes to the kinetic energy of the lithium ion (0.83 MeV) and the alpha particle (1.47 MeV), ranges of 2 μm and 4.2 μm in SrS were calculated respectively. These short path-lengths guarantee that all captured thermal neutrons deposit the full ionization energy in the OSL material.

PE with its high content of hydrogen is the preferred material to detect fast neutrons because a colliding particle can transfer from none to all its energy to the proton in one elastic collision. The average recoil energy will be half of the initial neutron energy. Hydrogen has a cross-section σ_s of the order of tens of barns for epi-thermal neutrons that falls to 4 barns for the energy of 1 MeV. It further decreases to approximately 1 barn when the neutron energy reaches 8 MeV as shown in Fig. 8.18. The recoil proton will move through the sensitive material with a path length depending on the energy transferred to it by the incident neutron.

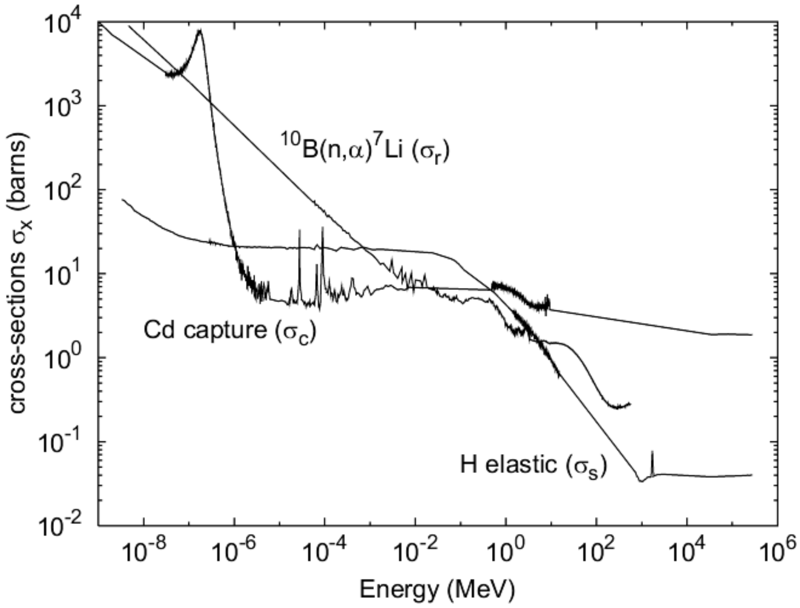

Figure 8.18: Plots of the neutron cross-section of interest for OSL materials.

8.6.1 Neutron-sensitive OSL materials

The pure OSL material and three compounds of OSL material doped with Boron and mixed with polyethylene were prepared and irradiated to different neutron fluences in different irradiation facilities. The four different types of OSL samples are shown in Fig. 8.19. They have a size of 5x5 mm^2 and various thicknesses. In particular, the used materials had the following characteristics:

1. OSL standard material *(OSL pure)*: specimens obtained from a 80 μm thick layer of SrS silk-screen printed on a Kapton foil (see also Sec. 8.1).

2. OSL doped with Boron *(OSL+B)*: specimens obtained from a 80 μm thick layer of SrS, 1 %-weight Boron doped, silk-screen printed on a Kapton foil. Boron was introduced in the OSL material through sintering and subsequent grinding procedures, ensuring the homogeneity of the obtained samples.

3. OSL mixed with Polyethylene *(OSL+PE)*: specimens gained from a bigger block in which the SrS was melted with polyethylene. The thicknesses of the samples were of a few mm.

4. OSL mixed with PE and Boron *(OSL+PE+B)*: OSL specimens containing both, PE and Boron. The thicknesses of these samples were also of a few mm.

Of each type of OSL material, 3 to 5 pieces were used during the irradiation test in order to prove the reproducibility of the results. They were packaged and irradiated in few micron-thick aluminum foils in order to protect them from light. Before irradiation, the samples were heated to 80 °C for 24 hours to anneal the charge in the OSL trap levels (i.e. to clear the dosimetric material).

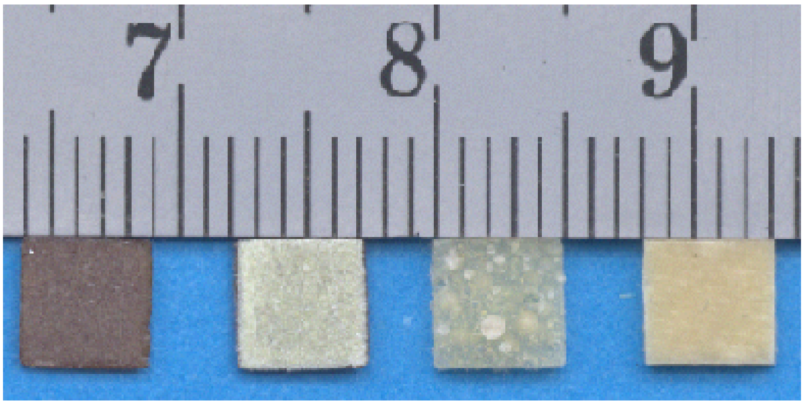

Figure 8.19: Samples of OSL materials. From left to right: pure OSL material, OSL doped with Boron, OSL mixed with Polyethylene and OSL mixed with Polyethylene and Boron.

8.6.2 Experimental procedure to characterize neutron-sensitive OSL materials

To qualify the different sets of OSL materials (see Sec. 8.6.1) in function of their neutron sensitivity and energy dependence, two specific irradiation facilities with complementary neutron spectra have been chosen.

In the facility IRRAD2 at the CERN-PS accelerator (see Sec. 4.1.1.3), the irradiations were performed in a cavity at 50 cm from the incident 23 GeV proton beam, in order to get an almost pure broad spectrum of high-energy neutrons. In this conditions, a hardness factor $k = 0.67$ has been calculated. In the TRIGA Mark II reactor at JSI, the irradiations were carried out placing the OSL samples into the reactor core through the F19 channel that occupies a fuel rod position and enters the reactor core from above as described in Sec. 4.1.2. In this way the irradiation is performed in a thermal-neutrons dominated particle spectrum. In this facility a hardness factor $k =$ 0.90 has been determined. The spectra of these two facilities have been plotted together in Fig. 8.20(a).

In the Ljubljana reactor, a series of OSL materials was exposed shielded by means of a 1.0 mm thick Cadmium (Cd) foil in order to irradiate them without the thermal neutron component of the reactor spectrum (see σ_c behavior in Fig. 8.18). The Cd thickness was chosen according to the thermal neutron mean-free-path that is of about 100 μm.

Together with neutrons, gamma rays are produced in both radiation environments. Gamma rays represent a contamination in both environments that is dependent on the operative conditions and thus needed to be measured during the OSL irradiations. Gafchromic Films HD-810 (see Sec. 3.1.7) and reverse biased silicon detectors (see Sec. 3.1.9) were used in both facilities to measure the Total Ionizing Dose (TID) and the neutron fluence respectively. Fig. 8.20(b) shows the results of the TID measurements performed in the two facilities. In the Ljubljana reactor, the TID measured for the samples irradiated in a Cd shielding (triangular markers) is presented separately from the unshielded samples (square markers). Due to the high gamma background in the Ljubljana reactor, the TID results are about a factor 10 higher than in the CERN

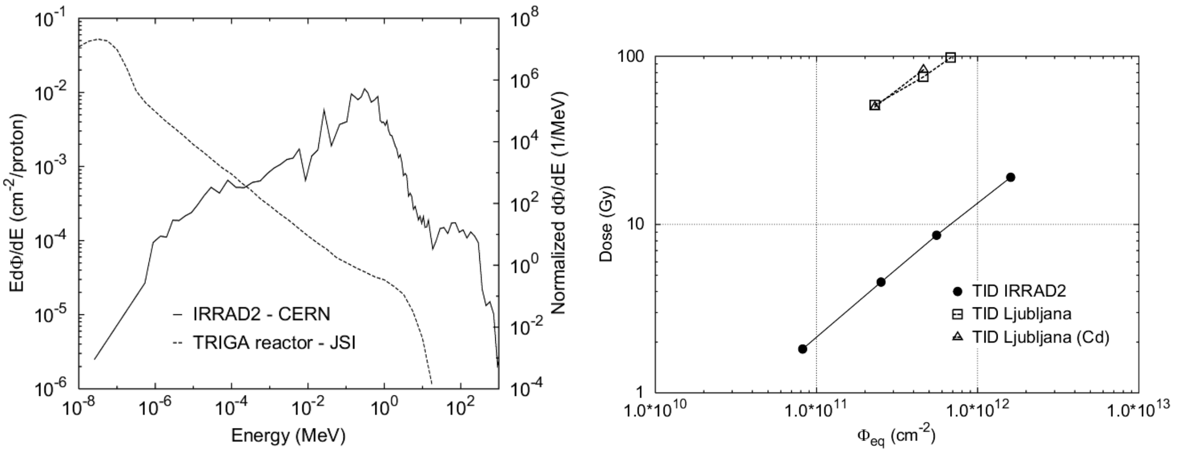

(a) (b)

Figure 8.20: Experimental facility for neutron irradiation of OSL materials. (a) Neutron spectrum in the IRRAD2 Facility (scale in left-hand y-axis) at 50 cm from beam axis normalized to one impinping proton (continuous line). TRIGA Reactor neutron spectrum (scale in right-hand y-axis) as measured from activation foils (dotted line). (b) TID measured in both irradiation facilities by means of radiometric films HD-810.

facility.

8.6.3 First irradiation test of neutron-sensitive OSL materials

In the two facilities, the OSL samples were exposed to increasing levels of Φ_{eq} in order to record the sensitivity curves for the different OSL materials. All samples were stored at room temperature and measured a few weeks after irradiation. As shown in Fig. 8.13 for the pure SrS material, the fading of the OSL materials was expected to be stabilized at the readout time. The OSL reader used for the readout of all these materials was the test-bench described in Sec. 4.2.2.

The signal (voltage) measured with the readout system has been normalized to the pure OSL sample's weight in order to take into account the different sample's volume. The so treated signals expressed in mV have been plotted versus the Φ_{eq}, and are presented in Fig. 8.21(a) and Fig. 8.21(b).

After both irradiations, the signal achieved with the *OSL pure* material is the smallest recorded in our tests, and is less than 10 mV as shown in Fig. 8.21(a). In the CERN facility (triangular filled markers), for values of Φ_{eq} below 1.0x10^{11} cm^{-2}, the signal was lower than the noise level since the gain of the read out system was set to measure high doses. For the Ljubljana facility (triangular empty markers) the signal is a factor 10 higher with respect to the one measured at CERN. This is in good agreement with the TID measurements presented in Fig. 8.20(b). As expected, the OSL pure material measured thus the ionizing component of the field and is essentially insensitive to neutrons.

Fig. 8.21(b) shows the first results obtained for the *OSL+B* and *OSL+PE* materials. In the higher fluence range saturation is observed. This is also expected for the OSL pure materials at fluences which are exceeding the range presented in Fig. 8.21(a) and this is

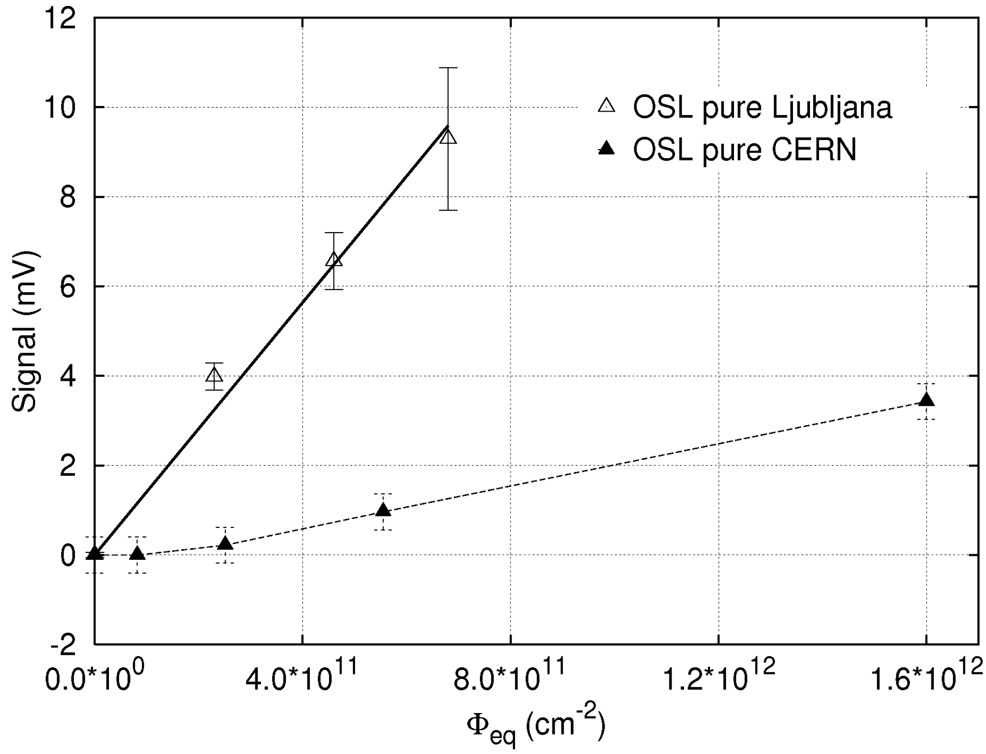

(a)

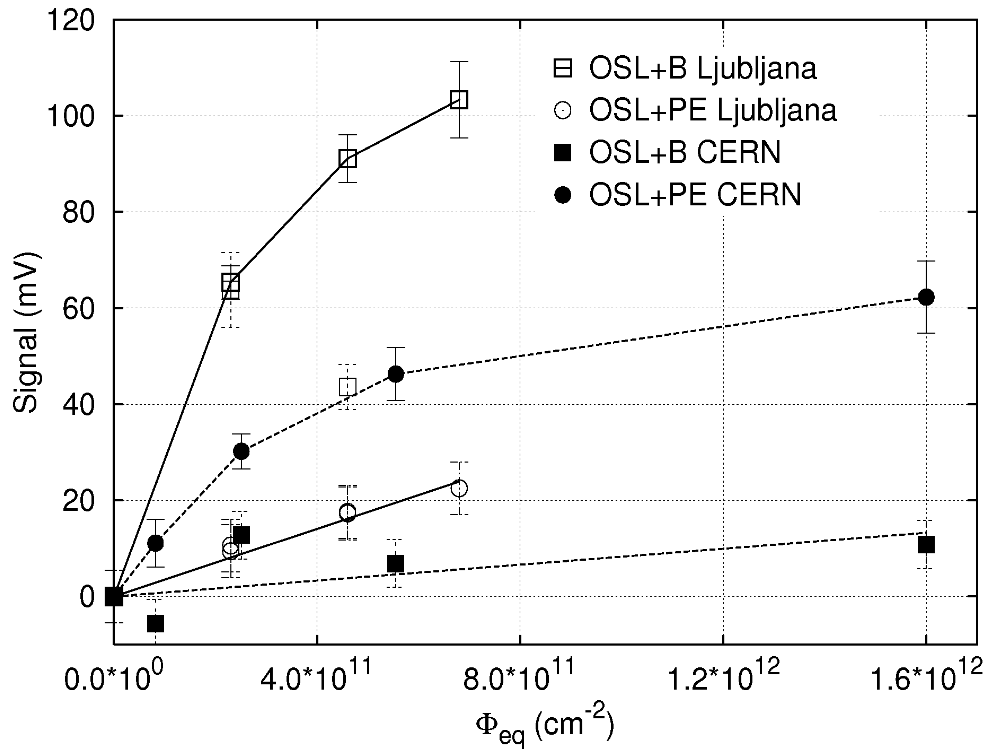

(b)

Figure 8.21: First irradiation for neutron-sensitive OSLs. (a) *OSL pure* material response after irradiation at CERN (filled markers) and Ljubljana (empty markers). *OSL+B* and *OSL+PE* material response after irradiation at CERN (filled markers) and Ljubljana (empty markers).

	$\frac{OSL+B}{OSLpure}$	$\frac{OSL+PE}{OSLpure}$
CERN - IRRAD2	4	25
Ljubljana - TRIGA	20.1	2.5

Table 8.1: Relative sensitivity of OSLs to neutrons.

	Thermal (< 1 eV)	Epi-thermal (1 eV - 50 keV)	Fast (50 keV - 4 MeV)	High-Energy (> 4 MeV)
CERN - IRRAD2	0.2 %	15.3 %	81.3 %	3.2 %
Ljubljana - TRIGA	52 %	28 %	17 %	3 %

Table 8.2: Spectra composition in the CERN (IRRAD2) and Ljubljana (TRIGA reactor) neutron facilities.

agreement with the experimental data for the charged particles that have been presented in Fig. 8.2 and in Ref. [Dus01]. For a comparison between the neutron-sensitive and the pure material linear fits have been applied to the data measured in the low fluence range. A 20 times increased sensitivity has been found in this way as presented in Tab. 8.1.

Assuming that the total neutron signal is given by the sum of the *OSL+B* and the *OSL+PE* signals, in the Ljubljana facility (continuous lines in Fig.8.21) for a $\Phi_{eq} = 2{\times}10^{11}\ cm^{-2}$, the measured signals from the *OSL+B* (square empty markers) and *OSL+PE* (round empty markers) samples represent 85 % and 15 %, respectively, of the total neutron signal. At CERN (dotted lines in Fig.8.21) and for the same neutron fluence, the signals obtained from the *OSL+PE* samples (round filled markers) represent more than 93 % of the neutron signal, as the *OSL+B* (square solid markers) samples gave only a little signal. All the above results are in good agreement (about 10-15 %) with the spectra composition of the two neutron environments shown in Fig. 8.20(a) and summarized in Tab. 8.2.

The strongly fluctuating signal of the *OSL+B* samples obtained at the CERN facility can be explained as a difficulty in the measurement of a signal that is close to the electronic noise level of the readout apparatus. Moreover, one of the samples irradiated in Ljubljana also shows a reduced response in the same fluence range (see the square empty markers at $4.6{\times}10^{11}\ cm^{-2}$ of Fig. 8.21). Again, an experimental problem is suspected, which requires cross checking in a forthcoming irradiation.

For the *OSL+PE+B* only the Ljubljana data are available. This material gave the same response as the *OSL+PE* that is already plotted in Fig. 8.21. The method employed to produce *OSL+PE+B* specimens leads to a predominant polyethylene fraction compared to the Boron one and is likely to account for this effect.

Finally, for the Ljubljana samples, an inter-comparison of *OSL+B* and *OSL+PE* samples irradiated with and without the thermal neutron component of the spectrum (i.e. without or with Cd shielding) is presented in Fig. 8.22. The shielded OSL+B and OSL+PE samples show a 10 % reduced response. However, according to calculations using the cross-sections of Fig. 8.18 and the Ljubljana neutron spectra of Fig. 8.20(a), the signals coming from the Cd-shielded *OSL+B* and *OSL+PE* samples were expected

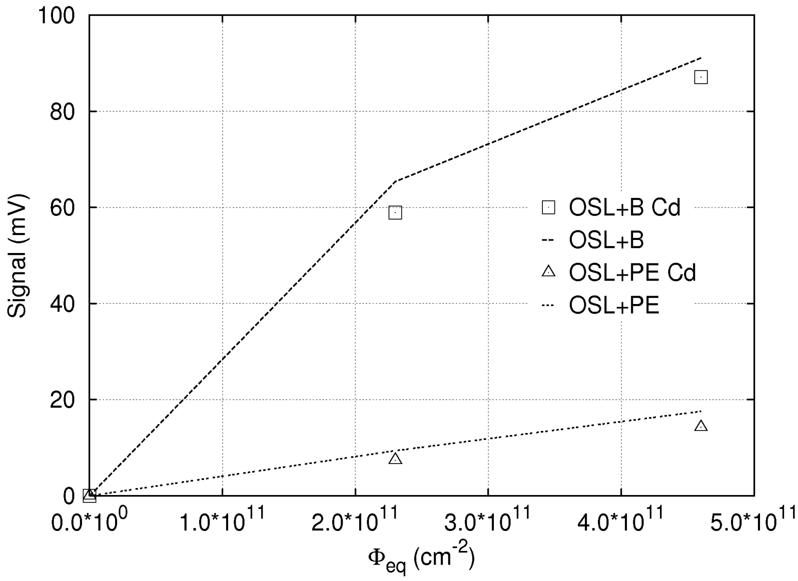

Figure 8.22: Series of samples irradiated in the Ljubljana reactor while a Cd shielding suppressed the thermal neutron component of the spectrum (markers). The signals measured for the samples irradiated with the whole spectrum (unshielded samples) are also shown for comparison (dashed lines).

to be reduced by about 70 % and a few percent with respect to the unshielded ones. The calculation for the *OSL+PE* samples take into account that recoil protons of energies < 100 eV release a negligible amount of energy in ionization processes into the sensitive material. The Cd shielding shouldn't thus have an effect on the signal measured from the *OSL+PE* samples. This is also observed in the experimental data presented in Fig. 8.22 where the difference between the shielded and the unshielded OSL+PE samples is within the relative errors of the experiment.

However, the drastic expected reduction of the signal for the Cd-shielded *OSL+B* samples is not observed. This could be due to the mechanical difficulties in the realization of a tight shielding using 1 mm thick Cd foil and will need to be clarified in a future experiment.

The maximum relative error evaluated on voltage measurement of samples of the same type exposed to the same irradiation environment (usually 3 to 5 samples used per data point as described in Sec. 8.6.1) over all series of irradiated OSL materials was 7.9 % and 12.0 % for the Ljubljana and for the CERN samples respectively, proving a good reproducibility of the measured results.

One error source to take into account in the presented neutron measurements is probably a misalignment that can occur during the positioning of the irradiated specimens in the samples holder of the test-bench. For the difference in their manufacture, not all samples were fitting the samples holder in the same way.

8.6.4 Validation tests for neutron-sensitive OSL materials

The irradiation tests presented in the previous Sec. 8.6.3 let some open questions about the response of the OSL materials to neutrons. In particular:

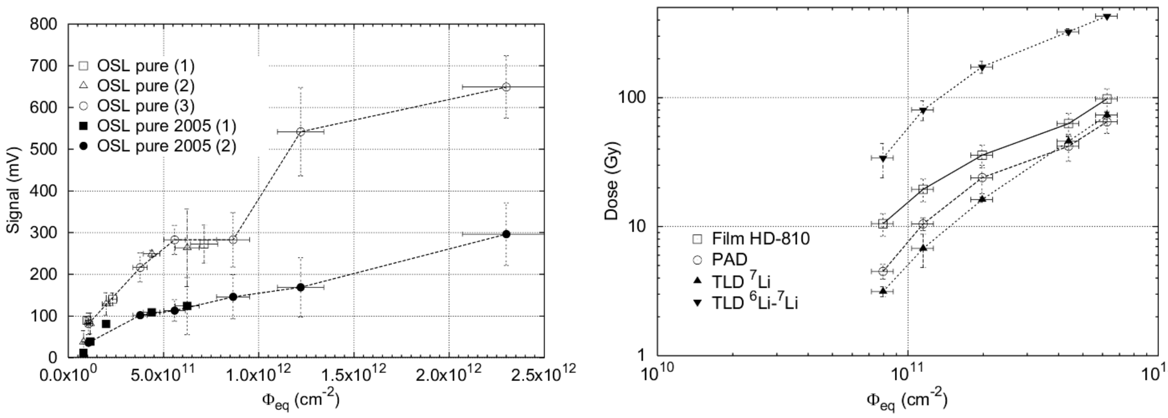

(a) (b)

Figure 8.23: Complementary irradiations for neutron-sensitive OSLs. (a) Data of three independent irradiation on *OSL pure* materials. The empty markers correspond to the irradiation of the standard material, while the filled ones are the results of irradiations for a new series of OSL produced in 2005 in which the OSL powder was grinded to a grain size lower than 50 μm. The lines have been plotted as guidelines within different data sets. (b) Independent TID measurements in the Ljubljana TRIGA reactor carried out with Film HD-810, PAD and TLD with ^{7}Li and ^{6}Li passive dosimeters.

1. the response of the *OSL pure* material to neutrons was not investigated at Φ_{eq} levels greater than $5{\times}10^{11}$ cm^{-2};

2. the characterization of the response of the *OSL+B* material has to be detailed in order to better understand the role of the boron doping in such materials.

To answer to the first question, three new series of *OSL pure* have been independently irradiated in the Ljubljana TRIGA reactor until a Φ_{eq} of about $2.5{\times}10^{12}$ cm^{-2}. The measurements of these samples, performed with the usual OSL test-bench and after several weeks of storage after irradiation, have been plotted in empty markers in Fig. 8.23(a). The *OSL pure* response curve follows a linear behavior up to a Φ_{eq} of $5{\times}10^{11}$ cm^{-2} as it has been already shown in Fig. 8.21. At higher fluences, the signal show a saturation level up to about $1{\times}10^{12}$ cm^{-2}. After this point the signal start to growth linearly again, with a different slope with respect to the previous one. In all OSL measurement results presented in this section, the x-axis error bars indicate the error in the fluence measurement that has been quoted to 10 % from the readout of reverse-biased silicon detector structures exposed together with the OSLs. The y-axis error bars represent instead the random error valuated by averaging several OSL samples exposed to the same particle fluence level.

These measurements can be compared with a set of independent TID measurements performed by means of passive dosimeters as shown in Fig. 8.23(b). Due to their low thermal-neutron sensitivity the Film HD-810, the PAD and the ^7Li based TLDs are supposed to measure mainly the reactor photon background and the fast-neutron KERMA as the *OSL pure* material. The dose deposed by thermal neutrons is instead an order of magnitude higher as shown by the curve (reverse triangular markers) plotted in

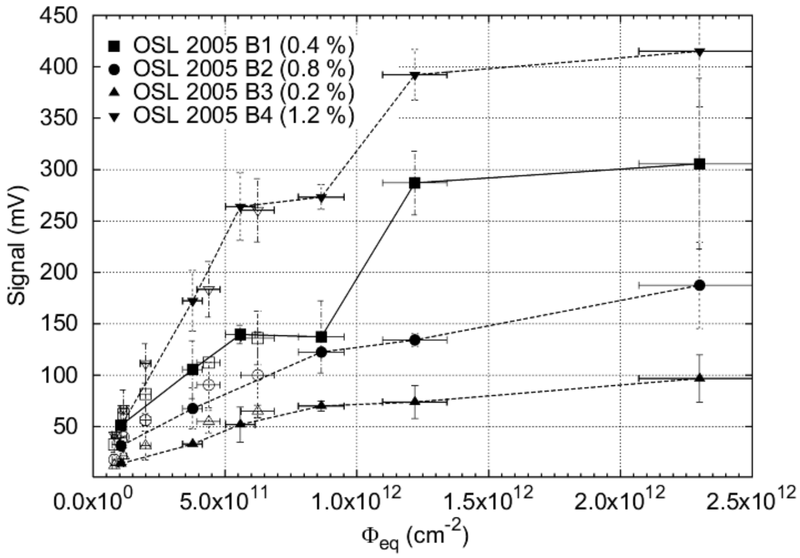

Figure 8.24: *OSL+B* samples prepared on the new 2005 OSL material. The four materials have been made by four different boron doping and are labeled from B1 to B4 (see details in the text). For any materials two independent set of samples have been irradiated and plotted with empty and filled markers respectively. The lines have been plotted as guidelines within different data sets.

Fig. 8.23(b) that represent the differential dose measured by means of TLDs ^{6}Li and ^{7}Li. All measurements presented here agrees that in the region of $5{\times}10^{11}$ cm^{-2} a TID level in the reactor reached 100 Gy that has been identified as the saturation limit of the used material after charged particle irradiations (see Fig. 8.2).

Together with the first version of *OSL pure* material, a new raw OSL material has been produced in 2005 by the *University Montpellier II* and tested at the Ljubljana TRIGA reactor. This OSL powder has been grinded to a grain size lower than 50 μm and it has been labeled *OSL pure 2005* in the following plots. From this new base product, four different *OSL+B* samples have been produced and their sensitivity to the mixed γ/neutron field have also been measured for the first time.

Fig. 8.23(a) show, with filled markers, the sensitivity of two sets of the OSL 2005 material in the TRIGA reactor. This new OSL shows a reduced sensitivity of about a factor 2 and doesn't show evidence of saturation in the investigated Φ_{eq} range. The lower sensitivity is most likely due to the lower grain size of the OSL powder.

From this new *OSL pure 2005* four boron-doped OSL samples have been prepared. These samples, labeled from B1 to B4, contained 0.4 %, 0.8 %, 0.2 % and 1.2 % (weight) of boron respectively. Moreover, the material B1 was submitted to a double thermal cycle during the OSL sintering procedure. The results of the exposure of these materials in the radiation field of the JSI TRIGA reactor are shown in Fig. 8.24. Two different sets of *OSL+B* materials have been exposed and they are plotted by filled and empty markers in the figure.

Altought a more accurate calibration of this materials has to be performed, this first irradiation test allow to underline the following points that should be taken into account in the future preparation of new series of thermal-neutron sensitive materials:

- The *OSL+B* sensitivity scales with the boron doping-level for the materials prepared with the same procedure. This is shown in Fig. 8.24 where the materials B3, B2 and B4 (various markers linked with dotted lines) show an increasing sensitivity as the doping level increases (from 0.2 % to 1.2 %).

- An higher boron doping level can lead to the appearance of signal saturation at the same fashion of the *OSL pure* materials as observed in Fig. 8.23(a).

- The processing conditions can affect the OSL sensitivity as shown from the OSL B1 (0.4 %-doped) that after being submitted to a supplementary thermal cycle, results more sensitive than the material B2 doped with a doubled boron concentration (0.8 %).

- The amplitude of the signal measured with lightly B-doped samples (0.2 % to 0.8 %) is lower than the one measured with the *OSL pure 2005* material. Although further tests are needed to understand the origin of this phenomenon, at this moment it is not possible to exclude a possible influence of the Boron doping on the OSL's fading behavior.

8.7 Conclusion

In this chapter an evaluation of the OSL material response to hadron environments has been carried out as well as tests of different types of OSL-based integrated sensor assemblies.

The response of the "pure" OSL material has been studied in detail as well as its neutron sensitivity. The fading of the material has been measured at different temperatures and it has been found to be a possible limiting factor in the operation of an integrated sensor in facilities where temperatures can exceed 30 °C. Studies on the possibility to enhance the neutron sensitivity of the OSL materials have been carried out. Specially prepared OSL samples mixed with polyethylene or doped with boron were manufactured for the measurement of fast and thermal neutrons respectively. Although it was possible to measure and discriminate with a good accuracy (within about 20 %) two complete different neutron spectra, these new materials are still in the development phase and the reproducibility within the different sensor batches has still to be improved. In particular the response of the boron-doped OSL is very dependent on the samples manufacturing. The measurements presented here supply several results that are giving valuable indications for the preparation of a new generation of boron-doped samples.

The characterization of integrated sensors based on OSL-material in hadron environments has also be discussed in this chapter. The integrated sensor considered here was based on a sandwich LED/OSL/photodiode exposed, together with its readout electronics, to the radiation field to be measured. This assembly proved already to work successfully in space applications. This sensor scheme was investigated at CERN with the aim to include it in a fully integrated systems together with the RadFETs and *p-i-n* diode active devices studied in this thesis work. Unfortunately, the LHC-like hadron environment results to be very effective in damaging the commercial electronics required for the OSL readout. Several improvements have been realized on the electronic design and in the component selection. However, it was not possible, with such a readout scheme and taking into account dimensions, weight and power consumption constraints, to fully exploit the high sensitivity properties of the employed OSL material.

By using another OSL-sensor approach, the radiation hardness issues have been faced by moving the readout electronic out from the radiation environment under measure. This has been realized by means of radiation hardened optical fibers that are used to collect the light signals from a small OSL crystal. This readout scheme opens the possibility to the utilization of a couple of commercial laser/PM devices for the OSL readout. The high efficiency achieved in the optical stimulation and in the light collection, gives to the first prototype tested at CERN a sensitivity to ionizing doses down to the mGy range. This sensor approach became therefore a promising possibility for the radiation monitoring at the LHC experiments.

Chapter 9

Dosimeters low dose-rate response in mixed-hadron environment

The two RadFET devices (REM and LAAS) and the two *p-i-n* diode (BPW34F and CMRP) semiconductor dosimeters selected for the LHC experiments (see Chapter 6 and Chapter 7) will be employed at the Experiments of the CERN LHC accelerator in different conditions with respect to the ones encountered during the characterization phase.

The calibration curves presented in the precedent chapters have been produced in "accelerated" radiation tests (e.g. carried out during a few days) that bring the sensors to the final exposure level in a very short time with respect the real LHC operation schedule where TID and Φ_{eq} will be integrated over 10-years time. During calibration runs, the particle type and energy, the radiation intensity as well as the environmental condition are kept constantly under control. On the other hand, once these semiconductor sensors will be installed in their array positions at the LHC experiments, they will be exposed to challenging operational conditions including:

- particle runs of variable intensity with monthly shutdown periods (see Sec, 2.2.1);
- radiation compositions varying with the distance and the angle with respect to the interaction point;
- different operating temperature in different measurement sites.

In these conditions, the sensor stability and reliability issues become fundamental to provide precise radiation field measurements over time.

Even if a comprehensive simulation on the 10-years of LHC is clearly not possible, the goal of this chapter is to validate the performances of the above four semiconductor sensors by placing them in a low dose-rate (LDR), mixed-particle accelerator environment that is close to the one expected inside full working LHC particle detectors.

To do this, the sensors were exposed over three months in the secondary environment of the CERN-IRRAD6 facility that provides mixed high-energy particles at low rates by working off-axis in the 23 GeV proton beam-line directed to the IRRAD1 shuttle system as described in Sec. 4.1.1. Placing the sensors at different distances from the beam axis, various rates of high-energy photons, neutrons and charged particles in the

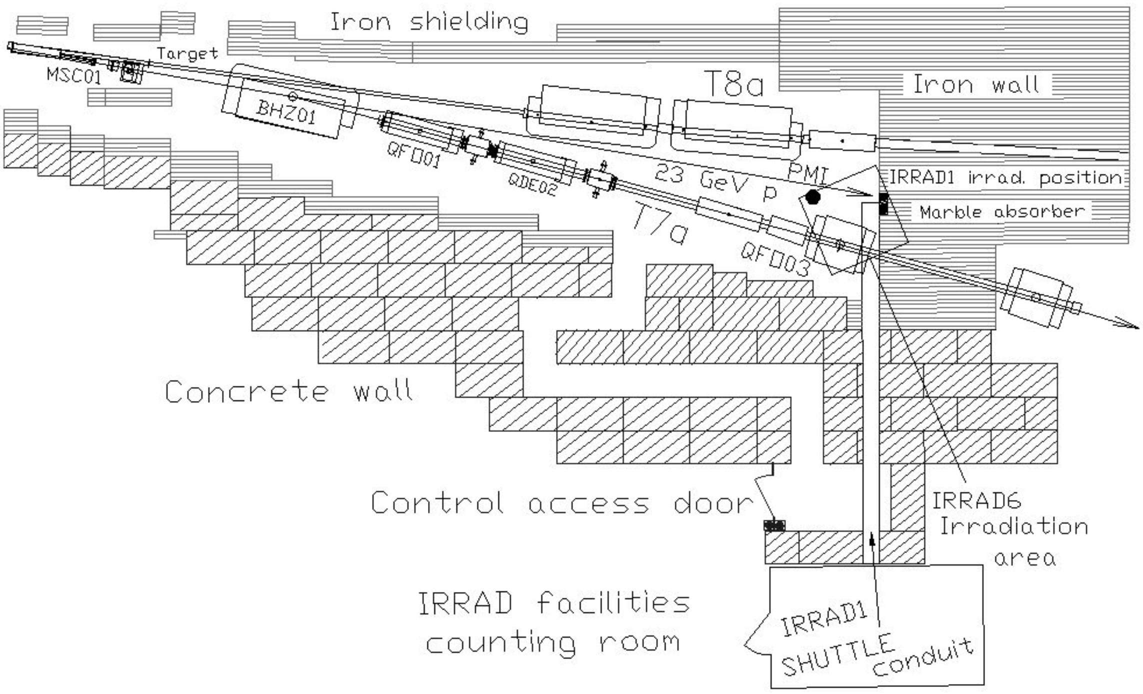

Figure 9.1: Layout of the IRRAD1 and IRRAD6 facilities at the CERN-PS Accelerator.

GeV energy range were therefore simultaneously available. Moreover, changes of beam conditions and the alternation of operation and shutdown periods, made this facility an ideal test-bench to validate the device's stability over time.

The results of this long-term irradiation campaign are presented in the following sections and are discussed and compared with measurements by other dosimetric means as well as Monte Carlo simulations.

9.1 Experimental setup for the LDR test

9.1.1 Irradiation conditions

In the T7 beam-line of the *East-Hall* Experimental Area of the CERN-PS Complex, primary 23 GeV proton bursts of $2\text{x}10^{11}$ particles each are delivered towards a marble absorber placed in front of a cast iron beam-dump as shown in Fig. 9.1. In that location, where the IRRAD1 facility is located as explained in Sec. 4.1.1, the protons produce a uniform irradiation spot over a surface of about 2x2 cm^2 [Gla99]. Typically from 2 to 4 proton bursts per machine cycle of 16.8s are extracted from the PS accelerator and delivered toward T7. This irradiation layout will be referred as *"Primary Beam conditions"* in the following. During the operation of IRRAD1, the 23 GeV proton interactions produce in the surrounding area a radiation field mainly composed by neutrons, photons, pions and protons. This setup has been described earlier in this work as the IRRAD6 facility (see further details in Sec. 4.1.1.2).

Moving downstream along the T7 beam-line, another test-beam facility (called "T7-secondary") can run in order to provide the users with a non-separated lower-energy

Label	r = 60	r = 90	r = 100	PMI Loc.	Mag. QF003
Z (cm)	15	15	15	130	60
r (cm)	60	90	100	80	140

Table 9.1: Location of tested devices in IRRAD6.

secondary particle beam composed by p^+, $\pi^\pm$ and $e^\pm$ [Sim93]. This secondary beam is produced by inserting a thick target in the 23 GeV proton beam and modifying the magnetic field of the BHZ01 element (see Fig. 9.1). In these conditions, particles from the target with a selected momentum are bent over the T7a beam-pipe located in the right-hand side with respect the IRRAD1 position. While the secondary beam is thus delivered to the users of "T7-secondary", the IRRAD1 facility, and consequently the IRRAD6 environment, is reached by a degraded primary proton beam. This irradiation set-up will be referred as *"Secondary Beam conditions"* in the following.

The instrumentation available in the T7 area consist of a Secondary Emission Chamber (SEC) labeled MSC01 in Fig. 9.1 that provides a measurement of the intensity for the primary protons delivered to IRRAD1 [Ber97]. An Ionization Chamber (PMI in Fig. 9.1) is also installed on the ceiling of the irradiation area for measuring the dose-rate due to induced activity during maintenance operations.

9.1.2 Setup of the devices under test

For this irradiation test, the REM and LAAS RadFET dosimeters were encapsulated in sealed TO-5 metal packages and the recorded signals were converted to dose D (Gy) following the power-low calibration curve of Eq. 3.5. The reader is sent to Chapter 6 for the details about the currents that have to be applied for the devices readout as well as the experimental calibration parameters for the two RadFET devices under studies.

As shown in Chapter 6 annealing phenomena that affect the RadFETs selected for the Experiments of the LHC are of the order of a few percent over years time-scale. For this reason, the data presented in this chapter were not corrected for such an effect.

To measure the Φ_{eq}, the two selected *p-i-n* diodes from CMRP and the BPW34F were instead used. For both devices, the recorded dosimetric parameter is the shift of the forward voltage V_F that increases linearly with the Φ_{eq} following Eq. 7.9 and Eq. 7.3 under 1 mA forward current bias. The BPW34F were exposed to the radiation field without being pre-irradiated.

Both RadFETs and *p-i-n* diodes were exposed in "zero bias" mode and the dosimetric parameters (voltages) were read-out by forcing different pulsed currents through them by using the DAQ system described in Sec. 4.2.1. The DAQ system was set to periodically run the sensors readout sequence. Finally, before converting the voltages to dosimetric quantities, the recorded signals from the sensors were corrected against temperature variations using the set of T_c reported in Chapter 6 and Chapter 7.

RadFET and *p-i-n* diode sensors were placed at five measurement points in the IRRAD6 area facing the cast iron beam-dump as indicated in Fig. 9.1. Table 9.1 details the measurement positions as well as their labeling used in the discussion of the results. The coordinate Z is the distance from the beam-dump calculated along the beam-line,

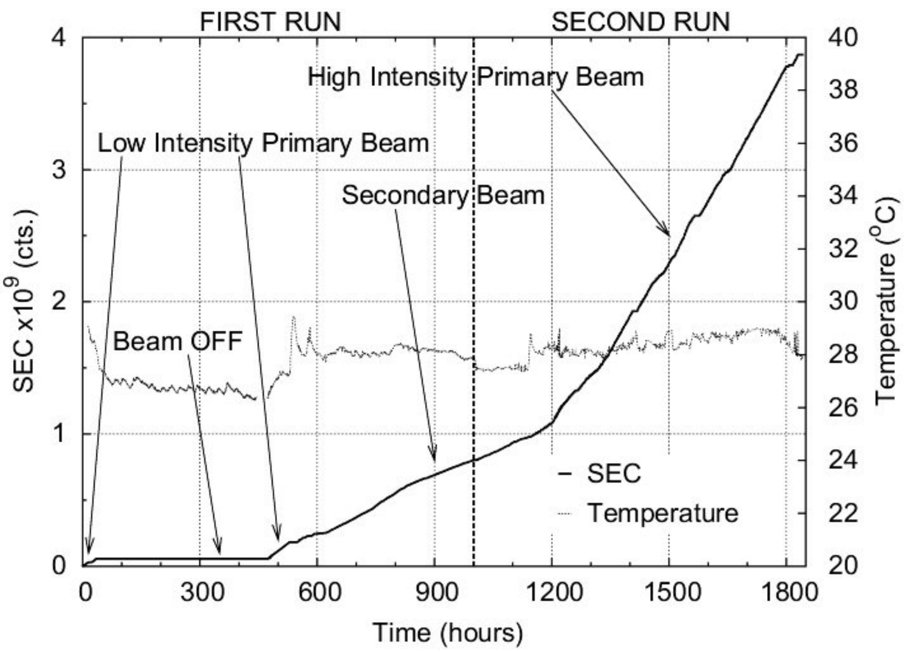

Figure 9.2: Intensity of the 23 GeV proton beam delivered to T7 for the LDR irradiation test.

while r is the radial distance from the beam-axis.

Three measurement positions were chosen, at different radii, close to the marble absorber (*r = 60, r = 90* and *r = 100*) while the other two were in proximity of the beam-line element named QF003 (*Mag. QF003*) and the PMI Ionization Chamber (*PMI Loc.*) represented as black dot in Fig. 9.1.

Each sensor was then connected to the readout system via 25-m coaxial cable. LAAS RadFETs and both CMRP and BPW34 *p-i-n* diodes were installed in their array positions from the beginning of the irradiation test. REM RadFETs were instead added to the setup during an accelerator shut-down period 1000 hours after the beginning of the experiments.

9.2 Results and Discussion of the LDR measurements

The irradiation period lasted about three months (1900 hours). The intensity of the primary 23 GeV proton beam delivered to the irradiation area in this period (in terms of counts from the SEC) is shown in Fig. 9.2. During the tests, the beam conditions in the T7 area were switched several times from *Primary* to *Secondary* beam and back, according to a pre-defined schedule. Therefore, to simplify the discussion of the results data have been grouped in two separate runs:

- *First Irradiation Run from 0 to 1000 hours*: After about 50 hours in which the PS beam was normally extracted and directed to the irradiation area (*Low Intensity Primary Beam*), a severe beam-line failure occurred and the T7 beam-line was shut down for about 500 hours (*Beam OFF*). Then, after about 100 hours from the recovery of the beam (i.e. 600 hours in Fig. 9.2) the T7 beam-line was setup for the delivery of the *Secondary Beam*.

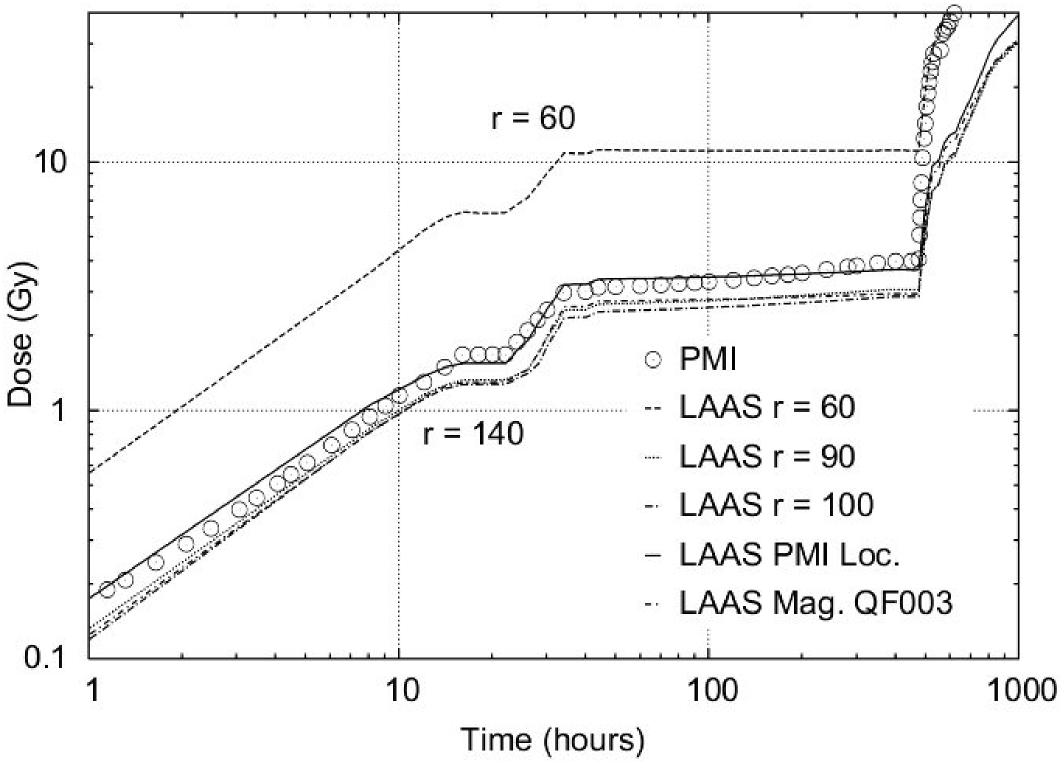

(a) Radiation Dose

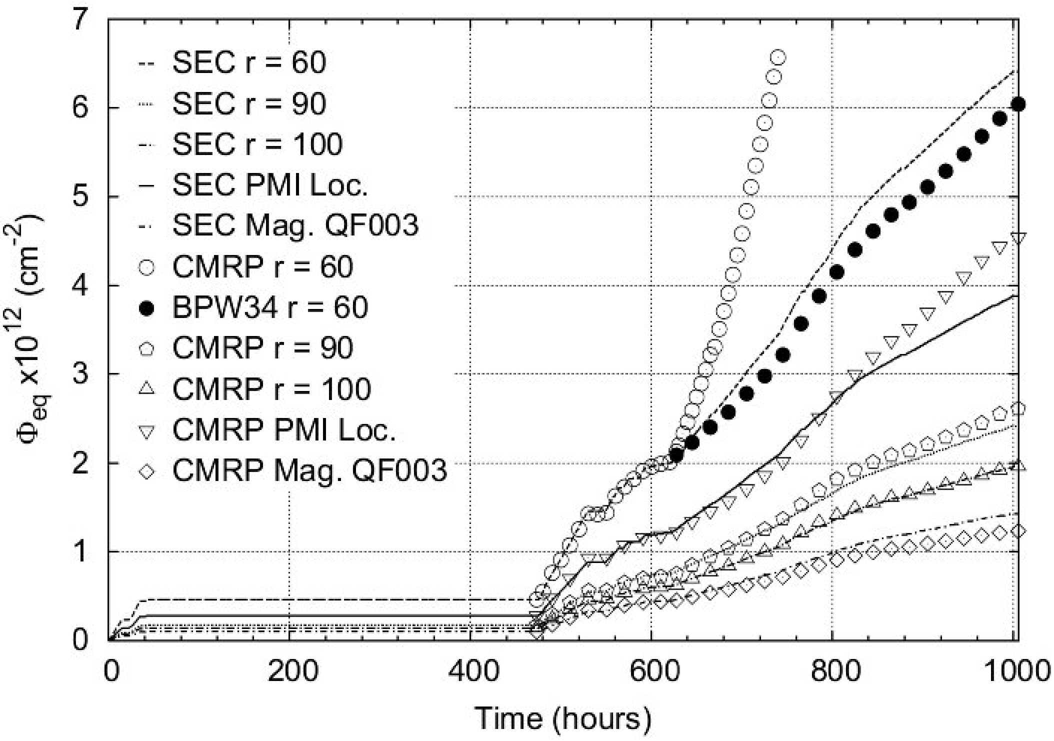

(b) Equivalent Fluence

Figure 9.3: Radiation measurements during the first irradiation run.

- *Second Irradiation Run from 1000 to 1900 hours*: The setup for the *Secondary Beam* was maintained for the first 200 hours before changing back to the *Primary Beam* conditions until the end of the experimental run. In this last part, starting from 1200 hours, the proton intensity was about twice the previous one (*High Intensity Primary Beam*).

The average temperature recorded in the test area was of 28 °C ± 1.5 °C as shown in the secondary y-axis of Fig. 9.2.

9.2.1 First Irradiation Run

9.2.1.1 Measurements

Fig. 9.3 shows all measurements recorded during the first irradiation run. In Fig. 9.3(a) the doses measured with the LAAS devices have been plotted with different lines for the various locations. The dose recorded with a LAAS device at the PMI Location is compared with the one directly measured with the PMI Ionization Chamber (circular markers in Fig. 9.3(a)). The agreement of the two measurements is very good for absorbed doses < 10 Gy.

It has to be noted that, even if the operation with protons was suspended during the period from 50 to 500 hours, the sensors were exposed at the PMI location to a remanent dose-rate of about 2 mGy/h due to scattered particles from the neighboring secondary beam-lines running in the *PS East-Hall*. During this period the signal of the LAAS devices continued to increase even at this very low dose-rate, demonstrating the high sensitivity of such devices. Once the operation with protons restarted, the dose-rate in the area increased to a level that saturates the PMI readout electronics (> 400 mGy/h), making a further use of this signal as a reference for the devices under test impossible [Vin06].

In Fig. 9.3(b) the Φ_{eq} recorded by the CMRP devices have been plotted with open markers. To verify the linearity in the response of these devices, the experimental data were linearly fitted by scaling the proton beam intensity of Fig. 9.2 with a series of conversion factors m_i (SEC counts $\mapsto \Phi_{eq}$) for any given measurement locations. The results of these calculations are plotted with different lines in Fig. 9.3(b). For all CMRP devices, the measurements fit well the data over the entire run when Φ_{eq} is lower than the sensor's dynamic range (i.e. < 2x10^{12} cm^{-2}). Even for the location in which the particle flux was the less intense (*Mag. QF003* plotted with diamond markers) the sensor behaves linearly with the calculation, proving that annealing phenomena that could affect such devices are lower than the measurement error.

For the measurement position *r = 60* on Fig. 9.3(b), in which the flux of particle was the highest recorded, the signal of the BPW34 diode has been plotted with filled circular markers. This signal has been normalized to the last measurement point of the CMRP device at Φ_{eq} = 2x10^{12} cm^{-2}. The BPW34 signal is in agreement with the calculation (dotted line) within the calibration error (20 %) if, already for this relative high particle intensity, the raw data are corrected against both short- and long-term annealing phenomena. Before converting the forward voltage shift to Φ_{eq}, ΔV_F has been corrected for the long-term annealing by using the parameterization described in

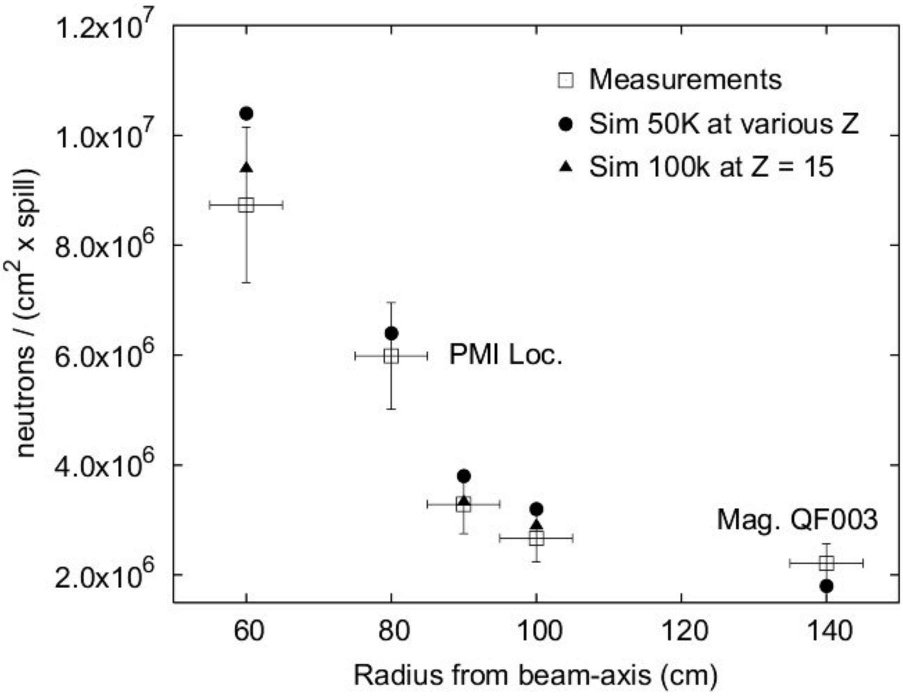

Figure 9.4: Monte Carlo simulations for IRRAD6 operated with *Primary Beam* and comparison with CMRP measurements.

Sec. 7.1.4. The applied corrections account also for the temperature variations over the experimental period displayed in Fig. 9.2.

9.2.1.2 Comparison with Monte Carlo Simulations

To validate the absolute Φ_{eq} presented in Fig. 9.3(b), the CMRP results have been compared with two sets of Monte Carlo simulations performed for IRRAD6 [Ler98] (See Sec. 4.1). The two simulations, labeled *Sim 50k* and *Sim 100k*, differ in the number of generated primary events (5x10^4 and 1x10^5 primary 23 GeV protons respectively) and slightly in the layout and materials used to model the T7 area. Moreover, while the *Sim 50k* has been run for different pairs of coordinates r and Z, the *Sim 100k* predicts only the variation of the radiation field along the radius from the beam axis at a fixed Z of 15 cm.

To compare particle fluence measurements and simulations, the set of scale parameters m_i previously calculated in Section 9.2.1.1 (1-MeV$_{eq}$ part./(cm^2 $\times$ counts)) were normalized to the intensity of a single primary proton burst (1-MeV$_{eq}$ part./(cm^2 $\times$ spill)). Knowing the *hardness factor* for the IRRAD6 area, it is then possible, via Eq. 2.2, to express the experimental data in terms of part./(cm^2 $\times$ spill) and proceed with the comparison.

Fig. 4.2(a) of Sec. 4.1 show the particle spectra predicted with the *Sim 100k* for the measurement position $r = 60$. In this location the neutron component appears already to dominate with respect to the charged particles that represent only a few percent of the total number of particles. The *hardness factor* was calculated to be $k = 1.21 \pm 9.1$ % folding the neutron spectra of Fig. 4.2(a) with known neutron NIEL

Kerma factors [AST94]. The error calculated for k takes into account the contribution of the charged particles to NIEL and the energy variation in the simulated neutron spectra moving in IRRAD6 form 60 cm to 140 cm in radius from the beam axis.

Fig. 9.4 shows the comparison between the measurements carried out using the diodes (open markers) with the two simulations (filled markers). The error associated to the measurement (± 16.2 %) takes into account the uncertainties in the CMRP diodes calibration (see Sec. 7.2.1) as well as the one in the evaluation of the k factor. The data of the *Sim 100k* (triangle markers in Fig. 9.4) are only available for Z = 15 while the *Sim 50k* has been run for different Z values (round markers). At positions closest to the beam axis, the Monte Carlo simulations overestimate the experimental measurements. This finding is in agreement with [Bac00] where similar results where found by means of experimental measurements using activation foils [Cha66]. The *Sim 50k* are shown to be overestimates with respect to the experimental measurement up to more than 20 % for the closest position to beam-axis where the higher particle gradient may enhance the errors for both measurements and simulations. The *Sim 100k*, show instead an agreement better than 10 % with the experiments. These two results confirm thus the validity of CMRP diode measurements.

9.2.2 Second Irradiation Run

Fig. 9.5 shows all measurements recorded during the second irradiation run. In Fig. 9.5(a) the results from REM devices have been compared with the TID measurements carried out with Polymer-Alanine dosimeters (PAD) [Con93]. In the figure, the PAD measurements are the filled markers at 1900 hours, while the lines are the scaling of the dose from PADs using the proton intensity plotted in Fig. 9.2. The TID values measured from RadFETs agree for all positions with PAD measurements within an experimental error of ± 10 %. The choice of PAD dosimeters to validate the measurement from REM RadFETs become clear if the contribution to the TID of photons (γ), neutrons (n) and charged hadrons ($Ch.H$) in the mixed radiation field are considered separately as shown in Eq. 9.1 and Eq. 9.2. In the formulas, K_i^j are the IEL Kerma factors [Cha99, Hub82] where $i = \gamma$, n or $Ch.H$ and j = P for PAD or R for REM devices. Φ are instead the different particle fluences, while the numerical factors take into account the relative sensitivity for neutrons of the two dosimeters with respect to the gamma rays.

$$D_{PAD} = K_\gamma^P \times \Phi_\gamma + (0.2) \times K_n^P \times \Phi_n + K_{Ch.H}^P \times \Phi_{Ch.H} \tag{9.1}$$

$$D_{REM} = K_\gamma^R \times \Phi_\gamma + (0.6) \times K_n^R \times \Phi_n + K_{Ch.H}^R \times \Phi_{Ch.H} \tag{9.2}$$

From the K_i^j factors of Tab. 9.2 it is easy to verify that, in the energy range from 4 MeV to several GeV, even if from Fig. 4.2(a) it is that $\Phi_{Ch.H} \sim 0.1 \times \Phi_n \sim 0.1 \times \Phi_\gamma$, the charged particle component delivers to both PAD and REM a TID about two order of magnitude higher than the one deposed by neutrons and photons. In such conditions PAD dosimeters are expected to be a good benchmark for the REM dosimeters.

With different filled markers, Fig. 9.5(b) shows the Φ_{eq} measurements recorded by the BPW34 diodes. The scaling of the primary beam intensity for any measurement

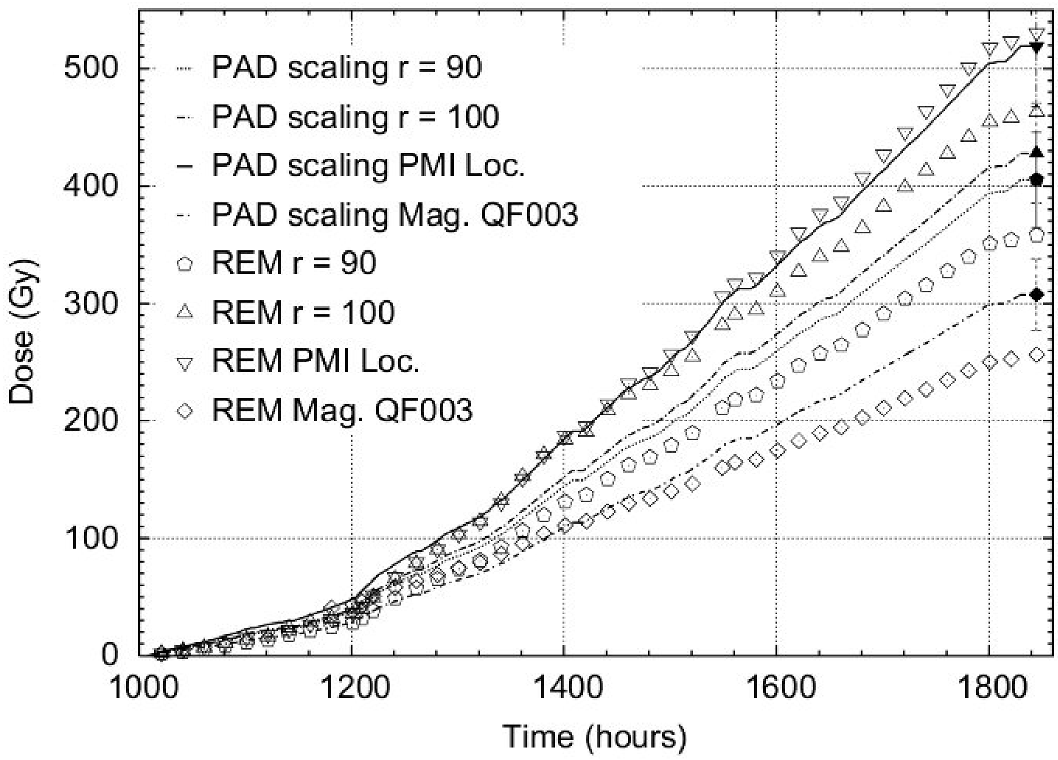

(a) Radiation Dose

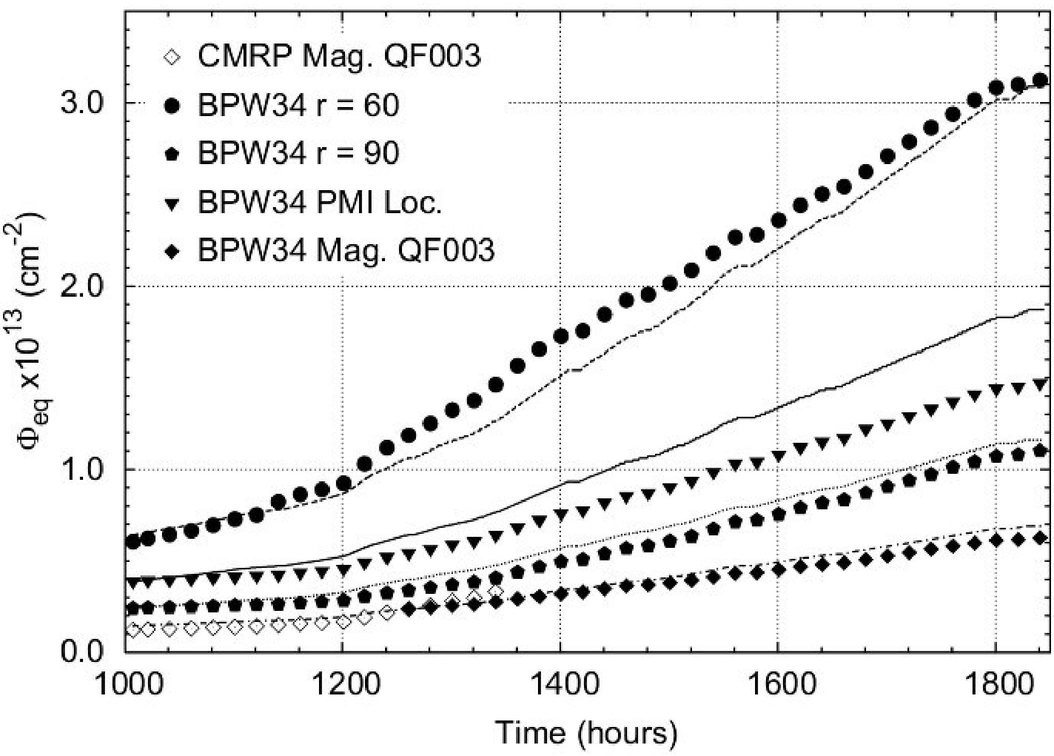

(b) Equivalent Fluence

Figure 9.5: Radiation measurements during the second irradiation run.

Dosimeter	KERMA Factors (pGy×cm^2)		
	γ	n	$Ch.H$
PAD	10 → 50	40 → 100	∼ 10^4 → 320 (MIPs)
REM	10 → 50	2 → 70	∼ 10^4 → 320 (MIPs)

Table 9.2: KERMA factor ranges from Ref. [Cha99, Hub82] for the radiation types and energies of the IRRAD6 facility at CERN-PS.

location, as calculated in Section 9.2.1.1, has been again plotted with lines for comparison with the experimental data. As previously pointed out, with the opportune annealing correction, the signal of such a devices match, in all cases, the predicted Φ_{eq} within the uncertainty of about ± 20 % that affects the calibration data.

9.2.3 Discussion of the ratio "REM response/LAAS response"

In the second irradiation run, the responses from the LAAS devices, already exposed to a TID exceeding some tens of Gy during the first run, are of interest. For doses exceeding 10 Gy their response curve becomes strongly sub-linear, i.e. begins to saturate. Although the responses of all MOSFETs under "zero bias" are always strongly sub-linear [Hol02, Hug86], the REM devices at the same total dose are not saturating in this way. The saturation mechanism is not known but it is clear that further electron escape might be retarded by built-in oxide fields due to oxide-trapped positive charge [Hug86, Pea01]. At a TID of 500 Gy the saturation of LAAS devices is nearly complete. The REM devices have been instead proven to have smoothly rising radiation response curves over a range of several tens of kGy under exposure to many different types of radiation [Rav05a].

In Fig. 9.6, we show the "R/L ratio", i.e. the sensitivity of the REM devices with respect the LAAS ones during the second irradiation run. *Primary Beam* registers a ratio of 3, while the *Secondary Beam* registers a factor of 2. In GeV proton experiments, it may be of practical benefit to monitor the "R/L ratio", as will be explained later.

As with the saturation effects in zero-bias cases, the exact mechanism of the clear-cut change in "R/L ratio" is not clear. The explanation is likely to arise from the plentiful creation of secondary (scattered) protons and other charged particles in the second case. This is because the *Secondary Beam* has been scattered from a thick target placed in the primary beam.

The number of secondaries in the IRRAD6 area is known to scale with the number of particles directed to the beam-dump, and these are duly counted by the SEC. However, many aspects of beam focusing are altered so that the beam-spot geometry changes. Many new possibilities of generating neutrons and photons at the measurement locations in IRRAD6 are created. In addition, the proton energies have degraded to just the region where previous workers [Pea01, Kro95] have discovered severe dependence of the MOSFET response on particle LET [Old00].

Further work is needed to decide whether the ratio changes more due to average proton LET (we could call this "softening" of the proton beam) or to the addition of photons and neutrons to the beam, which, given their high LETs [Hol02], we could

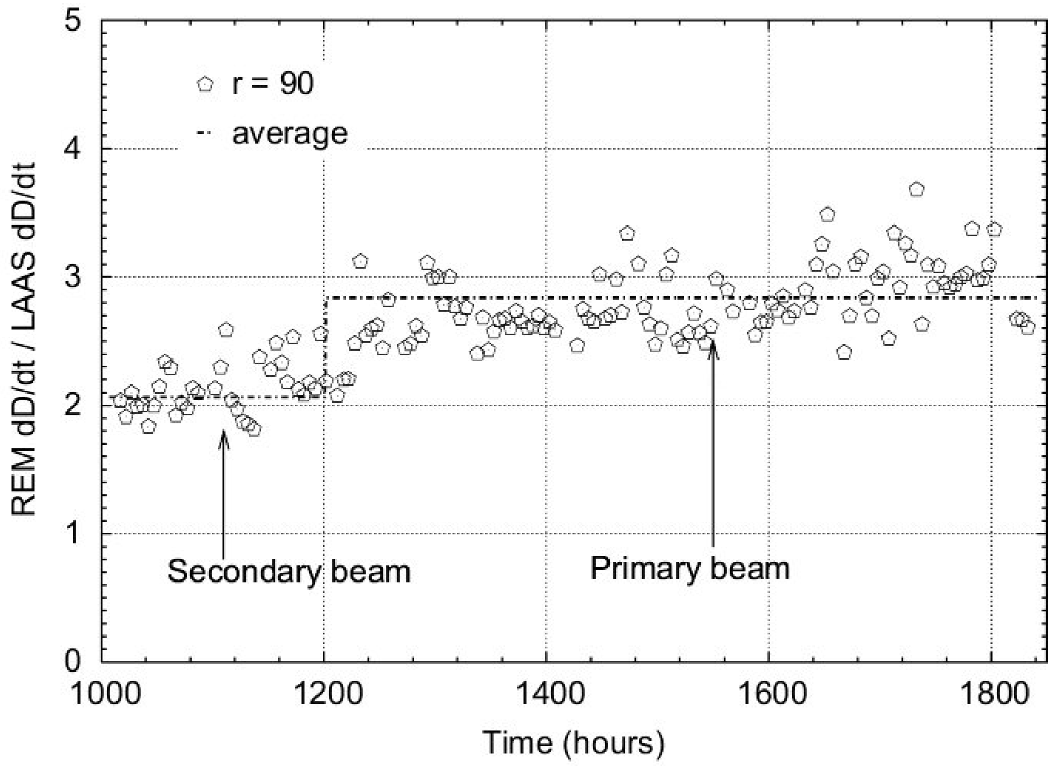

Figure 9.6: Sensitivity "R/L ratio" for RadFETs REM and LAAS during the second irradiation run. Plot relative to the couple of sensors installed at r = 90.

describe as "dilution" of the beam.

This finding suggests, using these RadFETs at the LHC, to monitor the REM/LAAS signal ratio to uncover important variations in the composition of the beam. Furthermore, during full LHC particle experiments, monitoring it may be able to give useful warnings of partial beam loss or bad beam tuning conditions.

9.3 Conclusion

The four semiconductor sensors tested in IRRAD6 were the issue of the characterization studies carried out in Chapter 6 and Chapter 7 of this thesis work. These sensors have been recommended for the radiation monitoring throughout the 10 years of LHC Experiments. These sensors would be placed within the detectors surrounding the four interaction points at the CERN LHC. The set of four devices are: RadFETs manufactured by REM and CNRS-LAAS and *p-i-n* diodes from CMRP and OSRAM.

The rate and the particle mix described for the irradiation test at the CERN IRRAD6 facility, gave integrated doses of several hundred Gy and particle fluences exceeding 10^{13} cm^{-2} over 1900 hours. These irradiation levels, together with some variations of the particle beam in time and in its tuning, were very effective as simulation of the LHC working conditions. The above mentioned radiation monitoring devices worked successfully in the simulated mixed-particle environment.

The accuracy achieved in the measurement of dose (TID) and Φ_{eq}, falls within the experimental calibration errors (10 % to 15 %) for REM, LAAS and CMRP devices. Previous calibrations of these devices were tests in relatively "high-rate" irradiation environments where annealing phenomena have not been explicitly considered. In the case of the BPW34 diodes the measurement have been found to be in agreement within 20 % only if opportune annealing corrections are used.

Finally, in this chapter, a new concept of using two RadFET sensors with very different oxide thicknesses has been discovered. Their signals at TID $>$ 10 Gy can be fruitfully used as complementary information to detect changes in the radiation field composition. This feature is thought to be a valuable indication of (intentional or accidental) changes in the LHC beam conditions induced by differing or faulty tuning of the primary beams.

Chapter 10

Integration of the radiation monitors at the LHC

10.1 Radiation monitoring at the LHC experiments

In the previous chapters it has been found out that the different dosimetric technologies investigated in this thesis work can provide a complete and quantitative map of the expected complex radiation environment of the LHC experiments. While the implementation of the RadFETs and the *p-i-n* diodes semiconductor sensors is straight forward, the integration of the OSLs still needs some development. Moreover, at the actual state-of-the-art, the results presented in Chapter 8 suggest to push the development of a single "real-time" OSL-sensor probe based on a fibered system. Such kind of radiation monitor combines the advantages of the OSL material (high sensitivity, absence of saturation, small dimensions, etc.) with the possibility to perform a remote measurement without driving electrical signals over long-distances. In the case of the experiments of the LHC this became an important constraint when the radiation monitoring has to be performed within particles detectors that are very susceptible to the injection of external electronic noises.

The set of the four recommended RadFETs and *p-i-n* diodes covers well the needs of the LHC Experiments in terms of sensitivity (3.5 mGy/mV, 1.7x10^8 cm^{-2}/mV) and dynamic range ($>$ 20 kGy, 4x10^{14} cm^{-2}). The whole sensor set can be read out by current injection so that their readout consist in a simple ohmic measurement. Moreover, the four types of sensors have dimensions in the range of a few square millimeters and can be read out over long distances. All these reasons justify therefore the production of an integrated sensor PCB with the aim to simplify the handling of the radiation sensor set. Thus, they can be integrated into a dosimeter Printed Circuit Board (PCB) which fulfills the requirements for the radiation monitoring of the LHC experiments.

10.1.1 Design of an integrated sensor carrier for IEL and NIEL measurement

To allow easy handling, and to provide a standard connectivity for all proposed sensors, an integrated PCB carrier was designed and produced at CERN as shown in Fig. 10.1.

This carrier is made of a thin (200 μm) double-sided PCB. It can host up to 5 *p-i-n* diodes in the places labeled from D1 to D5 in Fig. 10.1. In the middle of Fig. 10.1(a), the sensor mounted at the top is a CMRP diode, while the bottom one is a BPW34 diode sealed in a DIL package.

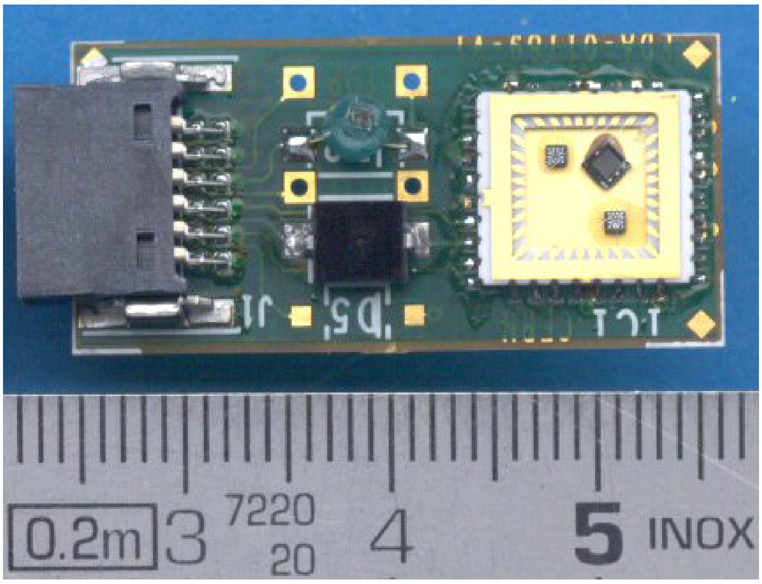

(a) PCB Front-side with 2 *p-i-n* diodes and 3 RadFET dies on board

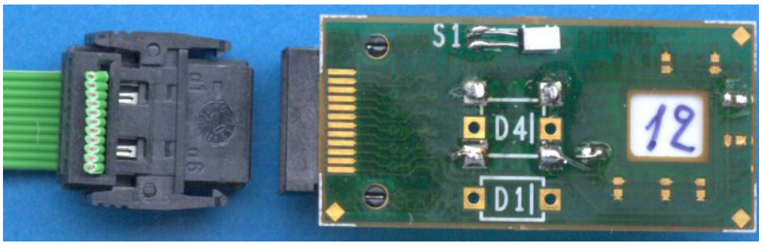

(b) PCB Back-side with external cabling

Figure 10.1: Integrated sensor carrier for the LHC Experiments.

The PCB carrier can also allow the readout of five other devices hosted inside a proper packaging. At the moment, a series of packages containing four RadFETs has been designed and produced for the LHC Experiments as it has been explained in Sec. 6.5. One of these can be seen, mounted on the sensor PCB, on the right-hand side of Fig. 10.1(a). A temperature probe (see S1 in Fig. 10.1(b)) is also provided. The 11 devices mounted on the integrated sensor PCB can be read out via a 12-way flat cable (11 for sensor signals and a common GND connection) as shown in the left-hand side of Fig. 10.1(b). The overall dimensions of the assembled PCB, including the connector plug, are of about $34 \times 15 \times 4$ mm^3.

It has been shown and extensively discussed in Sec. 6.5 that the distribution and composition of the materials around RadFETs can strongly interfere with TID measurements, especially in radiation fields containing neutrons and/or low energy photons. Dose enhancement effects are thus an issue. Moreover the space available for the installation of such kind of sensors is another important constraint in the case of the LHC. For this reason, many of the chip packages used for RadFETs in other applications may well be unsuitable for a direct application at the LHC, therefore the special ceramic carrier for the REM and LAAS sensors was designed to face these issues [Cap06]. In the same way, the thickness (200 μm) and the material (FR4) used for the construction of the integrated sensor PCB have been studied to minimize its interaction inside the radiation environment. Moreover, when possible, the material budget has been reduced as it is visible in the Fig. 10.1(b), where the "unnecessary" PCB material has been removed in correspondence of the RadFET carrier backplane.

The signals from the integrated carrier can be remotely readout up to very long distances using wired connections via the flat cable and the connector plug. However, a less cumbersome method is to directly solder the flat cable to the PCB using the pads located under the connector plug shown in Fig. 10.1(b). Moreover, as all mounted sensors keep stored the dosimetric information over time, the integrated PCB can be also used in a "passive" mode by exposing it to radiations with all connections grounded. For this latter application, the integrated sensor must be removed from the measurement field and plugged on a laboratory test-bench to perform the readout cycle.

While the present carrier was optimized for the LHC, the above features makes its utilization easily extendible to any application in which monitoring of cumulative dose and particle fluence is needed.

10.2 Example of radiation monitoring systems at LHC

The conception of the radiation monitoring sensors readout electronics adapted to the needs of the LHC experiments was out of the scope of this thesis work. This also because any LHC experiments and the LHC machine have different requirements to account and because they base the operation and the instrumentation control on different electronic standards. For duty of completeness, in this section the description of the application of the radiation monitoring sensors in the case of the ATLAS experiment will be given. An overview on the RADMON box that will be installed in the LHC tunnel and that mounts some of the sensors developed here (*p-i-n* diodes BPW34F) will be also given.

10.2.1 The ATLAS radiation monitoring system

The Ljubljana ATLAS group took care to design and produce an on-line radiation monitor for the ATLAS experiment based on the devices selected in this thesis work. The purpose of the radiation monitor is to provide online information about the TID and the Φ_{eq} at various locations in the ATLAS experiment [Kra06]. In addition to that, the radiation monitor will record the degradation of current gain in the *DMILL* bipolar transistors which has been demonstrated to give informations about the level of thermal neutron exposure [Man04].

The radiation monitor must measure doses in ranges from Gy to hundreds of kGy and from 10^{11} cm^{-2} to 10^{14} cm^{-2} Apart for the *p-i-n* diode devices characterized in this study, the ATLAS radiation monitor will measure Φ_{eq} from leakage current measurement of reverse biased diodes.

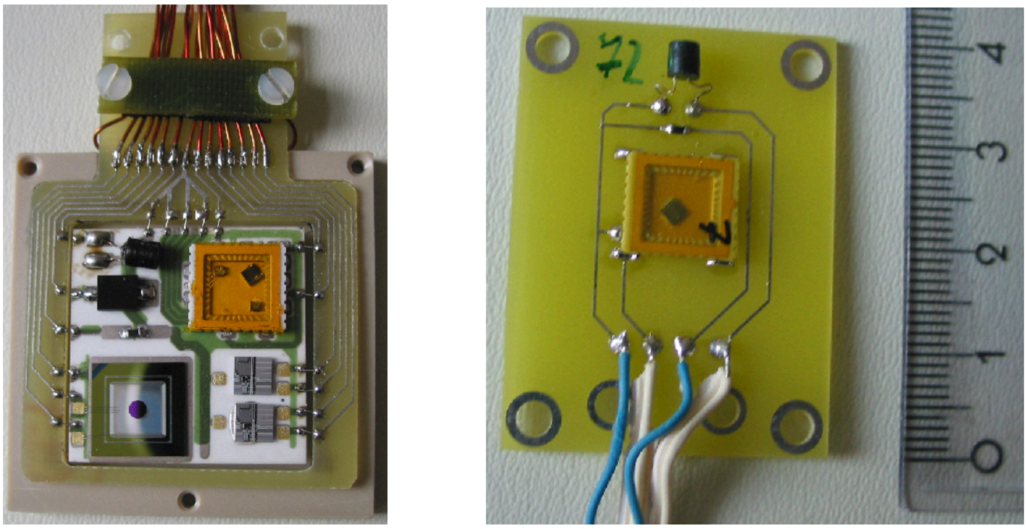

(a) (b)

Figure 10.2: Prototypes of the ATLAS RMSB. (a) top side of the populated ID hybrid connected to a PCB frame in the bottom part of PEEK plastic housing. The outer dimension of the housing box for the ID will be $40\times40\times8$ mm^3. The hybrid is populated with the RadFET package containing 3 RadFETs, CMRP diode, BPW34F diode, epitaxial Si diode, two DMILL test structures and a temperature sensor. (b) RMSB for Rest of ATLAS (RoA) locations.

The main part of the on-line radiation monitor is the *Radiation Monitor Sensor Board (RMSB)*. On this board radiation sensors and a temperature sensor will be mounted. There will be two types of RMSBs in ATLAS of which one will be used in the Inner Detector (ID) shown in Fig. 10.2(a) and the other on other measurement locations (RoA) as it is shown in Fig. 10.2(b).

Requirements for the monitoring in the ATLAS-ID are very demanding because the sensors must cover largest range of doses and because of very limited possibility for access for eventual interventions. Therefore, RMSBs in the inner detector will host a number of radiation monitors which will cover a broad dose-range and provide a high level of redundancy. Because of very uncertain temperature conditions at some locations in the inner detector (could vary between -20 °C and +20 °C) the RMSBs will be made of ceramics and will be equipped with a heater which will enable to keep the board at constant temperature few degrees above 20 °C.

For locations in the Rest of ATLAS (RoA) the RMSBs will be a simple PCB with dimensions of 3×4 cm^2, hosting the high sensitive pin diode (CMRP), a temperature sensor (10 kΩ NTC) and ceramic package containing one LAAS thick oxide RadFET. The RoA RMSB will therefore be connected with 4 wires: one for each sensor plus a return wire.

The RMSBs will be read out using standard ATLAS electronics. Sensors will be read out using ADCs on ELMB boards which communicate with the ATLAS Detector Control System (DCS) over the CAN bus[1]. Current pulses for biasing of sensors, which

[1]The Embedded Local Monitor Board (ELMB) is a general-purpose plug-on I/O module for the monitoring and control of sub-detector front-end equipment. The ELMB is based on the industry

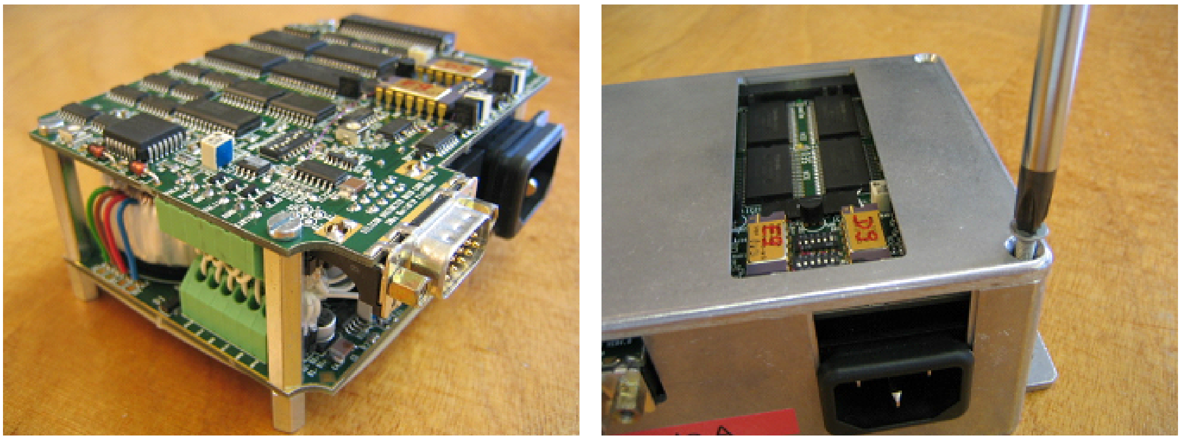

(a) (b)

Figure 10.3: RADMON radiation monitor for use in the tunnel, the underground areas and on the cavern walls. (a) RADMON box readout electronics. (b) RADMON box in its aluminium shielding.

can be converted to voltage via resistors, will be provided by ELMB-DAC boards which plug into ELMB boards. The ELMB-DAC board provides 16 DAQ channels. For the inner detector one DAC board will service one RMSB whereas for the rest of ATLAS up to 7 RMSBs could be connected to one DAC board. Each Inner Detector RMSB needs 13 ADC channels. Rest of ATLAS RMSB needs 4 ELMB ADC channels (2 for sensors, 1 for current monitoring and 1 for temperature) [Kra06].

10.2.2 Radiation monitoring in the LHC tunnel and experimental areas

The RADMON radiation monitors are designed to monitor radiation levels at the location of equipment in the LHC tunnel, the underground areas, on the walls of the experimental caverns. In the accelerator tunnel and on the cavern walls, in opposition to what has been discussed in the previous sections for the LHC experiments, there are no strict space limitations and the radiation levels are lower than the ones foreseen for the experiments themselves (see Sec. 2.1.1). Therefore, the RADMON units at these locations can host the readout electronics in the same sensor location and provide on-line digitized measurements of the dose, dose rate and hadron flux at a maximum 100 Hz [Wij05a].

This type of RADMON devices board is shown in Fig. 10.3(a) and they are packed in aluminum shielding of $13\times5\times9$ cm^3 as it is shown in Fig. 10.3(b). The radiation monitoring units will provide on-line measurements of the following parameters:

1. TID in silicon measured by RadFETs;
2. Φ_{eq}in silicon measured by the BPW34F *p-i-n* diodes;

standard CANbus and CANopen that has been implemented as high-level communication protocol. Further details available on: http://elmb.web.cern.ch/ELMB/ELMBhome.html

3. Hadron fluence with E > 20 MeV by means of a Toshiba TC554001AF-70L SRAM to count SEUs.

The monitoring system will have 250 junction boxes distributed in the LHC tunnel and underground areas. The maximum number of radiation monitoring units that can be attached to a single junction box will be 32. For the first particle runs of the LHC accelerator a total of 125 radiation monitors, that will all use the same electronic design, will be installed. Any variation in the radiation tolerance of the monitors will therefore be minimized to the lot-to-lot variation of the components. The data of this monitoring system will be made visible in the control room via a Graphical User Interface. The interface should allow combining data from the beam loss monitoring system and the quench protection system to provide a coherent view of the radiation levels around the ring to the engineer in charge [Wij05b].

Chapter 11

Summary & Conclusion

The aim of this thesis work was twofold. On the one hand, a series of radiation monitoring sensors were characterized with particular respect to the peculiarity of the environment that they would have to monitor at the LHC experiments. The characterization studies of the investigated devices (RadFETs and *p-i-n* diodes semiconductor sensors) were carried out for their selection and to determine the key parameters that will allow their utilization at the LHC. Furthermore, issues regarding the sensor encapsulation and integration were addressed in order to account for the specificity of the LHC environment and to make them ready for their installation into the LHC experiments. On the other hand, other dosimetric principles have been investigated to evaluate their possible application at the LHC. This is the case of the OSL materials that have been studied in particle fields of interest for CERN applications. Starting from the evaluation of the sensitive material, different layouts of OSL-based integrated sensors have been tested and their performances measured and discussed in this dissertation.

The complex radiation environment expected at the experiments of the LHC (constituted mainly of photons, protons, pions and neutrons) make its monitoring challenging. Very high radiation levels will be integrated in certain locations with the requirement to have high sensitivity in other locations where the radiation field will be much less intense. Moreover the particle spectra are variable as function of the angle with respect to the interaction point. The quantity of interest to be monitored in this radiation field are the Total Ionizing Dose (TID) expressed in Gy in silicon and the 1-MeV neutron equivalent particle fluence (Φ_{eq}).

To characterize devices suitable for the above mentioned complex radiation field, different irradiation facilities are needed. However, the irradiation facilities that provide "optimized" radiation fields for the characterization of the sensors for the LHC experiments (in the sense of particle types and energies) are the ones at the CERN-PS accelerator. For this reason, in the framework of this thesis work several measurement campaigns have been conducted there in order to improve dosimetric methods and means and supply reliable measurements to be used for the radiation sensors calibration.

The 23 GeV proton beam of the IRRAD1 facility at CERN delivers protons in "spills" of 5×10^{10} cm^{-2} particles/each. The proton fluence is usually measured by means of activation foils techniques while the beam profiles are obtained with different type of dosimetric films (Gafchromic and OSL). With these techniques an accuracy in the determination of the proton fluence of $\pm$ 7 % can be achieved and beam profiles and a precision of hundred of μm can be obtained in beam profiling. The first experiment made to prove the principle of operation of an on-line beam profile monitor based on the emission of secondary electrons from a thin aluminum foil (SEE) has been also presented in this thesis work. The neutron fluence in the mixed γ/n environment of the IRRAD2 facility is instead usually monitored by means of particle detector diodes, while the TID is measured with different passive dosimetry like PAD, RPL and dosimetric films. In this environment a TID of 1 Gy in silicon is deposed by a Φ_{eq} of 4×10^{11} cm^{-2}. The comparison of the measurement with Monte Carlo simulations shows an accuracy of 21 % in the Φ_{eq} measurement in IRRAD2.

In the following, the main conclusions in the characterization of the different radiation monitoring sensors for the LHC experiments will be drawn:

- **RadFET dosimeters**: From the used selection procedure it resulted that two RadFET devices are needed to fulfill the radiation monitoring requirements of the LHC experiments. The LAAS 1600 (t_{ox} = 1.6 μm) for the measurement of "low-LET, low intensity" fields and where a high sensitivity for the TID determination is required. The REM TOT-501C Type K with t_{ox} = 0.25 μm are instead the devices suitable for the measurement in "high-LET, high-intensity" fields where the effects of the initial recombination induced by high-energy hadrons within the silicon-dioxide layer of the devices themselves have to be minimized.

  The LAAS devices with their initial sensitivity of about 500 mV/Gy and their dynamic range from a few mGy to 10 Gy are therefore the best choice for the monitoring of the outer sub-detector regions of the LHC experiments. There the expected radiation field will be composed mainly of broad-spectrum neutrons and energetic photons that will lead to accumulated doses of tens of Gy over the 10-years LHC lifetime. Irradiation tests carried out at the CERN-IRRAD6 facility have proven that dose-rates of 2-3 mGy/h can be detected by this sensor. Annealing studies and direct measurements on these devices show that displacement damage effects can appear when these sensors are exposed to high radiation levels in a radiation field with similar characteristics with respect to the one expected at the LHC. However the different annealing investigations have proven that, even after an "over-exposure" the annealing of the dosimetric parameter is as low as 6 % over more than one year time. In the dynamic range of interest these devices have also proven to be essentially insensitive to fast-neutrons. These performances can guarantee an accuracy of ± 10 % in the TID measurements over time.

  The REM TOT-501C devices with their initial sensitivity of about 20 mV/Gy and they dynamic range from 100 mGy to some tens of kGy are instead the best choice for the monitoring of the inner sub-detector regions of the experiments. There the expected radiation field will be dominated by Minimum Ionizing Particles (MIPs) that will lead to accumulate doses in the 10 kGy over 10-year LHC lifetime. Irradiation tests carried out at the CERN-IRRAD6 facility proven that they successfully work in a environment with low dose-rates and dominated by charged hadrons. Annealing studies and direct measurements on these devices show that, even after TID of more than 30 kGy and Φ_{eq} grater than 1×10^{13} cm^{-2} the TID effects dominate in the device's radiation response and negligible signs of displacement damage effects were found. Also in this case, the different annealing investigations have proven that the annealing of the dosimetric parameter after exposure to kGy doses, is as low as 8 % over more than one year time even when the temperature variations over time are bigger than 15 °C. Using a readout current not corresponding to the MTC point of the devices, the temperature corrections for the ΔV_{th} as function of the TID have been determined in this work (see Pag. 94) and can be used when broad temperature variation occurs during measurements. In the dynamic range of interest these devices have shown a constant sensitivity to fast-neutrons lower by a factor of 2 with respect to the one determined for the directly IEL radiations. The above mentioned performances can guarantee an accuracy of ± 10 % in the TID measurements over time.

- ***p-i-n* diode sensors**: The BPW34F commercial *p-i-n* diodes were found as the solution to monitor the high Φ_{eq} that will be integrated over the 10-years of LHC in the inner sub-detector regions of the experiments. The studies carried out in this thesis work showed that the optimized conditions for their readout are reached when the current of 1 mA is delivered with a pulse of maximum 1 sec. width. The operation at higher injection levels (e.g higher forward currents) is not recommended as important "distortions" in the measured forward I/V curves (from about 10 mA to 100 mA) had been found when Φ_{eq} reached the level of 10^{13} cm^2. At 1 mA readout current these devices provide a sensitivity of 9.1×10^9 cm^2/mV when Φ_{eq} exceeds 2×10^{12} cm^2 and for fluence-rates starting from about 10^{11} cm^2/h. At lower initial Φ_{eq}, the devices did not show sensitivity to fast hadrons. A solution to bring the devices to their sensitive operational region is to operate a low-fluence pre-irradiation run on the devices. Irradiation tests carried out at the CERN-IRRAD6 facility have proved that for fluence-rates lower than 10^{11} cm^2/h the annealing of these devices has to be corrected in order to keep the accuracy of the measurements within ± 20 %. For this reason, a parameterization for the annealing correction is proposed in this work that consist in a combination of an exponential and a logarithmic term:

$$V_F(t) = A - \alpha \cdot \exp\left(-\frac{t}{\tau}\right) - \beta \cdot \ln\left(\frac{t}{t_0}\right) - (|T_c| \times \Delta T) \qquad \text{(see Eq. 7.4, page 126)}$$

that is valid for the time and the temperature range described in Sec. 7.1.4. Some of the parameters used in the above equation show dependence in both Φ_{eq} and in the temperature.

The high-sensitivity CMRP *p-i-n* diodes were found instead to be the solution to monitor very low Φ_{eq} levels as the ones that will be integrated over the 10-years of LHC in the outer sub-detector regions of the LHC experiments. The characterization studies carried in this thesis work showed, for the forward voltage growth, a linear sensitivity dependence of 1.7×10^8 cm^2/mV when Φ_{eq} is lower than 2×10^{12} cm^2. The different calibration curves were in agreement within ± 13 %. At higher levels of Φ_{eq} the response characteristics becomes super-linear going quickly toward a breakdown region. Irradiation tests carried out at the CERN-IRRAD6 facility proved that even for dose-rates in the order of 10^9 cm^2/h

the annealing of these devices is lower than the measurement error. This has been proven by direct annealing measurements. Moreover these devices show to be able to measure the particle fluences in the different IRRAD6 locations with an agreement of ± 16 % with respect to the predictions of Monte Carlo Simulations. Sec. 7.2.2 details finally the temperature dependence found for such a device type.

Preliminary irradiation tests were also carried out on two models of Czech silicon *p-i-n* diodes: LBSD type Si-1 and Si-2. The tests presented in this thesis work have been carried out in a 254 MeV proton beam and in a nuclear reactor neutron environment. This products have to be read out with a forward current pulse of 25 mA. This high current represent at the moment a limitation for the integration in the standard LHC experiments readout electronics. At such injection levels, the performances of the model Si-1 were found to be comparable to the one of the CMRP devices. The sensitivity of the model Si-2 were instead found to be of 2.7×10^7 cm^2/mV, namely a factor 6 higher than the other devices. Even if an investigation of their proprieties at lower injection levels (e.g 1 mA) has still to be done, they appear as a valuable option in the replacement and/or complement of the CMRP diodes currently used.

- **OSL materials**: The evaluation of OSL material in hadron environment has been carried out in this thesis work. The response of the "pure" OSL material to 23 GeV protons has been here studied in detail showing that the IEL of this particle is correctly detected over the dynamic range of the material up to 100 Gy. However, the fading of the material has been found as a possible limiting factor, especially in the operation of OSL-based integrated sensors. Studies on the possibility to enhance the OSL neutron sensitivity have been successfully carried out. Specially prepared OSL samples mixed with polyethylene or doped with boron were manufactured for the measurement of fast and thermal neutrons respectively. Although it was possible to measure and discriminate with a good accuracy different neutron spectra (within about 20 %), these new materials are still in the development phase and the reproducibility within the different sensor batches has still to be improved.

  The characterizations in hadron environment of different integrated sensors based on OSL have also been discussed. The first integrated sensor considered was based on a sandwich LED/OSL/photodiode exposed to the radiation field to be measured, together with its readout electronics. This assembly proved already to work successfully in space applications. Unexpectedly, the LHC-like hadron environment results to be very effective on damaging the commercial electronics for the OSL readout. Several improvement have been realized on the electronic design and in the component selection. However, it was not possible to fully exploit the high sensitivity properties of the employed OSL material. By using another OSL-sensor approach, the radiation hardness issues have been faced by moving the readout electronic out from the radiation environment under measure. This has been realized by means of radiation hardened optical fibers that drive and collect the light signals to and from a small OSL crystal. This readout scheme allows also the utilization of a couple of commercial laser/PM devices for the OSL readout. The high efficiency achieved in the optical stimulation and in the light collection, give to the first prototype tested at CERN a sensitivity to ionizing doses down to the mGy range. This sensor approach became therefore a promising possibility for the radiation monitoring at the LHC experiments.

Finally, in this thesis work the integration of four of the sensors presented above (LAAS, REM, CMRP, BPW34F) in a unique PCB carrier has been done. The integration relies on the fact that the different devices have similar readout parameters and all four are needed to insure a complete monitoring of the challenging radiation field expected at the LHC. The responses of the two RadFET dosimeters (LAAS and REM) are the most affected by the materials that surround the measurement point. For this reason a dedicated chip carrier has been designed for them. To validate the choice of the carrier base material and lids in the LHC environment, a GEANT4 Monte Carlo model has been built and its first validation tests have been presented in this thesis work. In particular the validation with 254 MeV protons show that the model can be already used to determine the effectiveness of the carrier layout in the devices responses for different proton energies. This RadFET packaging together with the two *p-i-n* diodes CMRP and BPW34F can be hosted on the integrated PCB carrier that allows a simple handling and readout for the four proposed sensors. The characteristics of the first prototype series produced at CERN have been discusses extensively in Sec. 10.1.1.

While some LHC experiments are already installing single sensors developed in this thesis work (October 2006) in proper readout systems (see Sec. 10.2.1), others express their interest in using the whole PCB integrated carrier presented here. Its installation has been foreseen early in the year 2007 to be ready for the measurement of the radiation field during the first engineering run of the LHC machine scheduled at the end of 2007.

Appendix A

Procurement specification for RadFETs REM TOT501C

This appendix specifies the procurement and the testing procedure that has been adopted in the selection of the remaining stock of chips diced from the RadFET wafer REM TOT501C. The testing procedure that has been carried-out to procure the majority of REM's stock of the wafer TOT501C, and select them with characteristics which satisfy CERN applications, will be detailed here.

The remaining REM stock is containing slightly over 600 pieces. The initial wafer probe test was only partial and took place several years ago. CERN is equipped to probe single die in large quantities minimizing the risk of electrostatic damage that can occur during the handling procedure. Thus, an initial series of tests will be executed with a probe-station, with the aim to select the structures suited for CERN purposes. Once the dies have been selected, sited and wire-bonded in a proper chip packaging, further electrical tests will be performed with the aim to check the FET's quality before the batch assignment. Details about the standard die's carrier actually specified for the dosimeters to be installed at the LHC are available in Chapter 6.

A.1 CERN test procedure

The electrical specifications relevant for the procurement of the "good FET" structures of Type-K for the wafer TOT501C are given in Tab. A.1. Tab. A.2 gives instead the parameter relevant for device quality. The customary precautions against electrostatic damage (ESD) shall be observed in all handling procedures. The selection procedure has been carried out as follows:

1. all the 600 single dies will be probed using a probe-card designed for the REM TOT-500 mask series with particular respect to the two Type-K structure;

2. on the basis of the parameters given in Tab. A.1 the "good Type-K FETs" will be extracted from the stock and made available for LHC utilization;

3. a die will be accepted for CERN when at least one of the two Type-K structures on each die falls into the given parameters range of Tab. A.1;

4. the selected "good" Type-K structures will be mounted on a chip carrier to evaluate their quality before their utilization following Tab. A.2.

A.1.1 ACCEPTANCE AND QUALITY CRITERIA

The criteria of a "good RadFET" depend mainly on its functionality in measuring radiation dose. The following overriding considerations must thus be taken into account as regards device performance:

A. an I-V curve stable with time at temperatures below 35 °C;

B. homogeneous initial threshold voltage;

C. I_{dss} leakage value less than 0.5 % of the nominal readout current;

D. moderate drift before and after irradiation (*dutti*[1]);

E. Punch-through voltage comparable with the required rail voltage after irradiation.

On the other hand, considerations of complementary parameters like:

F. Satisfactory BTS tests;

G. mild variability in T_C, MTC current, etc.,

give guidelines in the evaluation of the device quality. For these reasons, criteria like **F** and **G** will be tested by CERN and considered in the general picture of device quality or for batch sorting and they will be not intended as criteria for rejecting a device for use as a radiation detector.

Tab. A.1 contains the figures that will be considered as accept-reject values. That is any of the 600 unit delivery could be rejected contractually if falling outside the given parameters range. These figures are based on laboratory-book data by CERN or REM on this wafer lot. For the measurement of these parameters the ESD precautions will be strictly observed for all handling procedures inside CERN. Damage caused during probing of die will not be a cause for rejection.

The parameters $V_{th,0}$, $dutti, I_{dss}$ and $I_d - V_{ds}$ (base parameters) specified in Tab. A.1 are intended to be measured on all the devices with a probe station before irradiation. For the BV_{dss} the most reliable test is the measurement of the drain-source voltage level after 30 kGy irradiation when an I_{ds} current is forced throughout the devices. For this reason, 5-10 structure extracted form the batch of devices good base parameters will be mounted, wire-bonded and irradiated to 30 kGy. The test will be passed if all the structures will work up to the minimum voltage required as specified in Tab. A.1. In cases where the tested structure accepted on the basis of the four basic parameters, shows unexpected early breakdown voltage, measures will be taken in agreement with the producer to complete the die acceptance phase.

Tab. A.2 contains figures that will be used as indicators of quality for batch assignment. These parameters may be used for batch sorting, such as when selecting devices

[1] The acronym *dutti* stand for "**d**rift-up in any **t**wofold **t**ime **i**nterval".

for high-safety-risk and low-safety-risk areas of LHC. For these figures the specification are sometimes based on estimates and can be thus subjected to further modifications during the execution of the measurements.

A.1.2 DIE MAIN TESTING SPECIFICATIONS

A.1.2.1 I-V Characteristics

Using the connection layout shown in Fig. A.1(a) the transfer characteristic $I_d - V_{gs}$ of the MOSFETs for one value of V_{ds}, in the range from 0V to -6V has been measured. From the $I_d - V_{gs}$ curves the threshold voltage (V_T) and the Drain-Source Leakage Current (I_{dss}) parameter was extracted. Moreover the output characteristic $I_d - V_{ds}$ has been verified at different values of V_{gs}, typically four ranging from V_{gs} <-V_T to -6V.

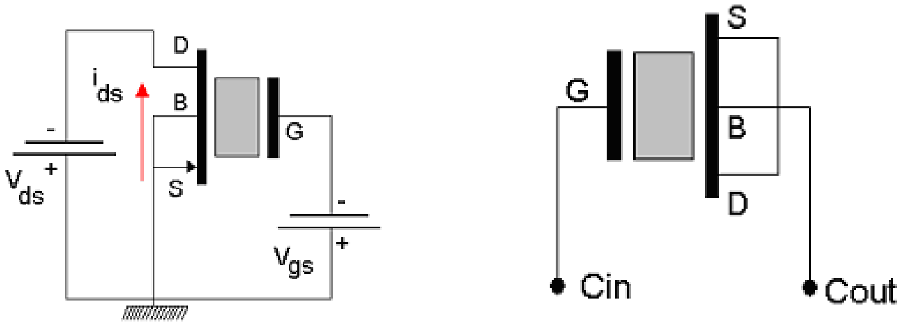

(a) (b)

Figure A.1: Devices layout for used in the selection and QA procedure. (a) Layout for the I-V characteristics measurement. (b) Device connections for BTS test.

A.1.2.2 Bias Temperature Stress (BTS)

To verify if any mobile-ion contamination has been introduced on the MOSFET oxide, BTS measurements will be carried-out using the following protocol:

1. connect the device to the Capacitance meter as shown in Fig. A.1(b);
2. perform an initial C-V test at room temperature sweeping the voltage from 10V to -10V recording the capacitance curve;
3. reverse the sweep;
4. apply a positive voltage through the gate to establish a field of 1 MV/cm (typically 20 V - 25 V) and heat the sample at 200 °C for 6 minutes. The heating time is chosen to reach thermal equilibrium as at that at that stage the devices tested will be mounted on a chip carrier;
5. maintain the voltage while the sample is being cooled down;
6. second C-V test repeating steps 2 and 3;

7. apply a negative voltage through the gate and heat the sample at 200 °C for 6 minutes;

8. maintain the voltage while the sample is being cooled down;

9. final C-V test repeating steps 2 and 3;

A.1.2.3 "Reader Circuit" Layout

All the parameters relevant for the dosimetric application of the RadFET structures are determined connecting the devices in the so called "Reader Circuit" configuration. The *source* terminal is connected to the *body* terminal and supplied with I_{ds}, *gate* and *drain* are instead shorted.

PARAMETER	SYMBOL	MIN.	TYP.	MAX.	UNIT	MEASUREMENT CONDITIONS	REMARKS
Initial threshold Voltage[(a)]	$V_{th,0}$	-3.20	-3.30±0.2	-3.40	V	"Reader circuit configuration" with I_{ds}=160. μA Unirradiated device.	Tested executed on probe-station
Stability of V_{th} with time	*dutti*	-	-0.23±0.15	1	mV	"Reader circuit configuration" as above. V_{th} measured 5 and 10 sec. after turning the reader on. Unirradiated device.	Test executed on probe-station
Drain-source leakage current	I_{dss}	-	~1μA at I_{ds}=160	0.5	% of I_{ds}	"$I_d - V_{gs}$ circuit configuration" at V_{gs}=0 and chosen V_{ds} the reader on. Unirradiated device.	Test executed on probe-station
Drain Characteristic	$I_d - V_{ds}$	-	-	-	-	4 curves at different V_{gs} starting from $V_{gs} < -V_T$. Unirradiated device.	**Immune to kink effects and parasitic bipolar signatures**
Drain-Source breakdown voltage[(b)]	BV_{dss}	27	-	-	V	"Reader circuit configuration" with I_{ds}=160. μA Irradiated device to 30 kGy.	Parameter that define the "rail-voltage" Test executed on test-bench

Table A.1: RadFETs TOT501C-8 Type K **SELECTION** Procurement Specifications at Room Temperature.

Notes:

[(a)] Remember that this parameter differs from the real transistor threshold voltage V_T. As explained in Chapter 3, V_{th} is the value of V_{gs} that support the forced readout current.

[(b)] See details in Sec. A.1.1.

PARAMETER	SYMBOL	MIN.	TYP.	MAX.	UNIT	MEASUREMENT CONDITIONS	REMARKS
Flat-band voltage shift	WV_{fb}	-	-	200	mV	Shift measured betw. the C-V curves from BTS at ±10 V. μA Unirradiated device.	Recommended frequency of the capacitance bridge: 1 MHz.
Readout current at MTC	I_{ds}	smooth variation			μA	"Reader circuit configuration". Unirradiated and irradiated devices.	Test executed on probe-station
Sub-threshold swing from $I_d - V_{gs}$	S	60	110	-	mV/dec.	"read circuit configuration" with I_{ds}=160. Unirradiated device.	Test executed on probe-station
Temperature dependence	T_c	-	< 0.05	0.25	mV/°C	"read circuit configuration" with I_{ds}=160. Unirradiated device.	Temp. range -20°C to 80°C Test executed on probe-station
Oxide leakage current	LI_{gbs}	-	-	1	nA	"C-V circuit configuration" with V_{gs}=30 V Unirradiated device.	Test executed on probe-station

Table A.2: RadFETs TOT501C-8 Type K **QUALITY** Procurement Specifications at Room Temperature.

List of Figures

List of Tables

List of publications

Listed in reverse chronological order:

1. **F. Ravotti**, M. Glaser, A. B. Rosenfeld, M.L.F. Lerch, A.G. Holmes-Siedle and G. Sarrabayrouse,
   Radiation Monitoring in Mixed Environments at CERN: from the IRRAD6 Facility to the LHC Experiments. Paper PH-2 145 to be presented at the Radiation Effects on Components and System (RADECS 2006) Workshop, Athens, Greece, September, 27-29, 2006. Also in CERN Preprint collections CERN-PH-EP/2006-024; CERN-TS-2006-003, 2 August 2006.

2. S. Guatelli, M. Glaser, B. Mascialino, M. Moll, M. G. Pia, **F. Ravotti**,
   Optimization of Radiation Monitoring Sensors for the LHC Experiments: GEANT4 Simulation and Experimental Validation. Paper PH-2 146 to be presented at the Radiation Effects on Components and System (RADECS 2006) Workshop, Athens, Greece, September, 27-29, 2006.

3. A. A. Fernandez-Fernandez, B. Brichard, F. Berghmans, S. O'Keeffe, C. Fitzpatrick, E. Lewis, J.-R. Vaillé, L. Dusseau, D. A. Jackson, **F. Ravotti** and M. Glaser
   Real-time fiber optic radiation dosimeters for nuclear environment monitoring around thermonuclear reactors. Paper submitted for publication in Fusion Engineering and Design, 2006.

4. **F. Ravotti**, M. Glaser, F. Saigné, L. Dusseau, G. Sarrabayrouse
   Prediction of the Thermal Annealing of Thick Oxide Metal-Oxide-Semiconductor Dosimeters Irradiated in a Harsh Radiation Environment. Applied Physics Letters, vol. 89 (8), 083503, 21 August, 2006.

5. M. Glaser, **F. Ravotti** and M.Moll
   Dosimetry Assessments in the Irradiation Facilities at the CERN-PS Accelerator. Paper presented at the 8^{th} European Conference on Radiation and its Effects on Components and Systems (RADECS 2005), Cap d'Adgde, France, September 19-23, 2005. IEEE Trans. Nucl. Sci, vol. 53 (4), pp. 2016-2022, 2006.

6. J-R. Vaillé, **F. Ravotti**, P. Garcia, M. Glaser, S. Matias, K. Idri, J. Boch, E. Lorfèvre, P. J. McNulty, F. Saigné and L. Dusseau
   Online Dosimetry Based on Optically Stimulated Luminescence Materials. Paper

presented at the IEEE Nuclear and Space Radiation Effects Conference (NSREC 2005), Seattle, USA, July 11-15, 2005. IEEE Trans. Nucl. Sci, vol. 52 (6), pp. 2578-2582, 2005.

7. **F. Ravotti**, M. Glaser, M. Moll, Ch. Ilgner, B. Camanzi and A.G. Holmes-Siedle *Response of RadFET Dosimeters to High Fluences of Fast Neutrons.* In Nuclear Science Symposium (NSS/MIC) Conference Record, 2004, IEEE Catalog Volume 1, Rome, Italy, October 16-22, pp. 335-339. IEEE Trans. Nucl. Sci, vol. 52 (4), pp. 959-965, 2005.

8. **F. Ravotti**, M. Glaser, K. Idri, J-R. Vaillé, H. Prevost and L. Dusseau *Optically Stimulated Luminescence Materials for Wide-spectrum Neutron Measurement at CERN.* In Proc. RADECS 2004 Workshop, Madrid, Spain, September 22-24, 2004, pp. 299-304. IEEE Trans. Nucl. Sci, vol. 52 (5), pp. 1568-1573, 2005.

9. **F. Ravotti**, M. Glaser, M. Moll, K. Idri, J-R. Vaillé, H. Prevost and L. Dusseau *Conception of an integrated sensor for the radiation monitoring of the CMS experiment at the Large Hadron Collider.* Paper presented at the IEEE Nuclear and Space Radiation Effects Conference (NSREC 2004), Atlanta, USA, July 19-23, 2004. IEEE Trans. Nucl. Sci, vol. 51 (6), pp. 3642-3648, 2004.

10. L. Fernandez-Hernando, M. Glaser, Ch. Ilgner, A. Macpherson, A. Oh, T. Pritchard, **F. Ravotti**, R. Stone, E. Tsesmelis, S. Worm *The Radiation Monitoring System for the LHC Experiments and Experimental Areas.* In Proc. TS Workshop, Archamps, France, May 2004. (CERN EDMS No. 473714), CERN-TS-Note-2004-006.

11. **F. Ravotti**, M. Glaser and M. Moll *Sensor Catalogue - Data Compilation of Solid-state Sensors for Radiation Monitoring.* CERN-TS-Note-2005-002, 13 May 2005, CERN EDMS No. 590497. [Online]. Available: www.cern.ch/lhc-expt-radmon.

Other contributions to conferences and workshops:

12. M. Moll, **F. Ravotti**, M. G. Pia, R. Capra, B. Mascialino, M. Glaser *Simulation for LHC radiation background: optimization of monitoring detectors and experimental validation.* Paper presented at the Computing in High Energy and Nuclear Physics Conference (CHEP06), Mumbai, India, February 13-17, 2006.

13. R. Capra, M. Glaser, M. Moll, M. G. Pia, **F. Ravotti** *GEANT4 Simulation of a Packaging for Solid-State Radiation Monitoring Sensors.* In Proc. of the SPENVIS & GEANT4 Workshop, Leuven (Belgium), 3-7 October 2005.

Acknowledgements

First of all I like to express my thanks to Prof. Laurent Dusseau (University Montpellier II) and to Dr. Michael Moll (CERN) for supervising this thesis work and their continuous support, advice and encouragement.

A very special thank goes to my *”boss”, colleague* but first of all, *friend* Maurice Glaser (CERN) to which I had the privilege to work with, during the last four years I spent at CERN, in a pleasant working atmosphere. This thesis work is born because of our day-by-day collaboration in the laboratory of ”building 14”. With his contagious enthusiasm he has been my teacher in several domains of the applied sciences as well as in the everyday life. With him I had the pleasure to share good moments as well as the difficult ones, in which he has been always of good advice to me. *Merci Beaucoup Maurice!*

I am grateful to the CERN groups TS-LEA and PH-DT2 in the persons of the two group leaders Emmanuel Tsesmelis and Christian Joram. They were always confident in my thesis project and hosted me within their teams where I have found a friendly and cooperating atmosphere. In particular I would like to thank Christoph Ilgner, Evangelia Dimovasili, Anne-Laure Perrot of the CERN TS-LEA group and Ian McGill, Antonie and Francoise from the CERN PH-DT2 *Bonding Lab* for their support in preparing the RadFET SM integrated carriers.

There are many people without whom this work would not have been possible. I like to thank all the people that provided irradiation facilities, test samples or irradiated them. Among them my special thanks go to Igor Mandic, Marko Mikuž, Vlado Cindro (Ljubljana), Eric Forton (UCL), Wojtek Hajdas and Roger Brun (PSI), Federico Faccio and Karl Gill (CERN). I wish to thank also the colleagues of Prague, Stanislav Pospišil (IEAP-CTU), Bruno Sopko and Michael Solar (CTU). Moreover, I like to thank Mika Huhtinen (CERN) for the discussions about particles energy deposition in silicon and silicon dioxide.

I am grateful to all device producers and especially to Anatoly Rosenfeld and Michael Lerch (University of Wollongong), Géerard Sarrabayrouse (CNRS-LAAS) for the continuous discussions on the physics and on the production process of some of the *p-i-n* diodes and the RadFET dosimeters employed in this study. I am especially grateful to Andrew Holmes-Siedle (REM) for his continuous help in all the fields of the radiation effects in electronics and also for the patience he demonstrated in correcting my English manuscripts.

I am indebted to many friends and colleagues of the *équipe "Electronique et Rayonnements"* of the CEM^2 - University Montpellier II where all the OSL materials tested in this thesis work have been manufactured, Katia, Jean-Roch, Samuel, Jerome, Hinde, Antoine and Muriel. Many thanks go also to Frederic Saigné for his help with the interpretation of the Isochronal Annealing data for the MOSFETs.

I am also grateful to Prof. Piero Quarati (Turin Polytechnic) that, even after the end of my MSc project at CERN, he continuously followed me during the years of PhD and he had always been of good advice to me.

A special thank goes to all the "non-academic" friends that I met during my stay in Geneva, Stephane, Philippe, Vincenzo, Emanuele, Vittorio, *Clarita*, *Nohrita*, Esther, Toni, Alex, to the *ASP* friends: Giuseppe, Boris, Lucia, Arianna, Cesare, Stefano, Alberto, and to my unbreakable Torino's friends Alessandro, Andrea and Antonello. Despite the distance which separate us, they still represent my best friends. Without the continuous support and encouragement of my family I would have not arrived here. A great thought goes to Vilma, that was very close to me in the first years of my stay in Geneva and now I am sure she is continuing to follow me from the sky.

I would like to conclude this thesis by expressing my gratitude to Dorota. She enter in my life only few months ago but she immediately gave me the power to face some important decisions and also the energy to bring this work to the end in the best possible way. *Bardzo Cię lubię Dota!*

Bibliography

[Ago00] S. Agosteo, S. Alteri, G. Belli, A. Bonifas, et *al.* A facility for test of large-area muon chambers at high rates. *Nucl. Instr. & Meth. in Physics Research*, A452:94–104, 2000.

[Ale94] A. G. Alekseev, E.N. Savitskaya, S.A. Kharlampiev, I.A. Kurochkin. Dose characteristics of high-energy neutrons for radiation damage evaluation of silicon semiconductor devices. *CERN Health Physics and Radiation Effects Preprint, IHEP 94-65*, 1994.

[ALI95] ALICE. Technical Proposal. *CERN/LHCC/95-71 LHCC/P3*, 1995.

[All06] J. Allison, J. Apostolakis, et *al.* Geant4 Developments and Applications. *IEEE Transactions on Nuclear Science*, 53(1):270–278, 2006.

[Ant77] W. Antwerp, J. Youngblood. Calculated and measured displacement damage in silicon for monoenergetic neutrons. *IEEE Transactions on Nuclear Science*, 24(6):2521–2526, 1977.

[Asc85] M. Aschalom, R.J. Florian, M. Tatcher. Neutron Dosimetry: a PIN diode reader. *Fermi National Accelerator Laboratory, FN-426*, 1985.

[AST94] ASTM Committee. Standard practice for characterizing neutron fluence spectra in terms of an equivalent monoenergetic neutron fluence for radiation hardness testing of electronics. *ASTM E772-94 (revision)*, 1994.

[ATL97] ATLAS. ID Technical Design Report. *CERN/LHCC/97-16 and 17*, 1997.

[Aub72] K.G. Aubuchon and J. Bereisa. Performance of hardened p-MOS devices in severe neutron environments. *IEEE Transactions on Nuclear Science*, 19(6):299–304, 1972.

[Aug82] L.S. August. Estimating and reducing errors in MOS dosimeters caused by exposure to different radiations. *IEEE Transactions on Nuclear Science*, 29(6):2000–2003, 1982.

[Bac00] I. Bacardit-Corrons. *Flux measurement of hadrons using activation methods at CERN AD target area and at T7 irradiation facility.* Diploma thesis, Universitat Politecnica de Catalunya, Barcelona, Spain, 2000.

[Bai00] I. Baishev. Proton losses in the dispersion suppressors of IR1 and IR5 of LHC. *CERN LHC-Project-Note-240*, 2000.

[Bal92] A. Balasinski and T.-P. Ma. Ionizing radiation damage near CMOS transistor channel edges. *IEEE Transactions on Nuclear Science*, 39(6):1998–2003, 1992.

[Bar05] S. Baranov, M. Bosman, I. Dawson, V. Hedberg, A. Nisati and M. Shupe. Estimation of Radiation Background, Impact on Detectors, Activation and Shielding Optimization in ATLAS. *ATL-GEN-2005-001*, 2005.

[Ber97] K. Bernier, G. de Rijk, G. Ferioli, E. Hatziangeli, A. Marchionni, V. Palladino, G.R. Stevenson, T. Tabarelli and E. Tsesmelis. Calibration of Secondary Emission Monitors of Absolute Proton Beam Intensity in the CERN SPS North Area. *CERN Yellow Report 97-07*, 1997.

[Ber06] K. Bernier, H. Boukhal, J-M. Denis, T. Bardouni, Gh. Grégoire, O. Grégoire, V. Tran. An intense fast neutron beam in Louvain-la-Neuve, 2006. Available: http://www.fynu.ucl.ac.be/themes/he/cms/ .

[Bho97] V.N. Bhoraskar. Device properties following MeV heavy ion, electron and neutron irradiations. *In Proc. Application of accelerators in research and industry, AIP press, New York*, pages 1025–1028, 1997.

[Bla86] N.G. Blamires, D. Totterdell, A. G. Holmes-Siedle, L. Adams. pMOS dosimeters: long-term annealing and neutron response. *IEEE Transactions on Nuclear Science*, 33(6):1310–1315, 1986.

[Boo98] S.N. Boon, P. van Luijk, J.M. Schippers, H. Meertens, J.M. Denis, j. Medin, E. Grusell. Fast 2D phantom dosimetry for scanning proton beams. *Medical Physics*, 25(4):464–475, 1998.

[Bpw] BPW34 silicon pin photodiode Datasheet Available online from OSRAM Opto-Semiconductors: http://www.osram-os.com.

[Bru95] G.J. Brucker, S. Kronenberg and F. Gentner . Effects of package geometry, materials and die design on energy dependence of pMOS dosimeters. *IEEE Transactions on Nuclear Science*, 42(1):33–40, 1995.

[Bue93] M.G. Buehler, B.R. Blaes, G.A. Soli, and G.R. Tardio. On-Chip p-MOSFET Dosimetry. *IEEE Transactions on Nuclear Science*, 40(6):1442–1449, 1993.

[Cam01] B. Camanzi, A. G. Holmes-Siedle and A. K. McKemey. The dose mapping system for the electromagnetic calorimeter of the BaBar experiment at SLAC. *Nucl. Instr. & Meth. in Physics Research*, A457:476–486, 2001.

[Cam03] B. Camanzi, M. Glaser, E. Tsesmelis, L. Adams. A study on the applicability of solid state, real-time dosimeters to the CMS experiment at the large hadron collider. *Nucl. Instr. & Meth. in Physics Research*, A500:431–440, 2003.

[Cap06] R. Capra, S. Guatelli, M. Moll, M. Glaser, M.G. Pia, F. Ravotti. Simulation for LHC Radiation Background: Optimization of monitoring detectors and experimental validation. *in Proc. Computing in High Energy and Nuclear Physics (CHEP 2006), Mumbai, India, February 13-17*, 2006.

[Car00] M.G. Carolan. *Semiconductor dosimetry of epithermal neutron beam for boron neutron capture therapy.* PhD thesis, University of Wollongong, Australia, 2000.

[CER04] CERN. The LHC Technical Design Report Vol. 1-4. *CERN-2004-003*, 2004.

[Cha66] S. Charalambus, J. Dutrannois, K. Goebel. Particle flux measurement with activation detectors. *CERN DI/HP 90 Health Physics, 14 July*, 1966.

[Cha99] M.B. Chadwick, H H, Barschall et *al.* A consistent set of neutron kerma coefficients from thermal to 150 MeV for biologically important materials. *Medical Physics*, 26:974–991, 1999.

[Che97] R. Chen and S.W.S. McKeever. *Theory of thermoluminescence and related phenomena.* World Scientific Publishing Co., 1997.

[CMS94] CMS. Technical Proposal. *CERN/LHCC/94-38*, 1994.

[Col03] GEANT4 Collaboration. GEANT4 - A Simulation Toolkit. *Nucl. Instr. & Meth. in Physics Research*, A-506:250–303, 2003.

[Con93] F. Coninckx, H. Schonbacher, M. Tavlet, G. Paic, D. Razem. Comparison of high-dose dosimetry systems for radiation damage studies in collider detectors and accelerators. *Nucl. Instr. & Meth. in Physics Research*, B-83:181–188, 1993.

[Con96] B. O' Connell, A. Kelleher, W. Lane, L. Adams. Stacked RADFETs for increased radiation sensitivity. *IEEE Transactions on Nuclear Science*, 43:985–990, 1996.

[Con98a] C. Conneely, B. O' Connell, P. Hurley, W. Lane, L. Adams. Strategies for milli-rad sensitivity in PMOS dosimeters. *IEEE Transactions on Nuclear Science*, 45:1475, 1998.

[Con98b] B. O' Connell, C. Connelly, C. McCarthy, J. Doyle, W. Lane and L. Adams. Electrical performances and radiation sensitivity of stacked PMOS dosimeters under bulk-bias control. *IEEE Transactions on Nuclear Science*, 45:2689–2694, 1998.

[Con00] B. O' Connell, C. McCarthy, B. Lane, A. Mohammadzadeh. Optimized stacked RADFETs for milli-rad dose measurement. *In Proc. Radiation Effects in Components and Systems Conference (RADECS 99). IEEE Catalogue 99TH8471, Fontevraud, France, September 13-17*, pages 101–105, 2000.

[Cor75] J. Corbett and J. Bourgoin. *Defect creation in semiconductors in Point defects in solids Vol. 2: Semiconductors and molecular crystals*. J.H. Crawford and L.M. Slifkin, Plenum Press, New York, first edition, 1975. ISBN 0-360-37512-5 (v.2).

[Cor03] G. Corti and L. Shekhtman. Radiation background in the LHCb experiment. *LHCb-Note-2003-083*, 2003.

[Cor04] M. Cornelius and A. Rosenfeld. Verification of Monte Carlo calculations in fast-neutron therapy using silicon microdosimetry. *IEEE Transactions on Nuclear Science*, 51 (3):873–877, 2004.

[Dan03] D. Dannheim. *Search for Events with Isolated Leptons and Large Missing Transverse Momentum in* ep *Collisions at HERA*. PhD thesis, University of Hamburg, 2003. DESY-THESIS-2003-025.

[Daw00] I. Dawson and C. Buttar. The radiation environment in the ATLAS inner detector. *Nucl. Instr. & Meth. in Physics Research*, A-453:461–467, 2000.

[Dea66] B.E. Deal, E.H. Snow and C.A. Mead. Barrier energies in metal-silicon dioxide-silicon structures. *J. Phys. Chem. Solids*, 27:1873, 1966.

[Dim05] E. Dimovasili. Total Dose Tests of Technical Equipment for the LHC, 2005. Presentation given at the 5th LHC RADIATION WORKSHOP, CERN 29 November 2005. Available online: http://www.cern.ch/lhc-radwg.

[Dre89] P. Dressendorfer and T.P Ma. *Ionizing radiation effects in MOS devices and circuits*. Wiley - Interscience, 1989. ISBN 0-47-184893-X.

[Dum02] I. Dumanoglu, N. Akchurin, U. Akgun, S. Ayan, P. Bruecken, E. Eskut, A. Fenyvesi, A. Kayis, N. Koca, K. Makonyi, J.-P. Merlo, D. Novak, Y. Onel, G. Onengut, A. Polatoz, I. Schmidt, M. Serin, and M. Zeyrek. Radiation-hardness studies of high OH^- content quartz fibers irradiated with 500 Mev electrons. *Nucl. Instr. & Meth. in Physics Research*, A490:444 – 455, 2002.

[Dus95] L. Dusseau. *Etude des potentialités des phénomènes de luminescence par stimulation optique (OSL) dans les sulfures alcalinoterreux - Application à la réalisation d'un lecteur portable de dosimètres OSL*. PhD thesis, University Montpellier II, France, 1995.

[Dus97] L. Dusseau, T. Randolph, R.D. Schrimpf, K.F. Galloway, Saigné, J. Fesquet, J. Gasiot, R. Ecoffet. Prediction of low dose-rate effects in power metal oxide semiconductor field effect transistors based on isochronal annealing measurements. *J. Appl. Phys.*, 81:2437–2441, 1997.

[Dus01] L. Dusseau, G. Polge, S. Matias, J.R. Vaillé, R. Germanicus R. Broadhead, B. Camanzi, M.Glaser, F. Saigné, J. Fesquet, J. Gasiot. High-energy particle irradiation of optically stimulated luminescent films at CERN. *IEEE Transactions on Nuclear Science*, 48:2056–2066, 2001.

[Dus04a] L. Dusseau, 2004. Basic Mechanisms in Space Technology Course, SREC 04, Toulouse, 14-18 June.

[Dus04b] L. Dusseau, J. Gasiot. Online and real-time dosimetry using optically stimulated luminescence. *Int. J. of High Speed Elect. and Syst.*, 14(2):605–623, 2004.

[Elk68] E. Elkin and G.D. Watkins. Defects in irradiated silicon: electron paramagnetic resonance and electron-nuclear double resonance of the arsenic- and antimony-vacancy pairs. *Physical Review*, 174(3):881–897, 1968.

[epi] L1050-35T52 High Power InGaAsP NIR LED Datasheet Available online from Epitex Inc.: http://www.epitex.com.

[Exf] EXFOR, Library of experimental nuclear reaction data. Release 1.10. IAEA Nuclear Data Service. Available: http://www.nds.iaea.org.

[Fac05] F Faccio, G. Cervelli. Radiation-induced edge effects in deep submicron CMOS transistors. *IEEE Transactions on Nuclear Science*, 52(6):2413–2420, 2005.

[Fas01] A. Fassó, A. Ferrari, J. Ranft, P.R. Sala. FLUKA: Status and Prospective for Hadronic Applications. *In Proc. of the Monte Carlo 2000 Conference, Lisbon, October 23-26, 2000, Springer-Verlag, Berlin*, pages 955–960, 2001.

[Fle93] D.M. Fleetwood, P.S. Winokur, R.A. Reber, T.L. Meisenheimer, J.R. Schwank, M.R. Shaneyfelt, L.C. Riewe. Effects of oxide traps, interface traps, and "border traps" on metal-oxide semiconductor devices. *J. Appl. Phys.*, 73(10):5058–5074, 1993.

[Fle95] D.M. Fleetwood, W.L. Warren, P.S. Winokur, T.L. Meisenheimer, J.R. Schwank, M.R. Shaneyfelt, L.C. Riewe. Effects of interface traps, and border traps on MOS post-irradiation annealing response. *IEEE Transactions on Nuclear Science*, 42(6):1689–1706, 1995.

[Fue04] M. Fuerstner. TLD, RPL and Alanine dosimeters, 2004. Presentation given at the 4th LHC RADIATION WORKSHOP, CERN 1 December 2004. Available online: http://www.cern.ch/lhc-radwg.

[Fur03] C. Furetta. *Handbook of Thermoluminescence*. World Scientific Publishing Co., first edition, 2003. ISBN 981-238-240-2.

[Fyn02] C. Fynbo and G. Stevenson. Radiation Environment in the Dispersion Suppressor regions of IR1 and IR5 of the LHC. *CERN LHC-Project-Note-296*, 2002.

[Gaf] Gafchromic Radiochromic Dosimetric Films by ISP Technology, Wayne, NJ, USA. Available online: http://www.ispcorp.com.

[Gaw74] E.T. Gaw and W.G. Oldham. Properties of heavily irradiated MOSFETs. *IEEE Transactions on Nuclear Science*, 21:124–129, 1974.

[Gaz04] R. Gaza, S. McKeever, M. Akselrod, T. Akselrod, C. Yoder, M. Andersen, C. Aznar, J. Marckmann, and L. Bøotter-Jensen. A fiber-dosimetry method based on OSL from Al_2O_3:C for radiotherapy applications. *Radiation Measurements*, 38 (4-6):809 – 812, 2004.

[Ges93] F. Gessin and G. Sarrabayrouse. MOS transistors with $> 1\ \mu$m thick gate oxide for ionizing radiation dosimetry. *In Proc. Mat. Res. Soc. Symp.*, 302:555–560, 1993.

[Gil05] C. Gill. CERN: radiation hardness issues for the next generation of accelerators and experiments. *In RADECS 2005 short course notebook - New challenges for radiation tolerance assessments*, 2005.

[Gla99] M. Glaser, L. Durieu, F. Lemeilleur, M. Tavlet, C. Leroy, P. Roy. New Irradiation zones at the CERN-PS. *Nucl. Instr. & Meth. in Physics Research*, A-426:72–77, 1999.

[Gla00] M. Glaser, F. Lemeilleur, M. Tavlet. Radiation Test Facilities in the New PS East Hall at CERN. *IEEE Transactions on Nuclear Science*, 44:136–141, 2000.

[Gou05] A. Gouldwell-Bates. *Developments in Silicon Detectors and their impact on LHCb Physics Measurements*. PhD thesis, University of Glasgow, 2005. CERN-THESIS-2006-003.

[Gri96] P. Griffin et al. SAND92-0094 (SANDIA National Laboratories, Nov.93), 1996. neutron cross sections taken from ENDF/B-VI, ORNL. See also http://sesam.desy.de/members/gunnar/Si-dfuncs.html .

[Gro00] D.E. Groom et *al.* (Particle Data Group). Review of Particle Physics (RPP). *Eur. Phys. J.*, 15:1–878, 2000.

[Haj02] W. Hajdas, F. Burri, Ch. Eggel, R. Harboe-Sorensen and R. de Marino. Radiation Effects Testing Facilities in PSI during implementation of the Proscan Project. *In Proc. 2002 IEEE Radiation Effects Data Workshop*, pages 160–164, 2002.

[Ham] Photo-detectors data-sheets. Available online from HAMAMATSU photonics products page: http://sales.hamamatsu.com/en/products.php.

[Har04] A. Haran, A. Jaksic, N. Refaeli, A. Eliyahu, D. David, and J. Barak. Temperature effects and long term fading of implanted and un-implanted gate oxide RADFETs. *IEEE Transactions on Nuclear Science*, 51(5):2917–2921, 2004.

[Hel03] A. Helienek, 2003. Investigation on photodiodes for fast particle dosimetry - Summer Student Project CERN EP-TA1-SD.

[Her04] L. Fernandez Hernando. *Development of a Beam Condition Monitor system for the experimental areas of the LHC using CVD diamond*. PhD thesis, Ecole Polytechnique Federiale de Lausanne, Switzerland, 2004. These 3122.

[Hol74] A.G. Holmes-Siedle. The space-charge dosimeter - General principles of a new method of radiation detection. *Nucl. Instr. & Meth. in Physics Research*, 121:169–179, 1974.

[Hol83] A.G. Holmes-Siedle and L. Adams. The mechanism of small instabilities in irradiated MOS Transistors. *IEEE Transactions on Nuclear Science*, 30(6):4135–4140, 1983.

[Hol85] A.G. Holmes-Siedle, L. Adams, B. Pauly and S. Marsden. Linearity of p-MOS radiation dosimeters operated at zero bias. *Elect. Lett.*, 21:570–571, 1985.

[Hol86] A.G. Holmes-Siedle and L. Adams. A review of the use of metal-oxide-silicon devices as integrating dosimeters. *Radiat. Phys. Chem.*, 28(2):235–244, 1986.

[Hol91] A.G. Holmes-Siedle, L. Adams and G. Ensell . MOS dosimeters improvement of responsivity (Dosimétres MOS, amélioration de reponsivite). *In Proc. Radiation Effects in Components and Systems Conference (RADECS 91). IEEE Catalogue 91THO400-2, Montpellier, France, September 9-12*, pages 65–69, 1991.

[Hol02] A. Holmes-Siedle and L.Adams. *Handbook of Radiation Effects*. Oxford University Press, second edition, 2002. ISBN 0-19-850733-X.

[Hub82] J.H. Hubbell. Photon mass attenuation and energy absorption coefficients from 1 keV to 20 MeV. *Int. J. Appl. Radiat. Isot.*, 33:1269–1290, 1982.

[Hug75] R.C. Hughes, E.P. Eernisse and H.J. Stein. Hole transport in MOS oxides. *IEEE Transactions on Nuclear Science*, 22(6), 1975.

[Hug85] R.C. Hughes. Theory of response of radiation sensing Field Effect Transistors. *J. Appl. Phys.*, 58(3):1375–1379, 1985.

[Hug86] R.C. Hughes. Theory of response of radiation sensing Field Effect Transistors in zero bias operation. *J. Appl. Phys.*, 60(3):1216–1217, 1986.

[Huh93a] M. Huhtinen and P. Aarino. Estimation of pion induced displacement damage in silicon. *HU-SEFT R 1993-02*, 1993.

[Huh93b] M. Huhtinen and P.A.Aarnio. Pion induced displacement damage in silicon devices. *Nucl. Instr. & Meth. in Physics Research*, A 335:580, 1993.

[Huh95] M. Huhtinen. Radiation Environment Simulations for the CMS Detector. *CERN CMS Tech. Note 95-198*, 1995.

[Huh00] M. Huhtinen and F. Faccio. Computational method to estimate Single Event Upset rates in an accelerator environment. *Nucl. Instr. & Meth. in Physics Research*, A-450:155–172, 2000.

[Huh02] M. Huhtinen, 2002. Radiation Environment in Experimental (CMS) area - Presentation given at the Radiation Effects course, 10 April 2000.

[Idr04] K. Idri. *Développement d'un système de cartographie par luminescence stimulée optiquement: applications aux contrôles des traitements en radiothérapie avec modulation d'intensité et aux contrôles des faisceaux de protons de haute énergie.* PhD thesis, University Toulouse III, France, 2004.

[Jak02] A. Jaksic, G. Ristic, M. Pejovic, A. Mohammadzadeh, C. Soudre, W. Lane. Gamma-ray irradiation and post-irradiation responses of high dose range RadFETs. *IEEE Transactions on Nuclear Science*, 49(3):1356–1363, 2002.

[Kat86] Y. Katsumura, Y. Tabata, T. Seguchi, N. Morishita, T. Kojima. Fast neutron irradiation effects - III. Sensitivity of alanine systems for fast neutron having an energy of 1 MeV. *Radiat. Phys. Chem.*, 28(4):337–341, 1986.

[Kel91] A. Kelleher, M. O' Sullivan, J.Ryan, B. O' Neill, W. Lane. Development of the radiation sensitivity of PMOS dosimeters. *In Proc. Radiation Effects in Components and Systems Conference (RADECS 91). IEEE Catalogue 91THO400-2, Montpellier, France, September 9-12*, pages 60–64, 1991.

[Kel93] A. Kelleher, N. McDonnell, B. O' Neill, W. Lane. The effect of gate-oxide process variations on the long-term fading of pMOS dosimeters. *Sensors and Actuators*, A37-38:370–374, 1993.

[Kel96] A. Kelleher, W. Lane and L. Adams. Investigation of on-chip high temperature annealing of p-MOS dosimeters. *IEEE Transactions on Nuclear Science*, 43(3):997–1001, 1996.

[Kim93] Y. Kimoto, H. Koshiishi, H. Matsumoto and T. Goka. Total Dose Orbital Data by Dosimeter on-board Tsubasa (MDS-1) Satellite. *IEEE Transactions on Nuclear Science*, 50:2301–2306, 1993.

[Kla97] N.V. Klassen et *al.* Gafchromic MD-55: Investigated as a precision dosimeter. *Medical Physics*, 24(12):1924–1934, 1997.

[Kon92] A.Yu. Konobeyev et al. Neutron displacement cross-sections for structural materials below 800 MeV. *J. Nucl. Mater.*, 186:117, 1992.

[Kra66] G. Kramer. The semiconductor Fast-Neutron Dosimeter - It's Characteristics and Applications. *IEEE Transactions on Nuclear Science*, 13(1):104–110, 1966.

[Kra04] G. Kramberger. Development of ATLAS Radiation Monitor, 2004. Presentation given at the CERN RADMON meeting 16 November 2004. Available online: http://www.cern.ch/lhc-expt-radmon.

[Kra06] G. Kramberger, V. Cindro, I. Mandic, M. Mikuž, M. Zavrtanik. Conceptual Design and Functional Specification of ATLAS Radiation Monitor. *CERN ATL-IC-ES-0017 (EDMS Id: 498365)*, 2006.

[Kri98] E. Krištof. Characterization of neutron flux in the exposure channel F19 of the TRIGA MARK II reactor in Ljubljana. *In Proc. Nuclear Energy in Central Europe '98 Conference, Terme Catež, Slovenia, September 7-10*, pages 43–48, 1998.

[Kro95] S. Kronenberg and G.J. Brucker. The use of hydrogenous material for sensitizing pMOS dosimeters to neutrons. *IEEE Transactions on Nuclear Science*, 42(1):20–26, 1995.

[Kum95] H. Kumurdjian and G. Sarrabayrouse. Unbiased metal oxide semiconductor ionizing radiation dosimeters. *Radiat. Prot. Dos.*, 61(1-3):19–24, 1995.

[Leo93] E. Leon-Florián, H. Schönbacher and M. Tavlet. Data compilation of dosimetry methods and radiation sources for material testing. *CERN-TIS-CFM/IR/93-03*, 1993.

[Leo95] E. Leon-Florián, C. Leroy and C. Furetta. Particle Fluence Measurements by Activation Technique for Radiation Damage Studies. *CERN Divisional Report, CERN-ECP-95-15*, 1995.

[Ler98] C. Leroy, P. Roy. Calculation of particle fluxes in the PS silicon proton irradiation zone. *UdeM-GPP-EXP-98-03 and following updates*, 1998.

[LHC98] LHCb. Technical Proposal. *CERN/LHCC/98-4 LHCC/P4*, 1998.

[Lin80] V.A.J. van Lint, T.M. Flanagan, R.E.Leadon, J.A. Naber, V.C.Rogers. *Mechanisms of Radiation Effects in Electronic Materials.* John Wiley & Sons, 1980.

[Lin99] G. Lindström, M. Moll, E. Fretwurst. Radiation hardness of silicon detectors - a challenge from high-energy physics. *Nucl. Instr. & Meth. in Physics Research*, A-426:1–15, 1999.

[Lis93] H. Lischka, H. Henschel, O. Kohn, W. Lennartz and U. Schmidt. Radiation effects in light emitting diodes, laser diodes, photodiodes and opto-couplers. *In Proc. Second European Conference on Radiation and its Effects on Components and Systems, RADECS 93, Saint-Malo, France, September 13-16*, pages 226–231, 1993.

[Mac97] G.F. MacKay, I. Thompson, A. Ng and N. Sultan. Applications of MOSFET Dosimeters on MIR and BION Satellites. *IEEE Transactions on Nuclear Science*, 44(6):2048–2051, 1997.

[Mal92] L. Malfante. Utilisation de dosimètres semi-conducteurs au silicium autour des accélérateurs de particules a haute énergie. *CERN-TIS-CFM/IR/92-09*, 1992.

[Man04] I. Mandic, V. Cindro, G. Kramberger, E. S. Kristof, M. Mikuz, D. Vrtacnik, M. Ullan and F. Anghinolfi. Bulk Damage in DMILL *npn* Bipolar Transistors caused by Thermal Neutrons versus Protons and Fast Neutrons. *IEEE Transactions on Nuclear Science*, 51(4):1752–1758, 2004.

[McL96] W.L. McLaughlin et *al.* Novel radiochromic films for clinical dosimetry. *Radiat. Prot. Dos.*, 66(1-4):263–268, 1996.

[McW86] P.J. McWhorter and P. S. Winokur. Simple technique for separating the effects of interface traps and traped-oxide charge in metal-oxide-semiconductor transistors. *Appl. Phys. Lett.*, 48(2):133–135, 1986.

[Mer05] J. Merlo and K. Cankoçak. Radiation-hardness studies of high OH^- content quartz fibers irradiated with 24 GeV protons. *in Proc. 9th ICATPP Conf. on astroparticle, particle, space, detectors and medical physics applications*, 2005.

[Met05] Czech Metrology Institute (Inspectorate for Ionizing Radiations). Catalogue of Radioactive Standards. *See also: http://www.eurostandard.cz*, 2005.

[Meu75] J.P. Meulders, P. Leleux, P. Macq, C. Pirat. Fast neutron yields and spectra from targets of varying atomic number bombarded with deuterons from 16 to 50 MeV. *Phys. Med. Biol.*, 20:235, 1975.

[Mis91] O. Missous, F. Loup, J. Fesquet, H. Prevost, J. Gasiot. Optically Stimulated Luminescence of Rare-earth Doped Phosphors. *Eur. J. Solid State Inorg. Chem.*, 28/s:163–166, 1991.

[Mis92] O. Missous. *Contribution à l'étude du phénomenè de luminescence par stimulation optique dans le sulfure de magnésium dopé cérium, samarium en vue d'une utilisation en dosimétrie.* PhD thesis, University Montpellier II, France, 1992.

[Mol99a] M. Moll. *Radiation damage in silicon particle detectors - Microscopic defects and Macroscopic properties -.* PhD thesis, University of Hamburg, Germany, 1999. DESY-THESIS-1999-040, ISSN 1435-8085.

[Mol99b] M. Moll, E. Fretwurst, G. Lindström. Leakage current of hadron irradiated silicon detectors - material dependence. *Nucl. Instr. & Meth. in Physics Research*, A-426:87–93, 1999.

[Mol02] M. Moll, E. Fretwurst, M. Kuhnke, G. Lindström. Relation between microscopic defects and macroscopic changes in silicon detector properties after hadron irradiation. *Nucl. Instr. & Meth. in Physics Research*, B-186:100–110, 2002.

[Mor95] J. Morin, J.C. Arnoud, J. David and P. Zyromski. Widening the Range in Measuring Neutron Fluences with PIN Silicon Diodes. *In Proc. Third European Conference on Radiation and its Effects on Components and Systems, RADECS 95, Arcachon, France, September 18-22*, pages 476–480, 1995.

[Nag92] V. Nagarkar, G. Entine, L. Stoppel, L. Cirignano, P. Swinehart. Solid State Neutron Dosimeter for Space Applications. *IEEE Transactions on Nuclear Science*, 39(4):966–970, 1992.

[Old85] T.R. Oldham. Recombination along the tracks of heavy charged particles in SiO_2 films. *J. Appl. Phys.*, 57(8):2695–2702, 1985.

[Old00] T.R. Oldham. *Ionizing radiation effects in MOS oxides.* World Scientific Publishing Co., 2000. ISBN 9-81-023326-4.

[Oli94] M. Olivier. PIN diode and neutron spectrum measurements at the army pulsed radiation facility. *IEEE Transactions on Nuclear Science*, 41(6):2132–2138, 1994.

[Osr] Infrared emitters data-sheets. Available online from OSRAM Opto-Semiconductors: http://www.osram-os.com.

[Pal82] L.J. Palkuti and J.J. LePage. X-ray wafer probe for total dose testing. *IEEE Transactions on Nuclear Science*, 29:1832–1837, 1982.

[Pas02] B. Pastirčák, 2002. Radiation Levels in ALICE - Presentation given at the CERN ALICE Forum, 20 March 2002.

[Pea01] R. Pease, M. Simons, P. Marshall. Comparison of pMOS total dose response for Co-60 gammas and high-energy protons. *IEEE Transactions on Nuclear Science*, 48(3):908–912, 2001.

[Pla02] D. Plattard, G. Ranchoux, L. Dusseau, G. Polge, J-R. Vaillé, J. Gasiot, J. Fesquet, R. Ecoffet, N. Iborra-Brassart. Characterization of an Integrated Sensor Using Optically Stimulate Luminescence for In-flight Dosimetry. *IEEE Transactions on Nuclear Science*, 49:1322–1326, 2002.

[Pol00] G. Polge, L. Dusseau, S. Matias, D. Gensanne, D. Plattard, J. Fesquet, J. Gasiot, et *al.* Applications to radiotherapy of a dose-mapping system based on the optically stimulated luminescence. *In Proc. IEEE Medical Imaging Conference, Lyon, France, Oct. 2-6*, 2000.

[Pol04] J. Polf, E. Yukihara, M. Akselrod, and S. McKeever. Real-time luminescence from Al_2O_3 fiber dosimeters. *Radiation Measurements*, 38 (2):227–240, 2004.

[Pos95] S. Pospisil, J. Kubasta, I. Stekl, V. Vrba. Comparison of efficiencies of neutron shields containing boron and lithium. *ATLAS Internal Note TECH-No-016*, 1995.

[Pos97] S. Pospisil, I. Stekl, T. Cechak, J. Jakubek, J. Kluson, J. Konicek, V. Linhart, M. Sinor, C. Leroy, *et al.* Experimental tests of neutron shielding in the ATLAS forward region. *ATLAS Internal Note TECH-No-028*, 1997.

[Pot95] K. Potter, M. Höfert and G. Stevenson. Individual monitoring in high-energy stray radiation fields. *CERN TIS-RP/IR/95-19*, 1995.

[Pro82] Z. Prouza, A. Skubal, J. Bohacek and J. Trousil. Interpretation of the response of dosimetric Si-diode. *Jad. Energ.*, 28:318–323, 1982.

[Pro89] Z. Prouza, O. Bratz, B. Sopko, F. Spurny, A. Skubal, J. Kits and F. Latal. Dosimetric parameters of a new Czechoslovak neutron si diode. *Radiat. Prot. Dos.*, 28 (4):277–281, 1989.

[Pug02] V. Pugatch, K.T. Knopfle, Yu. Vassiliyev. Beam Profile Imaging Target. *Nuclear Physics*, A701:204c–208c, 2002.

[Rav02] F. Ravotti. *A study on the response of solid-state dosimeters to be used for the measurement of the radiation environment of the CMS experiment at LHC.* Diploma thesis, Turin Polytechnic, Torino, Italy, 2002. CERN-THESIS-2002-043, in Italian.

[Rav03a] M. Ravnik, R. Jeraj. Research Reactor Benchmarks. *Nucl. Sci. Eng.*, 145:145–152, 2003.

[Rav03b] F. Ravotti and M. Glaser. A study of the response of solid-state dosimeters to be used for the measurements of the radiation environment of the CMS experiment at the LHC. *Tech. Note EST-LEA/2003-03 (CERN EDMS Id. 394670), July*, 2003.

[Rav04a] F. Ravotti. Active dosimeters, 2004. Presentation given at the 4th LHC RADIATION WORKSHOP, CERN 1 December 2004. Available online: http://www.cern.ch/lhc-radwg.

[Rav04b] F. Ravotti, M. Glaser, M. Moll, K. Idri, J-R. Vaillé, H. Prevost, and L. Dusseau. Conception of an Integrated Sensor for the Radiation Monitoring of the CMS Experiment at the Large Hadron Collider. *IEEE Transactions on Nuclear Science*, 51(6):3642–3648, 2004.

[Rav05a] F. Ravotti, M. Glaser and M. Moll. SENSOR CATALOGUE - Data compilation of solid-state sensors for radiation monitoring. *TS-Note-2005-002 (CERN EDMS No.590497), 13 May*, 2005.

[Rav05b] F. Ravotti, M. Glaser, M. Moll, Ch. Ilgner, B. Camanzi and A.G. Holmes-Siedle. Response of RadFET Dosimeters to High Fluences of Fast Neutrons. *IEEE Transactions on Nuclear Science*, 52(4):959–965, 2005.

[Rei03] M. Reinhard. *Radiation hardness study of high purity silicon and the development of a radiation damage monitoring system for silicon devices in mixed radiation field.* PhD thesis, University of Wollongong, Australia, 2003.

[Ros90] A. Rosenfeld et *al.* p-i-n diodes with a wide measurements range of fast neutron dose. *Radiat. Prot. Dos.*, 33(1-4):175–178, 1990.

[Ros94] A.B. Rosenfeld, V. Khivrich, V. Kuts, M. Tavlet, L. Malfante, C. Munoz-Ferrada. Use of Ukrainian semiconductor dosimeters in a CERN particle accelerator field. *IEEE Transactions on Nuclear Science*, 41(4):1009–1013, 1994.

[Ros95] A.B. Rosenfeld, M.G. Carolan, G.I. Kaplan, B.J. Allen, V. Khivrich. MOSFET dosimeters: the role of encapsulation on dosimetric characteristic in mixed-gamma neutron and megavoltage x-ray field. *IEEE Transactions on Nuclear Science*, 42(6):1870–1877, 1995.

[Ros03] A.B. Rosenfeld, M. Yudelev, M. Lerch, I. Cornelius, P. Griffin, V. Perevertailo, I. Anokhin, O. Zinets, V. Khivrich, M. Pinkovaskaya, D. Alexiev, M. Reinhard. Neutron dosimetry with planar silicon p-i-n diodes. *IEEE Transactions on Nuclear Science*, 50(6):2367–2372, 2003.

[Ros06] A. Rosenfeld, 2006. Private communication with A. Rosenfeld, University of Wollongong, Australia.

[Sai97] F. Saigné, L. Dusseau, J. Fesquet, J. Gasiot, R. Ecoffet, J.P. David, R.D. Schrimpf, K.F. Galloway. Experimental validation of an accelerated method of oxide-trap-level characterization for predicting long term thermal effects in metal oxide semiconductor devices. *IEEE Transactions on Nuclear Science*, 44(6):2001–2006, 1997.

[Sai98] F. Saigné. *Une nouvelle approche de la sélection des composants de type MOS pour l'environnement radiatif spatial.* PhD thesis, University Montpellier II, France, 1998.

[Sai00] F. Saigné, L. Dusseau, J. Fesquet, J. Gasiot, R. Ecoffet, R.D. Schrimpf. Prediction of the one year thermal annealing of irradiated commercial devices based on experimental isochronal curves. *IEEE Transactions on Nuclear Science*, 47(6):2244, 2000.

[Sai01] F. Saigné, L. Dusseau, J. Fesquet, J. Gasiot, R. Ecoffet, R.D. Schrimpf, K.F. Galloway. Evaluation of MOS devices' total dose response using the isochronal annealing method. *IEEE Transactions on Nuclear Science*, 48(6):2170–2173, 2001.

[Sar94] G. Sarrabayrouse and F. Gessinn. Thick oxide MOS transistors for ionizing radiation dose measurements. *Radioprotection*, 29(4):557–572, 1994.

[Sar98] G. Sarrabayrouse and S. Siskos. Radiation dose measurements using MOSFETs. *IEEE Inst. & Meas. Mag.*, pages 26–34, 1998.

[Sar01] G. Sarrabayrouse and V. Polischuk. MOS ionizing radiation dosimeters: from low to high dose measurement. *Radiat. Phys. Chem.*, 61:511–513, 2001.

[Sav95] Z. Savić, B. Radjenović, M. Pejović, N. Stojadinović. The Contribution of Border Traps to the Threshold Voltage Shift in pMOS Dosimetric Transistors. *IEEE Transactions on Nuclear Science*, 42(4):1445–1453, 1995.

[Sch89] H. Schraube, E. Weitzenegger, A. Wieser, D. F. Regulla. Fast neutron response of alanine probes. *Appl. Radiat. Isot.*, 40:941–944, 1989.

[Shi99] Y.H. Shin, K.W. Min, J.G. Rhee, D.H. Lee, S.H. Kim, H.S. Kim, S.D. Park, D.K. Sung and S.D. Choi. Analysis of Anomalous TDE data on-board the KITSAT-1. *IEEE Transactions on Nuclear Science*, 46 (6):1586–1594, 1999.

[Shl02] B. Shleien *et al. Handbook of health physics and radiological health.* Lippincott Williams & Wilkins, 2^{nd} edition, 2002.

[Sil05] M. Silari. Passive Dosimeters in the LHC, 2005. Presentation given at the 5th LHC RADIATION WORKSHOP, CERN 29 November 2005. Available online: http://www.cern.ch/lhc-radwg.

[Sim93] D.J. Simon and L. Durieu. Secondary beams for tests in the PS East experimental area. *CERN PS/PA Note 93-21, 4 August*, 1993.

[Sop91] B. Sopko, J. Pavlu, I. Macha, Z. Prouza, F. Spurny, J. Kits and F. Latal. Dosimetric parameters and application of Czechoslovak Long Base Silicon Diode. *In Proc. Radiation Effects in Components and Systems Conference (RADECS 91). IEEE Catalogue 91THO400-2, Montpellier, France, September 9-12*, pages 81–83, 1991.

[Sou94] M. Soubra, J. Cygler, and G. Mackay. Evaluation of dual bias dual metal oxide-silicon semiconductor field effect transistor detector as radiation dosimeter. *Medical Physics*, 21 (4):567–572, 1994.

[Spe68] R.R. Speers. Neutron energy dependence of excess charge carrier lifetime degradation in silicon. *IEEE Transactions on Nuclear Science*, 15:9, 1968.

[SRI] SRIM, Stopping and range of ions in matter. Release 2003. Available: http://www.srim.org.

[Sul90] M. O' Sullivan, A. Kelleher, J. Ryan, B. O' Neill, B. Lane. Temperature Compensation of PMOS Dosimeters. *In Proc. ESA Electronic Components Conference, ESTEC, Noordwijk, The Netherlands*, pages 281–285, 1990.

[Sul92] A.H. Sullivan. *A Guide to Radiation and Radioactivity Levels Near High-energy Particle Accelerators.* Nuclear Technology Publishing, London, UK, 1992. ISBN 1-870965-18-3.

[Sum93] G.P. Summers et al. Damage correlations in semiconductors exposed to gamma, electron and proton radiations. *IEEE Transactions on Nuclear Science*, 40:1372, 1993.

[Swa63] M. Swartz and L. Browne. Experimental calibrations of a silicon rectifier developed as a fast neutron sub-miniature dosimeter. *IEEE Transactions on Nuclear Science*, 10:63, 1963.

[Swa66] M. Swartz, M. Thurston. Analysis of effect of fast-neutron bombardment on the current-voltage characteristic of conductivity modulated p-i-n diodes. *J. Appl. Phys.*, 37(2):745–755, 1966.

[Sze81] S.M. Sze. *Physics of semiconductor devices.* John Wiley & Sons, 2^{nd} edition, 1981.

[Sze85] S.M. Sze. *Semiconductor Devices - Physics and Technology -.* John Wiley & Sons, 1985.

[Tav91] M. Tavlet, M.E. Leon-Florián. PSAIF: The PS-ACOL irradiation facility at CERN. *In Proc. First European Conference on Radiation and its Effects on Components and Systems, RADECS 91, La Grande-Motte, France, September 9-12*, pages 582–585, 1991.

[Tav05] M. Tavlet, 2005. Presentation given at the CERN RADMON meeting, 22 March 2005. Available online: http://www.cern.ch/lhc-expt-radmon.

[Tel97] Telefunken Semiconductors, 1997. Infrared emitters and detectors data book.

[Tem04] K. Temming, 2004. Radiation monitoring with commercial p-i-n diodes - Summer Student Project CERN PH-TA1-SD.

[Tho98] I. Thompson, A. Hartshorn, M. Brown, L. Adams, R. Nickson, A. Ng, T. Cousins, and T. Jones. Dose-Depth and SEU Monitors for the STRV-1c Satellite. *IEEE Transactions on Nuclear Science*, 45(6):2765–2770, 1998.

[TOT99] TOTEM. Total Cross Section, Elastic Scattering and Diffractive Dissociation at the LHC. *CERN/LHC/99-7*, 1999.

[Tui95] P. Tuinenga. *SPICE, A Guide to Circuit Simulation and Analysis Using PSpice.* Prentice Hall, Upper Saddle River, NJ, 3^{rd} edition, 1995.

[Vai03a] J.-R. Vaillé. *Développement, caracterisation et durcissement d'un dosimètre basé sur la luminescence stimulée optiquement destiné aux applications spatiales.* PhD thesis, University Montpellier II, France, 2003.

[Vai03b] J-R. Vaillé, S. Ducret, K. Idri, F. Saigné, S. Matias, N. Iborra, R. Germanicus, R. Ecoffet, L. Dusseau. Hardening of a radiation sensor based on optically stimulated luminescence. *IEEE Transactions on Nuclear Science*, 50(6):2358–2362, 2003.

[Vai05] J-R. Vaillé, F. Ravotti, P. Garcia, M. Glaser, G. Boch, K. Idri, F. Saigné, S. Matias, L. Dusseau et *al.* Online dosimetry based on optically stimulated luminescence materials. *IEEE Transactions on Nuclear Science*, 52(6):2578–2582, 2005.

[Van69] M.H. Van de Voorde. Effects of radiation on materials and components - Megarad dosimetry. *CERN Yellow Report 69-12*, 1969.

[Vet96] F. Vettese, C. Donichak, P. Bourgeault and G. Sarrabayrouse. Assessment of a new p-MOSFET usable as a dose-rate insensitive gamma dose sensor. *IEEE Transactions on Nuclear Science*, 43(3):991–996, 1996.

[Vin02] H. Vincke, I. Brunner, M. Huhtinen. Production of radioactive isotopes in Al, Fe, Cu-samples by stray radiation fields at proton accelerator. *CERN TIS-2002-007-RP*, 2002.

[Vin06] H. Vinke, 2006. Private communication with H. Vinke, CERN SC/RP.

[Wal89] M.P.R. Waligorski, G. Danialy, K.S. Loh and R. Katz. The response of the alanine detector after charged-particle and neutron irradiations. *Appl. Radiat. Isot.*, 40:923–933, 1989.

[Wal94] H.C. Walter. PSI Accelerator facilities users' guide. *PSI Internal Report*, 1994.

[Weg98] M. Wegrzecki, W.Slysz, S.Krzeminski, B.Jaroszewicz. PIN silicon structures processed at ITE. *in Proc. "4th ROSE Workshop on Radiation Hardening of Silicon Detectors", CERN-LEB 98-11, 2-4 December,*, 1998.

[Wij03a] T. Wijnands. On Line Silicon Dosimeter for the LHC Machine electronics, 2003. Presentation given at the 3rd LHC RADIATION WORKSHOP, CERN 4 December 2003. Available online: http://www.cern.ch/lhc-radwg.

[Wij03b] T. Wijnands for the CERN RADWG working group. Electronics and their radiation tolerance for the control of the LHC machine. *in Proc. Workshop on electronics for LHC Experiments (LECC), CERN-2003-006*, pages 97–101, 2003.

[Wij04] T. Wijnands C. Pignard, A. Tsoulou, A. Presland. Increasing radiation levels in the LHC. *in Proc. Workshop Chamonix XIII, CERN-AB-2004-014 ADM*, pages 222–226, 2004.

[Wij05a] T. Wijnands. Interfacing with the LHC accelerator during physics operation. *in Proc. 11th Workshop on electronics for LHC Experiments (LECC), Heidelberg, Germany, TS-Note-2005-054*, 2005.

[Wij05b] T. Wijnands. Radiation monitoring for equipment in the LHC tunnel. *CERN, Functional Specification LHC-PM-ES-0006*, 2005.

[Zup92] C.D. Zupac, K.F. Galloway, R.D. Schrimpf, P. Augier. Effects of radiation-induced oxide-trapped charge on inversion-layer hole mobility at 300 and 77K. *Appl. Phys. Lett.*, 60(25):3156–3158, 1992.

RESUME en Français:

L'accélérateur LHC du CERN et les expériences associées en physique des hautes énergies produisent un environnement radiatif dont la métrologie représente un défi technologique. Le champ de rayonnement produit par les collisions de protons accélérés sera très complexe et localement très intense. La mesure des dépôts d'énergie IEL et NIEL dans les matériaux semi-conducteurs contribuera á assurer la fiabilité des systèmes électroniques pendant le fonctionnent du LHC.

Des dosimètres RadFETs et des *p-i-n* diodes adaptées aux champs de rayonnement du LHC ont été caractérisés sous différents types d'irradiations. A l'issue de cette qualification, deux RadFETs et deux *p-i-n* diodes ont été sélectionnés. L'intégration de ces dispositifs au LHC a été étudiée avec le support des simulations Monte Carlo. En parallèle, différents matériaux OSL synthétisés pour la dosimétrie en champ mixte ont été caractérisés en vue d'une future utilisation au LHC.

TITRE en Anglais:

Development and Characterisation of Radiation Monitoring Sensors for the High Energy Physics Experiments of the CERN LHC Accelerator

---

RESUME en Anglais:

The Radiation monitoring at the High Energy Physic experiments of the LHC, the next CERN particle accelerator, will be a challenge for the existing dosimetry technologies. The radiation environment generated by the high-energy proton collisions will be complex reaching locally very high levels. The measurement of the energy deposition, in the IEL and NIEL channels, for semiconductor materials will therefore help to insure the reliability of the electronic systems during the LHC operation.

In this work, the qualification of RadFET and *p-i-n* diode dosimeters, suitable for the measurements in the LHC radiation field, is presented. A series of two RadFETs and two *p-i-n* diodes have been then selected and characterized in detail in view of their installation at the LHC. Sensors integration issues, supported by dedicated Monte Carlo simulations studies, are also presented. Finally, the applicability of OSL materials for the dosimetry of the mixed fields at the LHC has been also discussed here.

DISCIPLINE:

Dosimétrie, Composants et Systèmes

MOTS-CLES:

Dosimétrie, accélérateurs de particules, CERN-LHC, RadFETs, diodes *p-i-n*, Luminescence Stimulée Optiquement (OSL).

Intitulé et adresse du laboratoire:

INSTITUT D'ELECTRONIQUE DU SUD (IES) UMR UM2-CNRS 5214
ancien Centre d'Electronique et de Micro-Optoélectronique de Montpellier (CEM^2)
Université Montpellier 2
Place Eugène Bataillon, cc83
34095 Montpellier CEDEX 05